UNIVERSITY OF SOUTHAMPTON

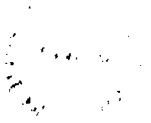

Experimental investigation of dynamic loads on offshore racing yachts

By

Paolo Manganelli

Thesis submitted for the degree of Doctor of Philosophy in March 2006

FACULTY OF ENGINEERING, SCIENCE AND MATHEMATICS
FLUID-STRUCTURE INTERACTION RESEARCH GROUP

March 2006

to my father and mother...

UNIVERSITY OF SOUTHAMPTON

ABSTRACT

FACULTY OF ENGINEERING, SCIENCE AND MATHEMATICS
FLUID-STRUCTURE INTERACTION RESEARCH GROUP

Doctor of Philosophy

Experimental investigation of dynamic loads
on offshore racing yachts
by Paolo Manganelli

With the aim of achieving better understanding of the dynamic phenomena affecting sailing boat structures, the present study investigates the nature of slamming loads experienced by offshore racing yachts and the behaviour of keels subject to inertial loads.

Firstly the implementation of an autonomous data acquisition system on full scale yachts for obtaining information on the frequency and magnitude of slamming is outlined. A specific data processing method is described in detail and considerable attention is given to the recording of the environmental conditions such as sea state and sailing conditions. Results from an extensive series of measurements performed on different boats are discussed.

An experimental investigation of the physical parameters affecting slamming loads and structural response is then presented, highlighting some of the key concepts related to water impact problems. An analytical method for predicting structural response to slamming loads, that should be sufficiently simple for being used as a design tool and yet still capable of accounting for complex features like hydro-elastic phenomena is then devised. Good agreement is shown between some of its predictions and experimental data gathered on model scale yachts.

Finally the response of keel structures is studied: experimental measurements performed on a specific Open60' yacht are used to calibrate an analytical model that is then successfully implemented for deriving estimates of internal loads from the previously discussed full scale measurements.

Contents

List of Tables

List of Figures

Acknowledgements

Most of the work presented in this document has been made possible by the generous support of Jean-Marie Finot. To him goes my most sincere gratitude.

I would also particularly like to thank my supervisor Professor Philip A. Wilson for his patience and support throughout these years, and Professor Anthony Molland for his help with the final version of this document.

I am extremely grateful to Josh Hall, Alex Thomson, Mike Golding and Bernard Gallay, for having allowed me to fit my data acquisition equipment on their boats.

I have greatly benefitted from the help of all the staff at the Wolfson Unit for Marine Technology and Industrial Aerodynamics. I would like to address a special thank to Ian Campbell for his advice and encouragement at the early stages of my work.

Thanks to Geert Kapsenberg for sharing his knowledge about slam patches, to Dr Jan Alexander Keuning for letting us have the two Open60' models, and to Bob Wagemakers, David Grant, Jeremy Elliot and Daniel Holman for helping with all the testing.

I would also like to thank Professor Joe Hammond for all that time spent answering my questions. Never would I have expected to find lectures on signal processing so captivating!

I cannot begin to express my gratitude to my friends and colleagues at "Ship Science": RichyP, Sandy, Martyn, Spyros, Marcos, Mark, I hope we will have plenty more laughs together. All those "espresso" would not have tasted so good without you.

Finally, I would like to thank my parents and my wife Bea. Without your encouragement, understanding and patience, none of this could have been possible.

Nomenclature

$[K]$	stiffness matrix
$[M]$	mass matrix
$[R]$	generic damping matrix
$[R_s]$	structural damping matrix
α	angle of attack
β	deadrise angle (figure 2.1)
Δ	displacement weight
γ_y,γ_z	rotary spring stiffness
$\mathcal{C}(k)$	Theodorsen function , page 152
μ	wave encounter angle - angle between ship positive x axis and dominant wave direction
∇	displacement volume
∇_b	bulb volume
ω	generic circular frequency, expressed in rad/s
ω_e	wave encounter frequency, expressed in rad/s
ω_{sp}	slam patch natural frequency
$\overrightarrow{\omega}$	angular velocity
$\overrightarrow{a_k}$	vector of keel linear acceleration
ϕ	heel angle
ψ	modal shape function
ρ	density of water
τ	time
θ	trim angle
θ_u, θ_v, θ_w	nodal angular displacements relative to local element reference system

θ_x, θ_y, θ_z	nodal angular displacements relative to keel reference system
$\tilde{F}$	generalised force
$\tilde{k}$	generalised stiffness
$\tilde{m}$	generalised mass
$\xi(\tau)$	impulse response function
AR_0	effective aspect ratio of the keel
B	beam
B_{WL}	maximum beam at design waterline
c	horizontal coordinate of the intersection between the hull and the free surface, page 91
C_D, C_L	respectively fluid-dynamic drag and lift coefficient
D	fluid-dynamic drag force
d_b	bulb maximum diameter
DSA	downwind sail area
E_K	Young's modulus or modulus of elasticity of the keel fin material
F	force
F_m	force measured by a slam patch
f_s	sampling frequency
F_{panel}	hydrodynamic force acting on the slam patch panel
Fr	Froude number
G_K	shear modulus of the keel fin material
H_W	wave height (for periodic waves)
$H_{1/3}$	Significant wave height: average of the highest one third wave heights
I_{pp}	pitch moment of inertia about model pivot point
I_{yy}	pitch moment of inertia
k	reduced frequency, page 152
k_{sp}	slam patch equivalent stiffness , page 81
k_{yy}	pitch radius of gyration
L	fluid-dynamic lift force
L_C	unsteady circulatory fluid-dynamic lift
L_p	length of slam patch panel

L_W	wave length
l_{fin}	length of keel fin
L_{OA}	length overall
L_{QS}^{C}	circulatory part of fluid-dynamic quasi-steady lift
L_{QS}^{NC}	non-circulatory part of fluid-dynamic quasi-steady lift
L_{WL}	length of waterline
m_{sp}	slam patch equivalent mass , page 81
N_{el}	number of elements in FE model
p	pressure
q	modal coordinate
r_{sp}	slam patch equivalent damping , page 82
$S_\zeta(\omega)$	generic wave energy spectrum for long crested waves
T	draft
t	time
T_k	draft of keel
U	boat velocity
USA	upwind sail area
V	velocity
V_e	effective impact velocity (cf. equation 4.8)
V_i	measured impact velocity
V_{rb}	velocity component associated with rigid-body motion
X_f	vector of unconstrained modal displacements
$\mathcal{U}, \mathcal{V}, \mathcal{W}$	reference system associated with each element of a finite element model
$\mathcal{X}_k, \mathcal{Y}_k, \mathcal{Z}_k$	reference system associated with the keel, page 131
ADC	Analog-Digital converter
AP	aft perpendicular
DWL	design waterline
EUSP	equivalent uniform static pressure (cf. definition in section 4.4)
FD	Fast Delivery: data obtained in near real-time from satellite instruments
FE, FEM	finite element, finite element model

FP	fore perpendicular
FSO	Full scale output
g	acceleration of gravity, taken as $9.80665 m/s^2$
GRIB	GRIdded Binary, standard file format established by the World Meteorological Organisation for the exchange of gridded meteorological data [135]
GRP	glass reinforced polymer
LCG, L_{CG}	longitudinal centre of gravity
LVDT	Linear Variable Differential Transformer (a type of displacement transducer)
MRE	Maximum Relative Error
NRE	Normalised RMS Error
OPR	Ocean Product or Operational data: data from satellite instruments including corrections made by the space agencies
rms	root mean square
SA	Satellite Altimeter
SNR	signal-to-noise ratio

Chapter 1

Introduction

> Ma prima farò alcuna esperienza avanti ch'io più oltre proceda, perché mia intenzione è allegare prima l'esperienzia e poi colla ragione dimostrare perché tale esperienzia è costretta in tal modo ad operare. E questa è la vera regola come li speculatori delli effetti naturali hanno a procedere, e ancora che la natura cominci dalla ragione e termini nella sperienzia, a noi bisogna seguitare in contrario, cioè cominciando, come di sopra dissi, dalla sperienzia, e con quella investigare la ragione
>
> Leonardo da Vinci

1.1 Background and Objective

The past twenty years have witnessed a formidable progress of the performance of racing yachts. Advances can be ascribed in large part to the new possibilities offered by the use of polymeric composite materials. The science of structural design has moved forward in parallel. Better understanding of the mechanical phenomena together with wider availability of powerful tools like finite element analysis and fast computers have contributed to this development. At present, there is wide agreement on the fact that the main issue for structural designers is not so much "how to design and build a structure to resist a given load", but rather "what loads should the structure be designed for?". As performance is continuously increased, new problems appear, that need to be understood and then solved.

One of the challenges currently faced by designers is the prediction of the dynamic loads acting on and within sailing yacht structures. In this respect, the phenomenon of

slamming and its effects on the structure present one of the areas of greatest interest. A general definition of "slamming" may be given as "the violent impact of the hull of a vessel with the water surface". This can induce extremely high transient local and global loads, which in turn may affect the integrity of the secondary and primary structure.

Historically, the first relevant studies of water-impact loads were published by Von Karman [131] and by Wagner [133] respectively in 1929 and 1932. Their work concentrated on the entry on V-shape sections, typical of planing hulls. By the second half of the twentieth century, a considerable literature had developed on the subject. Most studies were aimed at planing craft (or high speed craft in general) while a lesser part dealt with large displacement vessels (e.g. cargo ships and military vessels). It may be argued that the problem of slamming really began to be addressed in the field of sailing yacht design with the spread of off-shore sailing. Typically, the first serious slamming-induced damage was observed on yachts that entered long off-shore regattas like the British Steel Challenge or the Sydney-Hobart Race. The latter was mentioned by Joubert who, to the author's knowledge, was the first to publish scientific work about slamming loads on sailing yachts back in 1982 [74]. Since then relatively few authors have published on this particular subject [18,19,61,92,110] and the principal reference for design has been found in the rules issued by classification societies (particularly in the ABS "Guide for building and classing off-shore racing yachts" [3]). Most of these rules are largely based on a few major studies, namely the ones by Heller and Jasper [59], Allen and Jones [2], and Savitsky and Brown [117]. which, significantly, were all conducted on high speed planing craft. Hence some of the empirical formulae and parameters that are currently referred to for the definition of slamming loads on sailing yachts, were actually devised for a very different type of vessel.

Nowadays, many structural designers that are involved with sailing yachts, admit to have developed their own methods for the calculation of slamming loads [46,48,95]. Most may be regarded as the result of a heuristic approach and, as the demand for performance and reliability is in continuous progress, a growing number of engineers and researchers agrees on the need for more accurate scientific knowledge on this subject.

It is within this frame that Groupe Finot Naval Architects and the author started a collaboration in 1999. Their initial aim was to build up a body of information

that may help answer questions like: *"what is the maximum hydrodynamic load the hull of a given yacht is likely to experience as the result of slamming during a long oceanic passage?"*, *"what parts of the structure are most loaded by slamming and to which level?"*, or *"how frequently is a given load level likely to be attained as a result of slamming?"*. In particular, the accuracy of the slamming-induced loads predicted by existing analytical and empirical methods, was to be verified through a series of experiments and, if needed, alternative techniques were to be devised.

1.2 Scope and Limitations

All the experimental data on which this study is based were gathered on Open class yachts (in particular on Open 50' and Open 60'). These yachts are designed and built to comply with the rules and regulations issued by the International Monohull Open Classes Association (IMOCA) [68] and by the ISAF Offshore Racing Committee [69]. The combination of their hull shape and displacement-to-length ratio and the conditions they are often sailed in, make these boats particularly prone to slamming. Moreover, structural failures are sometimes observed that are believed to be initiated or promoted by this phenomenon. Hence, studying slamming loads on Open class yachts is both a practical and a necessary task. Despite the study being focused on one particular type of yacht, the author has tried, whenever possible, to draw conclusions that may be applicable for a wider range of sailing boats.

The process of predicting slamming loads for a given yacht may be divided in three stages as follows:

1. the prediction of the sailing conditions: depending on whether ultimate or average loads are sought, this will consist of devising a set of parameters (e.g. encountered waves, wave encounter angle, boat speed, displacement, etc.) that will either result in the worst possible slamming loads or simply correspond to average sailing conditions. The worst case scenario is established either on the basis of previous experience or by cycling through the three stages presented herein. This procedure is sometimes referred to as the definition of the "design wave".

2. the calculation of the motion of the vessel relative to the water surface: this stage is aimed at confirming the occurrence of slamming and at predicting

the relative velocity of the hull before and after impact, indeed a particularly difficult task. Slamming is intrinsically associated with non-linear motion, which may only be described through direct time-domain simulation, a lengthy and computationally expensive technique. Besides, while state-of-the-art softwares are starting to give acceptable results for slender hulls with moderate flare and subject to mildly "non-linear motion" [9, 16, 64, 65, 84], the degree on non-linearity presented by sailing yachts (with very low displacement-to-length ratios, moving hydrodynamic appendages and flexible aerodynamic ones) makes the problem practically too complex to be solved with the currently available tools. It is then still normal practice to make use of empirical methods for the definition of extreme and average motion.

3. the derivation of the hydrodynamic loads and of the structural response: this is typically referred to as the water-impact problem, whereby, given an initial entry velocity and a hull shape, the pressure distribution and the resulting structural response are derived. When studying local loads and response (e.g. for a hull panel), the entry velocity tends to be considered as an independent variable which is generally obtained from seakeeping calculations. On the other hand. when the problem is addressed at a larger scale (e.g. for bow flare slamming, when investigating the response of the primary structure), the motion and the loads cannot be considered separately.

In the present study, no attempt has been made to predict the motion of the examined yachts by any analytical or numerical method. Instead, when needed. the variables that characterise slamming events, have been obtained directly from a very large set of experimental data. Furthermore, attention has been focused on the response of secondary structural elements as this appears to be the area where supplementary knowledge is most widely demanded.

The relation between external slamming loads and the structural response is generally not a straight forward one. More exactly, slamming loads are by nature transient and they act over very short periods of time. The response of the structure is therefore of a dynamic type and its amplitude is not a linear function of the excitation. Moreover, several authors have suggested that hydroelastic effects can play a significant role during slamming, that is to say that, even at a local level, the magnitude of the hydrodynamic loads depends on the way the structure responds. In order to simplify

the task of structural designers who, in most cases, do not wish to carry out complex calculations accounting for dynamics and hydroelastic effects, reference is often made to equivalent design loads. These are the loads which, if applied statically to the structure, would result in the same amount of stress and deformation as produced by the actual loads. The use of design equivalent loads allows structural designers to define scantlings by using only the laws and formulae of statics. With the aim of producing results that are directly usable by the designers, slamming loads are mostly presented in terms of design equivalent loads in the present study. Attention is brought on the fact that both actual and equivalent loads are structure-dependent and that care should be taken when applying the results published herein to yachts different from those presently examined.

Finally, slamming often gives rise to significant inertial loads on sailing yachts. Although such forces are generally not referred to as slamming loads, they are indeed a direct consequence of slamming and can lead to very serious structural failures. In particular, racing yachts with a low displacement-to-length ratio are often subject to very high linear and angular accelerations as the result of slamming. These translate into significant inertial loads, specially acting on the keel ballast and on the rig. While most structures are designed to withstand even the highest inertial loads, there is often concern about the possible relation between such loads and fatigue failures. A failure to gather a sufficient amount of experimental data concerning the rig allowed only the problem of inertial loads on the keel to be treated in the present study.

1.3 Present Study

The first part of the present investigation has been dedicated to the characterisation of slamming events on full-scale yachts. A custom data acquisition system has been developed to carry out measurements during long offshore passages. Compatibly with the constraints imposed by the specific environment in which the acquisition was performed, the rigid body motion of several yachts were recorded during a very large number of slamming events. Sailing and environmental conditions associated with slamming were equally logged. Overall, measurements have been taken during three transatlantic crossings, two round-the-world races and a multitude of shorter offshore passages. Details about these tests are presented in chapter 3.

A detailed study of the parameters affecting bottom slamming pressures on an

Open60' has been performed through a series of tests on a model scale yacht. Experimental results have been compared with a simplified theoretical method for the prediction of design slamming pressures. Some of the details about this part of the study are presented in chapter 4. The results of this investigation have been used to enhance the analysis of the full-scale measurements.

Finally, the problem of the response of the keel structure to inertial loads produced by slamming has been addressed. A finite element model of the keel of an Open60' has been set-up and its dynamic behaviour has been validated against experimental measurements. Particular attention has been devoted to the description of the hydrodynamic damping forces resulting from the transient vibration of the keel and a fully-coupled mechanical-hydrodynamic model of the keel has been established. The details of this model are presented in chapter 6. Ultimately, this part of the study is aimed at obtaining an history of the stresses in the keel structure produced by slamming over long offshore passages. For this, inertial loads associated with each slam are to be derived from the full-scale measurements described in chapter 3.

Chapter 2

Literature review

2.1 Water Impact

Slamming has been the subject of scientific investigation since the pioneering works of Von Karman [131] and Wagner [133]. Both studies were based on expanding plate analogy, whereby the force acting on a wedge striking the water, was considered to be equal to that acting on a flat plate of variable instantaneous width (figure 2.1). Von Karman considered the width of the plate to be equal to the distance between the points where the impacting body intersects the undisturbed free surface (figure 2.1(a)). On the other hand, Wagner's method included a calculation of the water "pile-up" (i.e. the elevation of the free surface due to the flow initiated by the striking body) and the instantaneous width of the plate was taken as the distance between the points where the hull surface intersects the actual free surface (figure 2.1(b)). As a result, the former method gives load estimates for constant entry velocity that are smaller by a factor of $\pi^2/4$ compared with the latter.

Several researchers worked to improve and to extend the models of Von Karman and Wagner. Different theories were developed to account for the effects of variable entry speed, gravity, water compressibility, air cushioning and three-dimensional flows. A comprehensive review of the different contributions can be found in [24], [107] and [137]. In particular, Schnitzer and Hathaway [118] extended Wagner's approach to elliptic section cylinders and found good agreement with experimental results from two-dimensional drops of a rigid circular cylinder with zero trim.

Campbell et al. carried out an extensive investigation of the parameters affecting

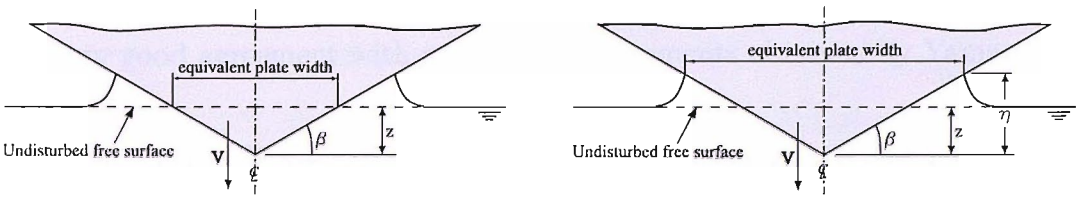

(a) Von Karman Model (b) Wagner Model

Figure 2.1: Expanding plate approximation: comparison of Von Karman and Wagner approach. Von Karman's theory assumes the equivalent plate instantaneous half-width to be $c_{VK}(t) = z(t)/\tan\beta = Vt/\tan\beta$. Wagner's theory considers the equivalent plate to extend up to the intersection between the wedge and the elevated free surface. The resulting half-width is $c_{Wag}(t) = \pi z(t)/(2\tan\beta) = \frac{\pi}{2}c_{VK}$

slamming loads on circular section cylinders, including trim angle variation, fouling of the cylinder surface, free-surface condition prior to impact and water aeration [21, 23–25]. Measurements of the circumferential pressure distribution and of the overall force were performed: a modified Wagner theory proposed by Wellicome showed better agreement with experimental results than the Von Karman method. Theoretical predictions of pressure rise phase along the girth were particularly accurate while account of the test rig dynamic response significantly improved estimates of the overall drag coefficient. Wellicome pointed out that the use of expanding plate analogies was less justified for the prediction of the actual pressure distributions than for the calculation of the total integrated force or of the position of the spray root. Faltinsen [41] showed that, when compared with experimental results, Wagner's solution predicted the position of the maximum pressure with good accuracy, but overestimated its magnitude. Conversely, the Von Karman assumption would lead to good estimates of the maximum pressure, but largely mispredicted its position along the circumference. Faltinsen also reported experimental results by Hagiwara et al. [52] showing that the value of maximum pressure could effectively be considered to be bounded by the value of the acoustic pressure in water.

In order to establish a more accurate model of the fluid flow and hence of the pressure distribution around the impacting body, Zhao and Faltinsen proposed both a matched asymptotic formulation and a numerical boundary element method that avoided the infinite pressure predicted by the original Wagner theory at the spray root [141]. The former was shown to give accurate results for wedges with deadrise angles of up to 30 degrees. The latter, while more computationally expensive, allowed

the exact boundary condition to be satisfied on any arbitrary shape and Faltinsen quoted very good agreement with pressure measurements obtained by Yamamoto et al. [139].

In general, relatively few attempts have been made to evaluate the three-dimensional flow around a body impacting an initially calm free surface. Chuang [28] generalised the asymptotic theory of Wagner into three dimensions. The expanding flat plate approximation was replaced by an expanding disc approximation, which made the new theory applicable to axi-symmetric bodies. Comparison with experimental results showed that this method tended to overestimate the maximum pressures observed for cones [124]. Similarly, Troesch and Kang [129] developed a simplified three-dimensional boundary element method, but could not achieve good agreement with experimental results.

Wraith studied the water impact of several different bodies, including flat plates, wedges, circular cylinders and doubly curved surfaces [137]. A Von Karman-type approach was adopted for wedges and cylinders, while a semi-empirical method was employed for the definition of the added masses of doubly curved hulls. Predictions of maximum local pressures were shown to be in good agreement with the measured values, thus confirming the prior statements of Faltinsen [41] and of Payne [107] that the Von Karman method yields satisfying estimates of the maximum pressures. Results about the overall forces acting on the bodies were less conclusive, particularly for small deadrise angles. The author identified two main reasons for the discrepancies observed on force measurements: firstly the adopted analytical model did not account for the cushioning effects of entrapped air, which would lead to overestimation of the overall hydrodynamic loads. Secondly, forces were obtained indirectly through the measurement of the impacting body vertical acceleration, which, in most cases, was affected by the vibrational response of the test specimens. Such sources of error are typically present in most experimental studies of slamming loads.

The phenomenon of air entrapment has been addressed first by Verhagen [130], Oakley [103] and Koehler and Kettleborough [80]. Verhagen, examined the air flow, pressure distribution and resulting free surface deformation prior to the impact of a flat plate, both through analytical and experimental methods. Oakley extended Verhagen's approach to curved sections approximated by second and fourth order polynomials. He found that the pressure history was very sensitive to the air gap dimensions at the time of first contact between the hull and the free surface and to

the following rate of change of the added mass. He also concluded that the usual assumptions of an initially perfectly flat free surface and infinitely rigid body both lead to significant overestimation of the actual maximum pressures. Koehler and Kettleborough presented an analytical model for the impact of a body falling upon a viscous incompressible fluid. Results were presented that confirmed the qualitative predictions of Oakley and good agreement with experimental results was quoted for flat plates and wedges with very small deadrise angle.

A study of the influence of the structure elasticity on maximum slamming pressures was performed by Sellars [119, 120]. He proposed a new formula for the calculation of the maximum impact pressure that was based on the ratio of the velocities of shock wave propagation in water and in the structure. Results from a wide variety of experiments were reviewed and compared on the basis of this approach. The author concluded that model-scale experiments generally gave conservative estimates of full-scale maximum pressures, mostly due to incorrect scaling of structural properties and of air entrapment effects.

Faltinsen, Kvålsvold and Haugen carried out a very comprehensive study about the influence of hydroelasticity on local slamming loads and structural response [42–45, 55, 85]. Kvålsvold studied the behaviour of the portion of the wetdeck between two transverse stiffeners: the structure was modelled as a Timoshenko beam and the hydrodynamic loads were calculated by taking into account the instantaneous deflection of the structure and the velocity components associated with its deformation. The method used was a two-dimensional one and air entrapment was not modelled. Results were analysed in terms of the maximum stress in the structure. For large initial impact velocities this was found to be linearly dependent on the impact velocity and relatively insensitive to changes of the wave curvature radius. Haugen went on to develop a three-beams model, describing a larger part of the wetdeck. The fundamental approach was the same as Kvålsvold. Theoretical results were compared with experimental results from drop tests of a three-beam plate and reasonable agreement was found. Haugen also presented a simplified study of the collapse of air pockets during the first stages of water impact for a one beam model. Qualitative results were shown suggesting that the presence of air pockets did not affect the maximum amplitude of the structural response. The main parameters affecting the structural response were found to be the impact velocity (in particular, the component of the velocity normal to the free surface), the relative angle between the beams and the free

surface and the bending stiffness of the beams. For small values of the relative angle, hydroelastic effects were shown to be important and maximum stresses were again almost proportional to the relative impact velocity. For larger angles, the response became almost quasi-static and the maximum stress proportional to the impact velocity squared. Global accelerations of the structure, when present, were shown to reduce the maximum stress levels. Drawing from some of the conclusions of Kvålsvold and Haugen, Faltinsen underlined that the design methods that ignore hydroelastic effect can lead to large errors. He argued that equivalent pressure loads (causing the same maximum stresses and strains produced by the actual loads) could be defined for convenience and that these would generally be one order of magnitude smaller than the maximum physical pressures. Besides, he pointed out that, while many researchers have concentrated their efforts on the determination of the maximum local slamming pressures, these are too concentrated in space and time to sensibly affect the response of typical secondary structural elements (e.g. panels, stringers, frames). Finally Faltinsen comments that the main problem in the theoretical analysis of slamming loads remains the definition of the impact velocity as current state-of-the-art computer programs still cannot predict this datum accurately.

Iafrati et al. [26, 67] investigated the influence of hydroelasticity on slamming loads by studying a model of a two-masses oscillator, with the lower mass being a two-dimensional rigid wedge impacting the water surface. Only theoretical results were presented. The influence of the stiffness of the spring connecting the two masses was particularly studied. Theoretical results indicated that the force transmitted by the spring is always lower than the hydrodynamic force acting on the impacting wedge. Also, the authors pointed out that a critical value of the spring stiffness existed that produced the highest hydrodynamic load on the wedge and that this did not correspond to the infinite stiffness case (i.e. perfectly rigid body).

Bereznitski [10] studied the effect of hydroelasticity on the structural response of two-dimensional wedges with variable deadrise angles and structural stiffnesses. Both the fluid domain and the structure were modelled through a finite element method. The phenomenon of air entrapment was described through elements with variable density and different equations of state. Results were presented in terms of the maximum deflection at the tip of the wedge. The author concluded that consideration of hydroelastic effects always lead to lower hydrodynamic loads and structural response when compared with a rigid-body approach. In particular the

reduction of the maximum amplitude of response was found to depend mainly on the ratio between the duration of the hydrodynamic impulse and the first natural period of the structure. The largest reductions (up to 73%) were observed for the smallest values of the ratio, that is, for the structures with the longest natural periods, suggesting that the common design methods founded on rigid-body assumptions give results that are more conservative for the softer structures. From a qualitative point of view, these conclusions were in agreement with those of Faltinsen and Kvålsvold.

2.2 Semi-empirical methods

Given the complexity and number of parameters involved in modelling water impact loads with analytical methods, from the second half of the twentieth century a number of researchers have sought to define methods for calculating slamming loads, which could be used directly in the structural design process.

In 1961 Heller and Jasper published the famous paper "On the structural design of Planing Craft" [59] in which they outlined a semi-empirical design procedure for predicting pressure loads on the structural components of the hull bottom, based on data measured on a 75ft torpedo boat. This was the first attempt at direct calculation of slamming pressures. Starting from pressure and acceleration data measured during full-scale trials, the authors went on to define a relation between acceleration at the vessel LCG, and pressures on the hull bottom. Their paper was ground-breaking in pointing out several key aspects of the slamming phenomenon, in particular:

- peak pressures do not occur over the whole bottom of the vessel at the same instant;
- instead a pressure peak appears on the keel line and travels towards the chine as the hull immersion increases;
- the maximum pressure on any given point of the hull and the maximum vertical acceleration at the LCG do not occur simultaneously: the former tends to appear in the very first instants after contact between the hull and the water, while the latter corresponds to the time when the overall upward hydrodynamic force is greatest, typically when most of the sections are immersed

- the design pressure for a given structural member should be inversely proportional to its area

Allen and Jones [2] worked to validate and extend the results of Heller and Jasper for a larger number of boats with different configurations (e.g. surface effect ships, swaths, etc.). This gave rise to a new design method, published in 1978, which became the reference for most following design-oriented studies. The work of Allen and Jones was based on new experimental data collected on full scale and model scale planing hulls tested by the U.S. Navy. These measurements confirmed most of the findings of Heller and Jasper and, by being performed on a wider set of hull configurations, they allowed the authors to obtain a better understanding of the physical phenomena involved. Owing to the poor correlation found between measurements of peak local pressures and overall hull panel deflections, Allen and Jones concluded that equivalent uniform pressures should be considered when designing structural members, and they outlined a precise design method for calculating these same pressures for different types of boats and structural elements.

In 1973 Ochi et al. [106], proposed a method for evaluating slamming loads at an early design stage. Their work was partly based on observations of slamming events gathered on large commercial and military vessels. They considered slamming to be an event occurring in time according to a Poisson distribution. The necessary and sufficient conditions leading to a slam were assumed to be the emergence from the water of the hull bottom and a relative velocity upon re-entry greater than a defined threshold value. This allowed the probability distribution of slam impact to be defined given the ship draft, the threshold velocity and the variances of relative motion and relative velocity. The slamming pressure was assumed to be approximately proportional to the square of the relative velocity at the instant of impact, with a multiplying factor which was function of the hull section shape. The authors proposed a formula to calculate this factor based upon three parameters of a conformal transformation mapping the hull bottom shape to a circle. The hull relative velocity at impact was approximated by a random variable following a Raleigh probability distribution, hence slamming pressures would be expected to follow an exponential probability distribution. By the laws of statistics, a most probable extreme pressure and an extreme pressure value with an assigned probability of being exceeded could then be defined.

Stavovy and Chuang [124] have proposed a method for calculating impact pressures by discretising the hull surface into infinitesimal areas in such a way that deadrise and buttock angles as well as speed relative to wave surface can be considered to be constant for each one of them. Their model assumed that slamming pressures are determined only by the component of the relative velocity between the hull surface and the water that is normal to the wave surface. With a known relative velocity, pressures could then be deduced from the results of Wagner's wedge impact theory and Chuang cone impact theory. Compared to the method proposed by Ochi et al., Stavovy and Chuang's approach allowed the effects of the forward velocity of the vessel to be accounted for. Besides, it may be argued that this approach could account for three-dimensional flow effects as the relation linking impact velocity to pressures could be based on empirical data from tests on three dimensional shapes.

Through the late 1970s and the 1980s several researchers worked to validate and if possible extend the works of Heller and Jasper and of Allen and Jones. A comprehensive description of all these contribution has been published by Grimsley [51]. Spencer and Henrickson [60, 123] combined the work of the former authors with the methods developed by Fridsma and by Savitsky and Brown [117] for predicting the vertical accelerations and running trim of vessels. The result was a new detailed method for predicting impact pressures intended primarily for the use of the U.S. Coastguard. By calculating design pressures as a function of hull dimensions, proportions, displacement and speed, this method offered a simpler alternative to the existing ones, however it has never been fully validated against model of full scale data.

2.3 Experimental Investigations

In 1984 Reichard [110] published a paper describing an attempt to measure the structural response of a sailing boats when slamming impacts occur. The author reported fitting instruments on several boats to measure boat motion, loads and structural strain. The instrumentation included accelerometers to monitor boat motion and panel movement, pressure sensors to measure hydrodynamic pressure on the hull and strain gauges to measure deformation of structural members. The paper presented data gathered on a 24 foot boat, but no conclusion could be drawn since very few impacts were recorded. The fact that data from pressure transducers and strain gages

showed no apparent correlation with the vessel's accelerations lead the author to conclude that the sensors had possibly been misplaced and that the adopted sampling frequency was probably inadequate.

In 1994 Hentinen and Holm [61] published some results obtained on the 9.4m sailing yacht "Sail Lab" which was instrumented with several different sensors. In particular the authors were able to gather direct measurements of pressure with transducers which had been fitted through the yacht hull. The slamming loads they measured, generally exceeded the expected values, even for a relatively low displacement yacht. The load reduction with increasing panel area was indeed observed but not to the extent predicted by the above mentioned semi-empirical methods and by the ABS Guide. They concluded that the fact that relatively few failures due to slamming loads have been recorded was to be explained by the fact that most yacht structures are more or less involuntarily over-dimensioned as the result of the poor understanding of the nonlinear behaviour of single-skin and sandwich composite structures.

In a series of papers published in the early 1990s, Hayman et al. [56, 57] have presented the research carried on by Det Norske Veritas to study the response of sandwich panels with foam cores and FRP laminates to slamming. In their study, attention was focused mainly on the response to individual slamming events, the influence of panel flexibility and the effect of repeated slamming loads. Experimental data were mainly drawn from drop tests: three different V-shaped hull models were dropped in calm water from different heights and at different heel angles. The models were instrumented with six pressure transducers distributed along the section girth. Recorded peak pressures appeared to be approximately proportional to the square of the velocity normal to the water. Drop tests were carried on until delamination appeared: this was initiated by extensive core shear failure. The authors remarked that equivalent slamming pressures derived on the basis of same maximum flexural deformation are lower than those that would be derived on the basis of maintaining the same shear value. This reduces the margin of safety for sandwich cores and may explain the high incidence of core shear failures observed in sailing and power craft. The comparison of pressure signals from tests with FRP sandwich and stiffened aluminum models of similar geometry showed little difference in the peak pressures while the decaying parts of the signals displayed different characteristics reflecting different dynamic responses. As the effect of repeated slamming loads on foam core materials was considered, it is interesting to note that no significant difference was

found between fatigue life for rapid slamming loads and sinusoidal loading.

Rosen and Garme have presented a series of papers discussing their study of slamming loads and structural response on small high-speed naval craft [112–115]. The main focus of their work was on performing measurements of slamming pressures and the resulting structural deformations and on validating predictions from analytical models. Their experimental investigation showed that, for a given sea state and sailing condition, the local slamming pressures tend to follow a statistical distribution, with the ordinary (lower) wave loads following a Weibull distribution and the higher slamming loads following an exponential distribution. Loads were shown to be proportionally higher when sailing in bow seas (i.e. $\mu = 150^o$), than in head seas (i.e. $\mu = 180^o$). This was attributed to the local deadrise angle being lower in the former case. The analytical model presented by the authors appear to predict the motions of the planing vessel under study with reasonable accuracy. Considering that analytical models exist that can accurately predict the pressure distribution on "V shaped" sections subject to water impact, the results presented by these authors could be considered to be encouraging in terms of being able to finally predict slamming pressures.

Chapter 3

Measurements on full scale yachts

3.1 Experimental set-up

3.1.1 The yachts

The measurements discussed in the present chapter have been performed on four different Open50' and Open60' racing yachts. All of them have been designed by Groupe Finot Naval Architects to comply with the regulations set out by the International Monohull Open Classes Association (IMOCA) [68].

The main characteristics of the yachts have been summarised in table 3.1. Typical lines plan and side elevation for an Open60'are shown in figure 3.1 and 3.2.

Table 3.1: Main test yacht characteristics

	Gartmore	**Group4**	**Voila.fr**	**Magellan**
Class	Open'60	Open'60	Open'60	Open'50
$\mathbf{L_{OA}}$	18.28m	18.28m	18.28m	15.24m
$\mathbf{B_{MAX}}$	5.60m	5.60m	5.75m	4.95m
$\mathbf{L_{WL}}$	18.28m	18.28m	18.28	15.24m
$\mathbf{B_{WL}}$	3.50m	3.50m	3.60m	2.93m
T	4.5m \	4.5m	4.5m	4.12m
$\mathbf{\Delta}$	9.4t	9.2t	10.3t	5.2t
USA	280m2	246m2	230m2	192m2
DSA	500m2	500m2	460m2	345m2
$\mathbf{L/\nabla^{1/3}}$	8.72	9	8.4	8.8
Material (hull)	Carbon Epoxy Nomex	Carbon Epoxy Nomex	Carbon Epoxy Nomex	Carbon Epoxy Nomex

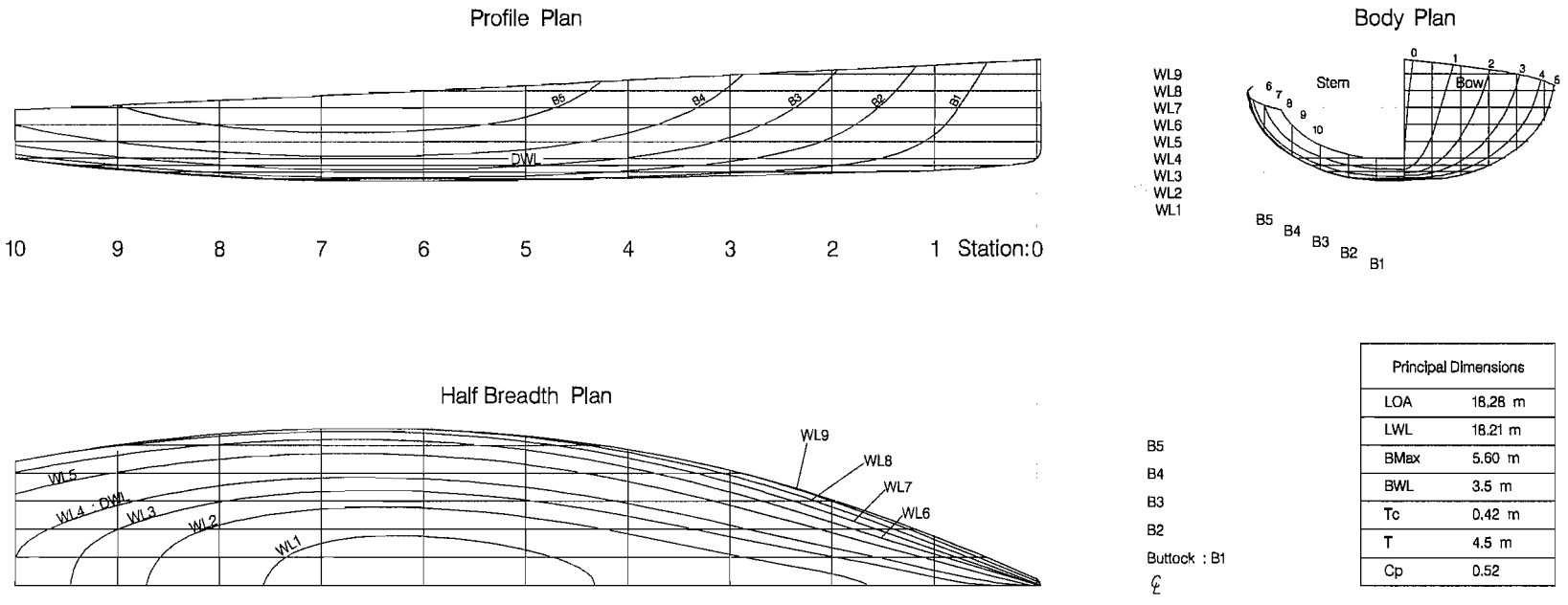

Figure 3.1: Typical Open60' lines plan.

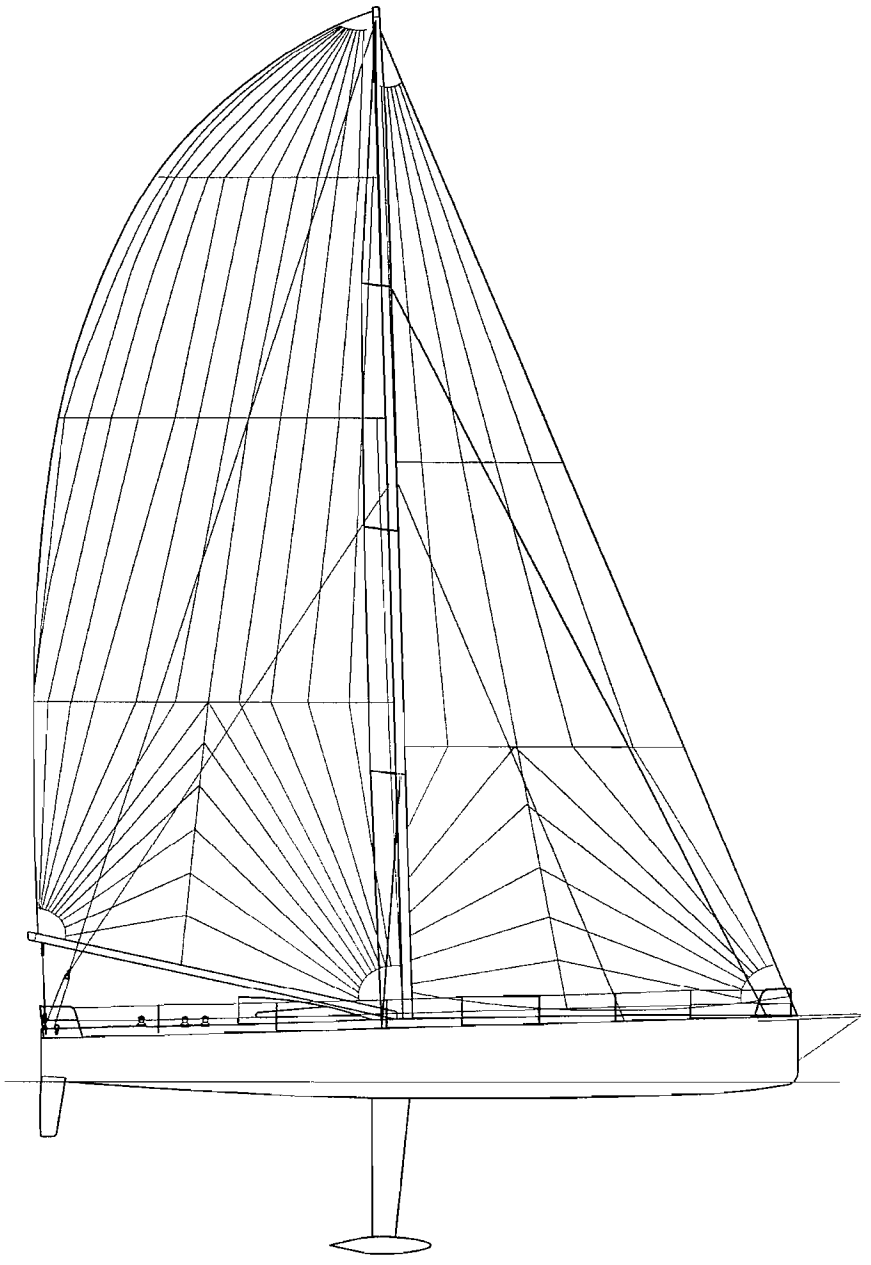

Figure 3.2: Typical Open60' side elevation. Copyright Groupe Finot.

3.1.2 Data acquisition system

A comprehensive description of the data acquisition system and of the types of acquisition used for the present study has been given in a technical report that is included in appendix A.

3.1.3 Series of measurements

Several series of measurements have been performed for the present study. The main ones are described in table 3.2.

For the first series, the author could be onboard to oversee the operation of the acquisition system. On this occasion, different trigger conditions, sampling frequencies and filter cut-off frequencies were tested. The possibility of transferring data from the logging unit to a laptop computer during the trip, allowed larger quantity of information to be stored. Hence, very long time histories of all the signals could be acquired to form a basis for the analysis of the amplitude and statistical distribution of motion data.

The first tests also allowed to further assess the reliability of the system in its actual operating environment (cf. appendix B for a description of preliminary tests in a laboratory). Minor hardware and software problems could thus be identified and corrected to guarantee proper unattended operation in all subsequent tests.

The validity of this approach was later confirmed as two data acquisition systems performed flawlessly and stored data for over 110 days during the Vendée Globe race.

Table 3.2: Principal series of measurements on full scale yachts

Yacht	Trip	Distance	Duration	Slam Rec's	Notes
Gartmore (Open60')	North Atlantic Crossing Guadeloupe - Cherbourg (France)	3484 nm	17 days	-	manual triggering
Magellan (Open50')	North Atlantic Crossing Plymouth (UK) - Newport (RI,USA)	2850 nm	13 days	121	Transatlantic race
Group4 (Open60')	North Atlantic Crossing Newport (RI,USA) - Southampton (UK)	2965 nm	12 days	24	delivery trip
Gartmore (Open60')	Round-the-world trip Les-Sables-d'Olonne - Les-Sables-d'Olonne	27000nm	111 days	1558	Vendée Globe Race
Voila.fr (Open60')	Round-the-world trip Les-Sables-d'Olonne - Les-Sables-d'Olonne	27000nm	111 days	1598	Vendée Globe Race
Gartmore (Open60')	Gulf of Biscay and English Channel Coastal Les-Sables-d'Olonne (France) - Caen (France)	440 nm	2 days	30	delivery trip

3.2 Wave data collection

The state of the sea is a dominant factor in determining the severity and the frequency of slamming. To perform a thorough analysis of the slamming phenomenon, it is then important to record detailed information about the sea state in parallel with the motion of a vessel.

Vessel-borne sensors exist that allow the profile of the waves to be measured in the close vicinity of a ship. These include bow-mounted microwave radars and systems based on standard marine radars. The former measure the relative elevation of the waves passing under the bow and deduce the actual wave height by accounting for the vessel rigid-body motion. The latter analyse the back-scatter in the signal from a conventional radar transceiver to provide estimates of the two dimensional wave spectrum for the near wave field [100]. Unfortunately, none of these devices has yet the weight and power consumption characteristics that would make them suitable for application on an offshore sailing yacht during a race.

Three particular alternatives have then been considered for the present study. They are:

- satellite altimeter observations
- hindcast data from computational wave models
- estimates deduced from recorded boat motion

Details about each one of these solutions are presented in the following sections.

3.2.1 Satellite Altimeter Data

Satellite altimeters are fundamentally nadir viewing microwave radars. Their primary function is to measure the height of the sea surface relative to the earth centre. However, by analysing the specific shape of the reflected signals, these instruments also allow the significant wave height, the moments of the wave spectrum and the velocity of the surface winds to be estimated [8, 36, 140].

Since the first altimeter specifically designed for oceanographic research was launched on the Seasat satellite in 1978, the quantity and quality of available satellite altimeter data has been growing constantly with the subsequent launchings of GEOSAT

(1985-1989), ERS-1 and -2 (active since 1992), Topex/Poseidon (active since 1992) and more recently Jason-1 (2001) and ENVISAT (2002).

The accuracy of satellite altimeter (SA) measurements has been extensively investigated and discussed by Cotton [32,33] and Tolman [127].

Satellite altimeter data are available in various forms. Fast delivery (FD) data can be obtained in near real time as they are transmitted to earth receiving stations from the satellite. FD data are normally affected by several types of errors: corrections must be made to the altimeter measurements to account for the presence of electrons in the ionosphere, the water vapour content of the atmosphere, and, most important, small deviations in the satellite orbit. The space agencies that administrate the satellites (e.g. NASA, ESA) address these errors and distribute the corrected data as operational data (OPR). Finally, OPR data are calibrated and quality controlled by different institutions (e.g. the Southampton Oceanography Centre) and then made available to the research community. Validation of the satellite altimeter data has generally been carried out by comparison against weather buoys data. The latter are considered to offer the most accurate measurements, continuously available over a wide range of locations. Typically, the errors affecting significant wave height measurements from wave buoys have been found to be less than 2% [31,50].

A most extensive collection of SA-buoy comparison data has been published by Cotton [31]. The results in terms of estimated accuracies (i.e. expected standard error) have been summarised in table 3.3. With respect to significant wave height, it has been observed that the rms difference between all satellites and buoy data could be ascribed entirely to co-location and averaging errors [31]. This has lead several authors to consider that $H_{1/3}$ measurements from satellite altimeters can be assumed to be at least as accurate as those from weather buoys [31,83,127].

The accuracy is somewhat lower for the measurements of zero-upcrossing period. The reason for the larger discrepancies lies mainly in the fact that the algorithm used to extract T_z is more recent than those applied for wave height and wind speed and has not been validated as thoroughly as the latter ones.

The main issue regarding the use of sea state measurements from satellite altimeters for seakeeping analysis is that satellite data are necessarily available only along the satellite track.

For the present investigation, only two satellites (ERS-2 and Topex/Poseidon) were operational during the period when data were gathered on the full scale yachts.

Table 3.3: Comparison of satellite altimeter and weather buoy data: rms difference.

ϵ_{rms}	ERS-2	Topex	Poseidon
$H_{1/3}$	0.32 m	0.27 m	0.28 m
U_{10}	1.20 m/s	1.24 m/s	1.27 m/s
T_z	0.65 s	0.58 s	0.48 s

Applying a co-location criterium of 50km maximum distance and 30min maximum time difference (i.e. the conditions typically adopted for comparisons with weather buoys), useful records of significant wave height and wave period occurred with an average period of 53 hours. This interval is considerably longer than the typical time scale for the variation of sailing conditions, hence it was concluded that satellite data had to be complemented with information from other sources.

3.2.2 Wave Model Data

Numerical wave models are commonly used to provide forecasts and hindcasts (i.e. estimates of current or past conditions based on confirmed sets of observations) of the sea state. Estimates of the wave spectra at several different locations are commonly constructed by using wind data from atmospheric models. To this end, the wave models account for growth of waves due to wind input, dissipation of energy by breaking waves, and transfer of energy between spectral component by non-linear interactions. Some models also consider the effects of tidal currents.

Several different wave models have been developed and maintained by meteorological organisations: for the present investigation, data have been sourced from the "WavewatchIII" model, which is run by the National Centres for Environmental Prediction (NCEP/NOAA, U.S.A). The choice was mainly motivated by the fact that the widest amount of information, including validation data, source code and an extensive archive of hindcast data, is publicly available for this model [102].

The global implementation of the "WavewatchIII" model covers all waters between latitudes 77 degrees South and 77 degrees North, with a resolution of 1.25 degrees of longitude by 1 degree of latitude. Hindcast data are available as GRIB files containing the following information for each grid point at 3 hours intervals:

- significant wave height;

- peak period i.e. the period corresponding to the highest peak in the one-dimensional frequency spectrum;
- peak wave direction i.e. the mean direction in the frequency bin corresponding to the peak period;
- wind speed at 10m above sea level;
- wind direction at 10m above sea level.

The model can additionally output estimates of the full two-dimensional spectra, however these are calculated and published by the NCEP for only a limited set of positions corresponding to the locations of moored wave buoys. In theory, since the source code and the necessary input data are publicly available, it would have been possible to perform custom runs of the model to obtain the specific wave spectra for the recorded positions of the test vessels. In practice, this would have required computational resources to which the author did not have access.

Extensive validation data for the "WavewatchIII" model have been published on the website of the NCEP [102]. The comparison of the model input (wind data) and output (sea state data) with weather buoys and ERS-2 FD data indicated that the model accuracy varies with different geographical areas and seasons. Hence, for the present study, a further analysis of the model hindcast data was performed for the time period and locations covered during the 2000 Vendee Globe race. The latter is described in detail in appendix D. In summary, regarding the accuracy of the NWW3 wave model, the following observations could be made:

- the largest discrepancies between model and satellite $H_{1/3}$ data are clearly found in the vicinity of small islands that are not resolved by the global model (e.g. Azores, Canary Islands, Falklands, etc.). In particular, because the model neglects the swell dissipation originated by small islands, estimates of significant wave height are consistently biased high in their vicinity.
- Both NWW3 significant wave height bias and standard deviation relative to wave buoy data increase with higher wave heights. Generally positive bias in swell dominated areas suggests that the model may tend to slightly overestimate this component of the wave spectrum. On average, the rms difference between model and buoy data is equal to 0.12 times the buoy measured wave height.

- Comparison against satellite measurements indicates the model wave height to be biased by less than 0.2 metres (positive and negative) on average. Positive bias is generally observed for the North East Atlantic during the winter season. The rms difference between model and satellite wave height is generally smaller than 0.6 metres with values of up to 1 metre occasionally found at latitudes exceeding 50 degrees North and South. Accounting for the rms error affecting satellite measurements (typically 0.25 metres) and for the error introduced by the co-location process (0.31 metres for the criteria used in the present investigation [31]), the rms accuracy of the model is estimated to be better than 0.45 metres on most instances. Such figures are in accordance with those obtained from the comparison with buoy data.

- Considering the 2000 Vendee Globe Race, the estimated accuracy of the NWW3 data over the recorded tracks of the instrumented yachts is summarised in figure 3.3. The curves represent the amount of time (as a percentage of the total race time) over which the rms accuracy of the model was estimated to be better than a series of given values. Hence, for instance, the figure indicates that the rms accuracy of the NWW3 data was estimated to be better than 0.45m for over 90% of the time, and better than $0.22m$ for more than 60% of the time. On approximately 37% of occasions, the rms difference between satellite and model data was within the typical accuracy range of the satellite measurements.

- Regarding wave period data, it is not possible to compare model output with satellite measurements since the former refer to modal period and the latter to zero-upcrossing period. Comparisons may be carried out between model and wave buoy measurements, however, to the best of the author's knowledge, no data have been published yet that allow the model accuracy to be assessed on a global scale.

- The correlation that can be observed between wind speed and wave height scatter indices suggests that errors in the model output may be attributed primarily to the lack of precision in the input wind data. For illustrative purposes only, a comparison of wind data used as input for the NWW3 model with measurements taken during the Vendee Globe race with the onboard anemometers has been given in figures 3.4-3.6. The comparison is not straight forward, particularly due to the fact that, initially, NWW3 and onboard anemometer data are

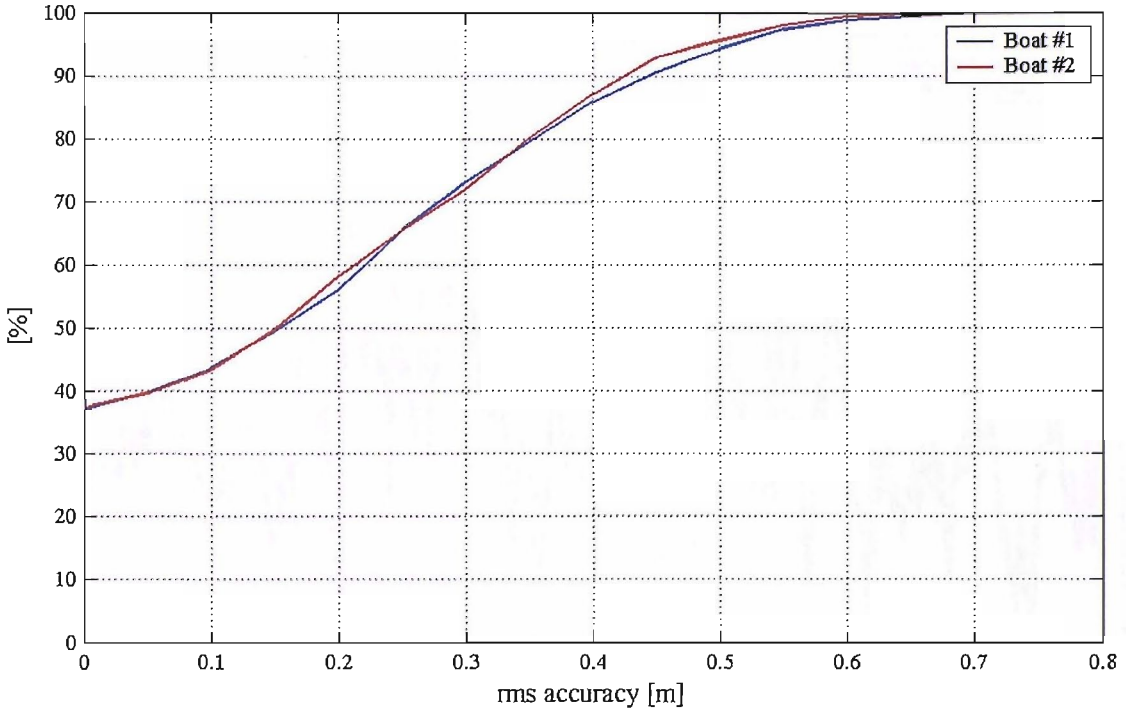

Figure 3.3: Summary of NWW3 estimated accuracy over Vendée Globe 2000 track.

referred to different heights above the sea level (respectively 10 and 26 metres). Besides, the accuracy of the onboard instruments could not be known a priori due to the lack of published calibration data.

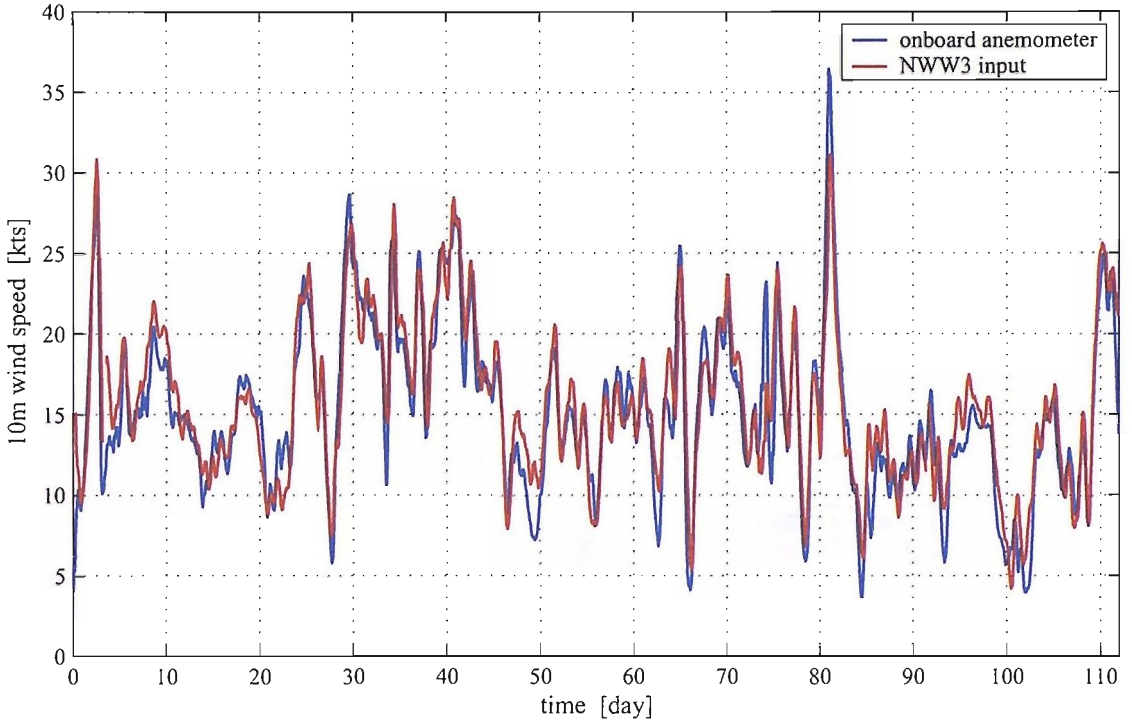

Figure 3.4: Comparison of NWW3 input wind speed with onboard measurements.

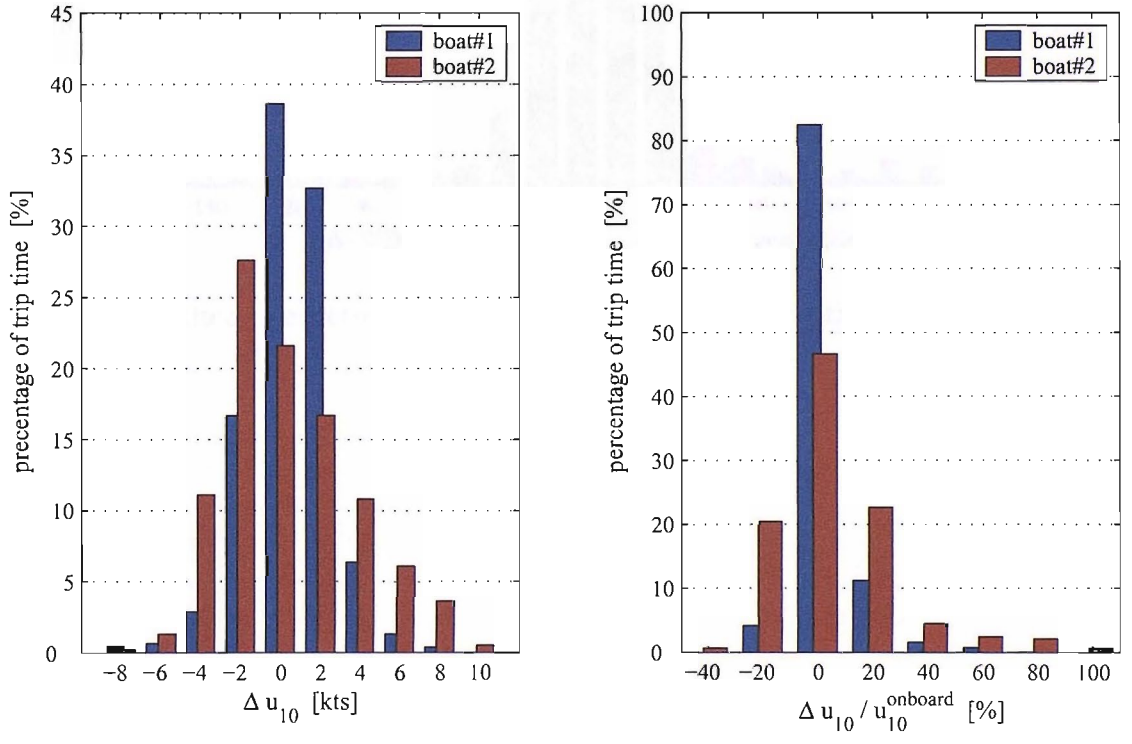

Figure 3.5: Comparison of NWW3 input wind speed with onboard measurements.

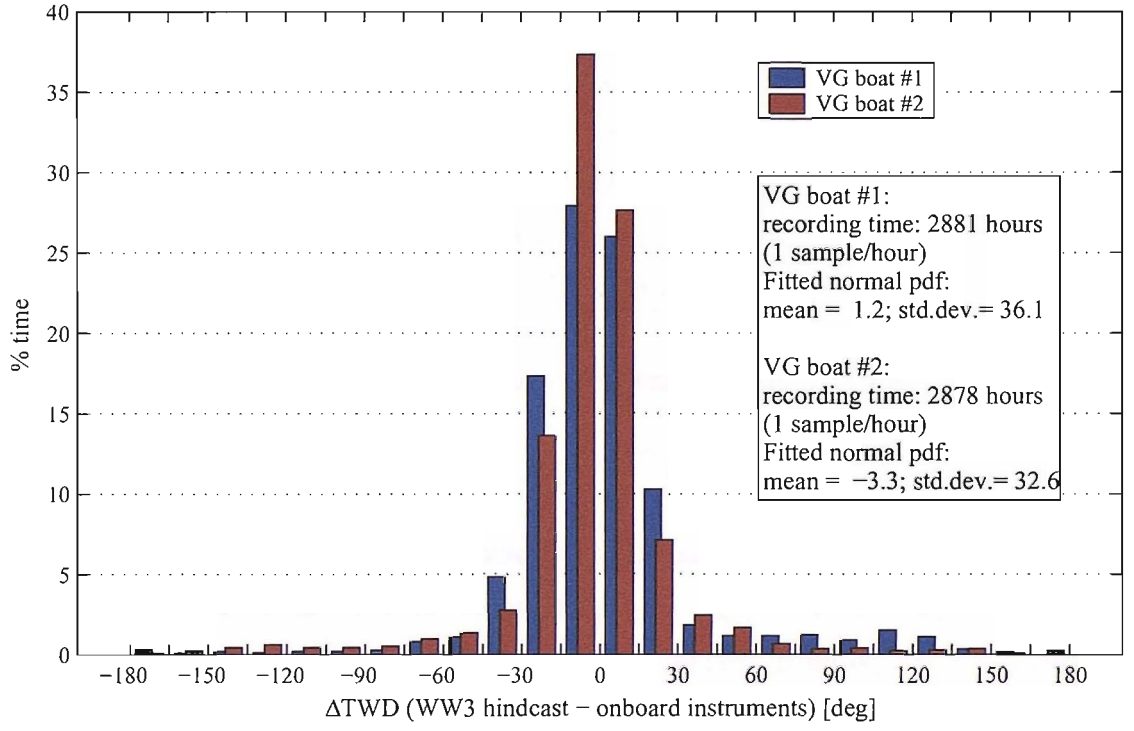

Figure 3.6: Difference between NWW3 hindcast wind direction and onboard measurement.

3.2.3 Wave Height estimate from vessel motion data

Since the motions of a vessel are closely related to the encountered wave spectrum, it is arguable that one should be able to deduce information about the latter from the former. In time, several authors have explored ways of obtaining sea state characteristics from records of ship motion. A brief summary of the different contributions can be found in references [90] and [63].

The standard approach to the problem is to assume that the response of a vessel in waves is almost linear and that waves are long crested. As long as these conditions are verified, the energy spectrum of encountered waves can be obtained as:

$$S_\zeta(\omega_e) = \frac{S_R(\omega_e)}{f_R^2(\omega_e, \mu, U)} \tag{3.1}$$

where $S_R(\omega_e)$ indicates a response energy spectrum (typically for heave, pitch or roll motion) and $f_R(\omega_e, \mu, U)$ is the associated transfer function. The wave energy spectrum observed at a fixed point in the ocean may then be calculated as:

$$S_\zeta(\omega) = \frac{g - 2\omega U \cos\mu}{g} S_\zeta(\omega_e) \tag{3.2}$$

where the relation between absolute wave frequency ω and wave encounter frequency ω_e is known to be:

$$\omega = \frac{g}{2U\cos\mu}\left(1 \mp \sqrt{1 - \frac{4\omega_e}{g} U\cos\mu}\right) \tag{3.3}$$

While this method is generally suitable for stationary floating objects of limited dimensions (like, for instance, wave buoys), two main difficulties arise when considering its application with larger vessels. Firstly, it can be seen from equation 3.3 that, for non stationary vessels (i.e. $U > 0$), the one-to-one correspondence between absolute and encountered frequencies breaks down for all values of μ between 90 and 270 degrees (i.e. quartering and following waves). Secondly, vessels hardly respond to waves with lengths much shorter than their waterline length. In other words, there is often no correlation between higher frequency waves and the motion of a vessel, and the characteristics of the former cannot be deduced from the latter. In mathematical terms, this is illustrated by the fact that, for large encounter frequencies, the value of the transfer function $f_R(\omega_e, \mu, U)$ tends to zero and the division in equation 3.1 produces unacceptable error amplification or simply cannot be carried out.

In order to provide a more accurate and generally applicable tool for determining sea state characteristics, a new method has been developed within the present study, which can be outlined as follows.

It has been assumed that most wave spectra in open waters can be closely approximated by the four-parameter formula:

$$S(\omega) = \alpha\omega^{-l}e^{-\beta\omega^{-n}} \tag{3.4}$$

This formulation is a more general version of the standard ITTC spectra and of the 3-parameter spectra proposed by Ochi [104], which is adequate also for the more sharply peaked narrow-band spectra typical of limited fetch conditions [98].

Assuming that the boat speed (U) and heading relative to the waves (μ) are known, and that the wave spreading is symmetrical about a primary direction of propagation, the problem becomes to determine the values of α, β, l and n that satisfy:

$$S^{U,\mu}_{(\omega_e)}(\alpha,\beta,l,n)f_R^2(\omega_e,\mu,U) = S_\zeta(\omega_e) \tag{3.5}$$

where the encounter frequencies ω_e can be determined univocally from the absolute frequencies ω through:

$$\omega_e = \omega - \frac{\omega^2 U}{g}\cos\mu \tag{3.6}$$

In practice, boat speed can be determined with good accuracy both from water speed sensors and position logs from GPS receivers. The heading relative to the waves may be derived by analysing the relative phase of heave and pitch motion in the lower encounter frequency range. This approach gives the direction of the swell component of the spectrum, which, in general, is associated with the highest peak in the wave energy spectrum and thus determines the dominant wave direction [128]. Particular caution should be exerted when the actual wave spectrum includes swell and wind waves propagating in very different directions.

Equation 3.5 may then be treated as an optimisation problem, where the objective is to find the values of the parameters that minimise the difference between the calculated and the measured motion spectrum "in a least squares sense" (cf. figure 3.7). Convergence to an absolute minimum can be guaranteed by constraining the total energy and the peak frequency of the theoretical motion spectrum to be equal to those of the measured data.

Figures 3.8-3.10 show a comparison of estimates obtained with the present method with data from the NWW3 model. Wave characteristics have been calculated from the motion recorded over a 22 hours period on sailing yacht "Gartmore" during a delivery trip across the Atlantic Ocean (approximately 800 miles East-Northeast of Bermuda Island, around position $34^o39'N, 48^o30'W$). On this occasion the boat was

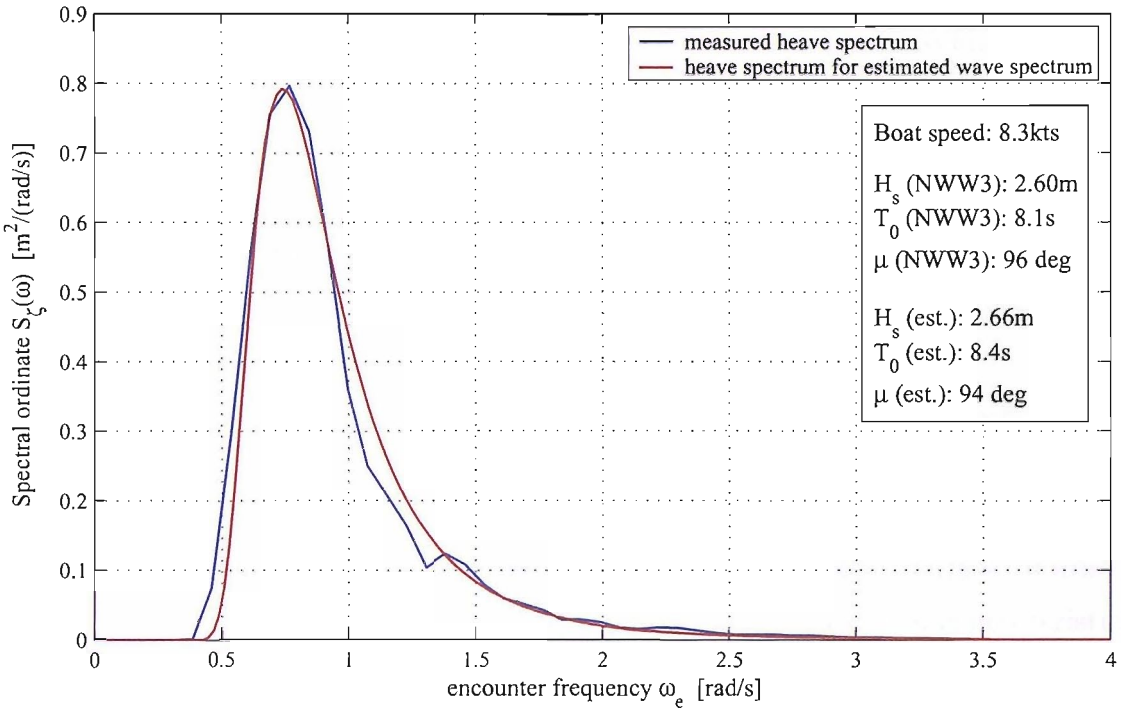

Figure 3.7: Comparison of heave motion spectrum as measured and as obtained from estimated wave spectrum.

sailing on a beam reach at an approximate speed of 11 knots, with a heading relative to the waves of between 80 and 110 degrees.

Both estimates of significant wave height and modal period appear to be in very good agreement with the wave model hindcast (cf. figures 3.8 and 3.9). The rms differences is $0.14m$ for wave heights, that is, within the typical accuracy of the wave model data (ref. 3.2.2), and $0.48s$ for wave periods. The agreement is particularly good towards the end of the sample period, while the wave model seems to underestimate both wave height and modal period in the first part. This may be explained partly by the fact that, as shown in figure 3.11, in the first nine hours of the sample period, the wind direction used for the wave model input is different from the recorded one and less aligned with the direction of the waves (cf. also figure 3.10). As a result, the model is likely to underestimate the amount of energy transferred from the wind to the waves, and consequently the total energy in the wave spectrum.

Figure 3.10 shows the NWW3 and estimated dominant wave direction to compare extremely well, particularly when considering that the boat heading varied by as much as 30 degrees over the sample period. By looking also at figure 3.11, it can be

seen that the direction of the waves tended to follow the evolution of the wind, as it veered under the effect of a low pressure system moving northwards. While the lower frequency components of the spectrum, from which the dominant wave direction was determined, appeared to lag the wind direction by a few hours, it is believed that higher frequency components more aligned with the wind directions were present. It is interesting to note that, by assuming these latter waves to propagate in the same direction as the swell (as the estimation method does), one would overestimate their encounter frequency, which, in turn, would lead to the estimated heave spectrum being skewed relative to the actual one in very much the same way as shown by figure 3.7.

Finally, it shall be remarked that, while extremely encouraging, the results in figures 3.8-3.12 are not sufficient to draw conclusions about the accuracy of either the NWW3 model or the method for the estimation of wave spectrum characteristics from boat motion. To this end, comparisons should be performed on a larger set of data, possibly covering a broader spectrum of conditions. It is expected that the estimation method based on boat motion should be less reliable in more severe sea states, where non-linear effects are more important. Besides, difficulties are likely to arise when particularly unstable weather conditions produce more confused seas with multi-peaked wave spectra.

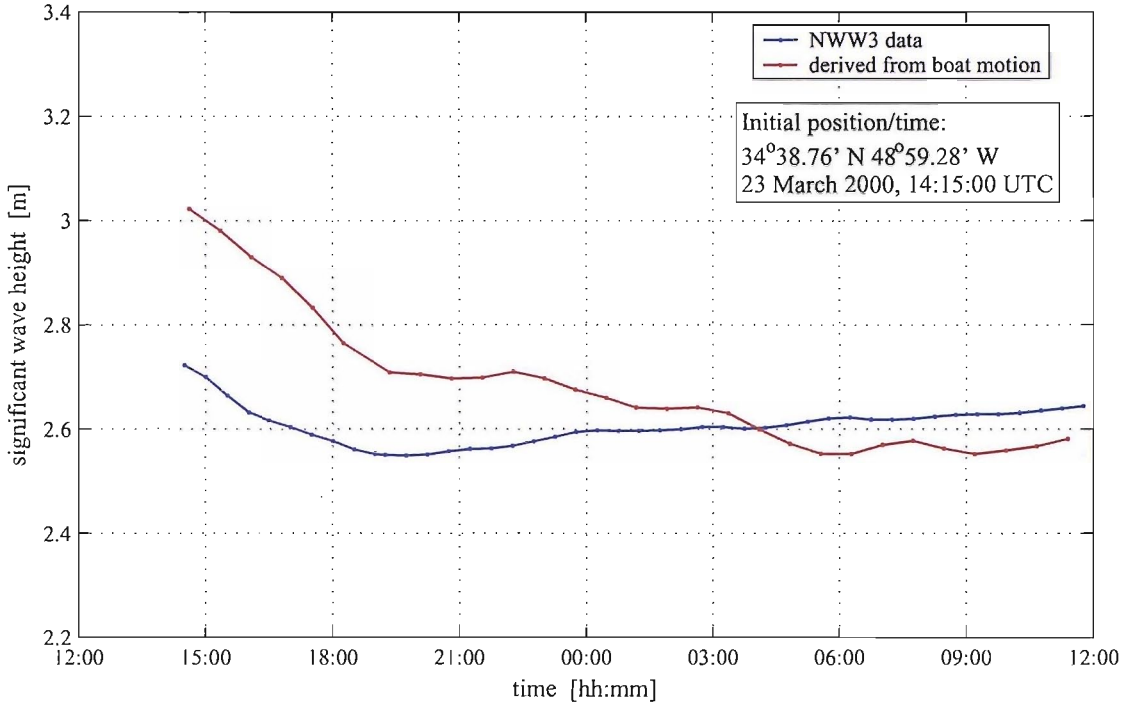

Figure 3.8: Comparison of NWW3 model significant wave height data with estimates from boat motion.

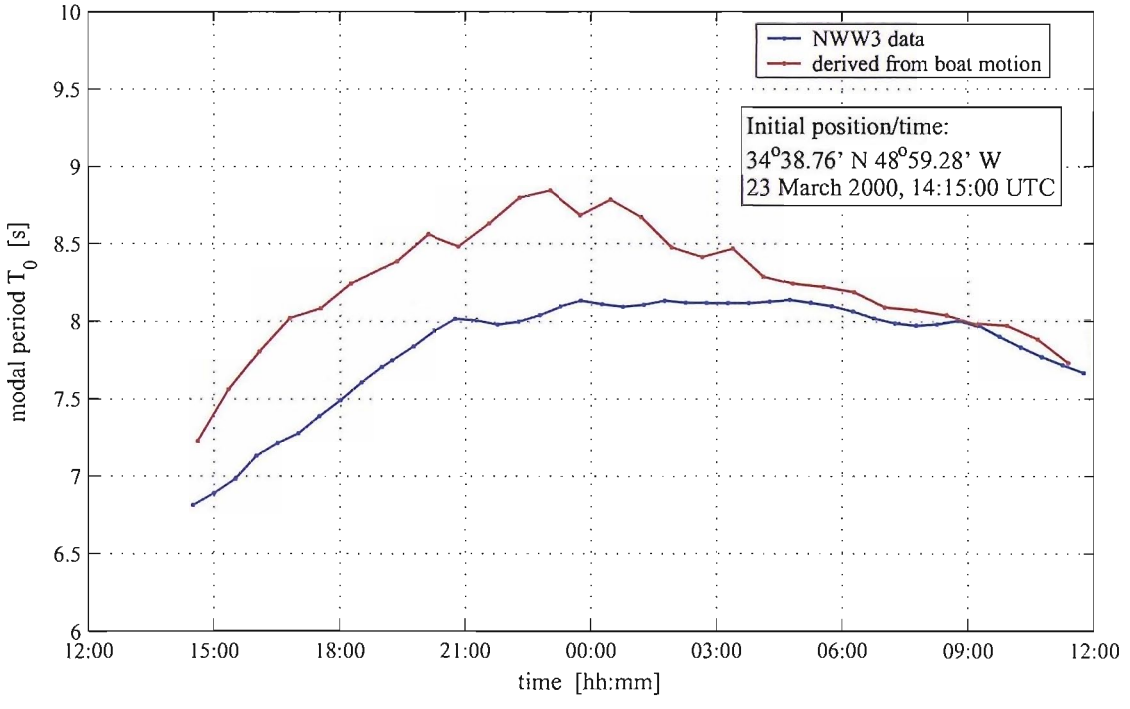

Figure 3.9: Comparison of NWW3 model modal period data with estimates from boat motion.

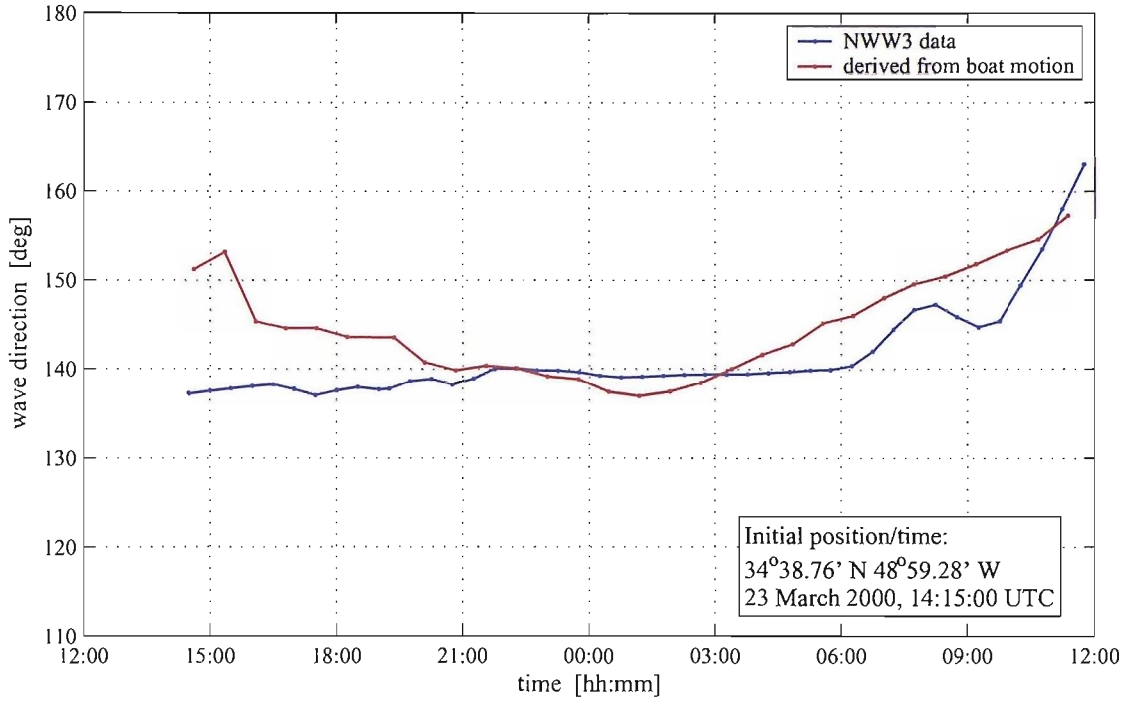

Figure 3.10: Comparison of heading relative to the waves derived from NWW3 data with estimates from boat motion.

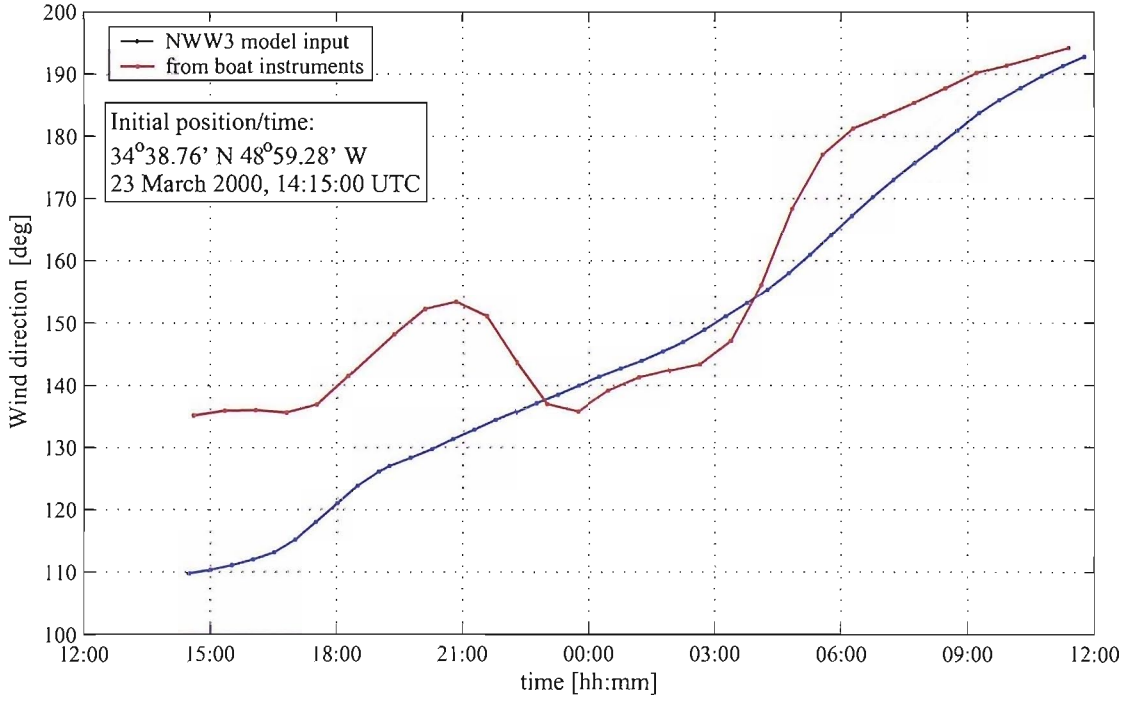

Figure 3.11: Comparison of wind direction recorded by the boat instruments with the input for the NWW3 model.

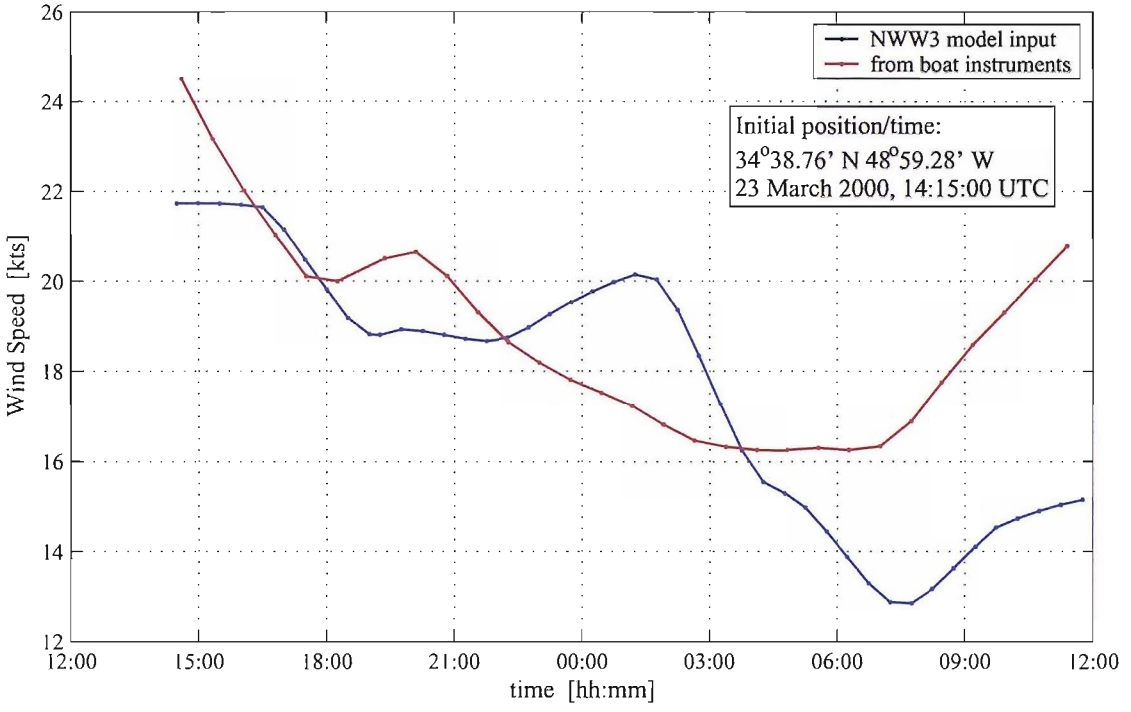

Figure 3.12: Comparison of wind speed recorded by the boat instruments with the input for the NWW3 model.

3.3 Integration of the equations of motion

The data describing the motion of the yachts in their six degrees of freedom have been derived from the measured accelerations through a numerical integration method based on the one described by Miles in [99]. Miles proposed a procedure to measure the oscillatory motion of free running models with a system of seven strapdown accelerometers. With a few minor modifications, his method was found to be applicable to full scale sailing yachts. The theoretical background and the numerical algorithm of the resulting procedure are outlined in the present section.

The notation adopted in the following explanation is illustrated in figure 3.13. Here the location and sensitive axes of the accelerometers (designated as $a1$ to $a7$) are shown relative to a "boat-fixed" reference system "XYZ".

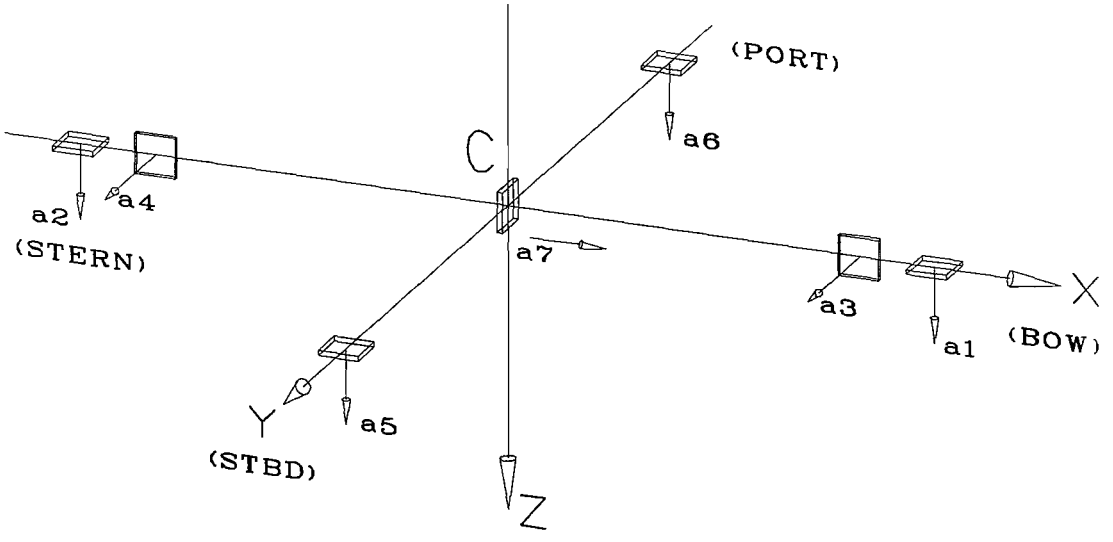

Figure 3.13: Configuration of strapdown accelerometers.

The acceleration of a generic reference point "C" on the vessel (typically the centre of gravity) can be written as:

$$\ddot{\overrightarrow{X_0}}(C) = A\overrightarrow{P} + g\hat{k}_0 \tag{3.7}$$

where $\overrightarrow{X_0}$ denotes a vector of three spacial coordinates relative to an inertial reference system $O\mathcal{X}_0\mathcal{Y}_0\mathcal{Z}_0$ which is orientated with an earth-fixed system and moves with the vessel average velocity. "A" designates the rotation matrix that relates components of a vector defined in the vessel-fixed frame of reference $C\mathcal{X}\mathcal{Y}\mathcal{Z}$ to a vector defined

in the axis system $O\mathcal{X}_0\mathcal{Y}_0\mathcal{Z}_0$. "A" can be written as:

$$A = \begin{bmatrix} \cos\theta\cos\psi & \sin\theta\sin\phi\cos\psi - \cos\phi\sin\psi & \sin\theta\cos\phi\cos\psi + \sin\phi\sin\psi \\ \cos\theta\sin\psi & \sin\theta\sin\phi\sin\psi + \cos\phi\cos\psi & \sin\theta\cos\phi\sin\psi - \sin\phi\cos\psi \\ -\sin\theta & \cos\theta\sin\phi & \cos\theta\cos\phi \end{bmatrix} \tag{3.8}$$

where ϕ, θ and ψ represent the three conventional Euler angles respectively for roll, pitch and yaw. "g" and $\hat{k}_0$ indicate respectively the acceleration of gravity and the unit vector oriented with the $\mathcal{Z}_0$ axis.

P represents a vector of linear acceleration measured at the reference point C along the vessel reference frame $C\mathcal{X}\mathcal{Y}\mathcal{Z}$. Following the notation described in figure 3.13, P is written as:

$$\overrightarrow{P} = \begin{bmatrix} a_7 \\ (x(a_3)\cdot a_4 - x(a_4)\cdot a_3)\,/\,(x(a_3) - x(a_4)) \\ (x(a_1)\cdot a_2 - x(a_1)\cdot a_2)\,/\,(x(a_1) - x(a_1)) \end{bmatrix}^T \times \begin{bmatrix} \hat{i} \\ \hat{j} \\ \hat{k} \end{bmatrix} \tag{3.9}$$

Equation 3.7 gives the translatory acceleration at point C in terms of the measured vector $\overrightarrow{P}$ and of the rotation matrix A, both time dependent. It appears then that, once the Euler angles are determined, A is known and each component of 3.7 can be integrated to obtain the surge, sway and heave velocities and displacements.

In order to obtain the time history of the Euler angles, one may proceed as follows. Firstly, it can be shown (cf. [17]) that:

$$\dot{A} = A\Omega \tag{3.10}$$

$$\text{where } \Omega = \begin{bmatrix} 0 & -\omega_z & \omega_y \\ \omega_z & 0 & -\omega_x \\ -\omega_y & \omega_x & 0 \end{bmatrix} \tag{3.11}$$

where ω_x,ω_y and ω_z indicate the components of angular velocity resolved along the vessel-fixed frame of reference. From 3.10 it follows that:

$$\ddot{A} = \dot{A}\Omega + A\dot{\Omega} = A\Omega^2 + A\dot{\Omega} \tag{3.12}$$

$$\text{hence, } \Omega^2 + \dot{\Omega} = A^{-1}\ddot{A} \tag{3.13}$$

The vector of the translatory acceleration at a generic point "Q" relative to the vessel-fixed reference frame can be obtained as:

$$\begin{aligned} \ddot{\overrightarrow{x}}(Q) &= A^{-1}\ddot{\overrightarrow{x}}_0(Q) \\ &= A^{-1}\left(\ddot{\overrightarrow{x}}_0(C) + \ddot{A}\overrightarrow{x}(CQ)\right) \end{aligned} \tag{3.14}$$

Hence, following the notation of figure 3.13, the acceleration measured by accelerometers 1 and 2 can be written as:

$$a_1 = \hat{k}\left[A^{-1}(\ddot{\vec{x}}_0(C) - g\hat{k}_0)\right] + x_{a_1}\hat{k}\left[A^{-1}\ddot{A}\hat{i}\right] \tag{3.15}$$

$$\text{and } a_2 = \hat{k}\left[A^{-1}(\ddot{\vec{x}}_0(C) - g\hat{k}_0)\right] + x_{a_2}\hat{k}\left[A^{-1}\ddot{A}\hat{i}\right] \tag{3.16}$$

It is then possible to define:

$$\begin{aligned} F_1 &= (a_2 - a_1)/(x_{a_2} - x_{a_1}) \\ &= \hat{k}\left[A^{-1}\ddot{A}\hat{i}\right] \end{aligned} \tag{3.17}$$

and, in a similar way :

$$\begin{aligned} F_2 &= (a_3 - a_4)/(x_{a_3} - x_{a_4}) \\ &= \hat{j}\left[A^{-1}\ddot{A}\hat{i}\right] \end{aligned} \tag{3.18}$$

$$\begin{aligned} F_3 &= (a_5 - a_6)/(y_{a_5} - y_{a_6}) \\ &= \hat{k}\left[A^{-1}\ddot{A}\hat{j}\right] \end{aligned} \tag{3.19}$$

From equations 3.13, 3.17, 3.18 and 3.19 it follows that:

$$\dot{\omega}_x = F_3 - \omega_y\omega_z \tag{3.20}$$

$$\dot{\omega}_y = F_1 + \omega_x\omega_z \tag{3.21}$$

$$\dot{\omega}_z = F_2 - \omega_x\omega_y \tag{3.22}$$

While the values of F_1,F_2,F_3 are derived from the measured data, equations 3.20-3.22 can be solved numerically to obtain the components of angular velocity ω_x,ω_y and ω_z.

It can be shown that, for small angle rotations, the relation between the Euler angles and the components of angular velocity is well approximated by:

$$\omega_x = \dot{\phi} - \dot{\psi} \tag{3.23}$$

$$\omega_y = \dot{\theta}\cos\phi + \dot{\psi}\cos\theta\sin\phi \tag{3.24}$$

$$\omega_z = -\dot{\theta}\sin\phi + \dot{\psi}\cos\theta\sin\phi \tag{3.25}$$

Solving this system of equations for the unknowns $\dot{\phi}$, $\dot{\theta}$, $\dot{\psi}$, yields:

$$\dot{\phi} = \omega_x + \tan\theta(\omega_y\sin\phi + \omega_z\cos\phi) \tag{3.26}$$

$$\dot{\theta} = \omega_y\cos\phi - \omega_z\sin\phi \tag{3.27}$$

$$\dot{\psi} = (\omega_y\sin\phi + \omega_z\cos\phi)/\cos\theta \tag{3.28}$$

Equations 3.26-3.28 can be solved numerically to obtain the Euler angles. The rotation matrix "A" is then defined and equation 3.7 can be integrated to obtain the surge, sway and heave displacements.

3.3.1 Numerical solution

The numerical solution of equations 3.20-3.22 and 3.26-3.28 has been carried out through an iteration process. Equations 3.20-3.22 can be re-written in the form:

$$\begin{aligned}
\dot{\omega}_x(n+1,t) &= F_3(t) - \omega_y(n,t)\omega_z(n,t) \\
\dot{\omega}_y(n+1,t) &= F_1(t) + \omega_x(n,t)\omega_z(n,t) \\
\dot{\omega}_z(n+1,t) &= F_2(t) - \omega_x(n,t)\omega_y(n,t)
\end{aligned}$$

The iteration is started with $\omega_x(1,t) = \omega_y(1,t) = \omega_z(1,t) = 0$ for all times t and, at each step, the value of $\omega_x(n+1,t)$, $\omega_y(n+1,t)$ and $\omega_z(n+1,t)$ is calculated by performing an integration in the frequency domain (cf. the following subsection).

Similarly, equations 3.26-3.28 are solved by re-writing them as:

$$\begin{aligned}
\dot{\phi}(n+1,t) &= \omega_x(t) + \tan\theta(n,t)(\omega_y(t)\sin\phi(n,t) + \omega_z(t)\cos\phi(n,t)) \\
\dot{\theta}(n+1,t) &= \omega_y(t)\cos\phi(n,t) - \omega_z(t)\sin\phi(n,t) \\
\dot{\psi}(n+1,t) &= (\omega_y(t)\sin\phi(n,t) + \omega_z(t)\cos\phi(n,t))/\cos\theta(n,t)
\end{aligned}$$

Here, at each iteration step, integration constants are introduced in order to satisfy the condition that, as per equation 3.9, the average values of the heel and trim angle remain respectively equal to $\bar{\phi} = -\arcsin(\overline{P_2(t)}/g)$ and $\bar{\theta} = \arcsin(\overline{P_1(t)}/g)$.

Both of the above mentioned procedures are very stable and normally require less than ten iterations to converge, even for the most extreme motion amplitudes.

3.4 Numerical integration in the frequency domain

Within the solution technique described in the previous sections, the integration of acceleration and velocity data is performed in the frequency domain. This method carries the advantage of being both numerically efficient and immune from the error amplification problem that typically affects standard time domain integration algorithms.

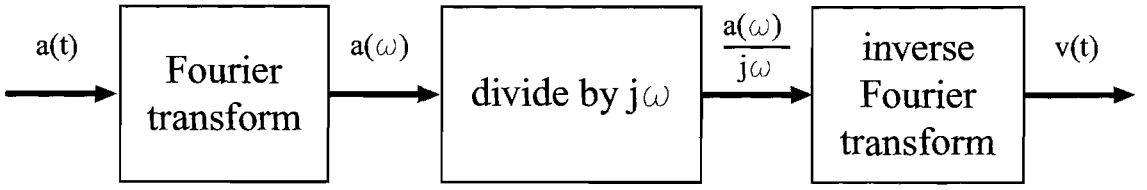

Figure 3.14: Integration in the frequency domain.

The main steps in the procedure are represented schematically in figure 3.14 and may be explained as follows. Consider a function $a(t)$ and its integral $v(t)$: if $v(t)$ has a Fourier transform $v(f)$, then

$$v(t) = \int_{-\infty}^{\infty} v(f) e^{j2\pi ft} df \tag{3.29}$$

from which

$$\dot{v}(t) = a(t) = \int_{-\infty}^{\infty} v(f) j2\pi f e^{j2\pi ft} df \tag{3.30}$$

so $a(f)$, the Fourier transform of $a(t)$, can apparently be obtained as

$$a(f) = (j2\pi f) v(f) \tag{3.31}$$

and since $2\pi f$ is equal to the cyclic frequency ω, it becomes apparent that the Fourier transform of a function can be obtained from the Fourier transform of its derivative by dividing by $j\omega$. Similarly, it may be shown that dividing the Fourier transform of a function by $(j\omega)^2 = -\omega^2$, provides the Fourier transform of the second integral, and so on.

This process is very appropriate for numerical implementation, thanks in particular to the extreme efficiency of the Fast Fourier Transform algorithm. At the same time, some difficulties arise from the conversion to a numerical algorithm that should be carefully taken into consideration.

Firstly, $x(\omega)/j\omega$ cannot be numerically implemented for $\omega = 0$. The mean value of the integral may then not be determined. Fortunately, when considering the motion of a vessel in a seaway, the mean values over time can safely be determined by alternative methods. Hence, for example, it is appropriate to assume that the vertical components of velocity displacement have a zero mean when considered over a sufficiently long period of time. Mean heel and trim angle vary sufficiently slowly for their values to be estimated from the mean of accelerometer signals, while small frequency and constant planar motion can be obtained with GPS receivers.

Secondly, the operation of dividing by $j\omega$ tends to amplify any low-frequency noise or drift that may be present in the spectrum of a signal. This often leads to unacceptable errors, hence, it is necessary to high-pass filter the signals before they are integrated. Miles [99], found that the optimum cut-off frequency for the filter was equal to $0.8 \cdot f_1$, where f_1 would be the frequency such that 99 percent of the energy in the encountered wave spectrum lies above it. This criterium has been found to be appropriate when analysing motion time histories longer than approximately 60 seconds. For shorter ones, it has been concluded that a filter cut-off frequency not lower than $1.2/T_h$ should be adopted, where T_h is the duration of the integrand time history.

Finally, it can be observed that, in order for the frequency domain approach to give the most accurate results, the fist and last value of the integrand functions and of their first derivative should be the same. This happens because the discrete Fourier transform intrinsically treats the functions as if they were periodic with a period equal to the duration of the analysed sample. Differences in the first and last value of the functions and their derivative result in a distortion typically described as the Gibbs phenomenon [82]. A solution for this problem is to effectively force the signals to be cyclic by tapering them at the ends and then overlapping the tapered parts to form a continuous splice [72, 99]. If one can afford to loose the information contained in the tapered parts, the increased accuracy of the results pertaining to the central part of the time histories definitely justifies this type of method.

The complete numerical procedure is summarised in figure 3.15. Numerous validation tests were carried out for this method: they are discussed in detail in the following section.

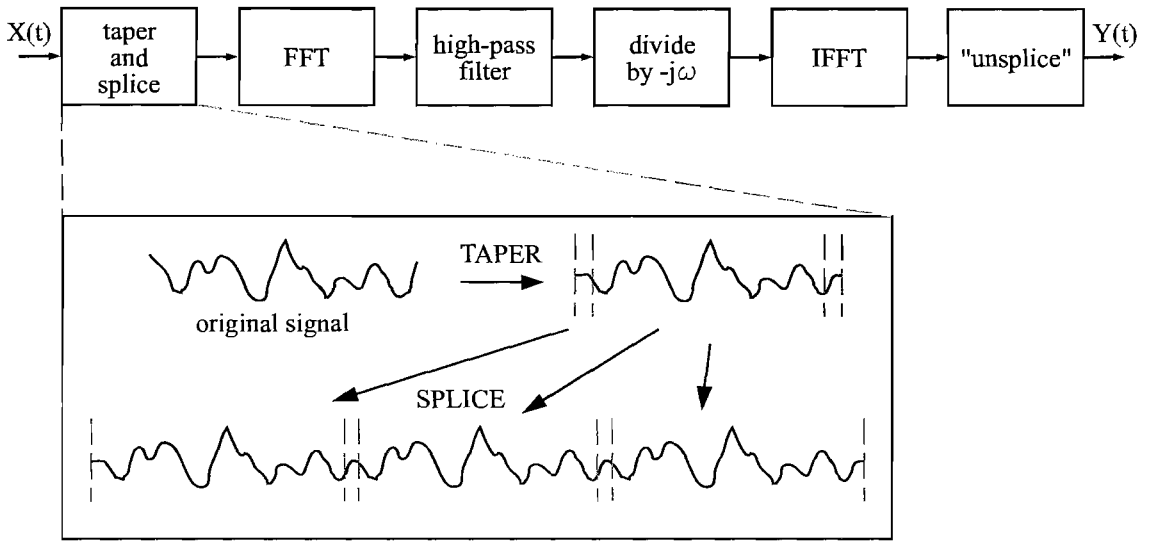

Figure 3.15: Summary of the frequency domain integration method.

3.5 Validation of the numerical integration method

The numerical integration scheme outlined in the previous section has been extensively tested before it was actually employed for the analysis of full scale data. The main aim of the validation tests was to check both the accuracy of the algorithm and its sensitivity to possible errors in the data. The validation procedure was split in two main parts: in the first, tests were performed with artificial simulated data. In the second, the data acquisition system was mounted on a scale model running in a towing tank and measurements were compared against those available from the tank equipment.

3.5.1 Tests with simulated motion data

In order to verify the accuracy of the numerical method, the first test consisted of simulating boat motion, calculating the corresponding acceleration at the location where the accelerometers would normally be fitted, and then checking how closely the original motion could be reconstructed from these data through our algorithm.

Artificial motion data were produced by generating time histories of wave elevation for different ITTC spectra, and then applying standard heave and pitch response amplitude operators measured for the same Open60' yacht [126]. Surge, sway, roll and yaw motion were then determined by assuming constant amplitude ratios and phase differences relative to heave and pitch. The rigid-body velocities and accelerations

corresponding to these motion could be calculated analytically, thus errors associated with numerical derivation were avoided.

The accelerations theoretically measured by each sensor - including the contribution of gravity - were taken as input for the numerical integration algorithm. The results in terms of accelerations, velocities and displacements at the centre of gravity of the boat could finally be compared with the original simulated data.

The influence on the accuracy of the method has been investigated for the following parameters:

- duration of the signals time histories
- average heel and trim angles
- motion amplitude
- encounter frequency
- noise affecting the recorded signals
- accelerometer offset and range errors
- accelerometers transverse sensitivity

The basis for comparison has been defined with the following parameters:

- test length : $60s$
- sampling frequency : $50Hz$
- average heel angle ($\bar{\phi}$) : 12deg
- average trim angle ($\bar{\theta}$) : 2 deg
- significant wave height : $4m$
- wave modal period (T_0) : $7s$
- boat speed : $9kts$
- wave encounter angle : $135deg$
- noise-free signals and no transverse sensitivity

The goodness of the fit between the actual and calculated data has been expressed through two indexes: the Normalised RMS Error (NRE) and the maximum relative error (MRE). They are defined respectively as:

$$NRE = rms\left[x(t) - \tilde{x}(t)\right] / (4 * rms\left[\tilde{x}(t)\right]) \tag{3.32}$$

and

$$MRE = max\left[x(t) - \tilde{x}(t)\right] / (max\left[\tilde{x}(t)\right] - min\left[\tilde{x}(t)\right]) \tag{3.33}$$

where $\tilde{x}(t)$ represents the actual motion and $x(t)$ the motion estimated from the accelerometer signals.

Even with a fixed set of conditions (i.e. significant wave height, encounter frequency, boat attitude, etc.), the NRE and MRE show a small variability depending on the particular time history of the motion. Hence, for each set of conditions, one hundred different irregular wave time histories were generated and the mean of all the resulting NREs and MREs was calculated.

Initially, tests were performed for both the case of perfectly correlated motion (i.e. constant phase difference and amplitude ratio between the different components) and totally uncorrelated motion (i.e. phase difference and ratio randomly variable). The second mode gave generally worse accuracy, hence it was adopted for all subsequent simulations.

The result of a typical test with the standard conditions is shown in figure 3.16. The initial and final 5 seconds of the record have been discarded because of the errors introduced by the splicing procedure described in the previous pages. The accuracy of the estimated motion is generally excellent. Heave, roll, and pitch show better precision than surge and sway motion. This effect is always present and is due mainly to the fact that, in normal sailing conditions, the longitudinal and lateral accelerations are strongly coupled with gravity through the sines of roll and pitch, while vertical accelerations are only weakly influenced by gravity. Hence, small errors in the estimate of roll and pitch result in much more substantial deviations in the estimates of surge and sway.

The numerical details illustrating the influence of each parameter are given in Appendix C. In summary, it can be observed that:

- The results are always more accurate for the acceleration estimates and they become less precise for velocities and displacements as each stage of integration introduces further small errors.

- The accuracy of the estimates is improved with increasing durations of the analysed signals. The larger errors at the shorter durations are explained by the fact that the approximation of zero mean motion introduced by the high-pass filtering process is not justified over short periods.

- No sensible degradation of the results is observed for average heel angles up to 30 degrees.

- The method is stable and gives accurate results for significant wave heights up to 8 metres. For up to 4 metres significant wave height, the iterative solution technique discussed in section 3.3.1 converges in less than 7 iterations, while for heights greater than eleven metres convergence is not always reached.

- The method appears to be very sensitive to the wave encounter angle (μ). This dependence actually reflects the influence of mean encounter frequency. As μ gets smaller, the motion spectrum is shifted towards lower frequencies and high-pass filtering combined with shorter recording times gradually introduce significant errors. However, with respect to the analysis of motion that involve slamming, the results given in table C.4 are believed to be conservative. These data have been obtained on the basis of a constant boat velocity of 9 knots: for an Open60', slamming in reaching and running conditions, where μ is generally smaller than 90 degrees, will take place at speeds typically higher than 13 knots.

- To ensure good accuracy, the rms noise affecting the accelerometers signals should not be greater than $0.2m/s^2$, the "zero-offset" error should be kept below $0.4m/s^2$, the "linearity" error below 2.5% and the transverse sensitivity of the accelerometers should be less than 2%.

3.5.2 Tests on a towing tank model

A further verification of the numerical integration scheme was carried out through a series of tests on a $1/6^th$ scale model of a 31' cruising yacht. Accelerometers were fitted to the model in the way they would be placed on a full scale yacht. The model was allowed to perform only heave and pitching motion as it was run through irregular waves. The motion data measured by the displacement transducers attached to the towing post could then be compared with those obtained from the accelerometers.

A total of 21 runs were performed with four different heel angles (0,11,19 and 23 deg), and constant speed, significant wave height and modal period. If scaled up for a 60' boat, the test conditions were equivalent to $V = 6.48kts$, $H_{1/3} = 4m$, $T_0 = 11.9s$.

The results of the comparison are summarised in figure 3.17, where the mean normalised rms errors are shown for each series of runs at a different heel angle. These data indicate a satisfactory but somewhat lower accuracy in comparison with the simulations discussed in the previous section. The reason is to be found in the relatively lower encounter frequency and recording length, both factors affecting the quality of the numerical results, as shown by tables C.4 and C.1.

Performing simulations with the same parameters used for the towing tank tests (i.e. recording length, significant wave height, modal period, boat speed, accelerometers nominal characteristics, etc.), yielded mean NREs very similar to those obtained with the actual tank data at 0 heel angle. On the other hand, the increase in the NREs with higher heel angles could not be reproduced. A possible explanation for this discrepancy could be found in the significant deformation that was observed in the model-towing post attachment under the action of the transient yaw and roll moments occurring at the higher heel angles.

From both the tests on the simulated motion and on the tank model it was concluded that the data acquisition system and the numerical algorithm could be trusted to measure the acceleration and velocity of a yacht with very good accuracy. Heave displacement and roll and pitch angles may also be regarded as accurate, while significant errors may be expected for surge, sway and yaw displacements, particularly at low wave encounter frequencies.

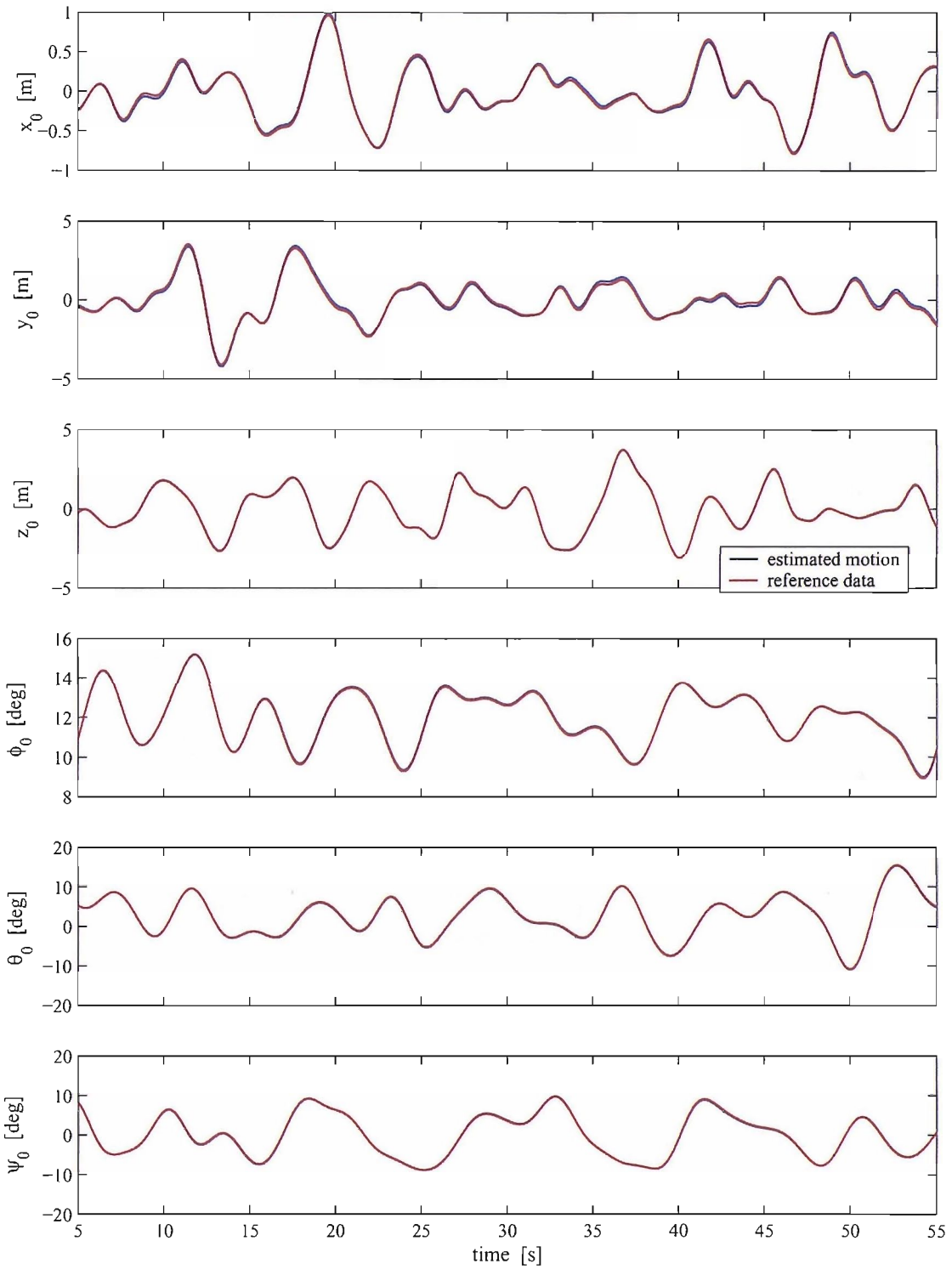

Figure 3.16: Example of comparison between synthesised and estimated motion data (uncorrelated case).

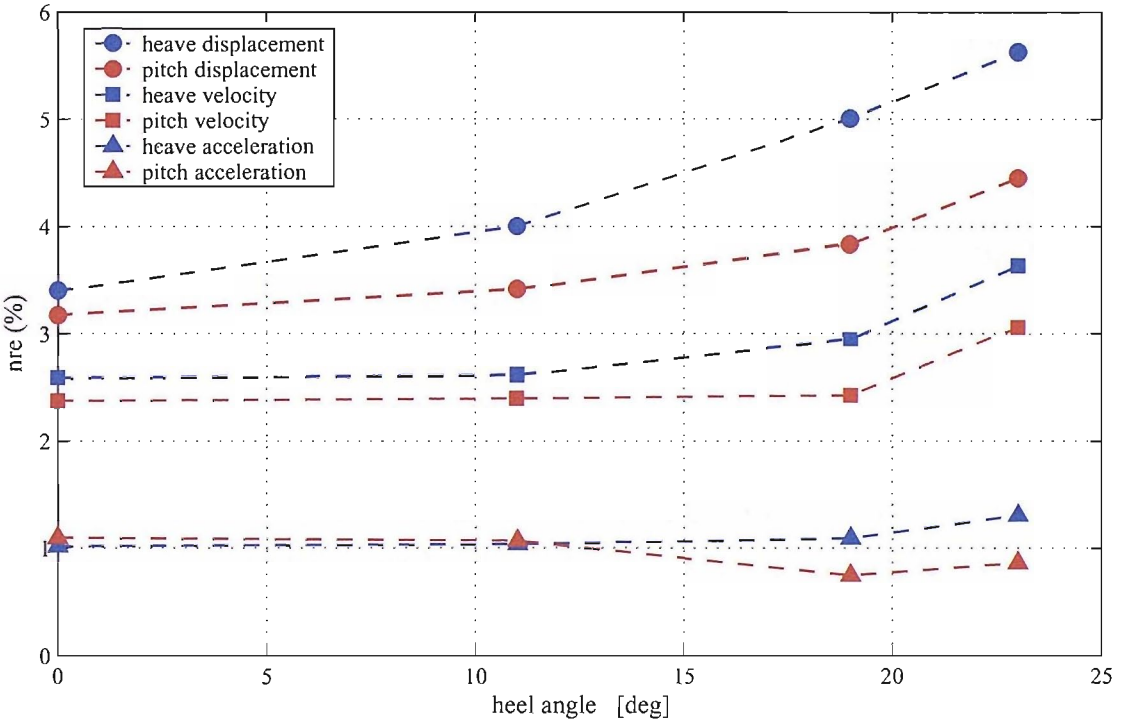

Figure 3.17: Mean NREs for motion recorded on towing tank model.

3.6 Experimental data

The present section discusses some of the experimental data obtained during the 2000-2001 Vendée Globe Race. Measurements performed at previous occasion have been described in [92] which has been included in appendix H. Owing to the extremely large quantity of data acquired through the different series of measurements, results are presented in this section mainly in graphical form.

Figures 3.18, 3.19 and 3.20 summarise the tracks, performance and environmental conditions of the two instrumented boats during the race. The two instrumented boats were "Gartmore" and "Voila.fr", identified in the present discussion respectively as "Boat#1" and "Boat#2". Both have been designed by Groupe Finot Naval Architects. The former was launched in 1997, equipped with a fixed keel and water ballast tanks for extra righting moment. Her displacement in racing trim at the start of the race has been estimated at 10.8 tons. The latter, was launched in 1993 in a fixed keel configuration and later equipped with a canting keel and twin daggerboards. Her displacement in racing trim at the start of the race has been estimated at 12.1 tons. Further information on these two boats may be found on the website of Groupe Finot Naval Architects (www.finot.com).

The two boats completed the race in a little less than 112 days, finishing only 3 hours and 40 minutes apart. As shown in figure 3.18, their tracks were extremely similar apart from the Southern Pacific and South Atlantic on the north-bound leg. However, during the first two thirds of the race, boat#1 accumulated a lead on boat#2 of up to 750 nautical miles, which meant that the two boats were sailing for several days in different weather systems. Towards the end of the race Boat#2 caught up with Boat#1 and as they sailed towards the finish line a few miles apart, both simultaneously encountered some of the worst conditions of the race while entering the bay of Biscay. The largest number of occurrences of slamming was recorded on this occasion on both boats as shown by figures 3.19 and 3.20.

Figures 3.21 to 3.23 further illustrate the conditions encountered by boat#2. The equivalent graphs for boat#1 show qualitatively similar data and have been included in appendix E for reference. Figure 3.21 confirms the perception that this edition of the Vendée Globe was essentially a downwind race, with more than 75% of the time spent sailing in reaching or running mode (i.e. with a TWA greater than 80 degrees). Expectedly, the highest winds were encountered while running downwind

in the Southern Ocean.

Figure 3.23 indicates that some of the highest waves were met with a relative heading of 80 to 100 degrees (i.e. beam on). It can be seen from figure 3.20 that this actually happened at the entrance of the bay of Biscay when most slams were recorded.

The distribution of the maximum measured transverse accelerations at the centre of gravity for each slamming event is shown in figure 3.24. By transverse acceleration we mean the sum of the y and z components of the acceleration along the boat-fixed reference system. It is evident from figure 3.24 that boat#2 experienced altogether lower accelerations compared to boat#1. This may be explained by the fact that boat#2 had a considerably heavier displacement. Also, one may consider whether the canting keel configuration of boat#2 may have acted to dampen extreme vertical motions, or, simply, whether the skipper of boat#2 sailed more conservatively in order to preserve the boat from being damaged by slamming.

The highest transverse acceleration measured through the race on boat#1 was $17.82 m/s^2$ (1.82g) while on boat#2 it was $14.61 m/s^2$ (1.49g). The former value is slightly higher than the one observed on the same boat during previous measurements (cf. [92]). Figure 3.24 shows that on eight occasions, a transverse acceleration higher than $15 m/s^2$ was recorded on boat#1.

The distribution of the accelerations along the longitudinal axis of the boat is presented in figure 3.25 (note that, with the convention of the x axis point forward, negative accelerations indicate that the boat is loosing forward velocity). It can be seen that longitudinal accelerations are almost one order of magnitude smaller than the transverse ones. Besides, while the peak acceleration along the boat y and z axis always tend to appear at the same time, maximum longitudinal accelerations often lag behind the former by a few hundredths of a second. Contrary to the results seen for the transverse acceleration, figure 3.25 indicates that boat#2 tended to experience higher longitudinal acceleration compared to boat#1. This fact could be explained by the latter yacht showing a narrower bow angle and generally finer sections in the bow with a slightly lower maximum breadth (cf. table 3.1). The maximum longitudinal backward acceleration recorded on boat#1 and #2 were respectively $4.05 m/s^2$ (0.41g) and $4.32 m/s^2$ (0.44g).

Figure 3.26 shows the distribution of pitching acceleration obtained for the two yachts. Again boat#2 appears to have undergone comparatively less violent motion

with a maximum value of $3.22 rad/s^2$ compared with $4.30 rad/s^2$ for boat#1. On average, peak pitching acceleration observed on boat#2 were lower than those of boat#1 by a factor of 1.35, while the average recorded transverse acceleration of boat#2 were lower by a factor of 1.52. It is somewhat worrying that such large differences may be found between yachts that are almost identical sailing on a very similar course. While it is most probable that they are due to a different style of sailing by the skippers as well as to slight differences in the yacht main characteristics and encountered weather, these data show how difficult it may be to accurately predict the peak values of motion experienced by a given boat over a round-the-world race.

Figure 3.27 presents a graph of the angle of acceleration of the vessel plotted against the instantaneous heel angle at the time of impact. The former variable is defined as the angle between the transverse acceleration vector of the vessel (cf. above) and a the boat vertical axis (i.e. the boat-fixed z axis). It is considered positive when the centre of gravity of the boat accelerates upwards towards starboard and viceversa. The acceleration angle may be regarded as a measure of how large the horizontal component of acceleration is relative to the vertical, or, equivalently, of the ratio between horizontal and vertical components of the hydrodynamic forces acting during a slam. In figure 3.27 there is an almost linear relation between heel and acceleration angle. This may be explained in two ways. Firstly, as the yacht heels, the local deadrise angle on the topsides become smaller, leading to higher hydrodynamic loads being exerted on this part of the hull. Secondly, as shown by figure 3.28, as the heel angle increases, the bow tends to acquire a larger horizontal velocity prior to impact with water. This latter phenomenon is particularly evident when sailing upwind in steep waves, where the bow can come well clear of the water and considerable yaw motion occurs before the leeward topside strikes the windward side of the waves.

Finally, figure 3.29 shows the distribution of recorded bow velocities upon impact. The variable is defined as the sum of the y and z components of velocity (relative to the boat fixed frame of reference) at a point on the keel line, one quarter of the waterline length aft of the bow. It is supposed to provide a good indication of the impact velocity in the slamming area. Again boat#1 appears to have experienced larger motions compared to boat#2, with the highest recorded velocity $8.48 m/s$ for the first compared to $6.62 m/s$ for the second.

As discussed in chapter 4, relative impact velocities are the most important variable affecting local slamming pressures. One may then extrapolate the relative impact velocities for different parts of the hull and impact configurations if only the instantaneous velocity of the water surface was known. Unfortunately, such data could not be gathered with the instruments used in the present investigation (but they could be measured by use of wave radar or ultrasonic sensors).However, an estimate of the magnitude of the wave surface velocity during the recorded slamming events may be obtained from figures 3.30 and 3.31. Here, the standard deviation of wave surface vertical velocity has been derived for different values of the significant wave height and peak period. This was made possible by assuming that actual encountered wave spectra could be idealised either as Bretschneider or as JONSWAP spectra. On each graph, dots have been plotted corresponding to the conditions encountered at the time of each recorded slam. Using the value of wave age derived from recorded wind speed and wave peak period(cf. [37]) to determine whether the sea spectrum was more likely to follow an open water-large fetch type pattern or coastal water-limited fetch, data points were distributed among the two graphs.

Using the model described in chapter 6, the loads and deflections of the keel of boat#1 have been calculated from the recorded time histories of motion and sailing condition. Figure 3.32 represents the distribution of the calculated lateral bending moments at the keel root. The moments have been normalised by the moment that would result from a static 1g lateral acceleration at the centre of gravity of the bulb (i.e. $M_{bulb} \cdot g \cdot l_{fin}$), that is also the load experienced when the boat lies heeled over at 90 degrees. The actual maximum calculated value of the normalised moment was 1.63. For reference, the ABS Guide for Building and Classing Offshore Racing Yachts [3] effectively requires that the keel and its supporting structure be designed for a lateral bending moment equivalent to the one produced by a 3g static acceleration at bulb centre of gravity. For structures that are prone to fatigue failure, one should also give careful consideration to the relatively large number of lower amplitude loadings shown by the graph.

Figure 3.33 provides some indications on the estimated level of dynamic amplification that occurs for lateral bending loads. In particular the left side graph shows that, in most occasions, the actual lateral bending moment at the keel root was expected to be lower than the one that would be experienced if the maximum inertial forces produced by slamming were to be applied statically. The right side graph confirms

that, for the present case, amplification factors higher than one are generally associated with lower excitations (which typically have longer impulse durations). While these graphs may suggest that, at the higher load levels, it is safe to consider that the dynamic amplification factor is lower than one, one should not forget that other structures with different dynamic characteristics may show higher amplification factors at the higher loadings. Typically this would happen if the whole keel structure was to be made stiffer in lateral bending for the same weight.

Figures 3.34 and 3.35 present similar data for the keel longitudinal bending moment. Here it may be noted that, for the boat under study, maximum longitudinal bending moments are generally expected to be higher than those that would result from the maximum inertial loads being applied statically. This may be explained by the fact that the natural frequencies in longitudinal bending tend to be higher than in lateral bending. Hence, the structure responds more to the high frequency components of the transient inertial loads. Besides, hydrodynamic damping effects are far lower for longitudinal vibration of the keel and bulb than in the transverse case.

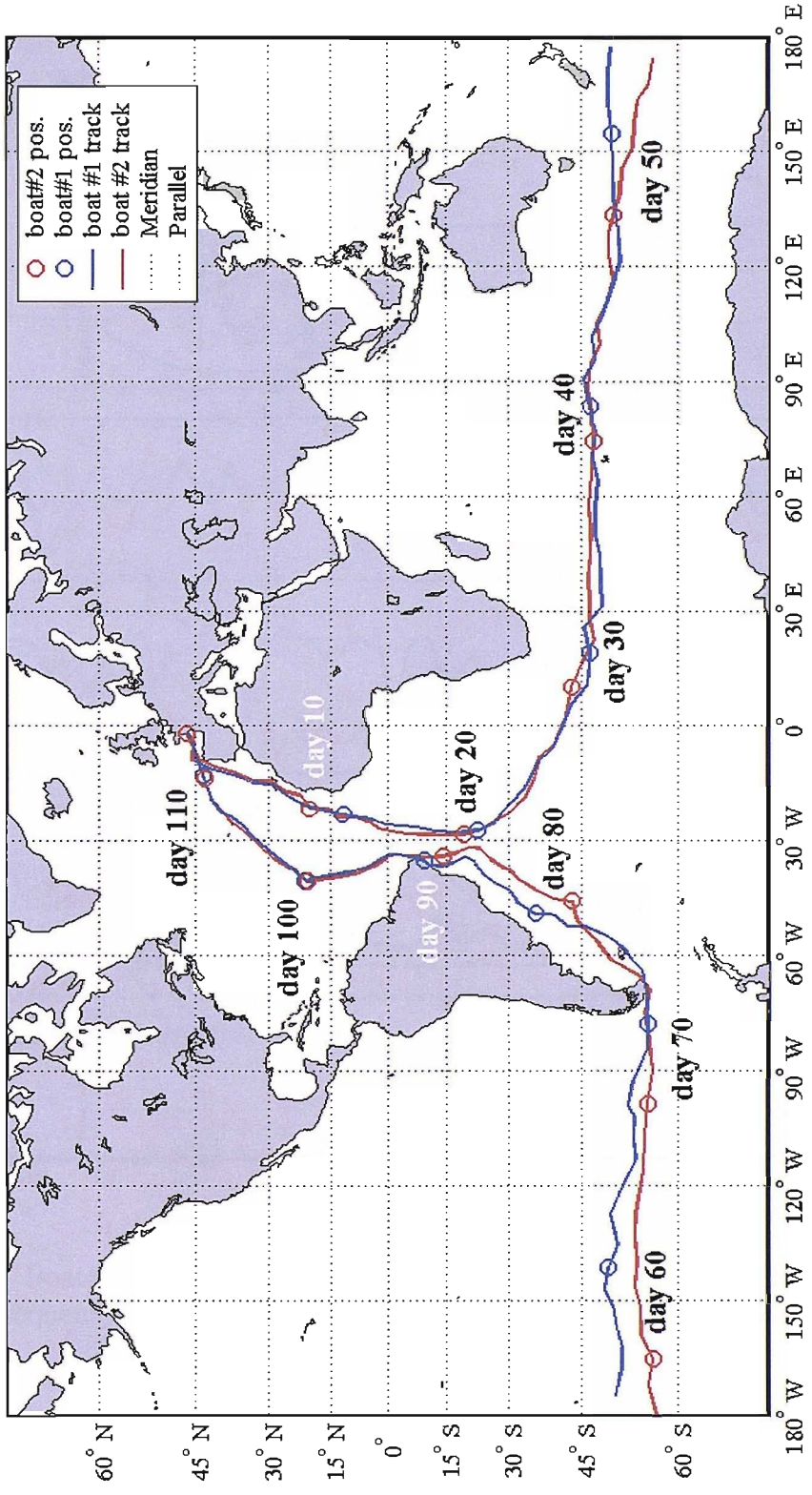

Figure 3.18: Tracks of the instrumented yachts during the 2000 Vendée Globe Race.

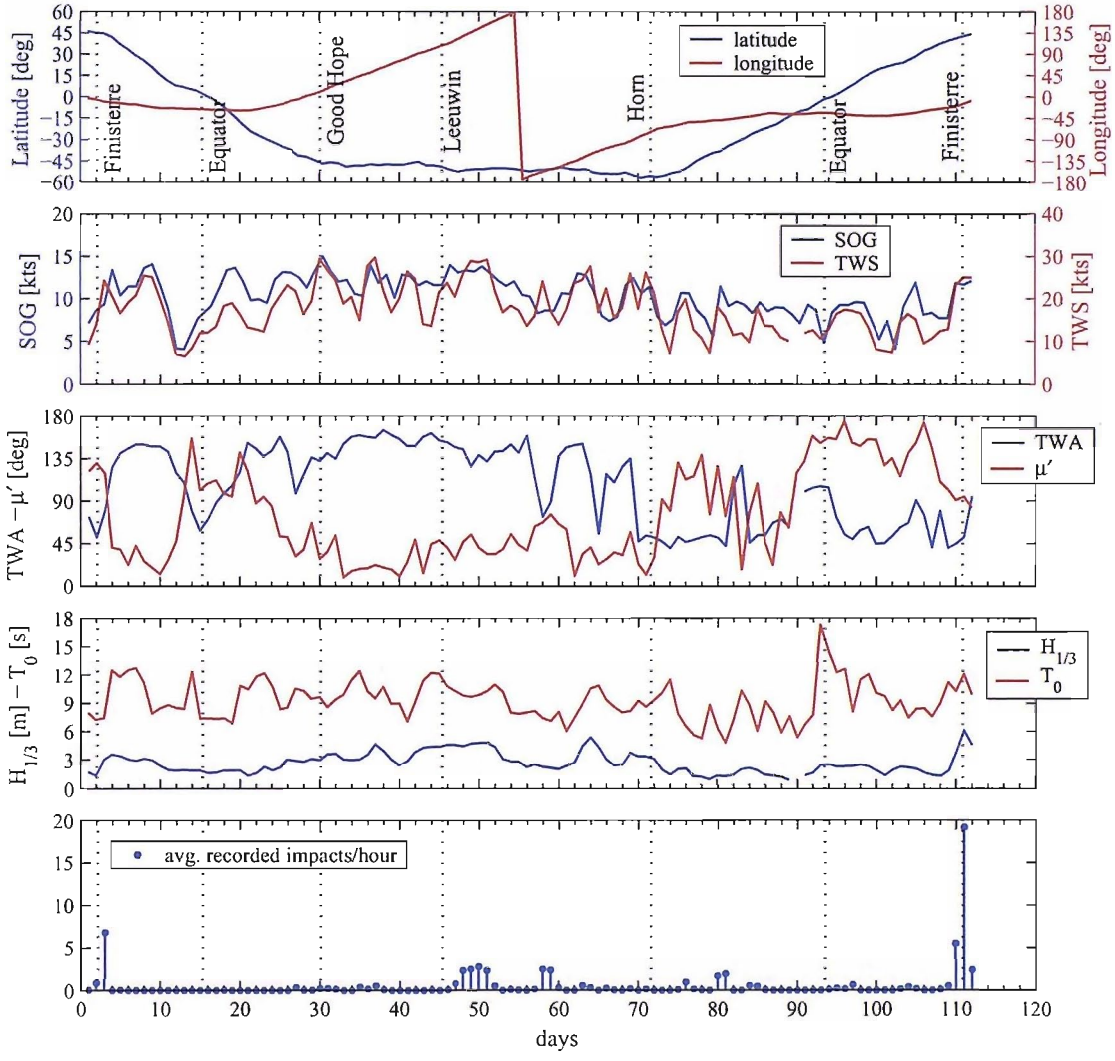

Figure 3.19: Boat#1: Summary of sailing conditions and corresponding positions and slamming frequency.

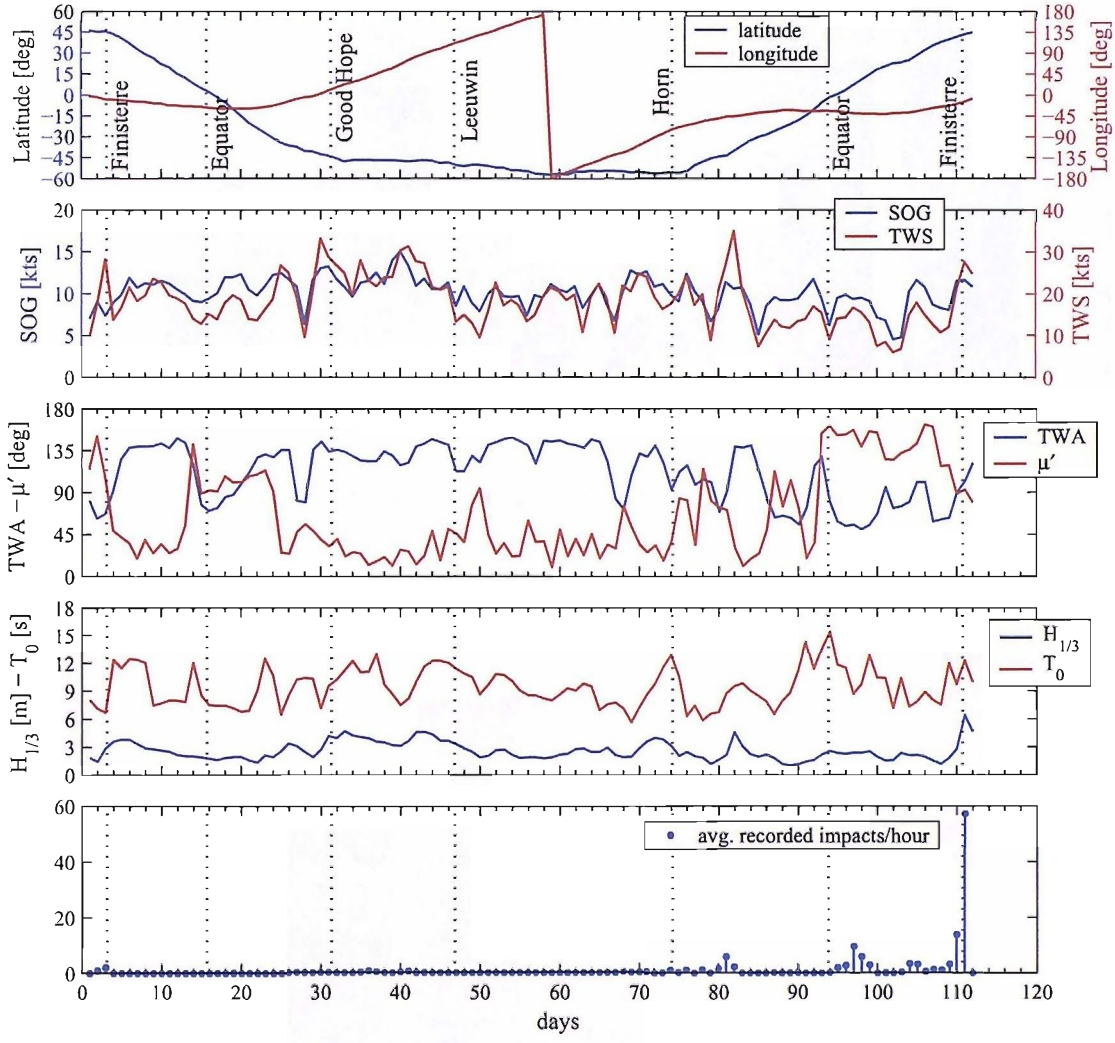

Figure 3.20: Boat#2: Summary of sailing conditions and corresponding positions and slamming frequency.

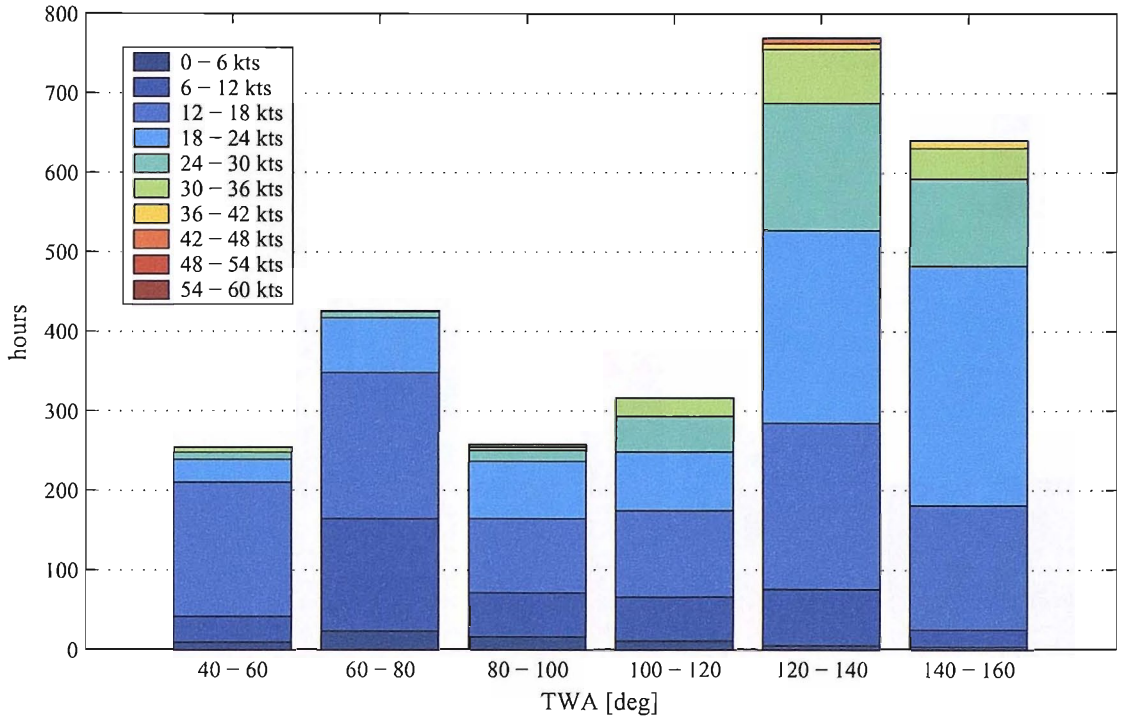

Figure 3.21: Boat#2: summary of measured true wind angle and true wind speed.

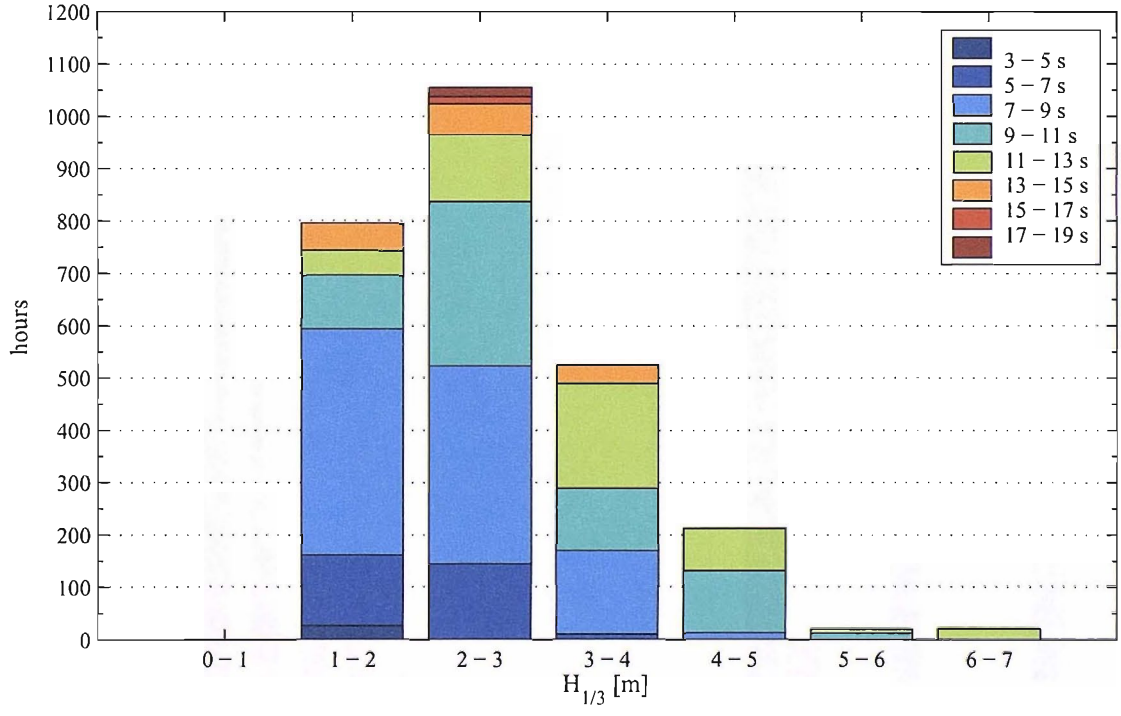

Figure 3.22: Boat#2: summary of encountered significant wave height and wave peak period.

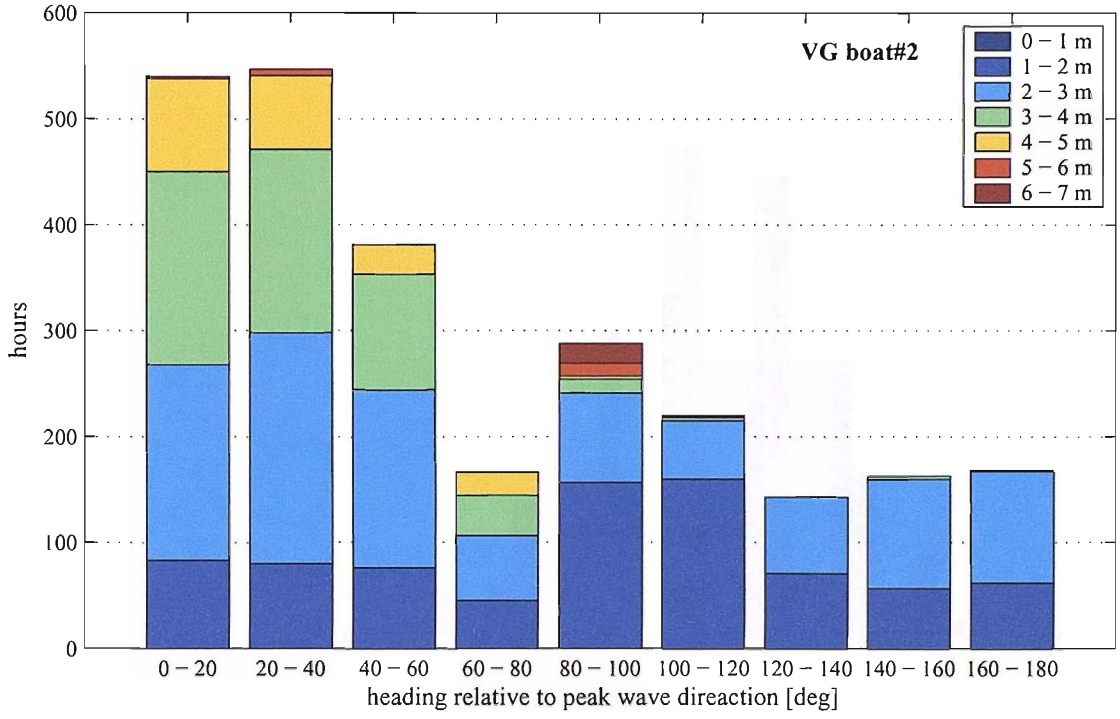

Figure 3.23: Boat#2: summary of heading relative to the peak wave direction and significant wave height.

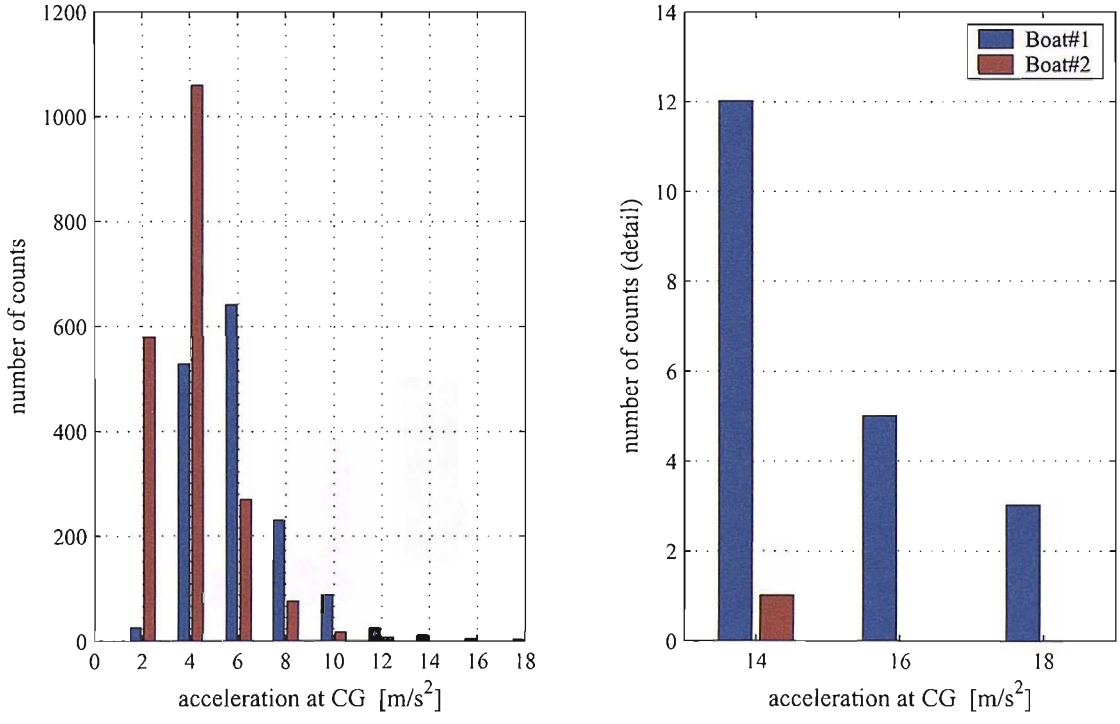

Figure 3.24: Distribution of recorded transverse acceleration at centre of gravity.

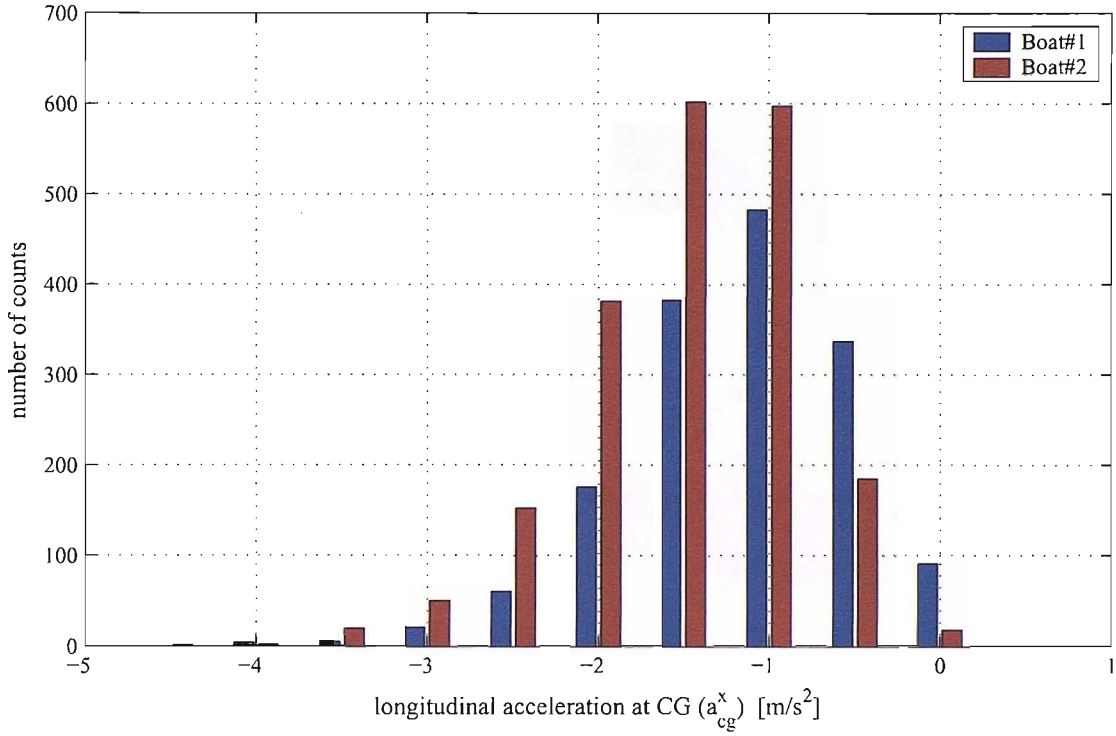

Figure 3.25: Distribution of recorded longitudinal acceleration at centre of gravity.

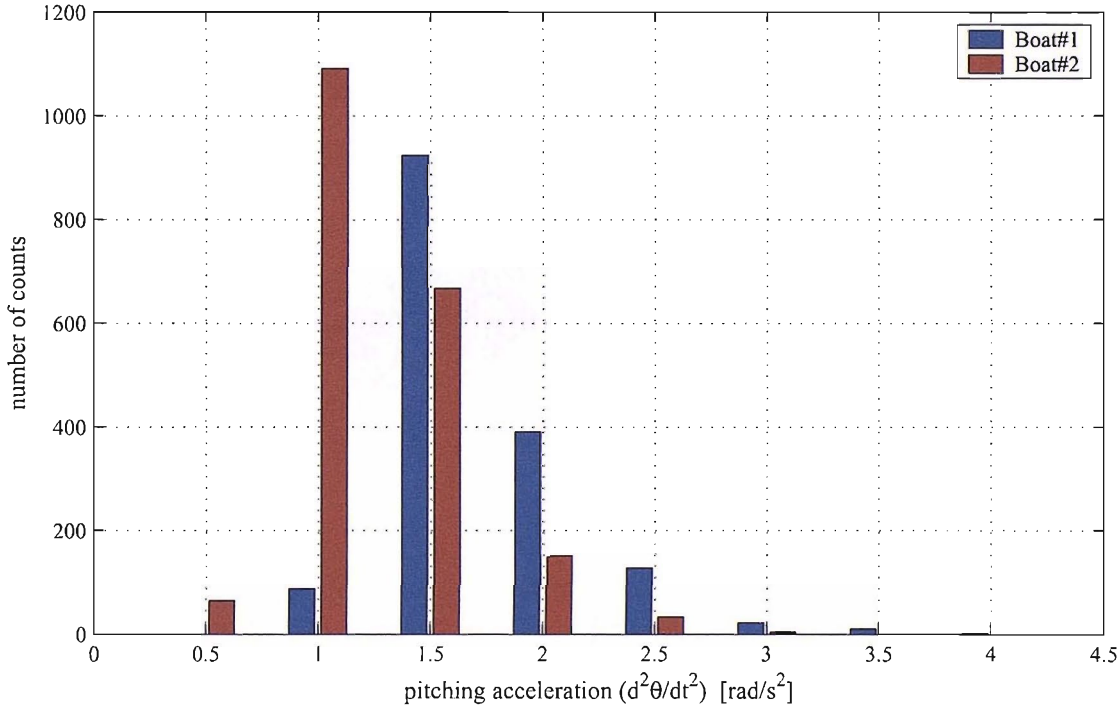

Figure 3.26: Distribution of recorded pitching acceleration around longitudinal centre of gravity.

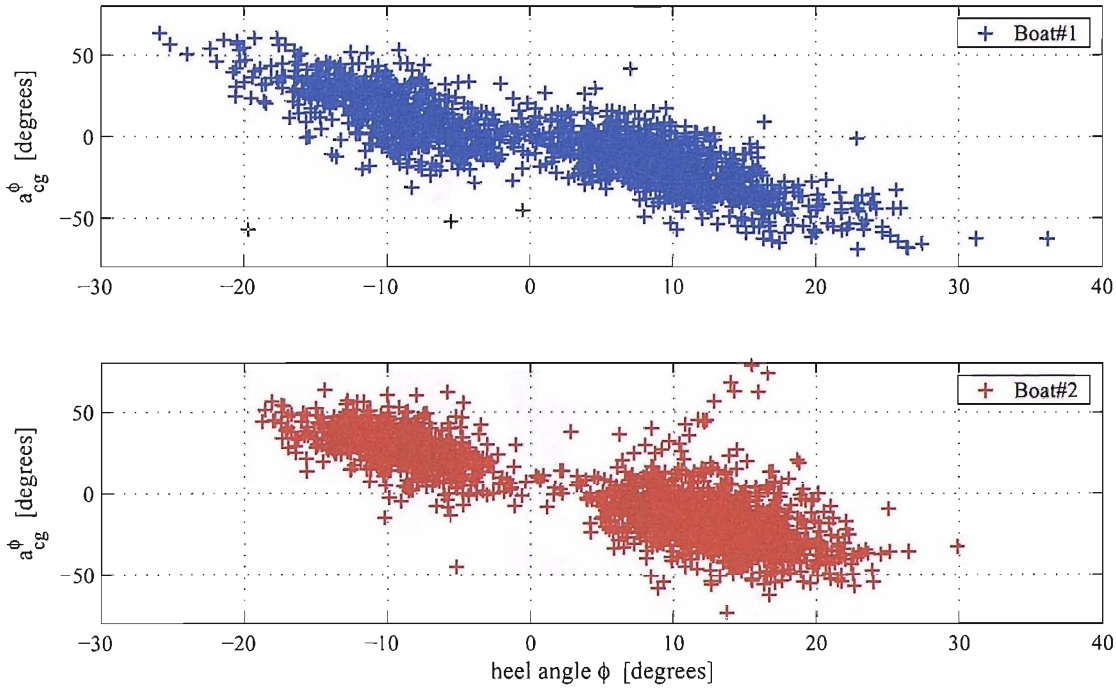

Figure 3.27: Relation between heel angle and angle of impact acceleration.

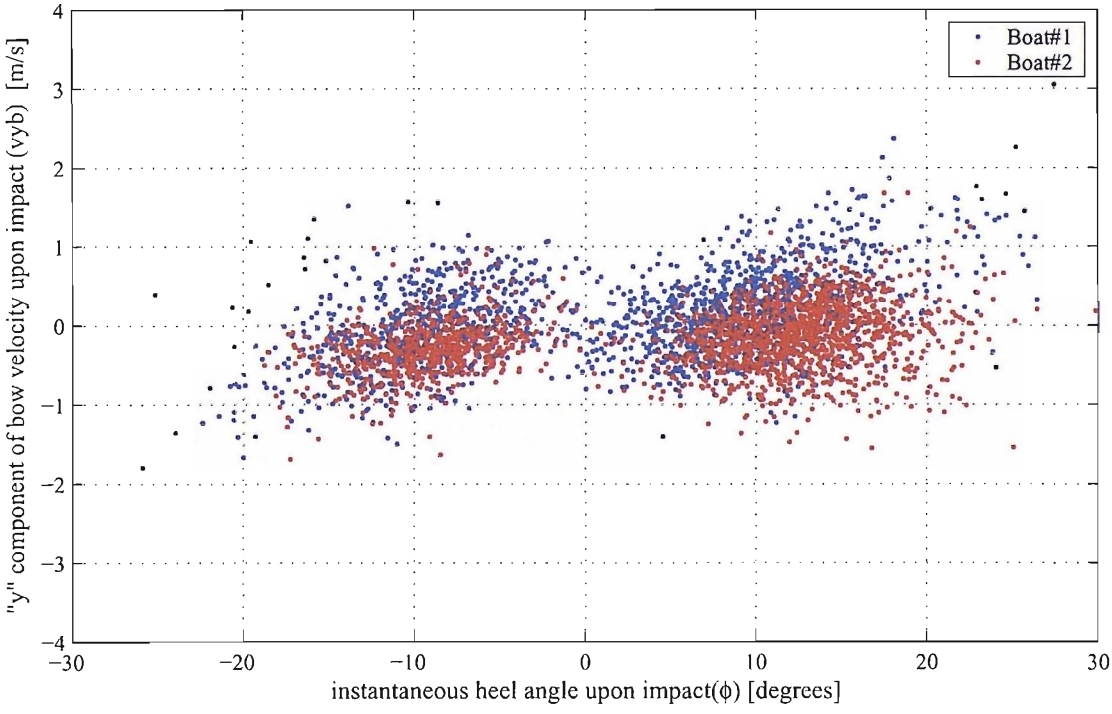

Figure 3.28: Relation between heel angle and horizontal component of bow velocity upon impact.

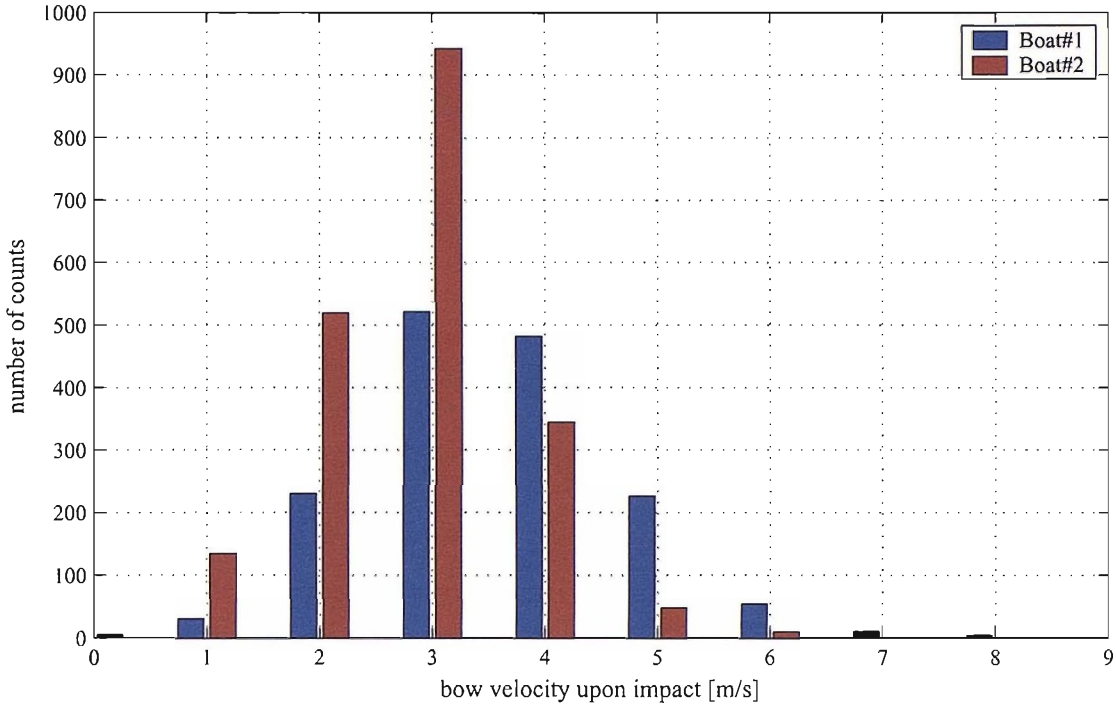

Figure 3.29: Distribution of recorded transverse component of bow velocity at the time of impact.

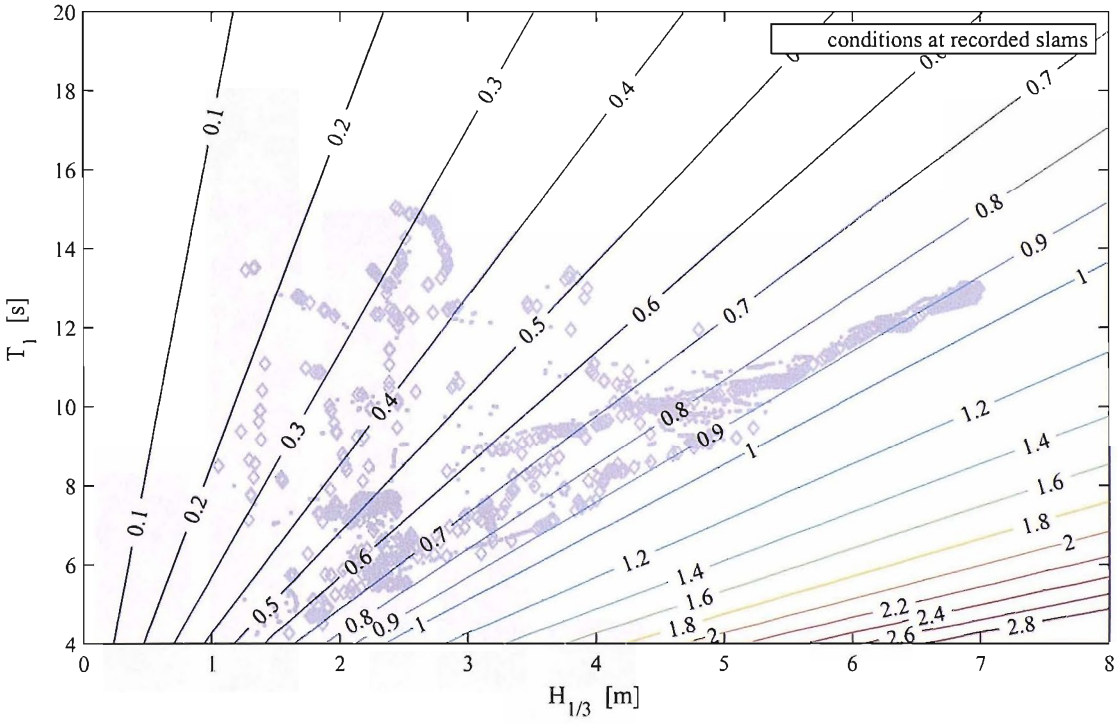

Figure 3.30: Estimate of the water surface velocity standard deviation expressed as a function of significant wave height and wave peak period. Data derived for Bretschneider spectra.

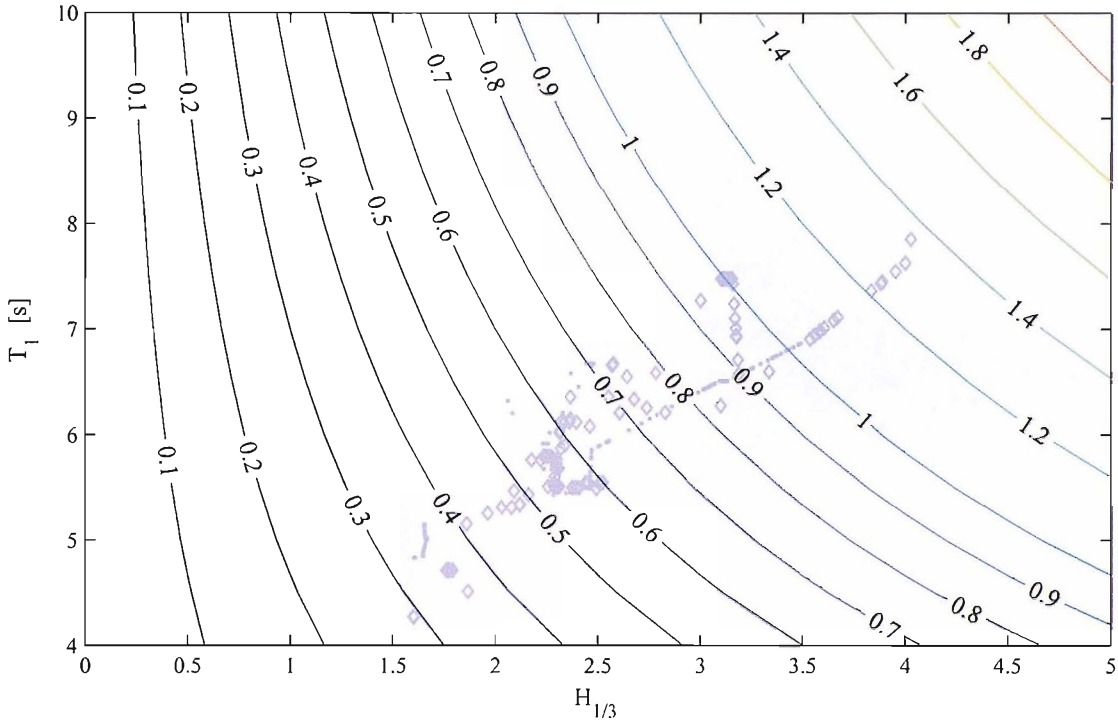

Figure 3.31: Estimate of the water surface velocity standard deviation expressed as a function of significant wave height and wave peak period. Data derived for JONSWAP spectra.

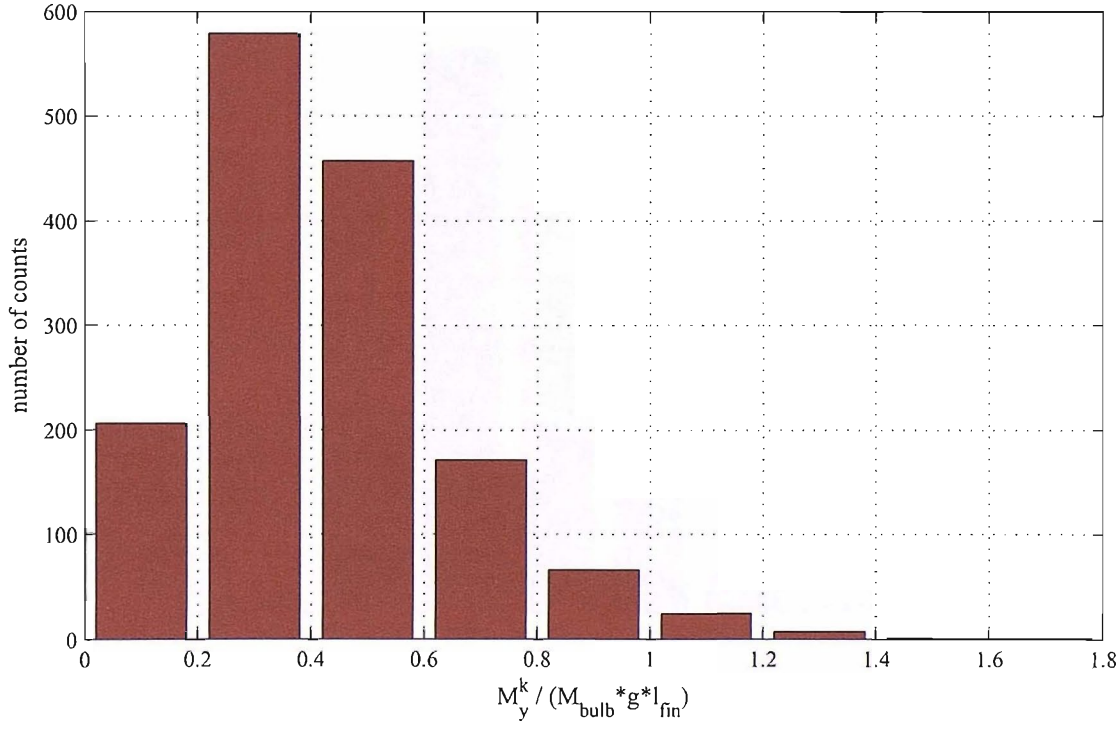

Figure 3.32: Distribution of normalised lateral keel bending moment M_y^k evaluated at the keel root.

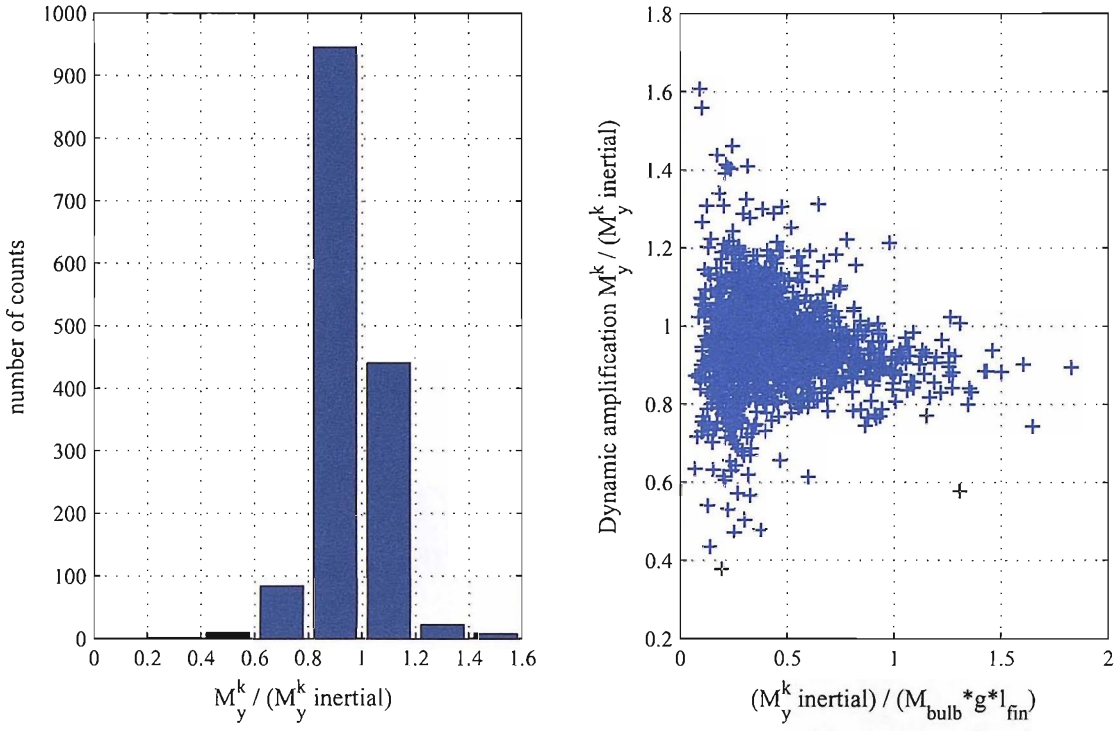

Figure 3.33: Dynamic amplification of keel lateral bending moment.

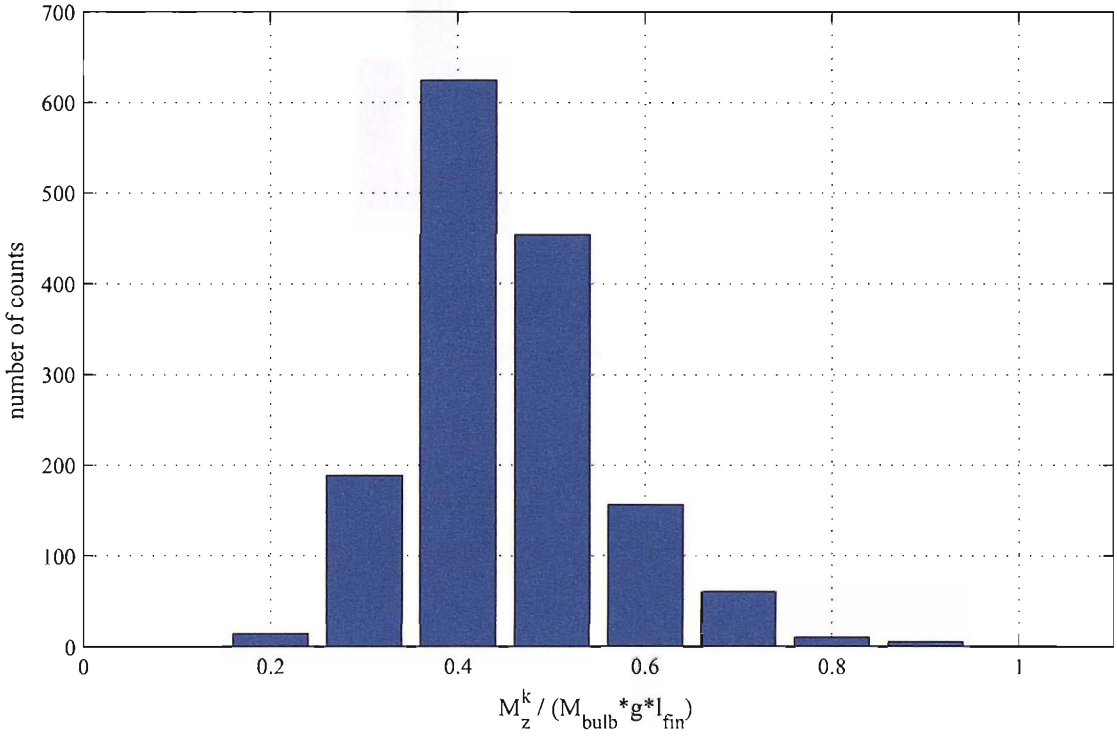

Figure 3.34: Distribution of normalised longitudinal keel bending moment M_z^k evaluated at the keel root.

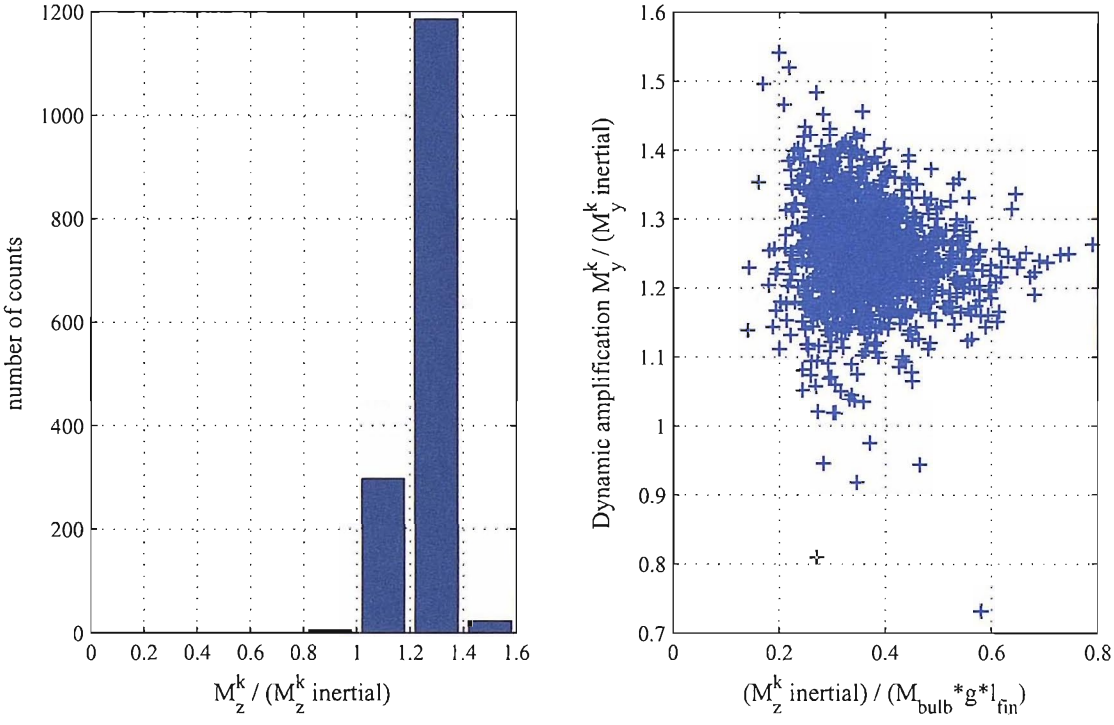

Figure 3.35: Dynamic amplification of keel longitudinal bending moment.

3.7 Summary

An autonomous data acquisition system has been set up for performing measurements on Open60' and Open50' type yachts during long oceanic passages. This has allowed a very large quantity of data to be collected on four different yachts over a period of two years, including measurements of motion and sailing conditions.

Information about the sea state encountered by the instrumented boats has been obtained from three different sources, including satellite altimeter observations, hindcast data from computational wave models, and the motions of the boats themselves. All three sources have been found to have comparable levels of accuracy, while being complementary in terms of the scales of geographical areas covered and of the resolution in time.

A numerical integration method has been developed along the lines of the work previously published by Miles, in order to derive all the variables of motion from the accelerations measured by sensors strapped onto the yachts structure. The method has been successfully validated through numerical and experimental tests.

A sample of the experimental data obtained during the Vendée Globe 2000-01 Race on two different boats has been presented in section 3.6.

Chapter 4

Scale model experiments

4.1 Experimental set-up

An analysis of the parameters affecting the slamming loads on the hull bottom panels of a sailing yacht has been carried out by performing a series of tests on a 1/7th scale model of an Open 60' (see table 4.1 for details) outfitted with "slam patches". The use of a similar method has already been reported by Kapsenberg et al. [75] and by Purcell et al. [108]. The principle of slam patches for the measurement of hydrodynamic bottom pressures is straightforward. A panel of a size representative of a full-scale hull panel (i.e. typically the portion of the hull delimited longitudinally by two bulkheads or ring frames and transversely by two girders or stringers) is cut out of the bottom of the model and replaced by a panel with a high specific stiffness. which does not touch the cutout sides. A load cell is fitted on top of this panel and supported by a rigid stud, which, in turn, is connected to the reinforced internal structure of the model (figure 4.1). By this arrangement, the external pressure loads acting on the panel are transmitted through and measured by the load cell.

Effectively, slam patches may be considered as pressure transducers with a very large diaphragm. By dividing the force measured by the load cell by the known surface of the scaled panel, the average pressure acting on the panel can be directly obtained.

Several authors have reported on experiments involving the measurement of slamming loads through the use of arrays of pressure transducers fitted on the hull of model and full-scale vessels [2, 59, 61, 108, 115]. It is generally observed that the pressure distribution following a slam is highly non-uniform. With diaphragm sizes

Table 4.1: Main characteristics of the full-scale and model scale yacht.

	Full scale	**Model scale** $(1/7^{th})$
Length overall (L_{OA})	18.28m	2.611m
Beam (B)	5.77m	0.824m
Waterline Length (L_{WL})	17.25m	2.450m
Waterline Beam (B_{WL})	3.89m	0.556m
Draft (T)	0.405m	0.058m
Displacement (Δ_0)	11020kg	32.13kg
Pitch radius of gyration (k_{yy})	$0.219 \cdot L_{OA}$	$0.219 \cdot L_{OA}$
Length-volume ratio $(L_{WL}/\nabla^{1/3})$	7.625	7.625

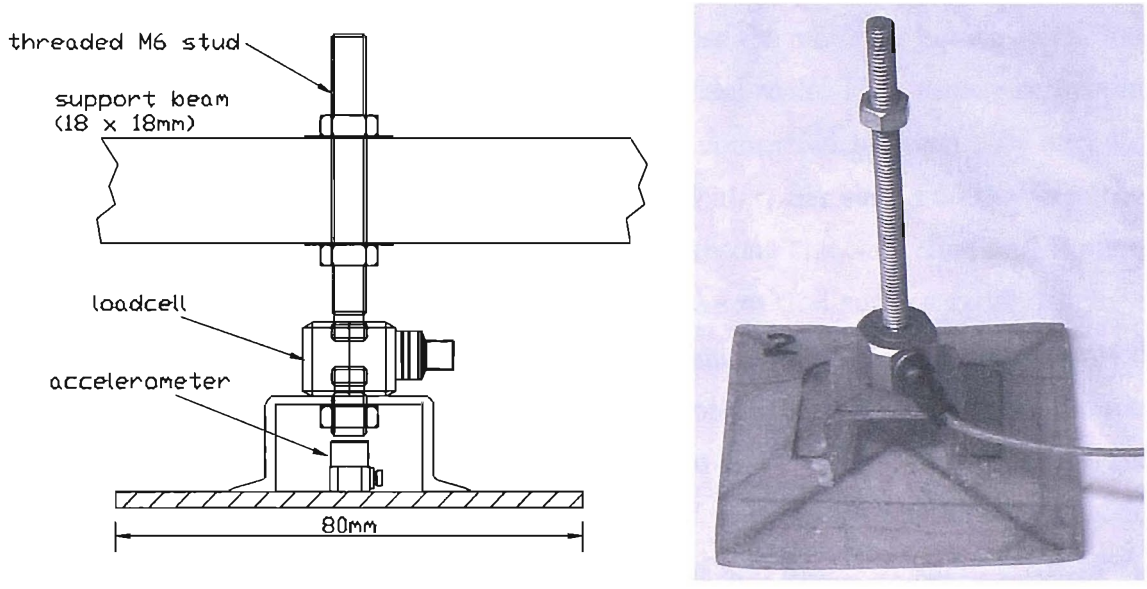

Figure 4.1: Slam patch assembly: sketch and picture

typically in the order of $1 - 4mm^2$, pressure transducers provide a very local measurement and several sensors must be used if an estimate of the pressure distribution over a hull panel is sought. Conversely, slam patches allow the average pressure to be measured over a set area with only one transducer, while local peak pressures may only be inferred. Among the authors who have studied the problem, there is a rather wide agreement on the fact that the average pressure values offer a better starting point for understanding the structural behaviour of the hull panels exposed to slamming. Allen and Jones [2], for example, stated that the "average uniformly distributed pressures should correlate much more closely with measured structural responses in plating, stiffeners and frames, than would the peak pressures as measured on individual gauges." Two main considerations support this statement: firstly, measurements of local pressures performed on vessels in a seaway, tend to show considerable scatter

as small variations of the impact angle and of the water surface state can produce very large differences. It is thus extremely difficult to repeat two identical slams even in a controlled laboratory environment. Secondly, the local pressure peaks tend to act for a very short time, (often smaller than the first natural period of the panel) and over a very limited area. The response of the first natural modes of deformation of the structure is then only marginally affected by these values and correlates more closely with the relatively slower variation of the average pressure.

Considering the design of the slam patches, their surface area was chosen to correspond to a typical full-scale panel of the Open60' yacht represented by the model, while a square shape was adopted in order to minimise the moments acting on the load cell. This produced a panel size of 80x80mm at model scale. Preliminary seakeeping tests [39] indicated the main slamming area to be comprised between 25% and 45% of the waterline length aft of the forward perpendicular. Six slam patches were then fitted in this portion of the hull, respectively three along the centreline and three on the starboard side, placed along the centreline of the wetted surface at 20 degrees of heel. In order to ensure sufficient stiffness and strength of the model and to provide a firm point of attachment for the support stud connecting the panel to the model, additional stiffening members were laminated into the model. All six panels were made of glass fibre and polyester resin, laminated in a female mould of the model. The thickness of the panels varied between 2.5mm and 3mm. A small GRP bridge structure was then laminated on the upper side to provide an attachment point for the load cell and to allow an accelerometer to be mounted at the centre of the panel. A 1.5mm gap was left between the panels and the hull cut-out: the reduced length of the support studs together with the stiff general construction ensured that the panel would never come in contact with the surrounding structure and that all the loads would be carried by the load cell.

Watertight integrity was guaranteed by a thin film of latex applied over the exterior side of the panels and attached only to the surrounding part of the hull. This method had been validated previously by Kapsenberg et al. [75] and offered the smallest interference with the panel movements under the applied loads.

Three piezoelectric load cells with a range of +/-250 N and a natural frequency of 70kHz were used, allowing the force to be measured only on three of the six panels at each slam. Several different arrangements were adopted in order to investigate the evolution of the pressure, both in the longitudinal and transverse direction.

It was initially planned to fit four pressure transducers at the corners of the aft-most centreline panel to provide an element for comparison with the slam patch measurements. However, at the time of performing the tests, only four sensors with a nominal range of 13.5kPa could be sourced. Although pressures in the range of $\pm 41.4kPa$ could actually be measured by allowing for a loss of accuracy (see table 4.3), it was anticipated that these sensors would not be suitable for recording the peak pressures. They were eventually used to provide an indication of the evolution of the pressure front over the adjacent panel.

Two accelerometers with a range of +/-10G were fitted on the bow and at the LCG of the model, while piezo-electric accelerometers with a range of +/-1000G were placed on the instrumented panels to measure their inertial response.

During the rotational drop tests, a linear potentiometer connected to the bow and to a fixed overhead point was used to obtain the vertical velocity of the model at the time of impact. During tests in waves with forward speed, this velocity was deduced from measurements of heave and pitch available from the transducers fitted on the towing post. All tests were filmed by using two video cameras (one under water an one just above the surface) to provide further visual information.

The layout and numbering of the sensors is shown in figure 4.2 while details about their technical specifications are given in table 4.3.

The experiments were performed with the model held stationary and also attached to a towing tank carriage in the following series: rotational drop tests with zero forward speed, rotational drop tests with forward speed and towing tests in waves. Rotational drop tests were performed by supporting the model from the transom with a purpose built rig and by letting the bow fall freely into the water from variable heights. To ensure repeatability, an electromagnet was used to hold and release the model. The point of first contact with the water and the trim angle at impact could be varied by adjusting the transom height. For drop tests with forward speed, the support rig was attached to the underside of the towing tank carriage and the model was released onto the calm water when the set speed was reached. Forward speed tests were performed in a way similar to standard seakeeping tests, by towing the model in regular waves: the model was allowed to heave and pitch freely and was restrained in sway, surge, roll and yaw. The tests were performed in regular waves rather than in a set of irregular waves because this would guarantee better repeatability of the measurements and allow a larger number of slams to be recorded at each run.

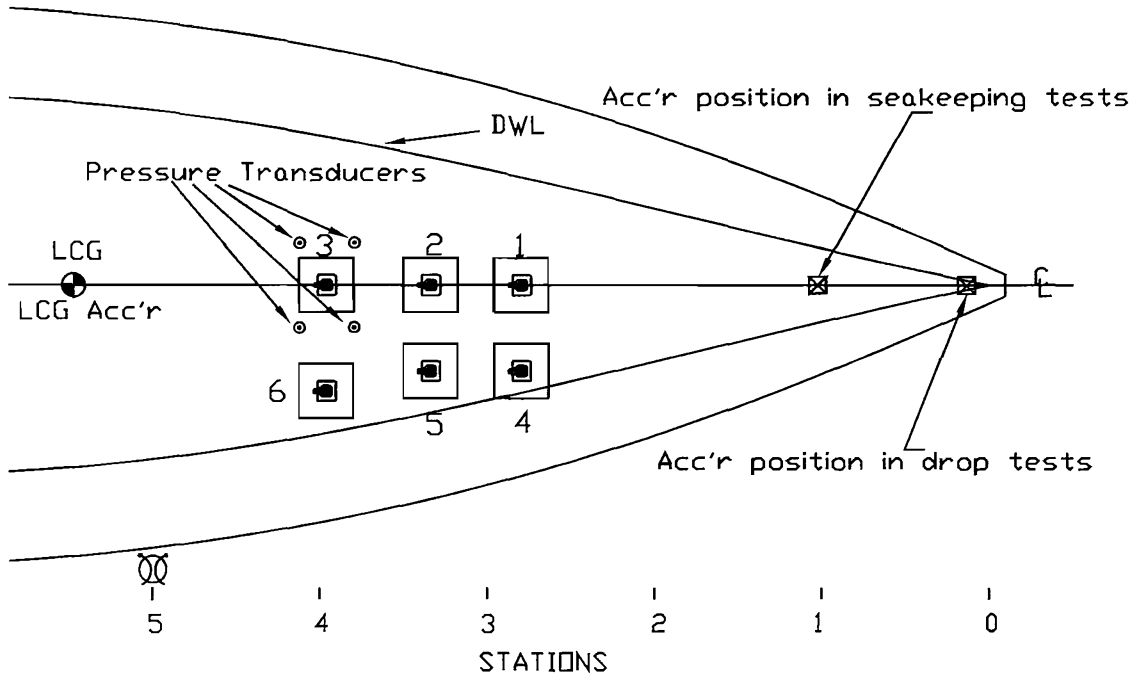

Figure 4.2: Sensors layout.

Where possible, a number of parameters were varied in isolation within each test series to investigate their influence. Thus, for the drop tests, impact velocity, forward velocity, displacement, longitudinal radius of gyration, point of initial impact/trim angle at impact and heel angle were varied. For the forward speed tests, displacement, forward velocity and wave height and slope were varied. A summary of the main test parameters can be found in table 4.2.

The analog signals from the sensors were digitised through two 8-channel A/D converters with 12bit resolution (a CED 1401 unit and a ComputerBoards PCM-DAS08 card) and recorded on two personal computers running TURBOAD data acquisition software. To allow perfect syncronisation of the recordings, the signal from one of the pressure transducers was split and logged by both computers.

The maximum sampling rates and recording times were determined by hardware and software limitations. Hence, for the rotational drop tests, sampling frequencies between 1kHz and 10kHz were used with recording times of 1 to 3.5 seconds respectively. For the tests in waves, a sampling rate of 2kHz and a recording time of 9 seconds were typically adopted. The implications of these settings are further discussed in section 4.2.

Table 4.2: Scale model test parameters.

Rotational Drop Tests Parameters (zero forward speed)

		(full-scale equivalent)
Drop Height:	$10 \div 70mm$	$(70 \div 490mm)$
Vertical velocity at impact:	$\sim 0.4 \div 1.3m/s$ (measured at the centre of panel 2)	$(\sim 1 \div 3.5m/s)$
Displacement (Standard condition):	$\Delta_0 = 32.13kg$	(11t)
Displacement variations:	$0.8 \cdot \Delta_0$, Δ_0, $1.19 \cdot \Delta_0$, $1.4 \cdot \Delta_0$	(9t, 11t, 13.5t, 15.9t)
Pitch moment of inertia about pivot point (Standard condition):	$I_{pp} = 64.893kg \cdot m^2$	$(1090657kg \cdot m^2)$
Pitch moment of inertia variations:	$0.82 \cdot I_{pp}$, $0.9 \cdot I_{pp}$, I_{pp}, $1.13 \cdot I_{pp}$, $1.27 \cdot I_{pp}$, $1.45 \cdot I_{pp}$	
Point of first contact with water:	13.4%, 34.5%, 57.2% of L_{WL} aft of FP	
Trim angle at time of impact:	-0.775 deg, -0.4 deg, -0.125 deg	
Heel angles:	0 deg, 10 deg, 20 deg	

Rotational Drop Tests Parameters (with forward speed)

		(full-scale equivalent)
Drop Height:	$10 \div 60mm$	$(70 \div 420mm)$
Vertical velocity at impact:	$\sim 0.4 \div 1.2m/s$ (measured at the centre of panel 2)	$(\sim 1 \div 3.2m/s)$
Forward speed:	$0.97 \div 3.5m/s$	$(2.57 \div 9.26m/s$ i.e. $5 \div 18kts)$
Displacement:	$\Delta = 32.13kg$	$(11.02t)$
Pitch moment of inertia:	$I_{pp} = 64.893kg \cdot m^2$ (about pivot point)	$(1090657kg \cdot m^2)$
Point of first contact with water:	34.5% of L_{WL} aft of FP	
Trim angle at time of impact:	-0.4 deg	
Heel angle:	0 deg	

Tests in regular waves (with forward speed)

		(full-scale equivalent)
Displacement:	Δ, $1.18 \cdot \Delta$, $1.33 \cdot \Delta$ $(\Delta = 32.13kg)$	(11t , 13t, 14.7t)
Pitch moment of inertia (about L_{CG}):	I_{yy_0}, $1.23I_{yy_0}$, $1.85I_{yy_0}$ $(I_{yy_0} = 12.67kg \cdot m^2)$	$(I_{yy_0} = 212945kg \cdot m^2)$
Wave encounter frequency:	6.787 rad/s	(2.565 rad/s)
Forward speed:	1.711 m/s $(Fr = 0.35)$	(4.53 m/s i.e. 8.8kts)
Wave Height (H_W):	$0.075 \div 0.16m$	$(0.525 \div 1.26m)$
Wave Slope (H_W/L_W)	$2.19\% \div 4.67\%$	
Heel angle (ϕ):	0 deg, 20 deg	

Table 4.3: Sensors technical specifications.

Sensor	**Brand, Model, Type**	**Measurement Range**[a]	**Accuracy**[a]	**Resonant Frequency**[a]	**Notes**
Load Cell	Kistler, 9712BE250, piezoelectric load cell	$\pm 250N$[b]	$\leq \pm 1\%$ FSO[b]	$> 70kHz$	stiffness:> $130kN/m$; weight: 19g
Pressure transducer	Endevco, 8507 C-2, piezoresistive	$\pm 13.8kPa$[c]	1.5% FSO[c]	70 kHz	diaphragm diameter: 2.26mm; area: $4mm^2$
Wave Probe	sword type, variable resistance probe	0-350mm	not available[d]	-	-
Low Frequency Accelerometer	IC-Sensors, 3140-010, piezoresistive	$\pm 10g$	1% FSO (typ. 0.2%)	1.2 kHz[e]	weight: 13g
High Frequency Accelerometer	Bruel and Kjaer, 4393, piezoelectric	$\pm 1000g$ (as wired)	$\pm 2\%$ FSO	55 kHz[f]	-
Linear displacement transducer (Rotational drop tests)	Sangamo, 1880, LVDT	0-355 mm	not available	-	-
Towing post: linear and angular displacement transducers (Sea-keeping tests)	not available	-	-	-	-

[a]Nominal values
[b]Forces of up to $\pm 360N$ can be measured with accuracy better than 7% of FSO
[c]Pressures of up to $41.4kPa$ can be measured with accuracy better than 7.5% of FSO
[d]See section 4.2 for further details
[e]Non linearity within $\pm 5\%$ in the range of $0 \div 700$Hz
[f]Non linearity within $\pm 5\%$ in the range of 0.1Hz$\div 12$kHz and within $\pm 10\%$ in the range of 0.1Hz$\div 16.5$kHz

4.2 Sensors calibration and error analysis

Before measurements were carried out, several checks were performed to find and - if possible - neutralise all sources of experimental errors.

4.2.1 Calibration

"Through-system" type calibration was generally performed in order to account for possible imperfections of the signal conditioning and transmission line (i.e. cables, connectors, analog-to-digital converters, etc.). Static type calibration was performed when possible. Hence the LVDT and the towing post linear and angular displacement transducers were calibrated against a series of known extensions and rotations. The low frequency accelerometers were calibrated by a standard "0 -2g" test. The pressure transducers were checked by submerging them under known heights of water through a purpose-built tube. The wave probe was calibrated against several known immersions. It was found that the sensor output was not a linear function of the immersion, hence the measured wave elevation (obtained by linear conversion) was corrected through the following formula:

$$h_c = 0.4345 - \sqrt{0.1888 - 0.8522 h_m} \tag{4.1}$$

where h_c and h_m indicate respectively the corrected and the measured wave elevation.

Both the load cells and the high-frequency accelerometers were piezo-electric type sensors, giving no response to a constant excitation. Therefore, static calibration could not be applied to these devices. The analog-to-digital converter (ADC) exact "bits/volt" conversion factor was then verified by applying known input signals (a constant voltage produced by a laboratory power supply and a sinusoidal signal of know amplitude generated by the accelerometer charge amplifier). Calibration values for the load cells and the high-frequency accelerometers were then obtained by combining the nominal sensitivities of the sensors (as certified by the manufacturers) with the ADC conversion factor. A further check was then performed for the load cells by carrying out load release tests, whereby a $2kg$ mass resting on a sensor was suddenly lifted. The differences between the measured and expected peak loads were smaller than the data acquisition system resolution, confirming that calibration was properly performed.

A full set of calibration tests was performed every day before starting and after completing the measurements. "Zero-level" calibration was performed before each run with the model held perfectly still. While most sensors showed negligible drift, temporary "zero offsets" of up to 10% of the full span were observed for the pressure transducers. This phenomenon had been predicted by the manufacturer and was due to the sensors being exposed to pressures exceeding their standard measurement range. It should be noted that, since the behaviour of the pressure transducers was not predictable after over-range, only pressures measured before impact could be trusted. Hence, as mentioned in the previous section, these sensors were only used to determine the time of contact with water and to eventually monitor pressure fluctuations produced by air entrapment before impact.

Ten minutes were allowed to pass between each drop test and twenty between each run in the towing tank, to allow the water surface to return to a perfectly calm state. This also guaranteed that the load-cells output would decay to zero before a new acquisition was performed.

4.2.2 Resolution

The measurement resolution obtained with the 12bit ADC for the different sensors is shown in table 4.4.

Table 4.4: Resolution of the measured variables.

Sensors	**Measured variable**	**Resolution**
Load Cells	Force on Slam Patch	0.1403-0.1484 N/bit
Pressure transducers	Pressure around panel 3	1.254 - 1.446 Pa/bit
Low Freq. Accelerometers	Acceleration at LCG and at bow	0.012 g/bit
High Frequency Accelerometers	Acceleration on slam patch panel	0.756 g/bit
LVDT	Vertical displacement at station 0	0.091 mm/bit
Wave Probe	Wave elevation	0.0631 mm/bit
Towing Post: Linear Displacement transducer	Heave	0.046 mm/bit
Angular displacement transducer	Pitch	0.0051 deg/bit

4.2.3 The effects of sampling frequency

As mentioned in section 4.1, sampling frequency was limited by the hardware specifications. In particular, a compromise had to be found between maximising the

duration of the acquisition, the number of acquired channels and the sampling rate. The sampling theorem (or Shannon theorem) states that, in order to sample properly a continuous signal, the sampling rate must be higher than twice the highest frequency component in the signal. The problem with slamming is that it generates nearly instantaneous steps in the value of physical variables like local pressure and acceleration. In theory for instance, pressure at a given point on the hull may be seen to rise instantaneously from the atmospheric level to the value of the acoustic pressure in water. In practice, the phenomenon of air entrapment (the aerodynamic pressure build-up in the layer of air between the hull and the water surface prior to impact and the air bubbles trapped in the water just after contact [103]), the finite size of the pressure transducers diaphragms and their finite response time are usually responsible for finite, albeit very small rise times. Several experimenters have then underlined the necessity of using very high sampling frequencies (typically greater than 20kHz) if local pressure peaks are to be accurately recorded [24, 137]. From the point of view of the Shannon theorem this is justified by the fact that a signal featuring a sharp step is characterised by a very broad frequency spectrum.

In the present study, recording local pressure peak values was not an issue as it was not allowed by the limited measurement range of the transducers. However, the acceleration of the slam patch panels measured by the high-frequency accelerometers could have provided useful information about the inertial response of the panels themselves (see section 4.3).

Figure 4.3 shows the power spectrum of the signal from a high-frequency accelerometer mounted at the centre of a slam patch panel. The first and highest peak in the region of 350Hz corresponds to the first natural mode of the slam patch, involving a significant deformation of the load cell and nearly uniform displacement of the fibre-glass panel. On the other hand, the energy observed in the region of 4500 Hz and 8700Hz is thought to be associated with higher modes involving deformation of the fibre-glass panels and almost no deflection of the load cells. The relatively lower power corresponding to these frequency components should not mislead the reader into considering that they represent lower amplitude accelerations. In fact the higher modes appear to be responsible for the largest amplitude accelerations and the lower peaks in the spectrum are explained by the fact that the higher frequency vibrations are of a much shorter duration than the lower frequency ones (which may also be guessed from the broader, more smeared out shape of the higher frequency peaks and

by the larger area, i.e. energy, they enclose). Consequently, according to the sampling theorem and on the basis of the spectrum in figure 4.3, a sampling frequency of at least 30kHz would have been required for the high-frequency accelerometer signals. Alternatively, assuming that only the rigid-body acceleration of the fibre-glass panel is of interest for the analysis of its inertial response, lower sampling frequencies may have been adopted in conjunction with the use of anti-aliasing low-pass filters (with a cut-off frequency around 600Hz).

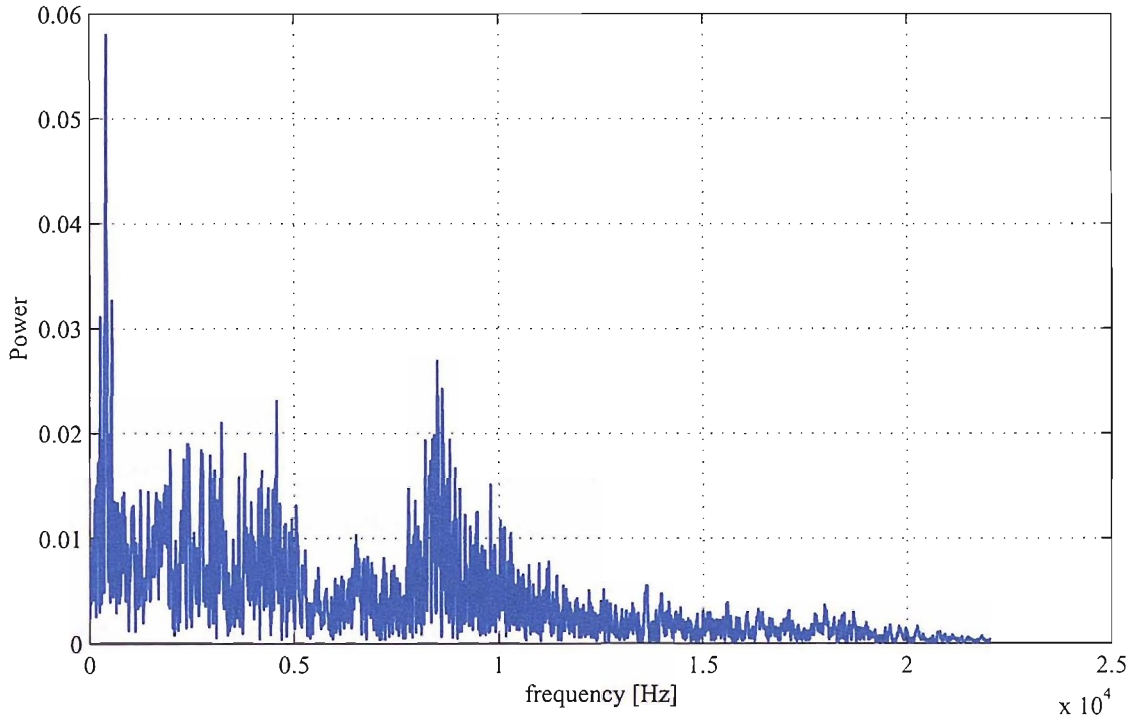

Figure 4.3: Typical power spectrum of the signal from a high-frequency accelerometer mounted at the centre of a slam patch fibre-glass panel. Sampling frequency: 44.1kHz. Fast-Fourier transform performed on 2^{13} samples.

For the present study, sampling frequencies higher than 10kHz could not be practically achieved. Besides, due to time and budget constraints, adequate low-pass filters could not be sourced. As a result, the recorded time histories of the local panel acceleration did show clear evidence of aliasing. The only valuable indication that could be obtained from the high-frequency accelerometers was then the time of first contact of the panels with the water surface (identified by the recorded acceleration suddenly diverging from the zero value). This could be determined with an accuracy better than $1/(2 \times$ sampling frequency), so typically 0.25 milliseconds. Section 4.3 further discusses whether the properly acquired acceleration of a sensor placed at

the centre of the slam patch panels could have provided useful information for the analysis of their inertial response.

Figure 4.4 shows the typical power spectrum of the signal obtained from a load cell during a rotational drop test. The main peak centred around 300Hz corresponds to the first wet natural frequency of the slam patch (cf section 4.3). It can be noted that the signal contains very little energy in the frequency range above 600Hz. Hence, sampling frequencies higher than 1200KHz should guarantee negligible errors due to aliasing. In order to confirm this, the results obtained by sampling the same load cell signal at different frequencies have been compared.

Figure 4.5 is based on the analysis of the force time histories obtained from nine different drop tests. It shows the mean relative error produced by sampling frequencies lower than 10kHz. Lower sampling frequencies are simulated by decimating a signal sampled at 10kHz by a factor "N" with $2 \leq N \leq 30$. By taking any sample between the first and the N^{th} of the original 10kHz series as the first sample of the decimated series, N different series can be obtained for each N. Each of the series thus obtained is then numerically resampled by a factor N using a polyphase filter implementation [93], and compared with the original 10kHz series. The mean value and the standard deviation of the relative difference between the original and the decimated series peak values is calculated for each N. Thus an estimate of the maximum and mean loss of accuracy produced by sampling rates lower than 10kHz can be obtained. For example, the figure shows that reducing the sample rate from 10kHz down to 1250Hz brings a maximum error of $\pm 8\%$ and a mean error of 1%. The 99% confidence interval for the relative error is bound by the mean error plus/minus 2.58 times the standard deviation of all observed errors.

Typically, for the drop tests a 2kHz sampling rate was used: according to figure 4.5 this resulted in a mean error smaller than 0.8% and in maximum errors smaller than 5%. For the forward speed tests, the sampling frequency had to be reduced to the minimum allowed in order to maximise the length of the acquisition (and hence the number of wave encounters). As a result a 1250Hz sampling rate was typically used: figure 4.5 shows that this involved a mean relative error of 1% and maximum errors smaller than 9%.

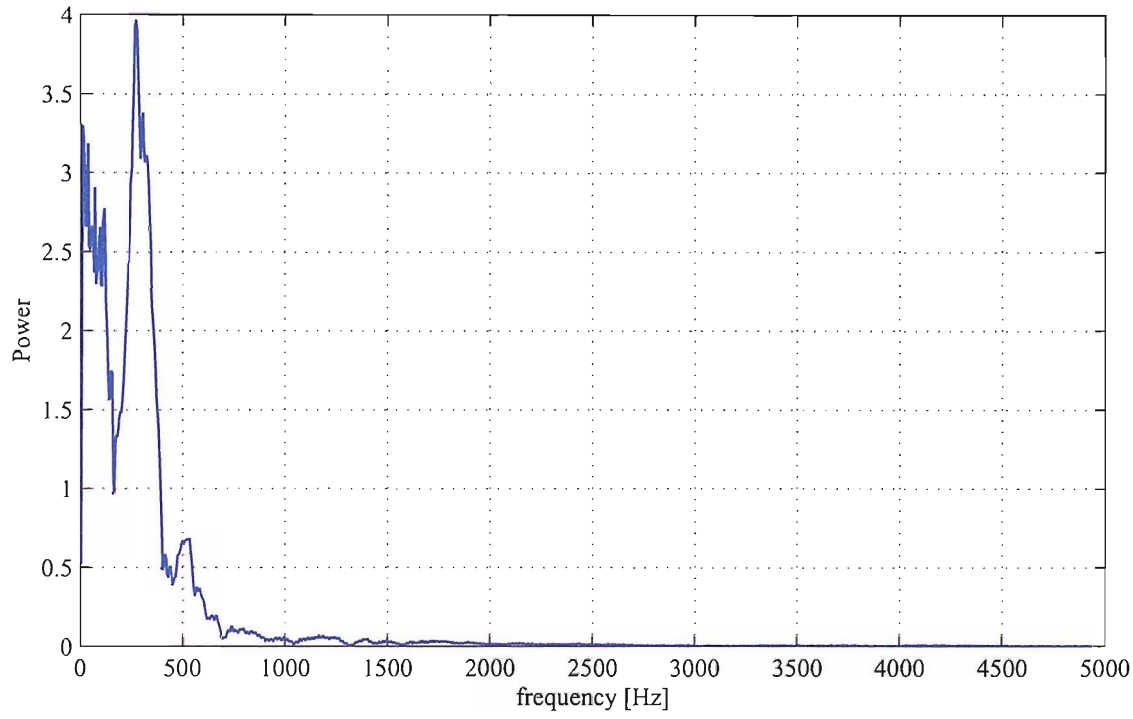

Figure 4.4: Typical power spectrum of the signal from a slam patch load cell. Sampling frequency: 10kHz. Fast-Fourier transform performed on 2048 samples.

4.2.4 Measurement of Impact velocity

During the rotational drop tests, the velocity of the model was obtained through the LVDT measuring the vertical displacement of station "0" relative to a fixed overhead point. In particular, the vertical velocity at station "0" was calculated as the time derivative of the data from the LVDT and the velocity at any point along the hull was subsequently found by linear interpolation between station "0" and the pivot point located behind the transom. It was then important to verify firstly that the velocity at station "0" was accurately measured and secondly that it was acceptable to assume that the model behaved like a rigid body rotating around the pivot.

All the acquired variables are subject to a quantisation error as the result of the analog-to-digital conversion. This error appears in the form of random noise with a maximum amplitude of 1/2 resolution and a standard deviation of $1/\sqrt{12}$ resolution [121]. As the result of the quantisation error, derivation in time introduces an error of maximum amplitude: $resolution \cdot f_s$. For the drop tests, typically performed with a sampling frequency $f_s = 2000Hz$ and a resolution of $0.091mm$ (see table 4.4), this could give a maximum error of $0.182m/s$, that is, up to 30% of the actual impact velocity for the lowest drop heights. In order to reduce this error, the signal from the

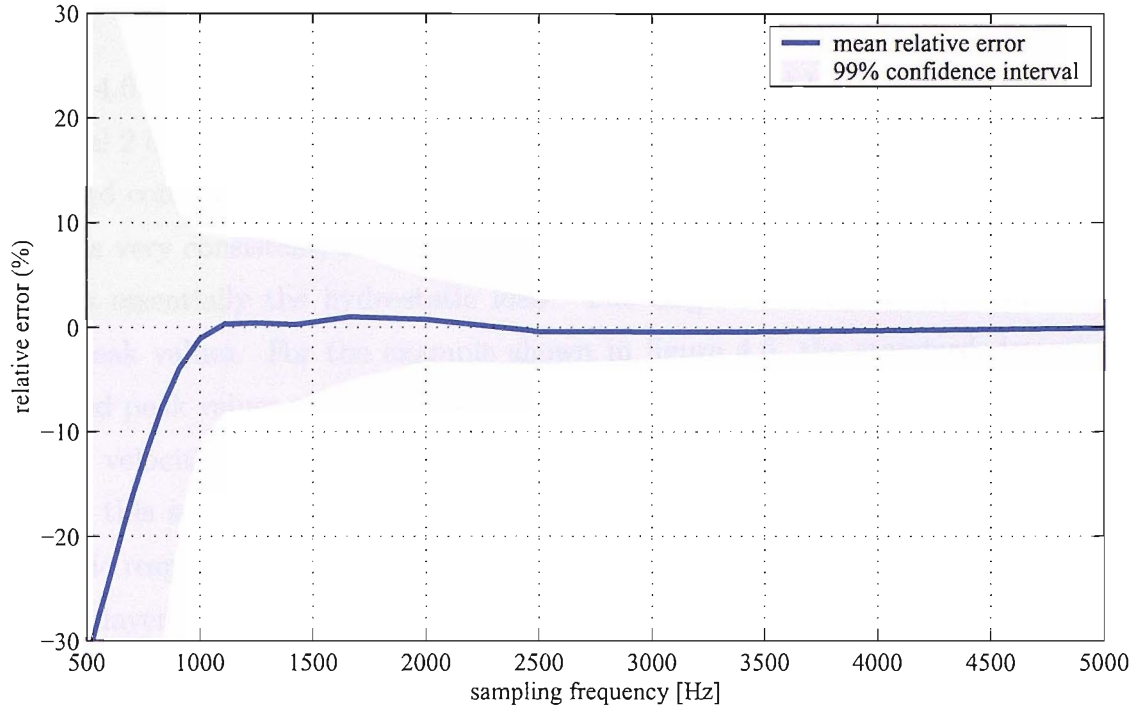

Figure 4.5: Relative error produced by sampling frequencies lower than 10kHz.

LVDT was low-pass filtered (by a "zero phase distortion" digital filtering algorithm with a 45Hz cut-off frequency) and then decimated down to the equivalent of a 100Hz sampling frequency. This guaranteed a maximum error of $0.00911m/s$ (equivalent to 0.024m/s at full scale), that is, less than 2% of the smallest recorded impact velocities.

The two "low frequency" accelerometers mounted respectively at the model LCG and near station "0" gave evidence of some longitudinal bending vibration initiated by the sudden release of the bow by the electromagnet. A natural frequency of 44Hz could be clearly identified and experiments carried out by moving around the two accelerometers indicated that this corresponded to a 2-node longitudinal bending mode with a node placed approximately at the pivot and another close to station "4". The velocity component associated with this vibration was estimated by analysing the accelerometers response. The acceleration produced by longitudinal bending was isolated by band-pass filtering the signals and its amplitude was divided by its cyclic frequency to provide the amplitude of the associated velocity. It could then be established that neglecting the influence of the vibration velocity affected the measured impact velocity by a maximum error of $0.02m/s$. Hence, the assumption that the model behaved like a rigid body before impact was found to be acceptable.

4.2.5 Repeatability

Figure 4.6 shows the time histories of the force measured by the load cell mounted on panel 2 during seven drop tests performed with the same drop height ($30mm$) and standard conditions (see table 4.2). It may be noted that the behaviour of the slam patch is very consistent, even in the last part of the acquisition, when the measured force is essentially the hydrostatic load. The largest differences are found for the force peak values. For the example shown in figure 4.6, the standard deviation of recorded peak values was equal to 5.2% of their mean value. Since the corresponding impact velocities showed only a small standard deviation (i.e. 0.6% of their mean value), this scatter was believed to be due mainly to other factors influencing the dynamic response of the slam patch. In particular, small changes in the behaviour of the air layer found between the hull and the water surface just before impact, may affect the quantity of air trapped under the hull and, consequently, the shape of the pressure rise during the very first stages of impact. This assumption is supported by the small differences that can be observed in figure 4.6 in relation to the slope of the force traces just after impact (i.e. approximately for $0 < t < 0.8ms$). Changes in the collapse behaviour of the air cushion may in turn be explained by small differences in the initial state of the water surface (due, for instance, to small amplitude long period waves left over from previous tests) or, simply, by the latex film not adhering perfectly to the panels. The influence of the air cushion collapse on the dynamic response of the slam patch is further discussed in section 4.3.

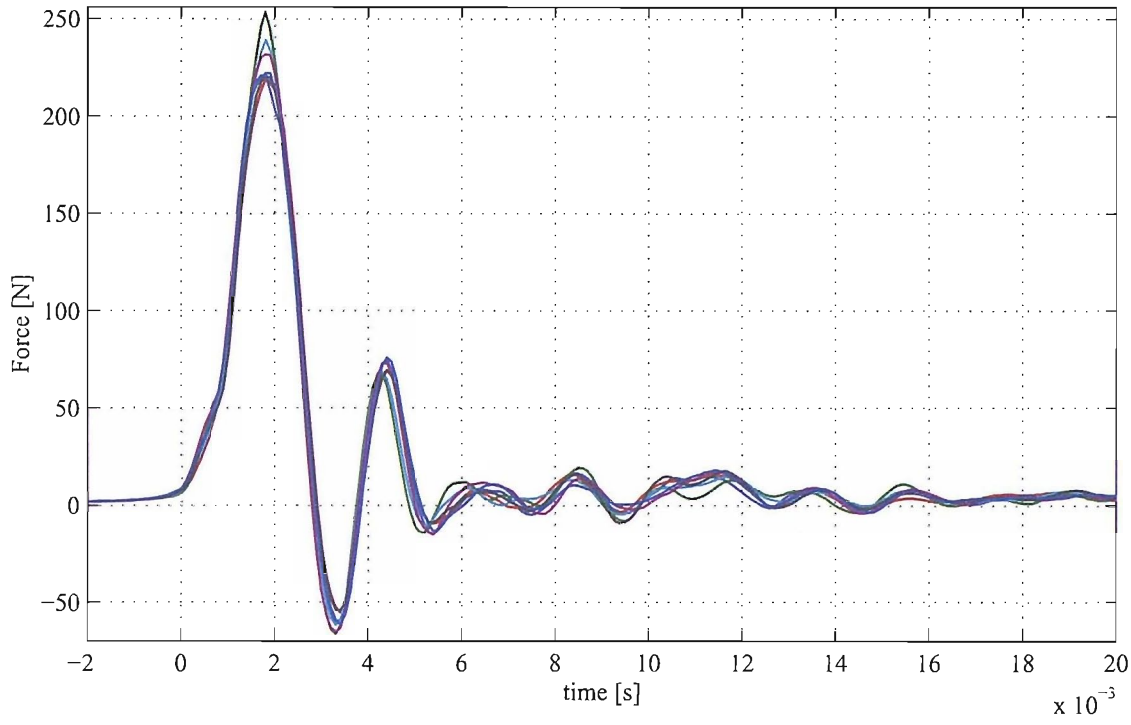

Figure 4.6: Repeatability of panel 2 measurements: force time histories from seven drop tests (drop height: $30mm$, standard displacement, standard moment of inertia, sampling frequency: 10kHz). Time $t = 0$ corresponds to the instant when the high frequency accelerometer placed at the centre of the panel responds to the impact.

4.3 Dynamic behaviour of a slam patch

The typical response of a slam patch to impact with water is shown in terms of the measured force by figure 4.8. In order to understand the behaviour of a slam patch as a mechanical system, it is useful to consider the analogy with the two-degrees-of-freedom assembly pictured in figure 4.7. Here, the lower mass "m_{sp}" represents the sum of the masses of the fibre-glass panel, of the elements that connect it to the load cell (threaded stud, nut and washer), of the high-frequency accelerometer attached at the centre of the panel and of half the load cell (cf figure 4.1). The spring stiffness "k_{sp}" represents the stiffness of the load cell: in particular, this is assumed to behave like a linear spring with the measured force being linearly proportional to its contraction/expansion. The viscous damper approximates the structural damping of the actual system. "F_{panel}" and "F_{model}" indicate respectively the overall hydrodynamic force acting on the panel and on the rest of the model. The higher mass "$m_{eq.mod}$" represents an equivalent mass of the model. Really, the structure supporting the slam patch would be more accurately represented by a complex assembly of masses,

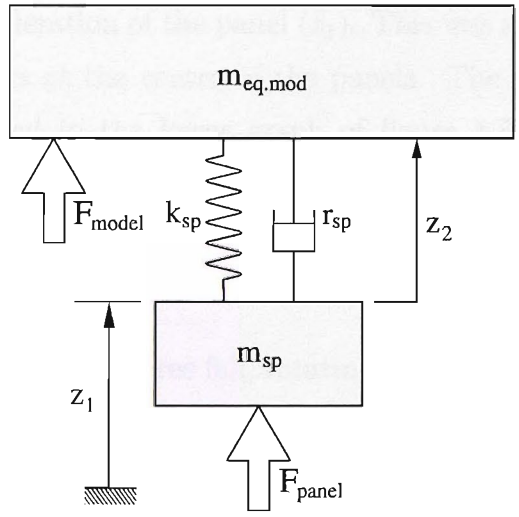

Figure 4.7: Two-degrees-of-freedom approximation of a slam patch assembly.

springs and dampers. However, the simplified system shown in figure 4.7 constitutes an acceptable approximation for studying the response of the slam patch in the very first stages of the impact. Its behaviour may be described by the following equations:

$$\begin{aligned} m_{sp}\ddot{z}_1 &= F_{panel} + k_{sp}(z_2 - z_2^0) + r_{sp}\dot{z}_2 \\ m_{eq.mod}(\ddot{z}_2 + \ddot{z}_1) &= F_{model} - k_{sp}(z_2 - z_2^0) - r_{sp}\dot{z}_2 \end{aligned} \tag{4.2}$$

By noting that the force exerted by the spring on the masses is equivalent to the measured force F_m (null when the distance between m_{sp} and $m_{eq.mod}$ is equal to z_2^0) and that the structural damping force is very small in comparison with the other forces (i.e. $r_{sp}\dot{z}_2 \ll [F_{panel}, k_{sp}(z_2 - z_2^0)]$), it follows that:

$$F_m = -k_{sp}(z_2 - z_2^0) = F_{panel} - m_{sp}\ddot{z}_1 + r_{sp}\dot{z}_2 \simeq F_{panel} - m_{sp}\ddot{z}_1 \tag{4.3}$$

Equation 4.3 indicates that the force measured by the load cell and the hydrodynamic force acting on the panel are not equal. In particular, their relative amplitude and phase differ depending on how the latter varies in time. If its frequency of variation is considerably lower that the slam patch natural frequency ω_{sp} , the measured force is equal to and in phase with the hydrodynamic force. If, on the other hand, the latter varies with a frequency far greater than ω_{sp}, the force measured by the load cell can be considerably different from the hydrodynamic one, both in phase and in magnitude. Kapsenberg [75] expressed this concept by commenting that a slam patch behaves like a "mechanical filter".

Equation 4.3 also shows that, theoretically, the hydrodynamic force acting on a slam patch (F_{panel}) can be obtained by measuring jointly the force from the load cell

(F_m) and the rigid-body acceleration of the panel ($\ddot{z}_1$). This was attempted by fitting high-frequency accelerometers at the centre of the panels. The resulting estimated hydrodynamic force is plotted in the lower graph of figure 4.8 together with the measured force.

The graphs of figure 4.8 are interpreted as follows:

- $t = -0.09s$: the model is released and begins to fall freely

- $-0.092s < t <\sim 0s$: the model is in free fall, rotating about the hinge placed at the transom. The panel is subject to a downward acceleration of 1.015g ($\ddot{z}_1 = -1.015g$). The load cell measures a force equal to 1.015 times the weight of m_{sp}

- $t \simeq 0s$: the accelerometer on the panel starts to show a positive acceleration. It is not possible to identify whether this is due to the panel touching the water or to a pressure rise in the air layer between the panel and the water surface. There is no clear discontinuity in either the load-cell or the accelerometer signal, suggesting that the transition between the aerodynamic and the hydrodynamic load is relatively smooth.

- $\sim 0ms < t <\sim 1ms$: the measured force F_m rises with increasing slope. The panel acceleration goes through at least one cycle of oscillation, which indicates that there may be an oscillation of the hydrodynamic load. It is believed that this phase may correspond to the air-cushion collapse as it has been described by Oakley [103]: the air bubbles that may have been trapped against the panel at the time of contact. break down into smaller bubbles that eventually leave the panel to escape towards the free-surface.

- $t \simeq 1.3ms$: there is a discontinuity in the slope of the load cell signal which may indicate a further step in the loading. The trace of the hydrodynamic force tends to confirm this step, however, it is plotted with a dashed line to indicate that the sampling frequency is not sufficient to accurately represent the original signal from the accelerometer. From this point on, a few large amplitude oscillations can be observed in the accelerometer signal: while their trace is not representative, they do correspond to a vibration of the panel. There are not enough indications to determine whether this vibration is forced by a fluctuation of the load, or if it corresponds to a natural mode of the panel excited by a single sharp step in the load.

• $t \simeq 1.8ms$: the slope of the load cell signal reaches its maximum. It can be shown that, in this phase, the velocity of the panel relative to the water surface can actually be inverted and become positive (i.e. the panel moves away from the surface). This produces a sharp drop of the hydrodynamic load, which is indeed observed after $t = 1.8ms$.

• $t = 2.3ms$: the load cell compression reaches its maximum value, while the hydrodynamic load is estimated to drop considerably. The measured force lags behind the hydrodynamic load and its maximum appears to be lower than the maximum hydrodynamic force.

• $\sim 2ms < t <\sim 12ms$: the slam patch vibrates with decreasing amplitude and increasing period of oscillation. The observed period ($3.1ms$ to $3.8ms$) is expectedly longer than the natural period of the slam patch measured in the dry condition($2.21ms$), due to the effect of the hydrodynamic added mass.

• $t > 3ms$: the hydrodynamic force appears to lag behind the panel motion, with a phase delay of approximately $\pi/4$. This corresponds to a situation where the slam patch performs free vibration in water.

In this phase, the hydrodynamic load seems to drop occasionally below the atmospheric pressure. This phenomenon has indeed been observed by other authors [45, 57, 85]: it is due to the velocity of the panel relative to the water becoming positive and it can sometimes lead to cavitation. In the present case, pressure is seen to never drop very far below the atmospheric value, despite the panel featuring occasionally large positive relative velocities. The fact that air can reach the lower side of the panel, by flowing between the latex membrane and the panel itself, explains why significant underpressures are never observed.

• $t >\sim 12ms$ the hydrodynamic load becomes in phase with the panel oscillation as the higher frequency vibrations gradually die out. The residual lower frequency vibrations that are then observed are believed to be related to higher modes of deformation of the model. The measured load F_m is then equal to the actual hydrodynamic load.

• $t > 0.15s$: the model oscillates about its final equilibrium position. The measured load varies about the hydrostatic value. As the higher frequency vibrations die out, a small amplitude oscillation corresponding to the first longitudinal bending mode of

the model (natural period $\simeq$ 0.03s) can be identified.

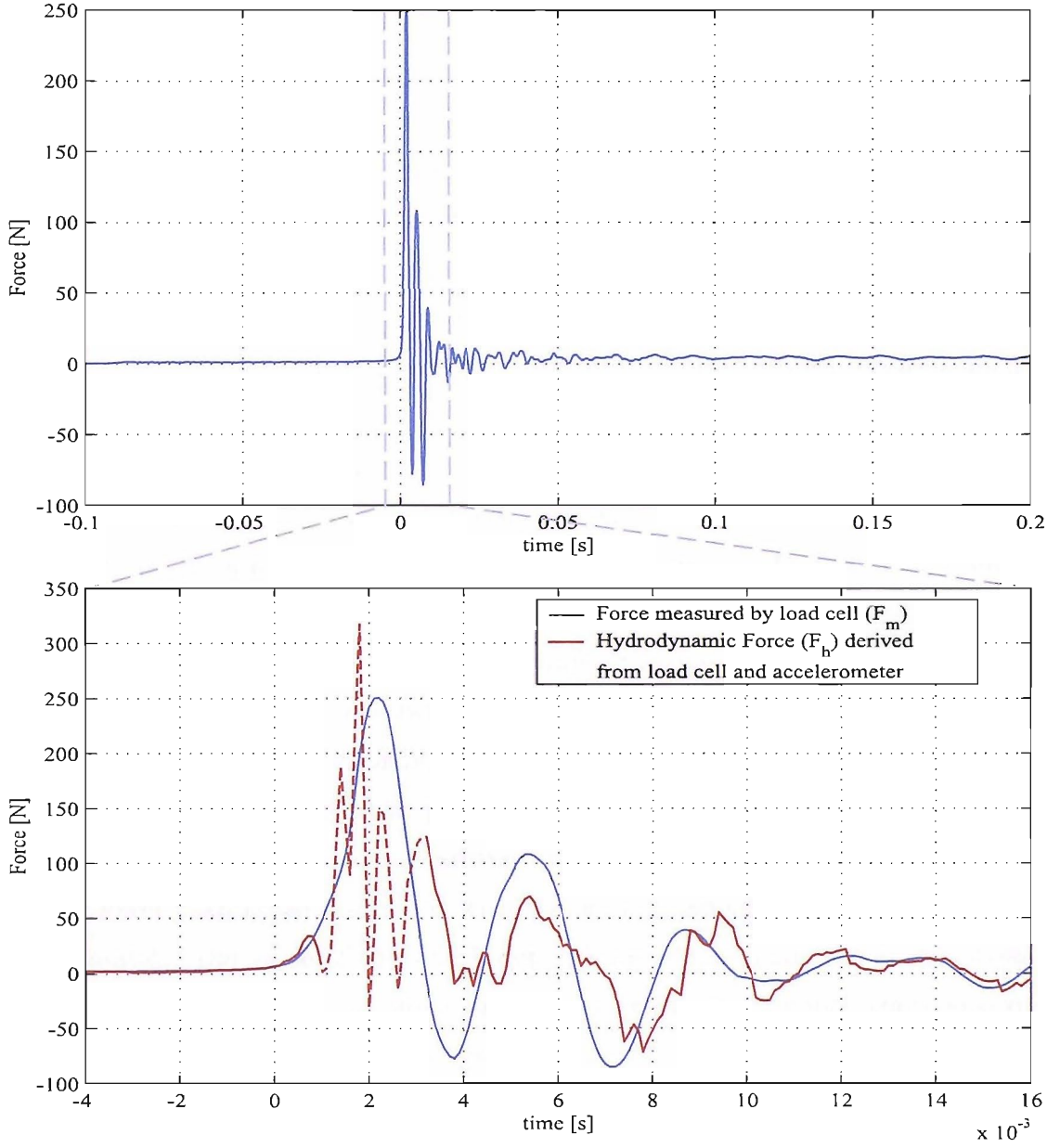

Figure 4.8: Typical response of a slam patch during a rotational drop test on flat water. The hydrodynamic force is estimated as $F_{panel} = F_m + m_{sp}\ddot{z}_1$ with $\ddot{z}_1$ equal to the acceleration measured by the high-frequency accelerometer fitted on the panel (cf figure 4.7). Where the hydrodynamic force is plotted with a dashed line, the sampling frequency is believed to be too low to obtain an accurate representation of the original signal. The present example corresponds to a recording taken on panel 3. Impact velocity: $0.69m/s$; sampling frequency: 5kHz.

4.4 Hydrodynamic loads and equivalent static loads

When studying slamming loads it is common practice to refer to equivalent uniform static pressures or effective pressures. These correspond to the pressures which, if applied to a particular structural component in a static way, will result in the same maximum deformation and maximum stress as produced by the actual dynamic loading [2, 59]. Expressing slamming loads in terms of uniform equivalent static loads makes the task of carrying out structural calculations significantly simpler: the complexities related to the spatial and temporal variation of the loads are removed and stresses and strains can be calculated according to the simpler laws of statics. Hence, classification societies and standard organisations typically publish recommended design loads in terms of equivalent static loads [3, 70].

The definition of the equivalent uniform static pressures (EUSP) corresponding to a particular slamming event and a specific structural element (e.g. a panel), is not univocal. As a matter of fact, the stress/strain pattern produced by a uniform pressure is generally different from the distribution of stresses and strains resulting from actual slamming loads. Thus, for example, Hayman et al. [57] showed that, for a panel of a V-section GRP sandwich hull, the ratio of the maximum core shear stress to the maximum laminate in-plane stress was larger for an actual slamming load than for a uniformly distributed static pressure. In other words, the EUSP corresponding to the maximum in-plane stress observed on their test specimen, induced core shear stresses lower than those associated with the actual loading.

Ultimately. the value of the EUSP depends on which maximum actual stress or strain of the structure (e.g. in-plane stress at the centre of the panel, transverse shear stress, etc.) is to be matched through a uniform static load. In the case of a slam patch, the main mode of deformation involves a compression/extension of the load cell and a quasi-uniform translation of the panel. Consequently, it is convenient to define a EUSP as the pressure that produces a compression of the load cell equal to the maximum observed during an actual impact. For each particular drop test, this value can be easily determined as the maximum compression force measured by the load cell, divided by the surface area of the slam patch panel.

It is arguable that equivalent static pressures provide a more immediate representation of the loading of a structure than the maximum hydrodynamic loads. In fact, in most cases, the relation between internal stresses and EUSP is linear. On the

other hand, there is no univocal correspondence between the magnitude of the hydrodynamic loads and the structural response. Typically, a very high pressure pulse of extremely short duration can result in lower maximum stresses than a moderate pressure applied over a longer period. This appears to be one of the main sources of misunderstanding when discussing slamming loads: maximum theoretical or experimental hydrodynamic pressures are often quoted without mentioning the relation between their time variation and the natural period of the structure they act upon.

Historically, most studies on slamming loads consider the water impact problem (i.e. the determination of the hydrodynamic pressures) and the structural response problem separately (e.g. [106]). Hydrodynamic loads are determined either by analytical methods or through semi-empirical procedures (e.g. [2,59,124]) and then taken as an independent input to the problem solving for the deformation of a specific structural element [27,73]. Behind this kind of approach, lies the assumption that local hydrodynamic loads produced by slamming are not affected by the response of the hull, or, at least, not in a way that can influence in turn the maximum amplitude of the response.

On the basis of theoretical and experimental evidence, Sellars was one of the first authors[1] to point out that, for a given hull and fixed impact conditions, local peak pressures could vary significantly depending on the structural characteristics of the hull. Faltinsen, Kvålsvold and Haugen have carried out an extensive investigation about the effects of fluid-structure interaction in the water impact problem [42–45,55, 85]. One of their main conclusions is that, when hydroelastic effects are significant, they lead to a considerable reduction of the hydrodynamic impact pressures. In simplified terms, this can be explained by considering that, as the portion of the hull that is exposed to impact responds to the sudden load by deflecting upwards, the relative velocity between the hull and the water surface is reduced, and the resulting hydrodynamic pressures are lower than those that would be observed for an infinitely rigid hull. Faltinsen and Kvålsvold rightly comment that, when hydroelastic effects are significant, the concept of design equivalent pressure looses meaning: one cannot obtain the hydrodynamic loading by assuming that the structure is rigid and then use it to calculate the structural response, as both are mutually dependent.

[1] Kvålsvold et al. [85] reported prior studies performed by Meyerhoff [97] on slamming of elastic wedges, however the author could access his publication

In conclusion, it is important to note that, ultimately, both slamming hydrodynamic pressures and equivalent static pressures depend on the structural characteristics of the hull they are measured on.

The data shown in figure 4.8 tend to confirm that, in the present investigation, the hydrodynamic loads were indeed affected by the response of the slam patch. Ideally, both variables should have been accurately measured, in order to fully describe the impact phenomenon. However, the determination of the hydrodynamic loads involved several practical difficulties. Firstly, as shown by figure 4.8 and previously mentioned in section 4.2.3, the data acquisition equipment used for the present investigation did not allow the high-frequency accelerometer signals to be properly sampled. Secondly, there is evidence that, during the very first part of the impact, the acceleration at the centre of the panel oscillated with a frequency higher than the slam patch natural frequency ω_{sp}. It is possible that these higher frequency oscillations were related to a deformation mode of the fibre-glass panel. In this case, equating the recorded acceleration to $\ddot{z}_1$ would result in a wrong estimate of F_{panel}. Examining the vibratory response of the panels in greater detail, would have required several accelerometers to be mounted on each panel and higher sampling rates to be adopted. Besides the latter option not being achievable with the available equipment, the former would have increased sensibly the mass of the slam patches (m_{sp}) and thus changed their dynamic characteristics [91]. It is believed that, in general, when hydrodynamic pressures are of interest, direct measurement by an array of pressure transducers offers a better solution than the slam patch technique (cf. [76, 112, 114]).

In the remaining part of the present chapter, the loads recorded during the slam patch tests are presented in terms of the equivalent uniform static pressures. Further details concerning the mechanical properties of the slam patches and the way in which full-scale pressures can be extrapolated from the model measurements are discussed in the following section.

4.5 Scaling of slamming loads

Before examining the experimental results of the present investigation , it is important to consider whether and how model scale data relate to full scale conditions.

In order to analyse the forces acting during a slam, it is customary to separate the impact problem in different time phases, each dominated by a different physical

phenomenon. For example, Oakley identified three phases, corresponding respectively to the time prior to contact between the hull and the free surface, the time between contact and full wetting, and the time following full wetting of the body [103]. Sellars described several time scales corresponding to the periods of the different waves propagating through the structure and the water, but chose to divide a slam into two main stages: during the first, elastic forces and compressibility effects played a major role, while the second was dominated by the rate of change of the added mass [120]. Kvålsvold et al., like Oakley, identified three phases, but did not take into consideration the effects of air entrapment [85]. In their study, the first phase, termed the "compressibility" phase, initiated after contact and lasted as long as the velocity of the intersection between the free surface and the hull was greater than the speed of sound in water. The second phase, described as the "structural inertia" phase, lasted until the structural member under study (a portion of a catamaran wetdeck in [85]) was fully wet. The third, described as the "added mass-restoring" phase, was characterised by the elastic restoring forces associated with bending of the hull element becoming of the same order of magnitude as the added mass terms.

Depending on the dominant forces, each phase of a slam is characterised by different non-dimensional parameters. For example, before contact, the aerodynamic pressure build-up and the ensuing deformation of the free surface are a function of the ratio of the downward velocity of the hull to the velocity of sound in air [103]. Immediately after contact, the air cushion collapse and the related pressure rise depend on both the Reynolds number and the Weber number. The variations of the hydrodynamic pressure associated with the effects of water compressibility are in turn related to the ratio of the hull velocity to the velocity of sound in water. Finally, the hydroelastic response of the structure and the forces associated with variation of the hydrodynamic added mass, can be scaled on the basis of the Cauchy number and of the Froude number.

Practically, it is then impossible to reproduce all the phases of a slam with a scale model experiment (unless, obviously, the scaling ratio is equal to one). The choice of the initial impact velocity determines which particular force components are appropriately scaled.

For seakeeping tests, velocities are normally scaled on the basis of a constant Froude number [88]: this guarantees that the ratio of inertia forces to gravity forces remains unchanged and, consequently, that the relative amplitude of motion in waves

is properly scaled. When slamming is involved, Froude scaling results in factors like bow emergence, relative velocity and trim angle at impact, being accurately reproduced. Moreover, like inertia forces, overall slamming forces are proportional to $\rho L^2 V^2$ (with L and V indicating respectively the characteristic length and velocity), hence their relative influence on the rigid body motion is equally preserved with a constant Froude number[2].

Froude scaling is not compatible with proper scaling of viscous forces and air entrapment effects. The former play a minor role during a slam, and it can be shown (cf. [119]) that errors due to differences in the Reynolds number are negligible. The latter, on the other hand, can bring a significant reduction of the local peak pressures, depending on the hull shape and on the impact velocity. Adopting a constant Froude number results in the cushioning action of air being comparatively smaller at model scale [103]. Hence, scale model tests tend to give conservative estimates of the full-scale slamming pressures.

The issues involved with the scaling of the hydroelastic behaviour of a hull panel subject to slamming can be illustrated by analysing the equation of motion describing its response to an impact. If compressibility as well as viscous and air entrapment effects are neglected, this can be written as:

$$\tilde{m}\ddot{q} + \tilde{k}q = \tilde{F}(\bar{V}, \dot{\bar{V}}, \dot{q}, \ddot{q}) \tag{4.4}$$

where q indicates a modal coordinate and $\tilde{m}$, $\tilde{k}$ and $\tilde{F}$ are respectively the generalised mass, stiffness and force. The generalised force acting on the panel may be written as:

$$\tilde{F}(\bar{V}_i, \dot{\bar{V}}_i, \dot{q}, \ddot{q}) = \int_{-a}^{a}\int_{-b}^{b} p(x,y,t)\psi(x,y)dxdy \tag{4.5}$$

with:

$$p(x,y,t) = -\frac{\rho\bar{V}(t,x)c(t,x)}{\sqrt{c^2(t,x)-y^2}} \cdot \frac{\partial c(t,x)}{\partial t} - \rho\frac{\partial\bar{V}(t,x)}{\partial t}\sqrt{c^2(t,x)-y^2} \tag{4.6}$$

The latter expression can be derived by solving the potential flow problem for an expanding flat plate penetrating the water and by applying Bernoulli's equation to obtain the pressure distribution (cf. [41]). It relies on the assumption that the fluid is incompressible and the flow irrotational. Furthermore, the three-dimensional hydrodynamic problem is treated as combination of independent two-dimensional problems

[2]In fact, the slamming force may be regarded as the inertia force of a mass of water being suddenly accelerated by impact with the hull

describing the flow in each section perpendicular to the longitudinal axis of the plate. This simplification is acceptable as far as the panel dimensions relative to the hull overall length and the trim angle at impact are both small. In equations 4.5 and 4.6 the x and y axes are considered to be aligned with the boat longitudinal and transversal axes, a and b represent respectively the half length and width of the panel, and $c(x,t)$ corresponds to the y coordinate of the intersection between the hull and the free surface. The flow is assumed to be symmetric about the X axis.
$\bar{V}(t,x)$ indicates the average effective impact velocity at x and it may be obtained as:

$$\bar{V}(t,x) = \frac{1}{2c}\int_{-c(t,x)}^{c(t,x)} V_e(x,y,t)dy \tag{4.7}$$

$$\text{with } V_e(x,y,t) = V_{rb}(x,t) + \dot{q}(t)\cdot\psi(x,y) \tag{4.8}$$

$V_{rb}(x,t)$ corresponds to the rigid-body velocity of the hull, while $\dot{q}(t)\cdot\psi(x,y)$ identifies the velocity component associated with the deformation of the panel. Hence, $V_e(x,y,t)$ represents the effective velocity of a specific point on the panel relative to the free surface. A similar approximation to that expressed by equation 4.6 has been adopted by Kvalsvold et al. and proved to be acceptable upon comparison with experimental results (cf. [85]).
For the sake of simplicity, only one mode of deformation (the first symmetric) is considered in the present discussion. Hence, $\tilde{m}$, $\tilde{k}$, $\tilde{F}$ and $q(t)$ all indicate scalar variables and $\psi(x,y)$ is a scalar function describing a single mode shape. The discussion would be conceptually similar if several natural modes were taken into account.

By considering $L = L_p$ (panel length), $T = 2\pi\sqrt{\tilde{m}/\tilde{k}}$ (the panel first dry natural period) and ρL^3 as respectively the characteristic length, time and mass scales, the following non-dimensional variables can be introduced:

$$x' = \frac{x}{L}, \quad y' = \frac{y}{L}, \quad t' = \frac{t}{T}, \quad q'(t') = \frac{q(t)}{L}$$

By multiplying both sides by $\frac{T^2}{\rho L^4}$, equation 4.4 may then be re-written in non-dimensional terms as:

$$\left(\frac{\tilde{m}}{\rho L^3}\right)\frac{\partial^2 q'}{\partial t'^2} + \left(\frac{T^2\tilde{k}}{\rho L^3}\right)q' = \int_{-a/L}^{a/L}\int_{-b/L}^{b/L} p'(x',y',t')\psi'(x',y')dx'dy' \tag{4.9}$$

$$\text{with} \quad \psi'(x',y') = \psi(x,y) \tag{4.10}$$

and

$$p'(x',y',t') = -\left(\frac{\bar{V}}{L/T}\right)\cdot\frac{c}{L}\cdot\frac{1}{\sqrt{c^2/L^2-y^2/L^2}}\cdot\frac{\partial c}{\partial t}\cdot\frac{T}{L}-\left(\frac{\partial\bar{V}}{\partial t}\cdot\frac{T^2}{L}\right)\sqrt{c^2/L^2-y^2/L^2}$$
$$= -\left(\frac{\bar{V}}{L/T}\right)\cdot\frac{c'}{\sqrt{c'^2-y'^2}}\cdot\frac{\partial c'}{\partial t'}-\left(\frac{\partial\bar{V}}{\partial t}\cdot\frac{T^2}{L}\right)\sqrt{c'^2-y'^2} \quad (4.11)$$

with

$$c'(x',t') = c(x,t)/L \quad (4.12)$$

$$\frac{\bar{V}}{L/T} = \frac{1}{2c'}\int_{-c'}^{c'}\frac{V_{rb}}{L/T}+\frac{\partial q'}{\partial t'}\cdot\psi'(x',y')dy' \quad (4.13)$$

and

$$\frac{\partial\bar{V}}{\partial t}\cdot\frac{T^2}{L} = -\frac{1}{2c'}\left\{\int_{-c'}^{c'}\frac{V_{rb}}{L/T}+\frac{\partial q'}{\partial t'}\cdot\psi' dy'\cdot\frac{1}{c'}\frac{\partial c'}{\partial t'}+\int_{-c'}^{c'}\frac{\dot{V}_{rb}}{L/T^2}+\frac{\partial^2 q'}{\partial t'^2}\cdot\psi' dy'+\right.$$
$$\left.+\frac{\partial c'}{\partial t'}\left[\frac{2V_{rb}}{L/T}+\frac{\partial q'}{\partial t'}\cdot\left(\psi'(x',c')+\psi'(x',-c')\right)\right]\right\} \quad (4.14)$$

It can be shown that, if the hull section at the longitudinal coordinate x can be described by a polynomial of the form $z(x,y) = p_1\cdot y + p_2/L\cdot y^2 + \ldots + p_n/L^{n-1}\cdot y^n$, then $c(t,x)$ may be safely assumed to verify the relation:

$$c(x,t)\cdot\alpha_1 p_1 + c^2(x,t)\cdot\alpha_2 p_2/L + \ldots + c^n(x,t)\cdot\alpha_n p_n/L^{n-1} = V_{rb}\cdot t \quad (4.15)$$

Hence:

$$c(x,t) = f(p_1, p2, \ldots, p_n, L, V_{rb}, t) \quad (4.16)$$

and, from equation 4.12,

$$c'(x',t') = g(p_1, p2, \ldots, p_n, \frac{V_{rb}}{L/T}, t') \quad (4.17)$$

Non-dimensional parameters appear in equations 4.9 to 4.17 as:

$$\frac{\tilde{m}}{\rho L^3}\ ,\quad \frac{T^2\tilde{k}}{\rho L^3}\ ,\quad \frac{V_{rb}}{L/T}\ ,\quad \frac{\dot{V}_{rb}}{L/T^2}\ ,\quad \frac{a}{L}\ ,\quad \frac{b}{L}\ ,\quad p_1, p_2, \ldots, p_n \quad (4.18)$$

It may be noted that, by substituting L/T with a characteristic velocity V, the parameter $(T^2\tilde{k})/(\rho L^3)$ can be rewritten as $\tilde{k}/(\rho V^2 L)$. The latter expression corresponds to the definition of the Cauchy number, which represents the ratio of elastic forces to inertia forces [119].

In order for the hydroelastic response of a scaled hull panel to be similar to that of a full scale panel, the following conditions must then be verified:

- The model and full scale hulls and hull panels must be geometrically similar: all linear dimensions should scale like L and, as a result, the parameters a/L, b/L and $p_1, p_2, \ldots, p_n$ must have the same value.

- Parameters $V_{rb}/(L/T)$ and $\dot{V}_{rb}/(L/T^2)$ must be matched. If the boat geometry, mass and moments of inertia are properly scaled, V_{rb} should scale like $\sqrt{L}$ and $\dot{V}_{rb}$ should be invariant [88]. Consequently, the first dry natural period of the hull panels T must also be scaled like $\sqrt{L}$.

- The generalised stiffness of the panel $\tilde{k}$ must scale like ρL^2 (ρ indicating the density of water). Since $T = \frac{1}{2\pi}\sqrt{\tilde{m}/\tilde{k}}$, if T is scaled like $\sqrt{L}$, the generalised mass $\tilde{m}$ will necessarily be scaled like ρL^3.

Under the assumption that the dynamic response of a panel subject to slamming is dominated by one single mode of deformation, the equivalent uniform static pressure measured for a given slam should be proportional to $\tilde{k}q_{max}/L^2$, where q_{max} indicates the maximum amplitude of response. Consequently, if all the conditions for similarity are met, equivalent uniform static pressures scale like ρL.

Equation 4.10 implies that the mode shape(s) of the full scale and model scale panels must be similar. This brings up two important considerations. On one hand, it is arguable that the mode shapes of a slam patch as built for the present investigation do not correspond to those of an actual hull panel. As illustrated by figure 4.9, the first mode shape of a slam patch involves a nearly uniform vertical translation of the panel while that of an actual panel is characterised by a maximum deflection at the centre and virtually no deflection at the edges. Consequently the hydroelastic response and, hence, the equivalent static loads measured by the slam patches used in this study should not be directly compared with those of an actual hull panel.

On the other hand, it must be noted that, from a practical point of view, it is extremely difficult if not impossible, to replicate at model scale the dynamic behaviour of an existing full-scale structure. This is due to the fact that the requirement for the generalised mass and stiffness to be properly scaled, imposes several constraints involving the density, the Young's modulus and the Poisson ratio of the model material, the thickness of the scaled panel, the boundary conditions and the scaling ratio. Such parameters can be varied only within limited ranges and are not mutually independent, hence, the full-scale mode shapes can rarely be matched.

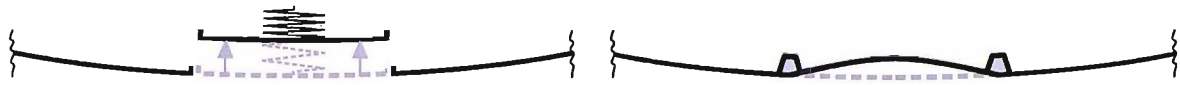

(a) Slam patch (b) Actual panel

Figure 4.9: Difference between the first mode shape of a slam patch and of an actual panel (approximative sketches).

In the present study, the choice of the slam patch configuration was based partly on practical considerations and partly on the fact that the simpler boundary conditions would be easier to replicate in an analytical model. For reference, the dynamic characteristics of actual model-scale panels are reported by table 4.5 together with those of their full-scale equivalent. A further discussion on how the loads measured for the present free-edge panels may compare with those found for more realistic constrained-edge configurations, will be presented in a further section.

Table 4.5: First dry natural frequency of the slam patches: values are obtained by identifying the first peak in the averaged response amplitude operator obtained from ten impact hammer tests.

Slam Patch (size: $80 \times 80mm$)				
Panel #	mass "$\tilde{m}$" [g]	1^{st} natural frequency [Hz]	1^{st} natural period [ms]	stiffness "$\tilde{k}$" [N/m]
1	69	503.6	1.99	6.91E+05
2	68	517.6	1.93	7.19E+05
3	72	456.6	2.19	5.93E+05
4	64	535.1	1.87	7.23E+05
5	69	484.2	2.07	6.39E+05
6	71	478.6	2.09	6.42E+05
Equivalent Full-scale Panel (size: $560 \times 560mm$)				
Panel #	mass "$\tilde{m}$" [kg]	1^{st} natural frequency [Hz]	1^{st} natural period [ms]	stiffness "$\tilde{k}$" [N/m]
1	24.3	190.3	5.25	3.47E+07
2	23.9	195.6	5.11	3.61E+07
3	25.3	172.6	5.79	2.98E+07
4	22.5	202.3	4.94	3.63E+07
5	24.3	183.0	5.46	3.21E+07
6	25.0	180.9	5.53	3.22E+07

4.6 Experimental results

The most relevant results obtained from all test series are discussed below. Data are presented for both the model-scale (top and right axes) and equivalent full-scale

conditions (bottom and left axes). In conformity with the considerations on scaling set out in the previous section, Froude scaling has been applied. Pressures are reported as measured by the load cells and no correction from the acceleration of the panel has been included. As mentioned previously, the loads thus obtained correspond to the equivalent uniform static pressures which are normally referred to for design purposes.

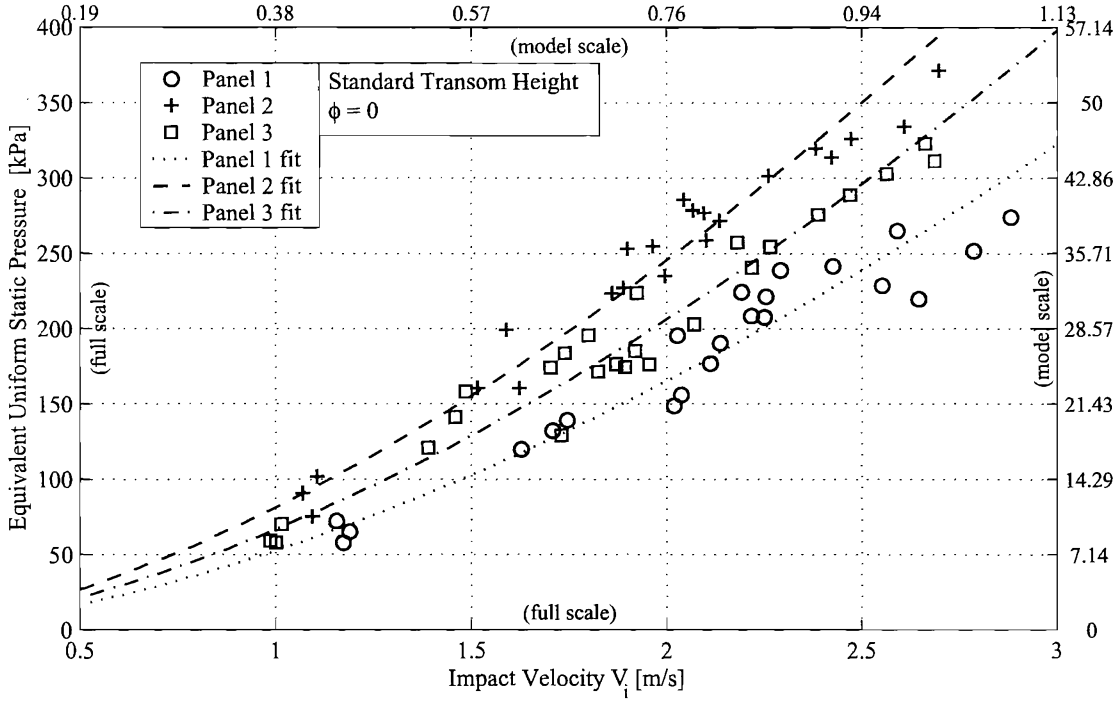

Figure 4.10: Relation between impact velocity and maximum equivalent pressure: zero heel angle.

The relation between impact velocity and maximum equivalent uniform static pressure is shown in figures 4.10 and 4.11. In particular, figure 4.10 presents the pressures obtained from rotational drop tests with zero heel angle. Impact velocities V_i are obtained for each panel from measurement of the rigid-body motion of the model through the vertical displacement transducer. Bearing in mind the large scatter that often affects experimental measurements of slamming pressures, the consistency of the present results was judged very satisfactory.

Trend lines of the form $P_n = \beta_n \cdot V_i^{\gamma_n}$ (P_n: maximum EUSP on panel "n") were originally fitted to the measured data and have been reported in the graphs. Values of γ_n have been reported in table 4 of appendix I: for all six panels, they were found to lie in the range between 1.59 and 1.79. While both theoretical considerations [41]

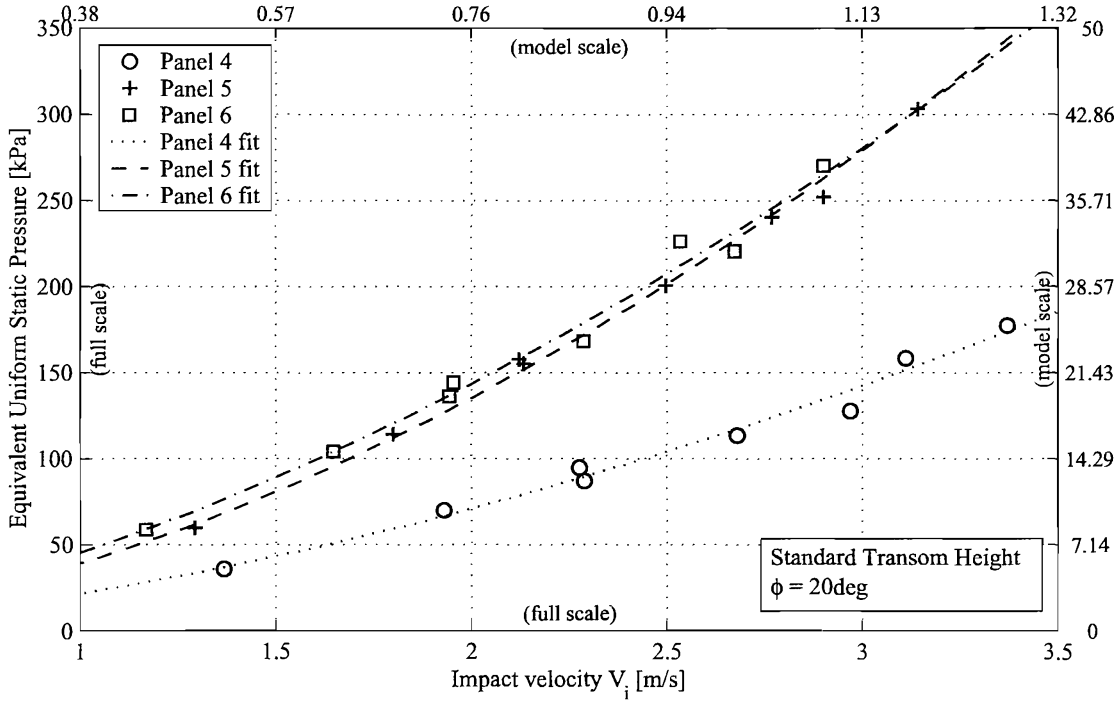

Figure 4.11: Maximum equivalent uniform static pressures measured at twenty degrees heel angle.

and experimental evidence [105] indicate that direct hydrodynamic pressures are proportional to the impact velocity squared, values of γ lower than 2 are expected in the expression relating the equivalent static pressures to V_i. For instance, fitting the EUSP measurements obtained by Hagiwara et al. [52] with a similar function, yields $\gamma \simeq 1.8$.

Experimental data presented by Faltinsen et al. [45] indicate that the relation between the equivalent static pressures and the impact velocity is actually quadratic for low impact velocities and tends to become linear for very high velocities. From a physical point of view, this behaviour is plausible and may be explained as follows: for very low impact speeds, the structure responds quasi-statically to the hydrodynamic impact pressures, which are proportional to the impact velocity squared. Conversely, at very high impact speeds, the duration of the hydrodynamic pressure pulse becomes significantly shorter than the structure first natural period: while maximum hydrodynamic pressures may still be assumed to depend on the velocity squared, the dynamic amplification factor tends to be inversely proportional to the impact velocity. Hence, the amplitude of the structural response becomes a linear function of the impact velocity.

It can be noticed from figure 4.10 that the pressures recorded at the highest impact velocities consistently lie below the trend line: this fact supports the conclusion that a function of the type $P_{eq} = \beta \cdot V_i^{\gamma}$ may represent a valid approximation only over limited ranges of impact velocities and that, eventually, the exponent γ should tend to a value of 1 for high impact velocities.

The data reported in figure 4.10 correspond to a series of drops carried out in the standard condition, i.e. with the standard displacement and mass moment of inertia (as indicated in table 2) and with the transom height set for a point of first contact between the hull and the water placed at 34.5% of the waterline length aft of the forward perpendicular. In this condition, panel 2 hit the water slightly before panel 1 and 3 in the upright tests, and similarly panel 5 preceded panel 4 and 6 in the heeled tests.

The effect of panel curvature may be observed by comparing the results for panel 2 and 5: as the curvature radius decreases from 6.2m to 1.94m, β shows a 52% reduction. On the contrary of what would be expected, in the same case, γ increases. This, however, may be explained by the fact that a lower number of data points was used for the calculation of γ_5.

The effect of the trim angle of the panel at the time of impact was investigated by performing rotational drop tests with different transom heights: as a result, the point of first contact with water was shifted fore and aft of the area where the slam patches were fitted. A summary of the results of these tests is presented in figure 4.12. It was noted that small changes in trim (i.e. of the order of 1 degree) did not have a significant effect on the values of γ while they altered β by as much as 50%.

Figure 4.13 gives evidence of the decay of maximum pressures along the girth: the indicated pressures were recorded by instrumenting both panel 2 and panel 5 during the same test. Rotational drops were carried out at zero heel angle and the maximum pressures have been plotted with respect to the impact velocity of panel 2. It may be noted that the values measured for panel 5 could be ascribed almost entirely to hydrostatic pressure. This was certainly the combined result the high average deadrise angle of the side panel ($\approx 37deg$) and of the considerable deceleration happening between the time of impact of panel 2 and the first contact of panel 5.

The analysis of panel response times and of vertical displacement time histories obtained from the linear potentiometer and from the accelerometers, indicated that no sensible change in the vertical velocity of the model happens between the time of

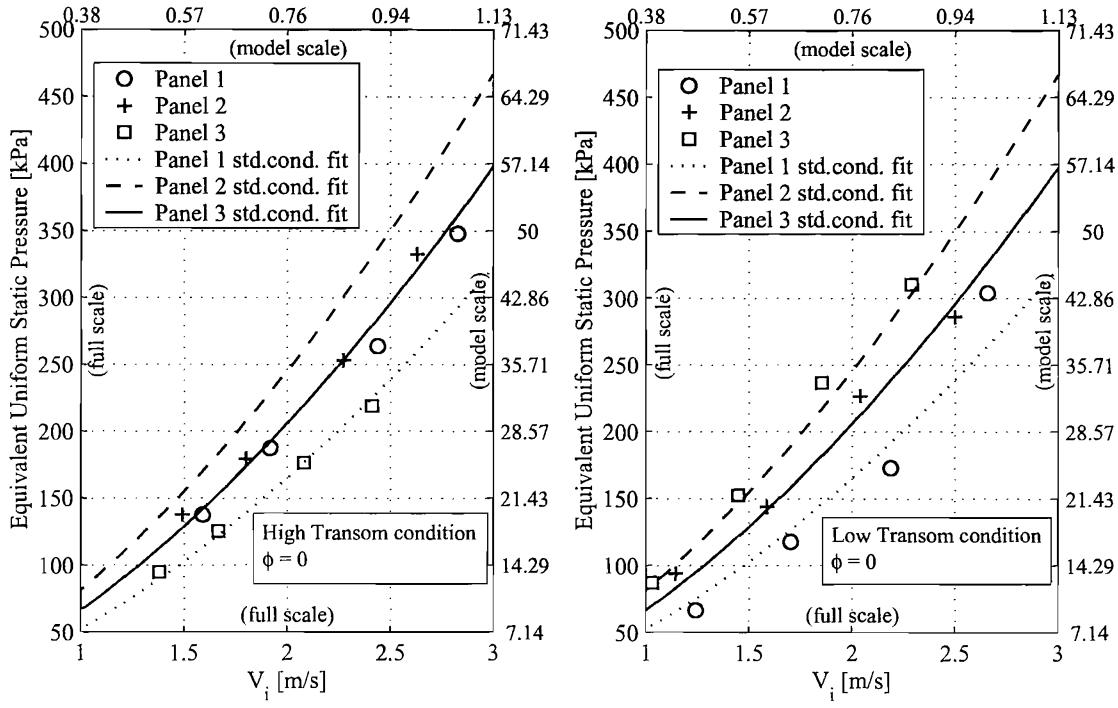

Figure 4.12: Effect of the change of longitudinal position of first contact with water. The reported lines are the trend lines fitting the standard condition data (intermediate transom height, point of first contact on panel 2): they are plotted here for the sake of comparison. In the "high transom" condition, relative to the standard condition, P1 loads increased by an average of 19.3%, P2 loads decreased by an average of 13.2% and P3 loads decreased by an average of 19%. In the "low transom" condition, relative to the standard condition, P1 loads decreased by an average of 8.6%, P2 loads decreased by an average of 10.5% and P3 loads increased by an average of 28.5%.

impact and the instant when the maximum force is measured by the load cells. This finding was further investigated by performing tests with different mass moments of inertia (the equivalent of changing displacement for standard translational drop tests) and constant impact velocity. The corresponding measured EUSP have been plotted in figure 4.14 together with uncertainty intervals bound by $\pm 1.96\sigma$ (where σ indicates the standard deviation of all the measurements performed on the same panel in the standard condition and with the same drop height; assuming the measurements to be affected by a random error that follows a normal distribution, the true value of EUSP has a 95% probability of being within 1.96σ of the measured values). Figure 4.14 shows that there is no consistent trend in the variation of the EUSP with increasing moments of inertia. Besides, the overlapping error bars indicate that the observed differences are within the range of experimental uncertainty. It may then be concluded that the different rigid body acceleration experienced upon impact by

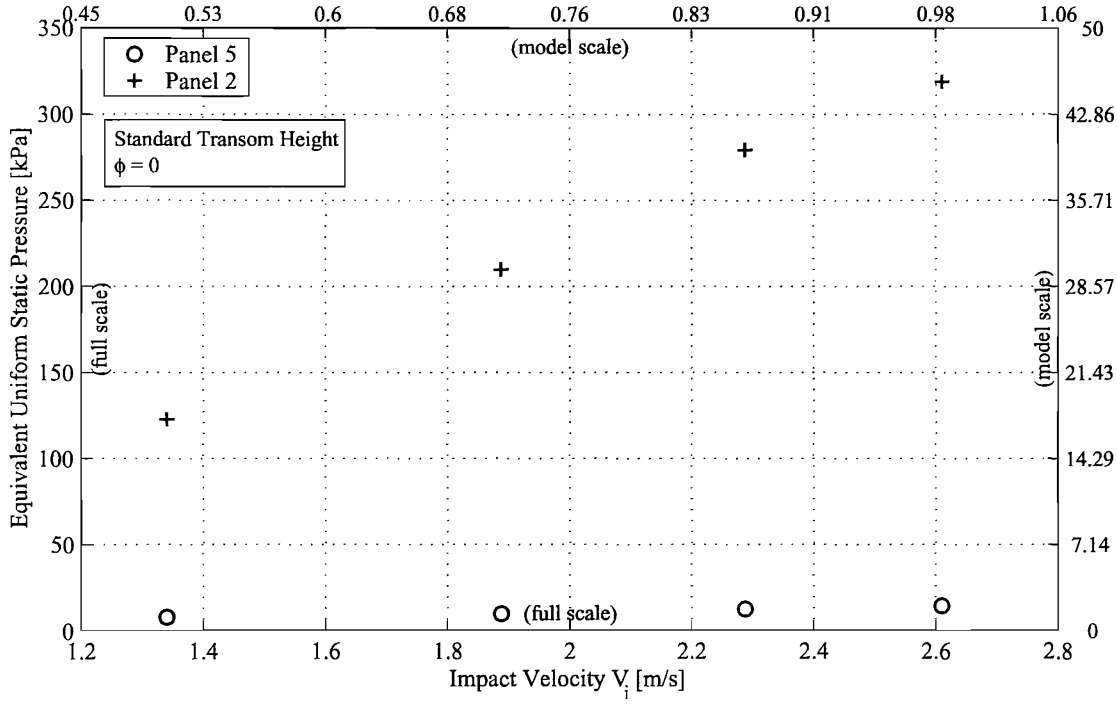

Figure 4.13: Variation of the impact pressure along the girth. Equivalent pressure measured for Panel 2 and Panel 5 during same drops. All pressures plotted with respect to Panel 2 impact velocities.

vessels with different inertia, happen on too large a time scale to sensibly affect the EUSP measured by the panels that contact the water first.

Results obtained with the model towed in waves are shown in figures 4.15 to 4.16. All tests were performed in regular waves in the towing tank of the Southampton Institute. The standard testing condition included the same displacement Δ_0 adopted for the drop tests and a boat speed of 8.8kts ($Fr = 0.35$ is considered to be representative of an Open60' sailing upwind in rough seas). Due to the size limits of the towing tank, tests were only performed in bow waves ($\mu = 180deg$). In order to maximise the occurrence of slamming, the wavelength was adjusted to produce the encounter frequency corresponding to the maximum value of the pitch RAO [39]. A wave height variation of 0.075m to 0.18m at model scale (i.e. $0.525 \div 1.26m$ at full-scale) was initially planned. It was later found that heights lower than 0.09m would not produce any slamming while waves higher than 0.16m would cause the bow of the model to hit the underside of the towing carriage. Between four and eight slamming events could be recorded at each run. In spite of all efforts made to guarantee good repeatability, impact velocities, and consequently impact loads, were

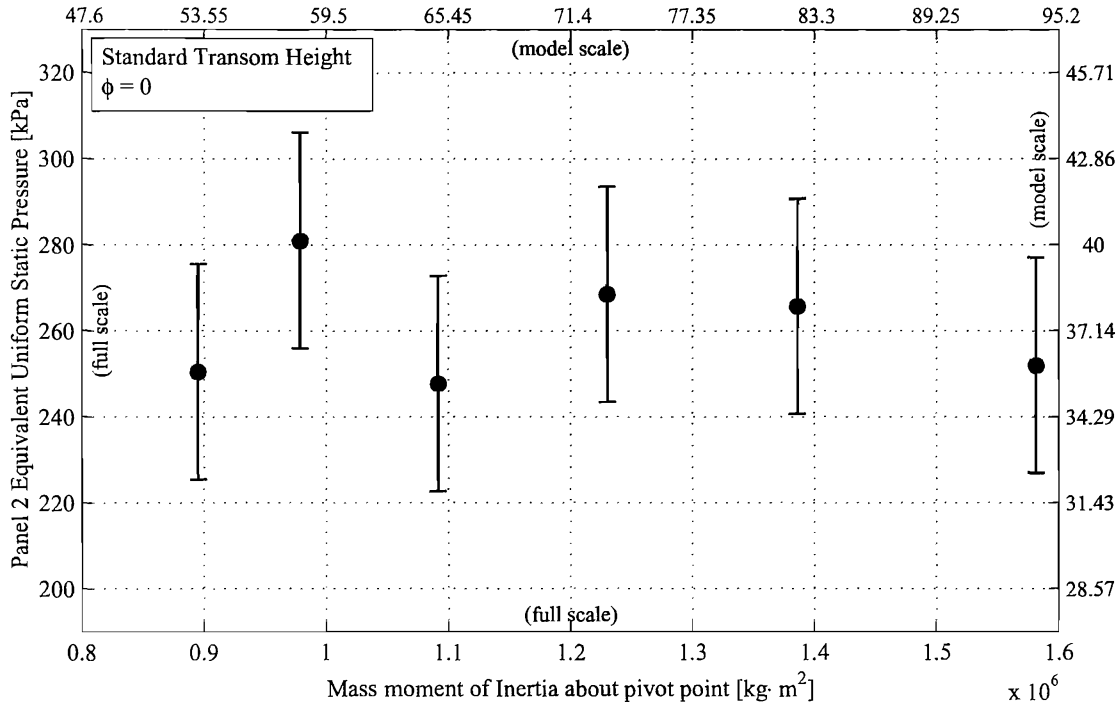

Figure 4.14: Effect of the variation of the mass moment of inertia on maximum equivalent uniform static pressures measured at Panel 2. Error bars are bound by the $measuredvalue \pm 1.96\sigma$ (σ: standard deviation of all measurements performed in the standard condition with $40mm$ drop height).

still affected by noticeable scatter. Typically a normalised rms scatter of 5% could be observed for impact velocities and of up to 35% for impact pressures, within the same run. Nevertheless, some clear trends could be identified in the acquired data.

Figure 4.15 shows the pressure-velocity relation obtained for panels 1 to 3 from tests in the upright condition with standard boat speed and increasing wave height. The mean values and standard deviations of impact speed and impact pressure were calculated for all slams in each run. This resulted in the data points and the error bars represented in figure 4.15. It will be noticed that, for the same impact velocities, the EUSPs generated by impacts in waves were almost always lower than those observed in the drop tests. Several factors were responsible for this reduction: first of all, the average trim angle of the panels at the time of impact ranged from -2 to +6 degrees: results from the drop tests series proved that smaller variations of the trim angle were sufficient to substantially decrease the maximum pressures. Also, footage obtained from both the underwater and above-water camera, confirmed that a considerable amount of water remained attached to the bottom of the hull in the phase between

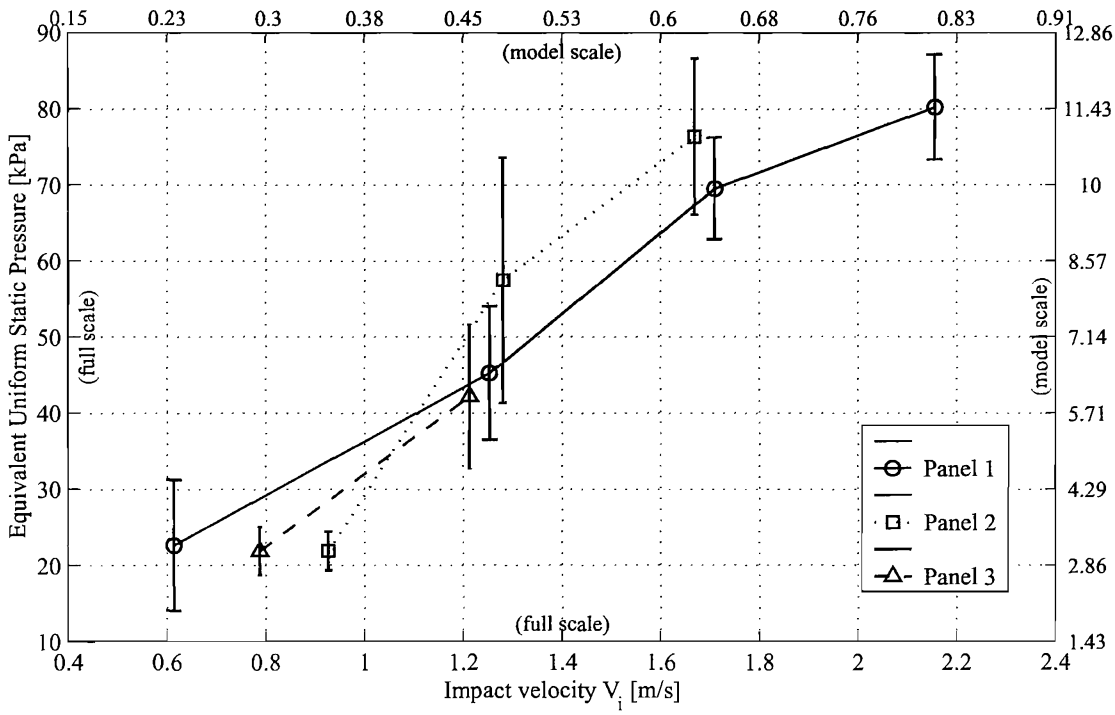

Figure 4.15: Regular waves tests with forward speed: mean EUSPs plotted as a function of the mean impact velocities. Data points obtained by calculating the average of the impact pressures recorded over each run. Error bars are bound by the mean values plus/minus the standard deviation of the EUSPs recorded over each run

emersion and re-entry, and that the associated dripping altered the state of the free surface prior to each slam. The effects of these irregularities were not covered by drop test investigations, however results published in [23] and [25] for cylinders with circular section indicate that, specially at small trim angles, they may reduce the maximum amplitude of response by up to 20%. More importantly, figure 4.16 illustrates that, while average pressures are generally lower for the tests in waves, occasionally some slams could produce loads equal or even marginally higher than those measured in the drop tests. It seems then reasonable to conclude that the results obtained from drop tests in calm water provide a good indication of the highest possible EUSP that can be experienced by the hull panels in a seaway.

Finally, the effects of displacement variation were analysed as shown in figure 4.17. In particular, tests were performed with three different displacements, by adding weights at the LCG of the model (thus leaving the moment of inertia virtually unchanged), equivalent to the mass of the water ballast taken onboard by some Open60s'. The wave encounter frequency was always kept the same as in the standard

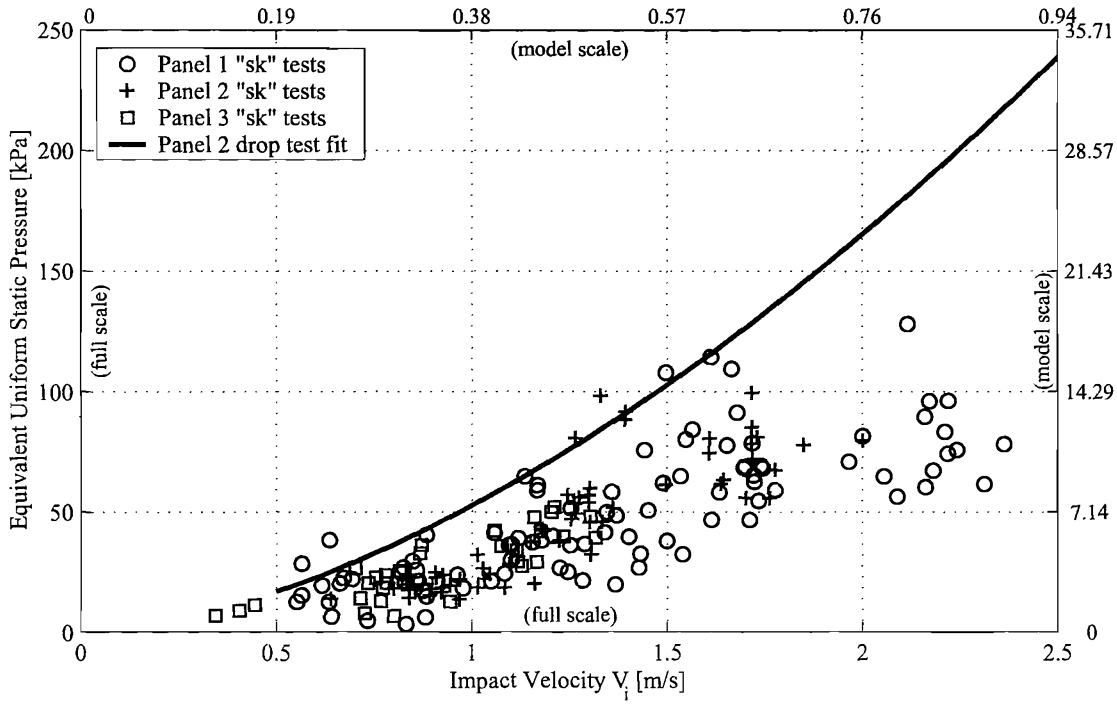

Figure 4.16: Comparison of EUSPs obtained from tests in waves and from rotational drop tests (Panel 2 fitting line is reported for reference).

test conditions. Hence, the relative amplitude and phase of the motion would be expected to change for different displacements. The common perception that increased displacement makes a boat more sea kindly, was confirmed by the measurements: indeed, in the higher ballast configurations, slamming was not observed on panel 2 and 3 for wave heights lower than 1 metre. A comparison of the loads on panel 1 showed that these remained approximately constant in the intermediate ballast condition and eventually decreased at the highest displacement. This latter phenomenon was most probably produced by the boat slamming "earlier" on the back of the wave and, consequently, with higher trim angles.

Although an investigation of the effects of forward speed variation was planned, due to a failure of the data acquisition system, a representative quantity of data could not be obtained.

Rotational drop tests with forward speed in the upright and heeled condition, reproduced closely the results observed for the zero speed homologues, to the only exception of the pressures measured on panel 4. This showed a marginal increase of the loads at the highest speeds. It was then concluded that slamming loads were only dependent on the component of flow velocity perpendicular to the panel surface,

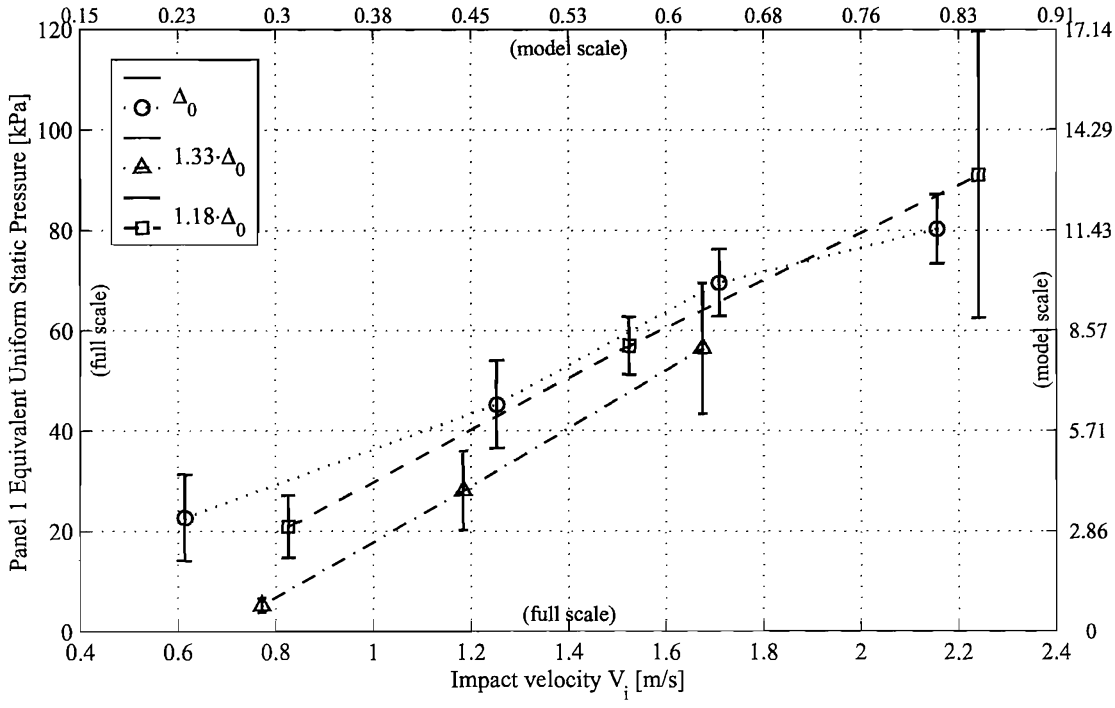

Figure 4.17: Regular waves tests: effect of displacement variation on Panel 1 pressures.

and that the increase shown by panel 4 was due to its normal vector being oriented slightly towards the bow.

4.7 Summary

An investigation of the parameters affecting slamming pressures and the resulting structural response has been performed by instrumenting a $1/7^{th}$ scale model with slam patches.

This technique has been proved to be extremely useful for analysing the physical phenomena involved with water impact on flexible structures. The practical details have been illustrated in detail and the good repeatability of the results has confirmed the validity of the experimental set-up.

The different aspects of the dynamic response of a slam patch have been discussed in sections 4.3 and 4.4. In particular, it has been shown that the loads measured by the present procedure can be regarded as equivalent uniform static pressures. The issues related to the scaling of the loads and of the structural response have been dealt with in section 4.5: it has been shown that all the fluid-dynamic forces acting

during water impact cannot be scaled in a consistent manner and that, as a result, the relative influence of the cushioning effect by entrapped air is not as large at model scale as it is at full scale.

The experimental results presented in section 4.6 have confirmed that the relation between EUSPs and impact velocities is quadratic for the lower impact velocities, and tends to become linear at the higher velocities. For hull panels of small to moderate dimensions, the influence of displacement and rotary inertia on the maximum measured loads has been shown to be negligible from both drop tests and standard seakeeping tests. Pressures measured during seakeeping tests have been shown to be almost always lower than those observed in rotational drop tests at equal impact velocities. This difference can be justified by the larger trim angles at impact, and by the irregularities of the water and hull surfaces typically observed during the seakeeping tests.

Chapter 5

Analytical method for the calculation of slamming loads and structural response

5.1 Overview

Following the work presented in the previous two chapters, the need became clear for an analytical model that could be used to further investigate the influence of different mechanical and geometric parameters on the response of hull panels to slamming loads, and, possibly, to assess the relative performance of different structural solutions with respect to slamming. Eventually, the model could become the basis for a new design tool for the elements of structures exposed to slamming. Hence, there was a requirement for it to be simple enough to be implemented on common personal computers, and to be based on reliable existing theories. This chapter discusses how this model was implemented, validated and, ultimately, used to investigate trends of slamming loads with different impact conditions and structural properties.

5.2 The water entry problem

Following the classic approach by Wagner [133], the two-dimensional flow generated by a body entering the water can be modelled by replacing the actual body with a moving flat plate. The width of the plate is assumed to increase with time in the same way as the wetted beam of the body increases (cf. figure 5.1).

Assuming the flow is irrotational and the fluid incompressible, the velocity potential on the body can be written as:

$$\phi = -U(t)\sqrt{c(t)^2 - \tilde{y}^2} \tag{5.1}$$

By neglecting the hydrostatic and the kinetic terms of Bernoulli's equation (cf. [41] for a justification), one can then write:

$$\begin{aligned} p(\tilde{y},t) &= \rho\frac{\partial\phi}{\partial t} = \rho\frac{\partial\phi}{\partial c}\frac{\partial c}{\partial t} = \\ &= \rho U(t)\frac{c(t)}{\sqrt{c(t)^2 - \tilde{y}^2}}\frac{\partial c}{\partial t} + \rho\sqrt{c(t)^2 - \tilde{y}^2}\frac{\partial U}{\partial t} \end{aligned} \tag{5.2}$$

and

$$L(t) = \int_{-c}^{c} p(\tilde{y},t)d\tilde{y} = \pi\rho U(t)c(t)\frac{\partial c}{\partial t} + \rho\frac{\partial U}{\partial t}\frac{\pi}{2}c(t)^2 \tag{5.3}$$

In order to apply equations 5.2 and 5.3, the wetted half beam "c" must be determined as a function of time from the geometry of the body.

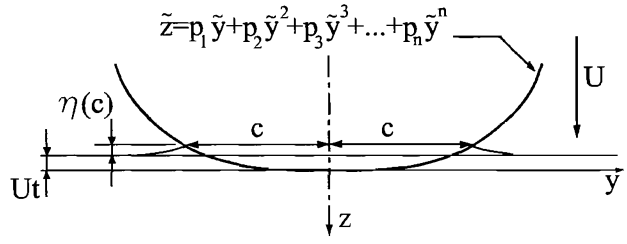

Figure 5.1: Water entry model.

For the present study, hull sections are assumed to be symmetric about the centre line and each half is approximated by a polynomial of the form: $\tilde{z} = p_1\tilde{y} + p_2\tilde{y}^2 + p_3\tilde{y}^3 + p_4\tilde{y}^4 + \ldots + p_n\tilde{y}^n$ where $\tilde{y}$ and $\tilde{z}$ are coordinates relative to a frame of reference centred at intersection between the section curve and the longitudinal plane of symmetry. It may be shown that, depending on the degree "n" of the polynomial, actual hull sections can thus be described to any required degree of accuracy. In practice, fourth degree polynomials are be sufficient to model the bottom of common sailing yacht sections with an accuracy better than the typical manufacturing tolerance (cf. figures 5.2 and 5.3).

If the instantaneous free surface elevation is defined as η, one may write:

$$\int U(t)dt + \eta(c(t)) = p_1c(t) + p_2c(t)^2 + p_3c(t)^3 + p4c(t)^4 + \ldots + p_nc(t)^n \tag{5.4}$$

It is assumed that, at each instant t, c(t) verifies:

$$\int U(t)dt = \gamma_1 c(t) + \gamma_2 c(t)^2 + \gamma_3 c(t)^3 + \ldots + \gamma_n c(t)^n \tag{5.5}$$

The vertical velocity of the fluid on the edge of the expanding plate can be written as [23]:

$$U(t)\left(\frac{y}{\sqrt{y^2 - c^2}} - 1\right) \tag{5.6}$$

It then follows that:

$$\begin{aligned}
\frac{\partial \eta}{\partial c} &= U(t)\frac{\partial t}{\partial c}\left(\frac{\tilde{y}}{\sqrt{\tilde{y}^2 - c^2}} - 1\right) \\
&= \left(\gamma_1 + 2\gamma_2 c(t) + 3\gamma_3 c(t)^2 + \ldots + n\gamma_n c(t)^{(n-1)}\right)\left(\frac{\tilde{y}}{\sqrt{\tilde{y}^2 - c^2}} - 1\right)
\end{aligned} \tag{5.7}$$

and

$$\begin{aligned}
\eta(\bar{c}) &= \int_0^{\bar{c}} \left(\gamma_1 + 2\gamma_2 c + 3\gamma_3 c^2 + \ldots + n\gamma_n c^{(n-1)}\right)\left(\frac{\bar{c}}{\sqrt{\bar{c}^2 - c^2}} - 1\right) dc \\
&= -\left(\gamma_1 + \gamma_2 \bar{c}^2 + \gamma_3 \bar{c}^3 + \ldots + \gamma_n \bar{c}^n\right) + \\
&\quad + \left(\gamma_1 \bar{c}\frac{\pi}{2} + 2\gamma_2 \bar{c}^2 + 3\gamma_3 \frac{\pi}{4}\bar{c}^3 + 4\gamma_4 \frac{2}{3}\bar{c}^4 + \ldots + n\gamma_n I_n\right)
\end{aligned} \tag{5.8}$$

with:

$$I_0 = \frac{\pi}{2}, \quad I_1 = a, \quad I_n = \frac{n-1}{n}\bar{c}^2 I_{n-2} \tag{5.9}$$

From equations 5.4, 5.5and 5.8 it follows that:

$$\begin{aligned}
\gamma_1 &= \frac{2}{\pi}p_1 \\
\gamma_2 &= \frac{1}{2}p_2 \\
\gamma_3 &= \frac{4}{3\pi}p_3 \\
&\ldots \\
\gamma_n &= \frac{n-1}{n} \cdot \frac{\gamma_{n-2} p_n}{p_{n-2}}
\end{aligned} \tag{5.10}$$

Hence, with the impact velocity $U(t)$ and the values of γ_n known, the wetted beam at any given time t can be obtained numerically as the smallest positive solution of equation 5.5.

By this notation, equations 5.2 and 5.3 can finally be rewritten as:

$$p(\tilde{y}, t) = \frac{\rho U(t)^2 c(t)}{\sqrt{c(t)^2 - \tilde{y}^2}\left(\frac{2}{\pi}p_1 + p_2 c(t) + \frac{4}{\pi}p_3 c(t)^2 + \ldots + n\gamma_n c(t)^{n-1}\right)} + \rho\frac{\partial U}{\partial t}\sqrt{c(t)^2 - \tilde{y}^2} \tag{5.11}$$

and

$$L(t) = \frac{\pi\rho U(t)^2 c(t)}{\frac{2}{\pi}p_1/c(t) + p_2 + \frac{4}{\pi}p_3 c(t) + \ldots + n\gamma_n c^{n-1}} + \rho\frac{\partial U}{\partial t}\frac{\pi}{2}c(t)^2 \qquad (5.12)$$

Wellicome has observed that the use of this type of model to predict actual pressure distributions is probably less justified than its use to predict the position of the spray root and the total integrated force. As a matter of fact, it can be readily observed that the theory outlined above predicts infinite pressures at the spray root (i.e. for $\tilde{y} = c(t)$). Experimental data from Campbell et al. have shown that, for circular sections, Wagner-type approaches actually predict the position and magnitude of the peak pressure with rather good accuracy, particularly after the very first stage of impact [24]. Also, Faltinsen has noted that, when one accounts for the compressibility of water, pressures cannot be higher than the acoustic pressure $p_{ac} = \rho c_e U$ (where c_e indicates the speed of sound in water). Data presented by Hagiwara et al. suggest that very good agreement can be obtained between theoretical and experimental load data by effectively clipping theoretical pressures to the acoustic value [52].

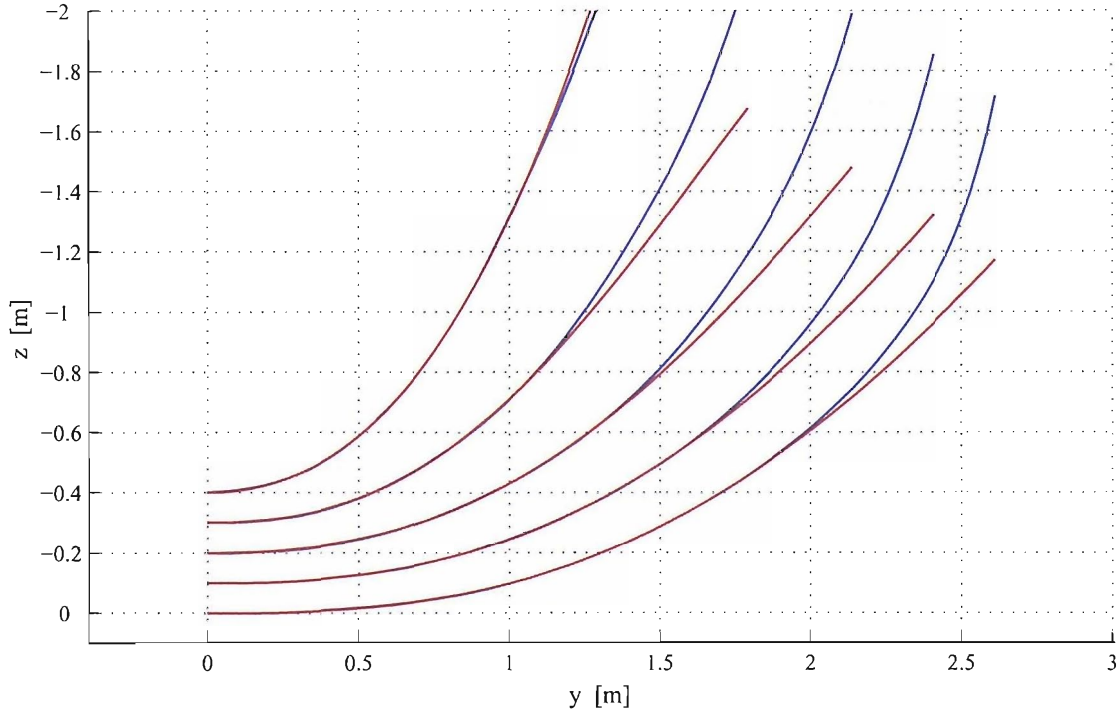

Figure 5.2: Hull sections approximation. Sections have been spread artificially along the "z" coordinate to improve the readability of the graph.

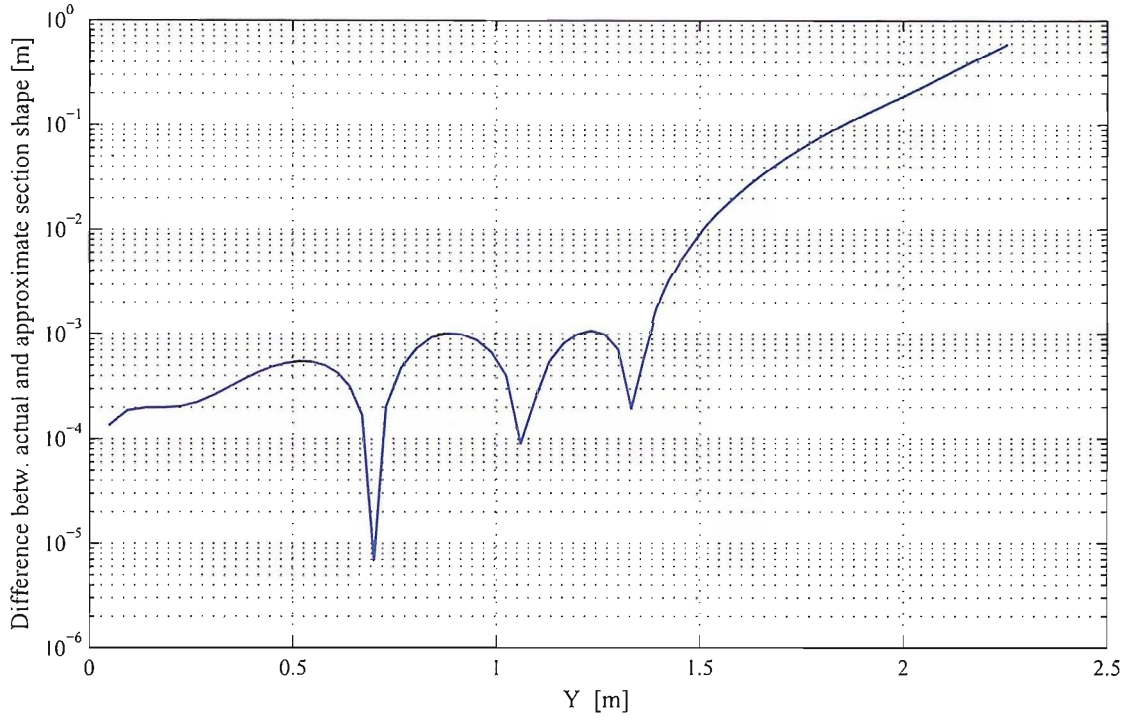

Figure 5.3: Typical difference between actual and approximated hull section z coordinate obtained by using a fourth order polynomial for the approximated section.

5.3 Calculation of the hydroelastic response

The method for the calculation of the hydroelastic response of a hull panel subject to slamming is described in figure 5.4. This consists of a standard time-stepping approach [30] where the hydrodynamic load is calculated at each step on the basis of the fixed external conditions (i.e. the rigid-body velocity) and of the panel response.

To begin with, the panel structural characteristics and boundary conditions are considered to determine the natural modes of deformation. The problem can then be treated in terms of modal coordinates.

The initial velocity of the panel relative to the free surface is derived from the relative rigid-body motion of the hull. It has been observed that it is acceptable to consider this component of velocity as constant [42] through the impact , since the change in the rigid-body velocity of the vessel is negligible over the period between first contact with water and maximum structural response of a panel.

The panel is divided longitudinally in strips and the section at the centre of each strip is approximated by a polynomial, as outlined in the previous section. The initial time for the calculation corresponds with the instant when the panel touches

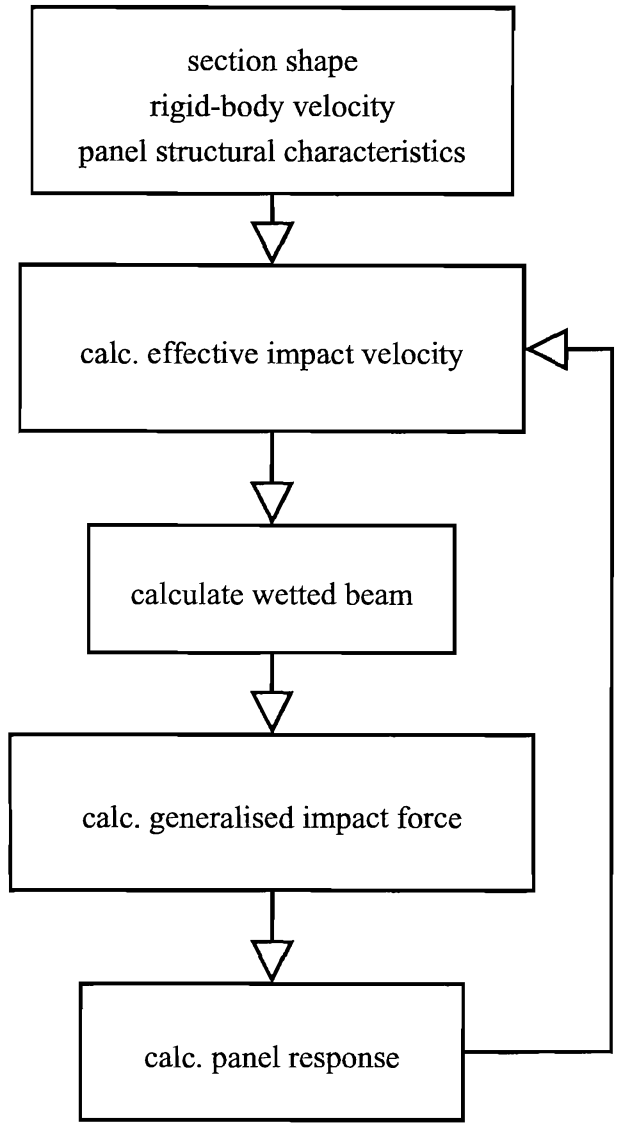

Figure 5.4: Description of the approach to the calculation of the hydroelastic response of a panel subject to slamming load.

the water. The wetted beam is calculated at the end of the first time step for each strip and the generalised load on the panel results from the integration of the pressures on each strip. The response at the end of each step is then calculated and the average velocity across each strip due to the panel deflection is added to the rigid-body component in order to determine the wetted length and pressure distribution at the following step.

Pressures higher than the acoustic pressure are clipped to the value of the acoustic pressure. The hydrodynamic added mass of the panel is accounted for in the forcing term, as can be noted from equations 5.2 and 5.3.

With a constant or decaying impact velocity, the maximum amplitude of deflection is attained during the first cycle of oscillation of the panel, hence the iteration is normally stopped after the first response peak is observed.

5.4 Validation against existing theories and experimental data

The theory outlined in the previous sections has been validated against existing theories by Wellicome et al. [23] and by Mei et al. [96] and against experimental data published by Campbell et al. [24] and produced within the present study (cf. section 4.6).

As the result of a very thorough investigation of wave slamming loads on circular section cylinders, Campbell et al. have published an extensive amount of data on pressure distributions, total impact forces and free surface elevation, for different impact configurations [21, 23–25]. Within the same study, Wellicome outlined a theoretical method for predicting impact forces on circular sections.

Mei et al. have presented a method for the solution of the water impact problem for generic two-dimensional bodies. While adopting the same potential flow formulation as Wagner, they used conformal mapping to solve the boundary-value problem at every instant, and were able to obtain closed-form solutions for wedges and circular sections. Theoretical predictions by this method appear to be in extremely good agreement with experimental data by Armand et al. [6] and by Zhao et al. [142], both for circular and generic sections [96].

Figure 5.5 shows a comparison of predicted and measured half wetted beam for a circular cylinder. Both the present theory and the one by Mei et al. appear in very good agreement with the measurements by Campbell et al.

Predictions of the total impact force for circular cylinders are also compared with experimental data in figure 5.6. Both the present theory and the ones by Wellicome and by Mei, appear to over predict this force, with the first two being the most conservative. The observed differences may be attributed for the largest part to the fact that the theoretical methods neglect the effects of air cushioning (if present). Also, experimental data tend to be attenuated as the conditions of perfectly two-dimensional flow and constant impact velocity are never exactly met.

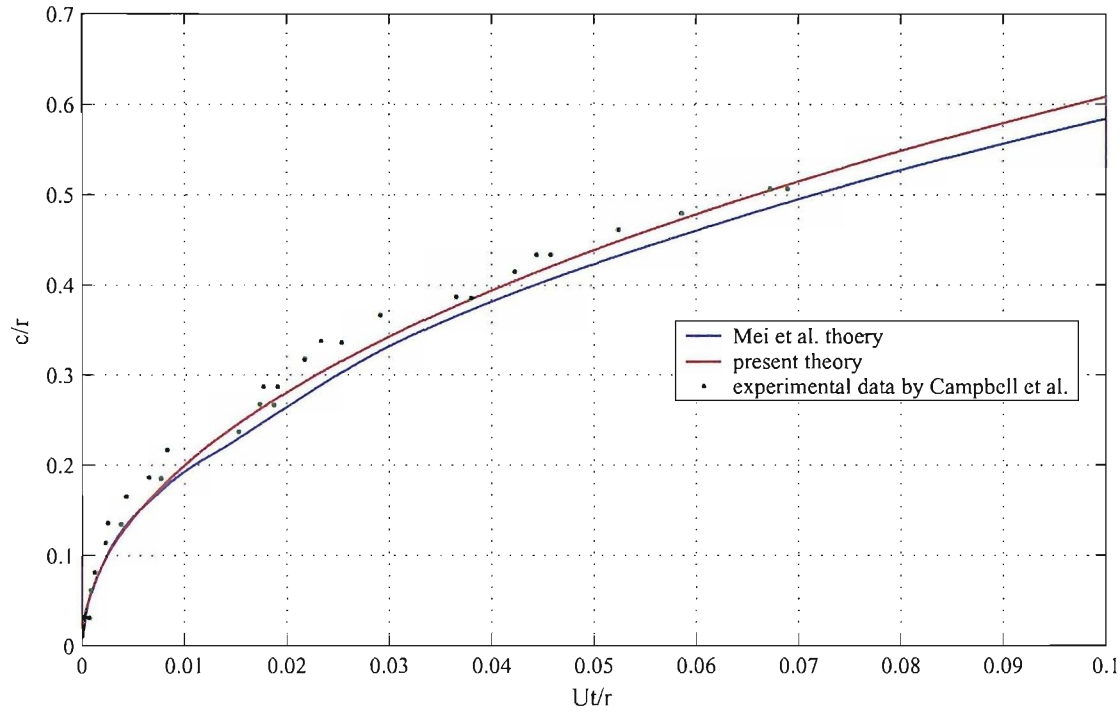

Figure 5.5: Comparison of theoretical and experimental data for half wetted beam of circular section cylinder.

The differences between the predictions of the present theory and the ones of Mei are due to the different approach to the calculation of the added mass of the impacting cylinder. Mei's theory refers to the added mass of a circular arc cylinder, hence it remains accurate as immersion increases. On the other hand, the expanding flat plate approximation adopted in the present theory becomes less justified as the slope of the body section at the intersection with the free surface increases with immersion.

More in general, it is observed that the smaller the deadrise of the impacting body, the more the present theory will be accurate. It is then considered appropriate to apply this theory to the calculation of slamming loads in the very first stages of impact, particularly for typical yacht hull sections which are relatively flat in their bottom.

The accuracy of the present theory for the case of a deformable body with variable impact velocity is illustrated by figure 5.7. Here, the theoretical prediction for the force measured by a slam patch can be seen to be in excellent agreement with the experimental data. For the lower impact velocities, the response of the slam patch is almost quasi-static and its amplitude does not result in significant attenuation of the hydrodynamic force. The relation between the panel response and the force is

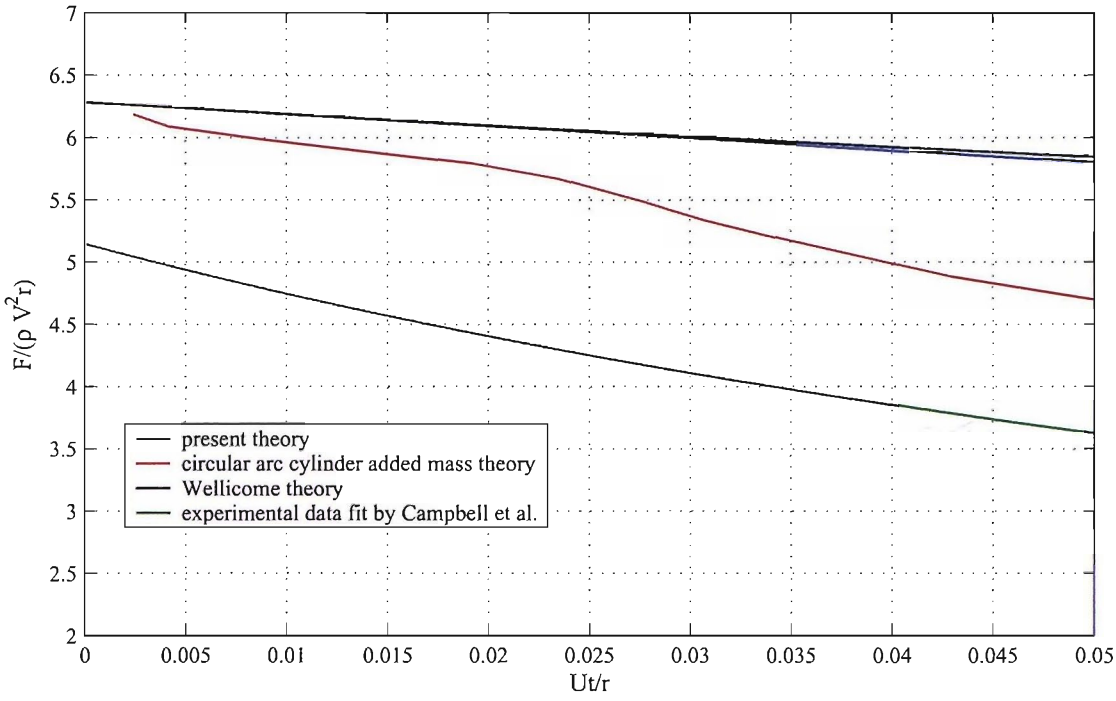

Figure 5.6: Comparison of theoretical and experimental data for vertical force on circular section cylinder.

then almost linear and the hydrodynamic force remains proportional to the impact velocity squared.

Conversely, at the higher impact velocities, the slam patch presents the typical shock load response: the duration of the pressure impulse is much shorter than the natural period of the patch and the pressure pulse has left the surface of the panel before the response of the latter can affect it. The amplitude of the response then becomes proportional to the magnitude of the mechanical impulse (i.e. to the integral of the force over time). The latter varies linearly with impact velocity as the amplitude is proportional to V_i^2 (cf. figure 5.8) and the duration to $1/V_i$. Hence, for the more severe impacts, the maximum force measured by the slam patch appears to be linearly proportional to the impact velocity.

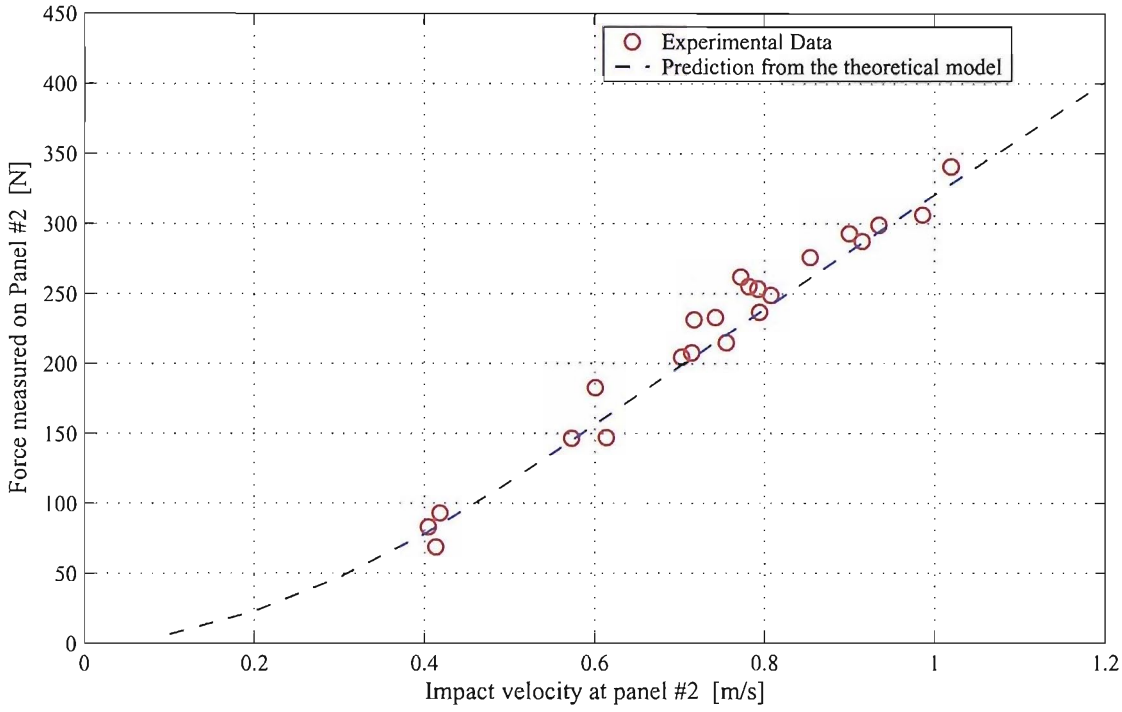

Figure 5.7: Comparison of predicted EUSP with experimental data for slam patch #2.

5.5 Considerations on the design load for hull panels

The theory illustrated in the previous sections has been applied to examine the influence of different parameters on hull panel design loads. The present discussion retains the same idealised model of water impact as previously described, that is, phenomena like air cushioning, cavitation and water aeration have not been taken into account. While, from a quantitative point of view, this most certainly leads to overestimating the hydrodynamic loads, qualitative considerations are expected to remain valid.

The main factors that determine the severity of slamming load are the relative velocity at impact V_i, the geometry (i.e. curvature, deadrise, etc.) and the attitude (i.e. trim, heel) of the hull relative to the free surface.

It is often suggested that the mass of the vessel also plays an important part. This idea usually stems from the perception that lighter craft experience higher rigid-body acceleration upon impact, leading to faster decay of the relative impact velocity and, hence, of the hydrodynamic impact loads (and vice versa) [137]. However, it can be argued that the highest local loads occur at the very first stage of impact and that

their duration is generally in the order of a few milliseconds. Within this time scale, the variation of the rigid-body velocity is negligible, whichever the displacement of a vessel.

On the other hand, velocity components associated with local structural deformation can contribute to the attenuation of hydrodynamic pressures, as discussed in section 4.3. Hence, consideration should be given to the mass of the structural parts directly exposed to slamming loads rather than to the overall displacement of the vessel.

The influence of relative impact velocity on the total hydrodynamic force on a rectangular hull panel is illustrated in figure 5.8. The panel dimensions and geometry correspond to those of a panel situated on the centreline at $1/4L_{WL}$ from the bow for and Open60' hull. Dimensions are $900mm$ by $300mm$ with the longest side aligned with the boat longitudinal axis. The shape of the hull section corresponding with the centre of the panel is shown in figure 5.12 and has been approximated by the equation $z = 0.0408y^4 - 0.1607y^3 - 0.0870y^2$. Results presented in figure 5.8 have been obtained while assuming the panel is infinitely rigid and the impact velocity constant.

Figure 5.8 clearly shows the impulsive nature of the impact force: upon contact with water, the load rises almost instantaneously to its maximum. A first phase of slow decrease is then present until the spray-root reaches the edge of the panel. The force than decreases sharply.

The influence of the panel transversal curvature is illustrated by figure 5.9. For this purpose, circular sections with different radii have been considered. It can be noted that the maximum force is inversely proportional to the radius of curvature. Also, in relative terms, the more the curvature of the panel, the longer the duration of the peak load and the gentler the following drop.

The influence of panel trim was studied for a slam patch and is illustrated by figure 5.10. The force on the inclined panels is calculated by dividing their surface into several transversal strips and by summing the load acting on each. The results are in good qualitative agreement with those presented by Campbell et al. [25] for inclined cylinders. It is interesting to observe that as little as 2 degrees of trim angle will reduce the maximum load by more than half compared to a perfectly "flat" impact. For trim angles above 4 degrees, the theoretical method is expected to overestimate the loads by an increasing margin as the hypothesis of two-dimensional flow

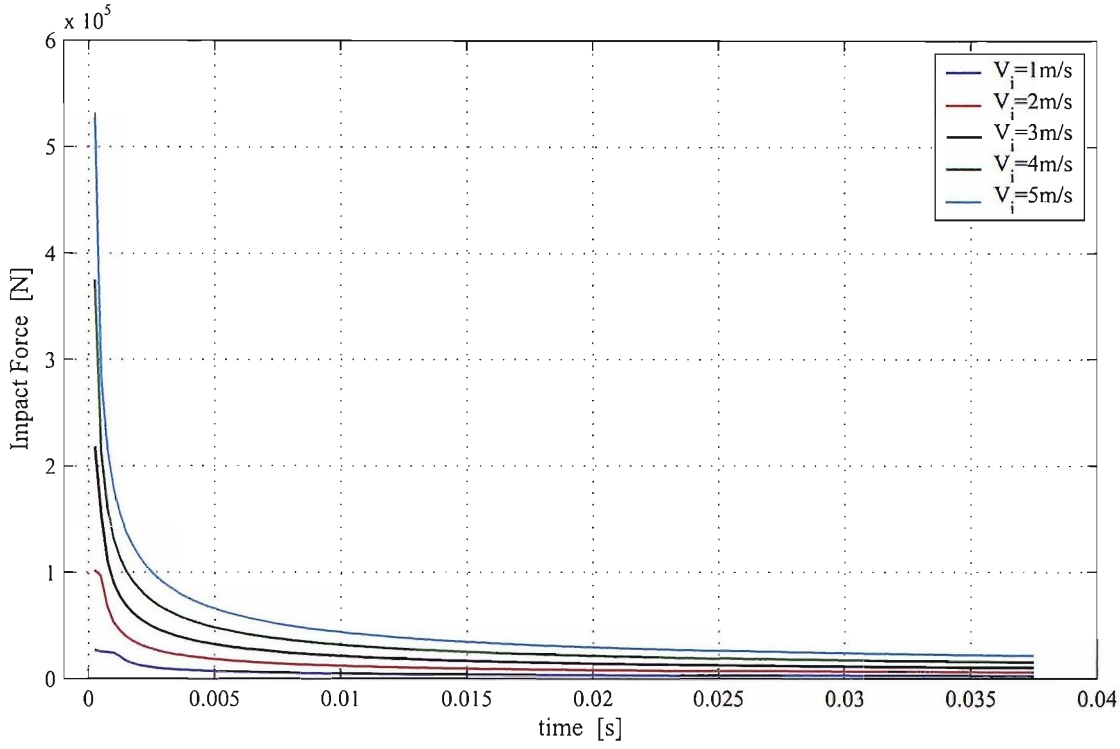

Figure 5.8: Hydrodynamic impact force on a $900 \times 300mm$ panel for different constant impact velocities assuming infinitely rigid structure. $t = 0$ corresponds to first contact with water.

gradually breaks down.

The influence of panel natural frequency on the value of equivalent uniform static pressures is illustrated in figure 5.11. The graph presents data derived for a slam patch which is considered as a single one-degree-of-freedom system. This allows the nature of the influence of dynamic characteristics to be more clearly identified. Different panel natural frequencies are simulated by varying the stiffness parameter while keeping the mass constant. As expected, EUSPs can be seen to increase with increasing natural frequency for a given impact velocity.

Figure 5.13 represents the relation between EUSP and panel impact velocity for different panel boundary conditions. EUSPs are calculated both on the basis of same maximum deflection and same maximum Von Mises stress (for the purpose of this part of the study, the panel is considered to be made of isotropic material, however the theory allows orthotropic materials to be also modelled). Figure 5.13 confirms that with increasing impact velocity, the relation between pressures and velocities tends to become linear. Values of EUSP obtained on the basis of same Von Mises stress are clearly higher than those for same deflections: this can be explained by the fact

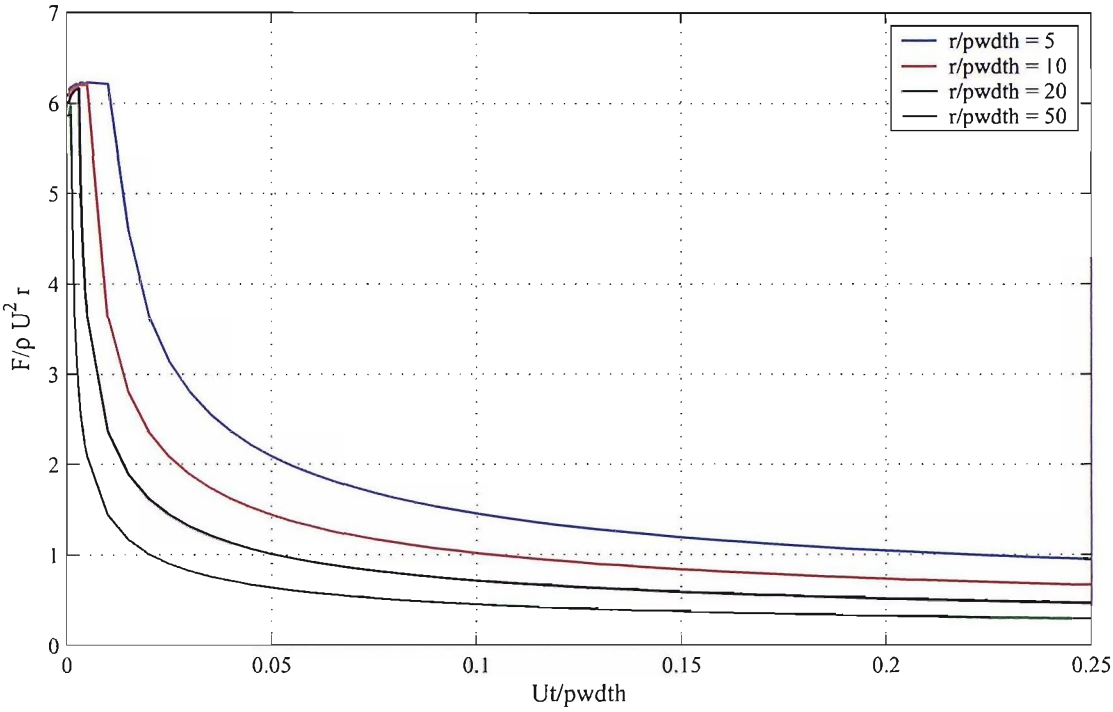

Figure 5.9: Relation between total force on a panel and panel curvature. Calculations performed for circular sections, assuming constant impact velocity.

that the actual non-uniform pressure load gives rise to very high local stresses near the panel edges which can only be matched by unrealistically high uniform pressures.

The relation between EUSP and panel width is illustrated in figure 5.14. this confirms the concept that larger panels should be designed for lower uniform pressures (cf. [2, 59]). However, in the present case, the reduction of EUSP is not just due to the effect of peak pressures averaging out over large area. The analytical model shows that, with the panel effectively becoming softer with increasing size, its relative dynamic response diminished for a given impulse load.

Finally figure 5.15 represents the effect of varying the panel material Young's modulus on the EUSP. It can be observed that particularly for low initial moduli, increasing the stiffness results in higher loads.

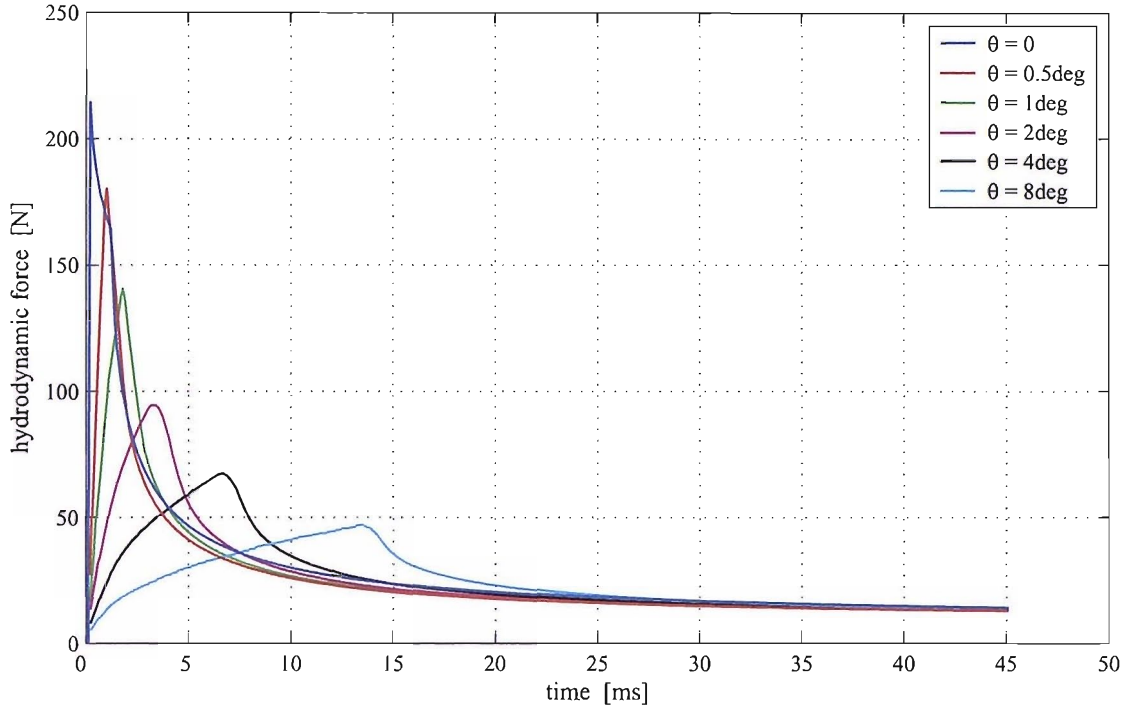

Figure 5.10: Hydrodynamic force on a slam patch for different patch trim angles, assuming constant impact velocity and infinitely rigid structure.

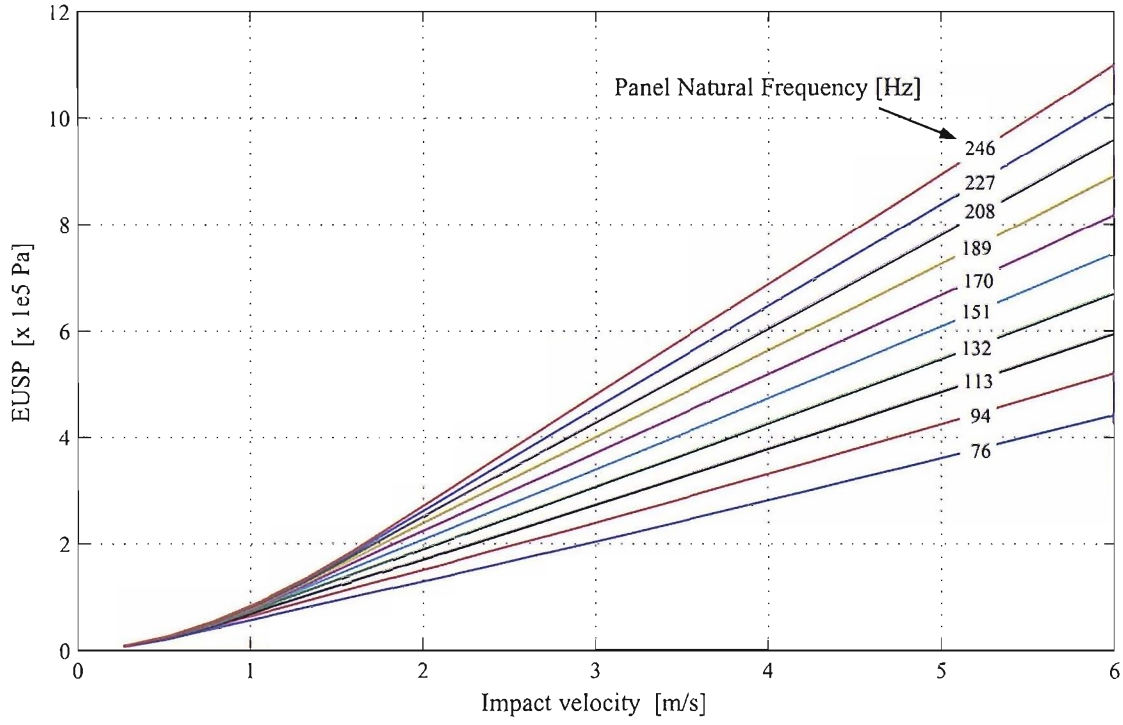

Figure 5.11: Influence of the slam patch natural frequency on the relation between measured EUSP and impact velocity.

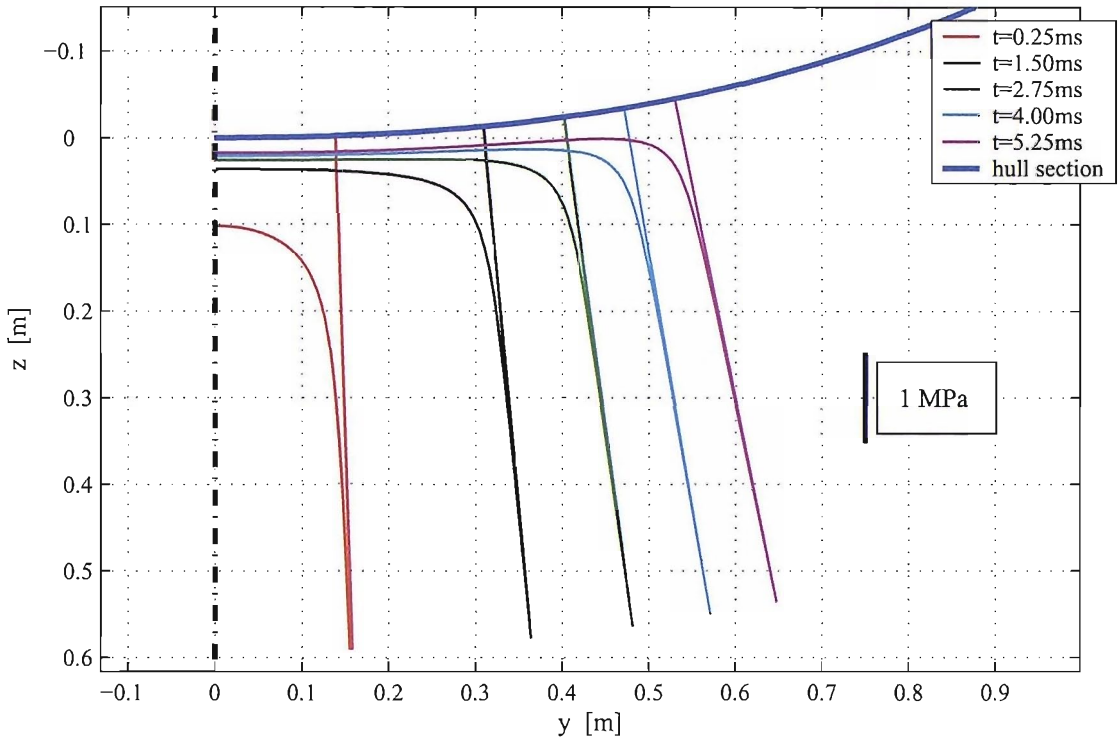

Figure 5.12: Evolution of the two-dimensional pressure distribution as predicted by the present theory (infinitely rigid structure, constant entry velocity $U = 4m/s$)

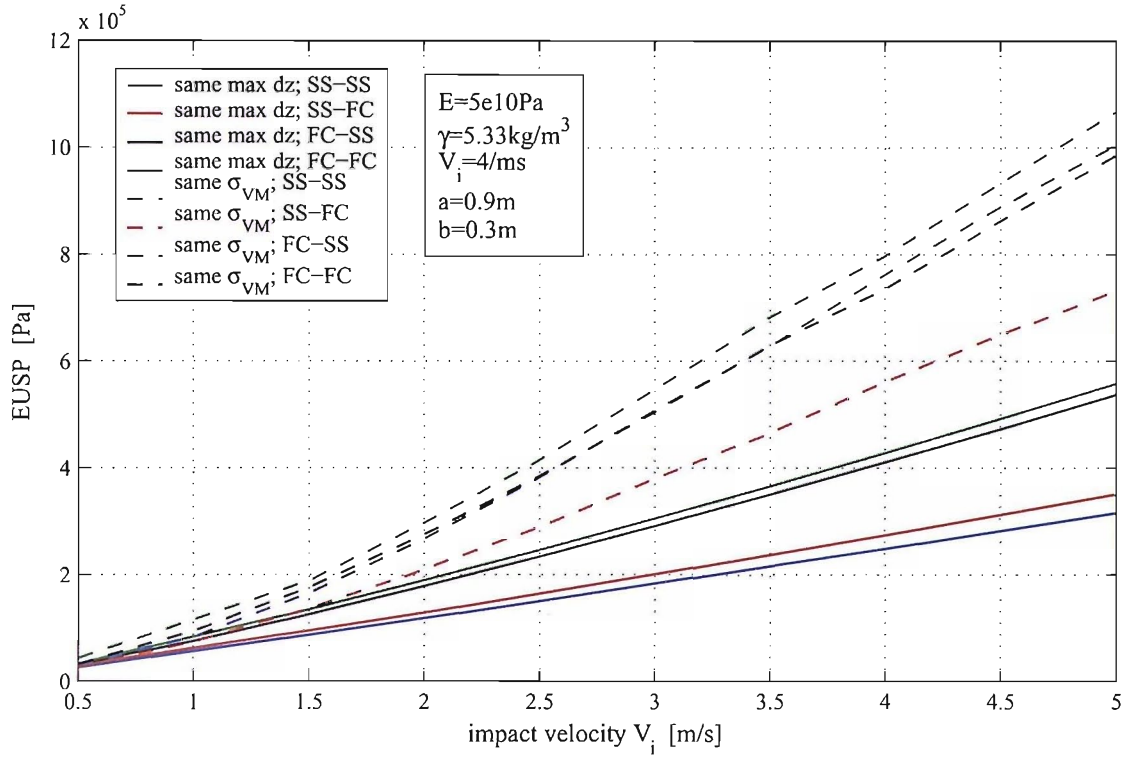

Figure 5.13: Relation between Equivalent Uniform Static Pressure and impact velocity (EUSP calculated both on the basis of same maximum deflection and same maximum Von Mises stress).

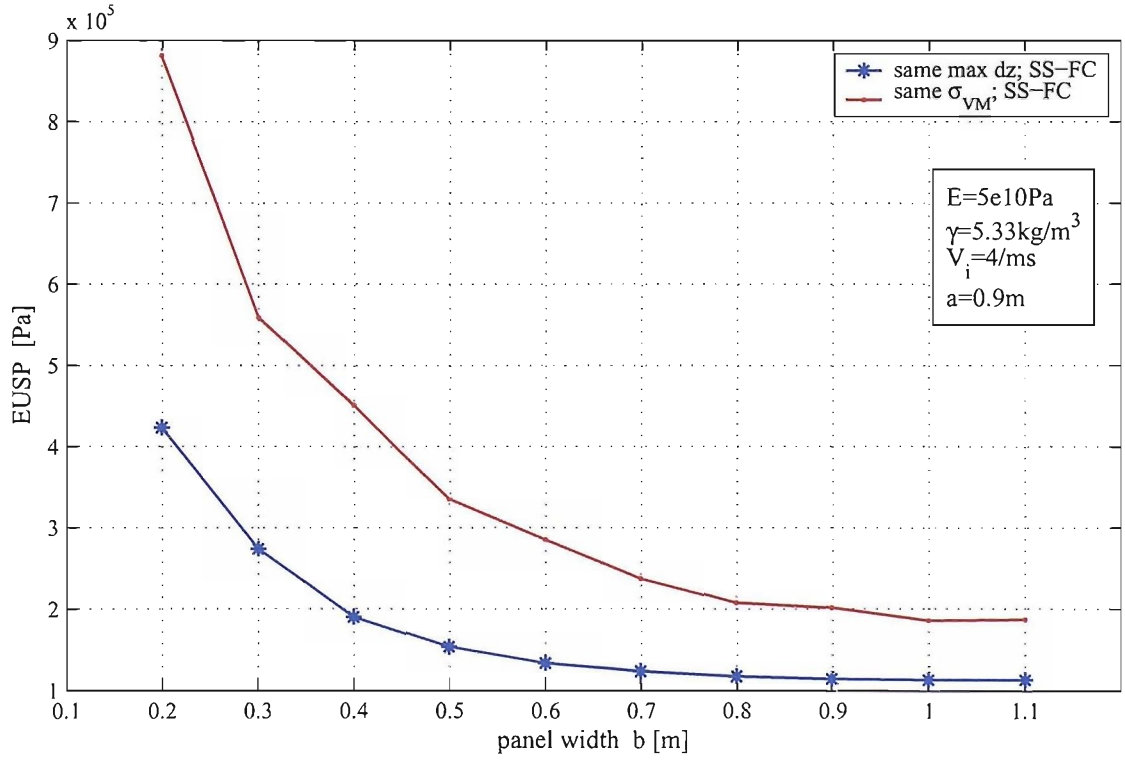

Figure 5.14: Relation between EUSP and panel width (panel length is kept constant).

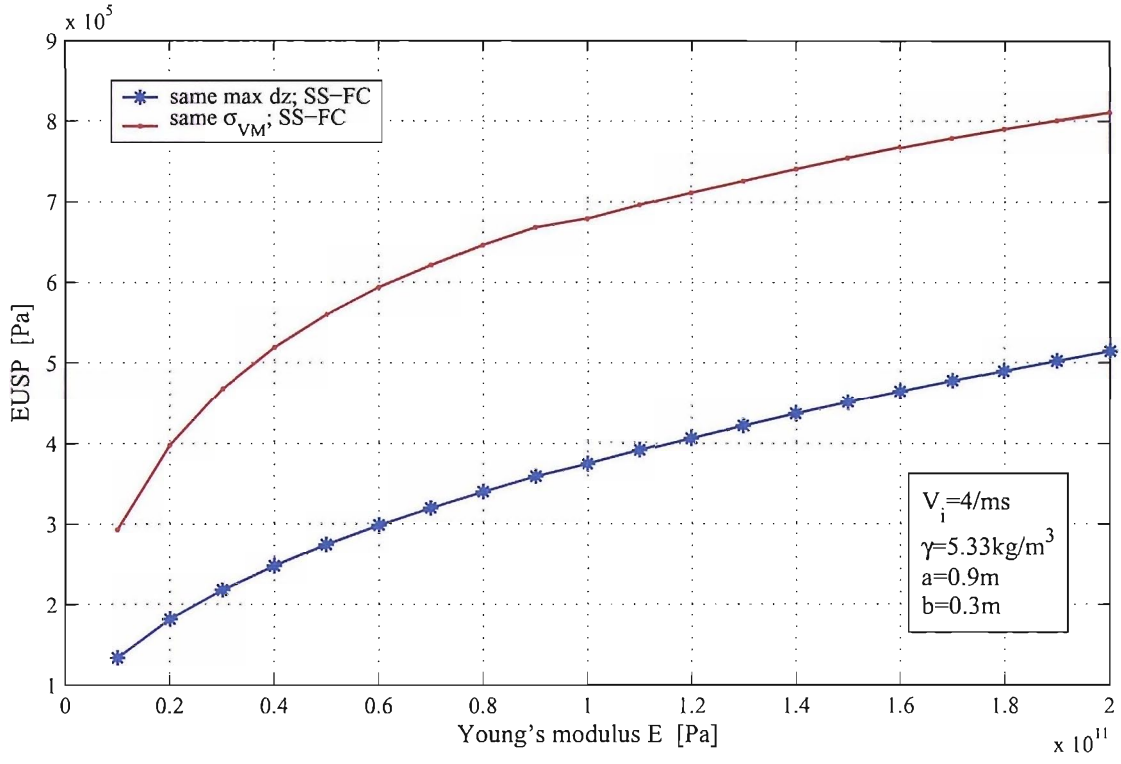

Figure 5.15: Relation between EUSP and panel material Young's modulus (panel weight and dimensions kept constant).

5.6 Summary

An analytical model has been developed to calculate the structural response of hull panels subject to water impact.

The hydrodynamic part of the water entry problem has been treated by a two-dimensional Wagner-type approach [133], similar to the one adopted by Wellicome for calculations on circular section cylinders [23]. A strip theory approach has been used to calculate the loads over entire hull panels, which is justifiable for the description of impacts with low trim angles, when the curvature of the hull is small. The structural response of the panel has been calculated by a time stepping procedure. Hydroelastic effects can modelled by this method as the hydrodynamic load is calculated at each time step on the basis of the actual relative velocity between the water and the impacting body.

The model has been successfully validated by comparing its predictions firstly with theoretical and experimental results presented by Campbell et al. [23–25] and by Mei et al. [96], and secondly with the experimental results presented in section 4.6.

Finally, the model has been used to study the influence of particular factors like hull curvature, hull stiffness and panel size on equivalent uniform static pressures.

Chapter 6

Dynamic loads in the keel structure

6.1 Overview

The integrity of the keel structure is of critical importance for the safety of a sailing yacht. With its ballast, the keel generates most of the righting moment that prevents a monohull from being capsized by the action of the wind and waves. Accidents like those experienced during the 1992-93 edition of the Vendee Globe Challenge by "Exide Challenger" (capsized in the Indian Ocean following complete failure of the keel fin; skipper Tony Bullimore had to be rescued by the Australian navy; the boat was abandoned) and by "Votre Nom autour du Monde" (capsized in the gulf of Biscay following complete failure of the keel fin; skipper Bertrand de Broc was airlifted and the boat abandoned) illustrate how failure of the keel structure can lead to the total loss of a sailing vessel and endanger the life of her crew.

The structural design of Open60' keels presents a particularly difficult challenge. On the one hand, with the boats often sailing in inhospitable regions where outside assistance cannot be relied upon, the requirements for self-sufficiency and safety are particularly important. The consequences of a keel failure, for instance, are more likely to be catastrophic for an Open60' sailing in the depths of the South Pacific Ocean, than for an America's Cup yacht competing in inshore waters, surrounded by numerous support and spectator boats. On the other hand, performance-related considerations favour the design of highly loaded high-aspect-ratio fins supporting extremely heavy bulbs. In this respect, the advent of canting keels in the late nineties

Figure 6.1: The upturned hull of "Exide Challenger" lying in the Indian Ocean after her keel fin broke. Skipper Tony Bullimore had to be rescued by a ship of the Australian navy and the yacht was abandoned. Photo credit: Guy Magowan/PPL.

has worsened the problem as, with the task of producing sideforce transferred to daggerboards, the only limits to the reduction of the fin thickness are posed by structural constraints.

Two particular issues involved in the structural design of an Open60' keel can be illustrated through examples of failures observed in recent times respectively on "Kingfisher" (figure 6.2) and on "Bobst Armor Lux" (figure 6.3). The former was discovered at the end of a round-the-world passage (the boat had then sailed approximately 50000 miles, including two North Atlantic crossings and a trip from New Zealand to Europe). A large crack appeared at the root of the fin, immediately above the pivot axis, suggesting a probable fatigue problem. The latter occurred during the 2002-03 edition of the "Around Alone" race: the skipper reported hearing a loud "crack" from the keel as the boat landed after falling from the back of a particularly steep wave. Further inspection revealed a large crack in the fibres around the pivot axis, due most probably to the internal stresses suddenly exceeding the ultimate strength of the laminate.

It is believed that, in both cases, the loads originated by the motion of the yacht

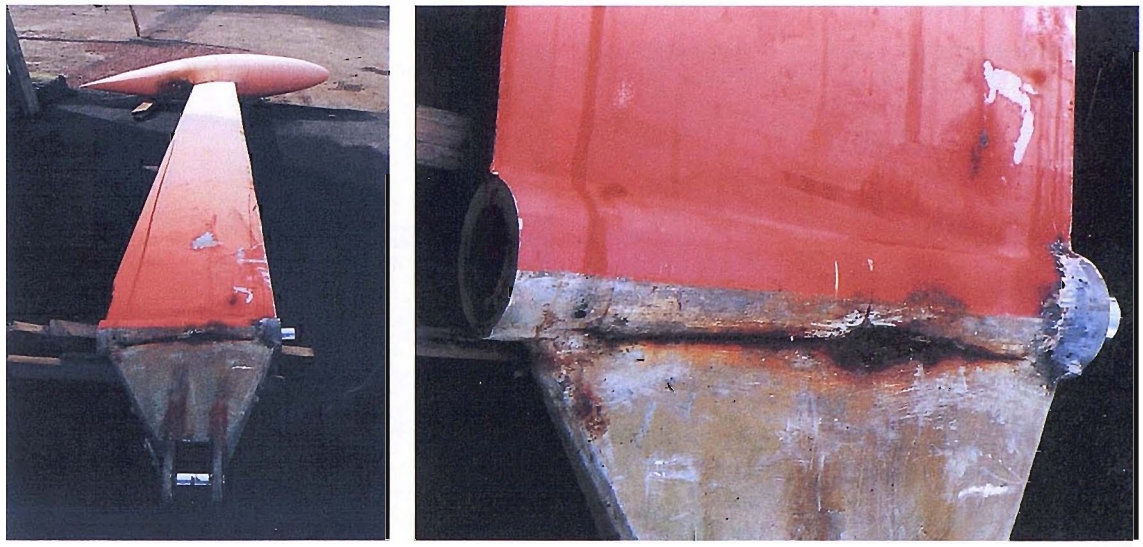

Figure 6.2: Damage found on the keel of "Kingfisher" after the 2000-01 Vendee Globe. The keel was made out of machined high-strength steel. A wide crack can be seen above the pivot axis, surrounded by signs of corrosion. X-ray analysis showed its depth to be significant and replacement of the whole keel was recommended.

were the main cause of the failure, however, very little analytical or experimental evidence exists to prove this point.

The present chapter outlines an analytical method that has been developed to deduce the internal stresses acting in the keel structure from known wave induced motion. The method accounts for the dynamic response of the structure to transient inertial loads and for the damping produced by the unsteady hydrodynamic forces. It is believed that application of this method to the data obtained from the full-scale measurements described in Appendix H, can provide valuable insight into the potential problems affecting the integrity of Open60' keels.

Figure 6.3: Damage suffered by the keel of "Bobst Armor Lux" during Leg 4 of the 2002-03 Around Alone Race. Top right: cracked fibres on the keel beam above the pivot axis. Middle right: wide crack between the pivot axis fairing and the keel beam. Bottom: the keel structure exposed for inspection.

6.2 Calculation of the response to a transient excitation

In the present study, the keel has been analysed as a mechanical system subject to excitation by the motion of the hull. As an example, let us consider the two degrees of freedom system represented in figure 6.4, where the mass "m", representing the bulb, is only allowed to move laterally along the x axis, the hull is considered to be infinitely rigid and only free to sway, and the fin is represented as a weightless spring applying a force on the hull and on the bulb that is linearly proportional to their relative displacement. The motion of mass "m" can then be described by the following equation:

$$m \cdot \ddot{x}(t) = -k \cdot (x(t) - u(t)) \tag{6.1}$$

which, by introducing the new variable $\delta_x(t)$, equal to the relative displacement $(x(t) - u(t))$, can be written as:

$$m \cdot \ddot{\delta}_x(t) + k \cdot \delta_x = -m \cdot \ddot{u}(t) \tag{6.2}$$

If function $u(t)$ (i.e. the motion of the hull) is known together with the initial condition of δ_x, equation 6.2 can be solved to find the relative displacement of mass "m" (i.e. the deformation of the keel) at any instant in time. Moreover, it can be noted that the forcing term in equation 6.2 corresponds to the inertial force acting on the bulb as a result of the acceleration of the hull: depending on the shape of $\ddot{u}(t)$ and on the parameters m and k, the actual response δ_x may exceed the quasi-static response $m \cdot \ddot{u}(t)/k$.

In order to model more accurately the behaviour of the keel structure and the forces that act upon it, a number of additional factors are to be considered. Firstly a more complex model of the structure is required to account for its multiple degrees of freedom and for their response to the different components of motion of the hull. In the present study, this is achieved by use of a finite element model as shown in section 6.3. Secondly, careful consideration must be given to the effects of the gravity force and of the hydrodynamic forces acting on the structure. Depending on the heel angle, the weight of the structure results in two force components, one acting along the span of the fin and one perpendicularly to it. The former affects the lateral oscillations of the bulb and can be modelled in terms of an equivalent added stiffness k_w. The latter produces a lateral deformation which must be added

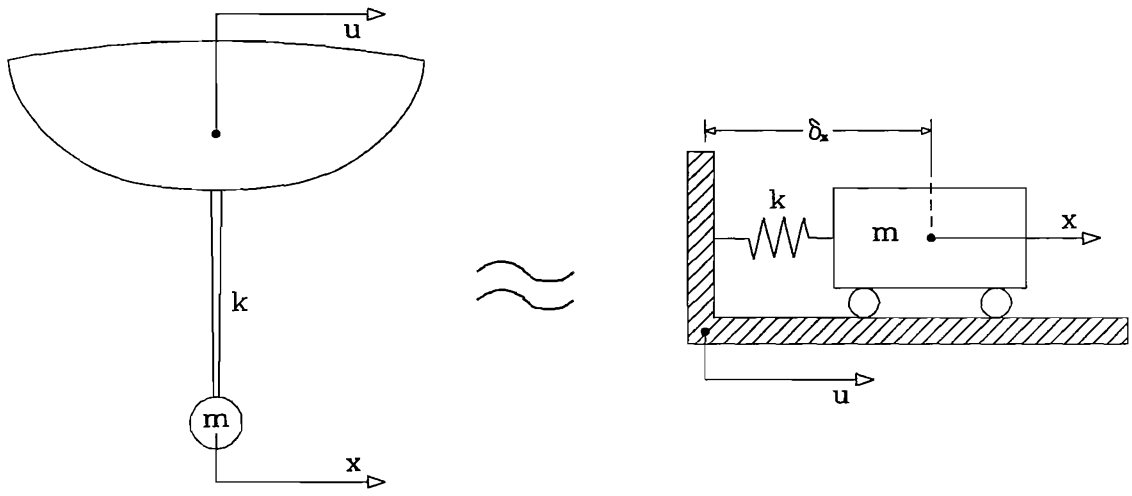

Figure 6.4: Example of two degrees of freedom system describing the lateral motion of the bulb relative to the hull.

to the one produced by inertial forces. Hydrodynamic forces are born as the result of boat forward speed and leeway angle, and of vibration of the keel. These are dealt with in more detail in section 6.6, where it is also shown that their effects cannot be considered separately. Finally, on boats with canting keel arrangements, the angle of swing of the keel is to be accounted for, as it has an influence on the way the different components of the inertial forces affect the structure.

6.3 Finite elements model of the keel

The particular model discussed in the remaining part of the present chapter refers to the keel of "Gartmore", an Open60' designed by Groupe Finot and built in 1997. Its main dimensions are reported in figure 6.5. The fin was built in female moulds with pre-impregnated carbon fibre and the bulb, made out of lead, has a design weight of 3300kg. The transverse sections of the fin and of the bulb correspond respectively to NACA 66-016 and 66-020 profiles, as defined in [1]. Assuming the material density and the mechanical properties to be uniform over each section, for these shapes the centre of gravity and the shear centre are located respectively at 45% and 43.5% of the chord length from the leading edge.

The keel fin has been modelled with Euler-Bernoulli beam elements, each with two nodes. A schematic representation of this model is given in figure 6.6. Elements and nodes are numbered in progressive order from the root of the fin to the tip, so

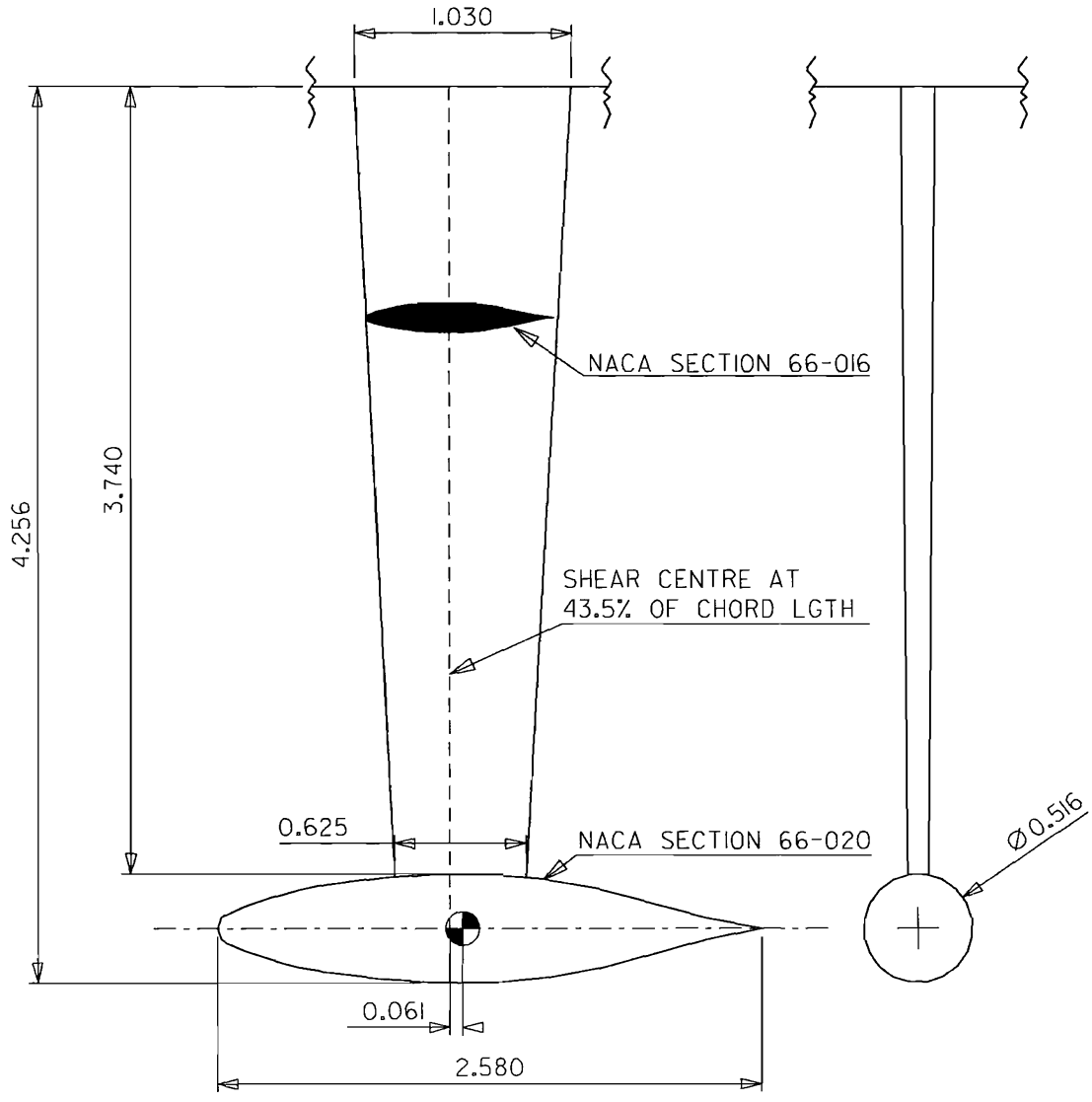

Figure 6.5: Main dimensions of the keel.

that the first node is placed at the intersection between the fin and the hull while the last node is on the longitudinal axis of symmetry of the bulb (the bulb is considered to have polar symmetry around its longitudinal axis). This model is valid only for a fixed keel. For a canting keel, additional elements would be required to model the portion of the fin comprised between the pivot axis (placed at the intersection with the hull) and the point where the canting force is applied.

A separate reference system is used for the keel: its axes $\mathcal{X}_k, \mathcal{Y}_k, \mathcal{Z}_k$ are respectively parallel to the boat $\mathcal{Z}$ axis, parallel and in the opposite direction to the boat $\mathcal{X}$ axis and parallel and in the opposite direction to the boat $\mathcal{Y}$ axis. The origin of the keel reference system $\mathcal{X}_k, \mathcal{Y}_k, \mathcal{Z}_k$ coincides with the location of the first node at the

root of the keel. All the elements are laying on the $\mathcal{X}_k$ axis and have their own local reference system $\mathcal{U}, \mathcal{V}, \mathcal{W}$ aligned with $\mathcal{X}_k, \mathcal{Y}_k, \mathcal{Z}_k$. Each node has six degrees of freedom identified as the three linear displacements along $\mathcal{U}$, $\mathcal{V}$ and $\mathcal{W}$ and the three rotations θ_u, θ_v and θ_w respectively about the same axes.

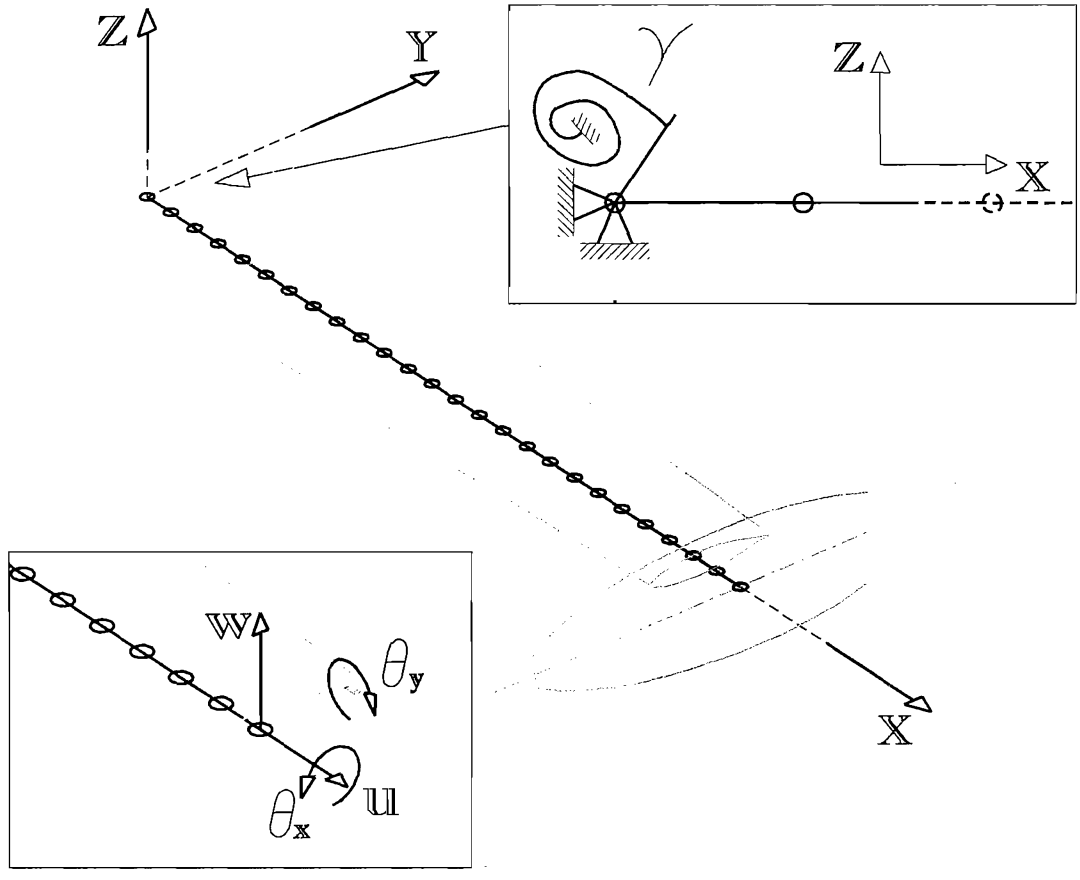

Figure 6.6: Finite element model of the keel.

Deformation of the bulb is considered to be negligible together with its displacements and rotations relative to the fin. Consequently, the bulb can be modelled through additional mass and rotary mass moments of inertia applied at the last node. The longitudinal distance between the centre of gravity of the bulb and the $\mathcal{X}_k$ axis introduces coupling between the inertia forces associated with linear acceleration of the bulb along $\mathcal{Z}_k$ and those related to angular rotation of the fin tip around $\mathcal{X}_k$. This effect is accounted for through additional diagonal terms in the mass matrix of the element modelling the fin tip. For the calculation of the stiffness matrix, the material of the fin was modelled as being isotropic with constant Young's modulus E_K, and shear modulus G_K. Furthermore, the boundary condition at the root of the keel has been modelled by constraining all linear displacements and by allowing

rotation around the $\mathcal{Y}_k$ and $\mathcal{Z}_k$ axes at the first node. The constraints on rotation about $\mathcal{Y}_k$ and $\mathcal{Z}_k$ imposed by the keel to hull joint have then been modelled through linear rotary springs of stiffness γ_y and γ_z as shown in the detail of figure 6.6. In this way the whole stiffness matrix can be assembled as a function of the four parameters E_K, G_K, γ_y and γ_z.

While information from design data has been considered to be sufficiently accurate for the determination of the mass properties of the structure, equivalent stiffness properties have been derived empirically through a procedure outlined in section 6.4. This approach is justified mainly by the two following considerations: firstly, due to the very large number of variables involved (e.g. build quality, actual material properties, etc.), it is extremely difficult to accurately estimate the stiffness characteristics of a composite structure. Secondly, the approximation introduced by describing the keel through an ideal model (i.e. Euler-Bernoulli beam, isotropic material, uniform weight distribution, etc.) is compensated by effectively tuning the finite element model to match the measured behaviour of the actual structure (cf. section 6.5).

Once the mass and the stiffness matrix are assembled (cf. appendix F for details), the natural frequencies and mode shapes of the undamped system can be found by solving the following equation describing its free vibration:

$$[M_f]\left[\ddot{X}_f\right] + [K_f]\,[X_f] = [0] \tag{6.3}$$

where X_f represents the vector of the unconstrained nodal displacements and $[M_f]$ and $[K_f]$ are the corresponding parts of respectively the mass and stiffness matrix. Solutions of equation 6.3 are obtained by solving numerically the eigenvalue problem:

$$\left(-\omega^2\,[M_f] + [K_f]\,X_f\right) = [0] \tag{6.4}$$

where ω is the vector of natural frequencies and the relative eigenvectors ϕ represent the associated mode shapes. Results obtained by this method are presented in figure 6.12, section 6.5.

6.4 Modal tests on the keel structure

The stiffness properties of the keel structure have been investigated by a technique similar to the one used for impact hammer tests. The fin has been instrumented with four accelerometers placed in different configurations as shown by figure 6.7.

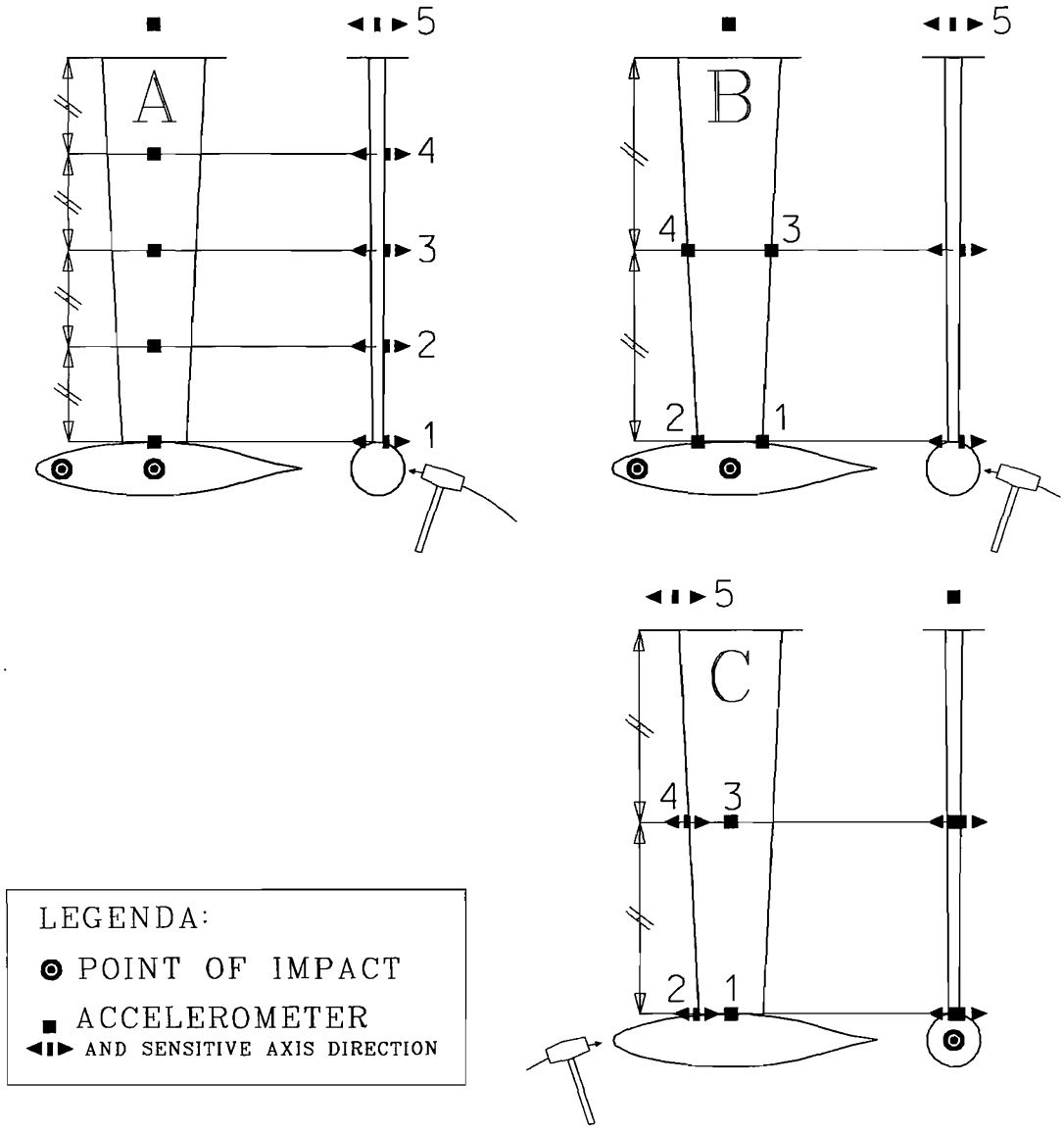

Figure 6.7: Keel structure test: configurations of the accelerometers.

In configuration "A" the sensors were placed respectively at l_{fin}, $0.75l_{fin}$, $0.5l_{fin}$ and $0.25l_{fin}$ from the root in the span-wise direction (l_{fin} being the length from the root of the fin to the point where it intersects the bulb) and at 50% of the chord in the chord-wise direction. The structure was excited by hitting the side of the bulb at a longitudinal position corresponding to the middle of the tip of the fin. This configuration was aimed at detecting mainly the lateral bending of the keel. In configuration "B" the sensors were placed at l_{fin} and $0.5l_{fin}$, two at the leading edge and two at the trailing edge. The sensitive axes were aligned with Z_k axis by fitting a suitably shaped small block of high density PVC foam between the fin and the

base of the sensor: the first resonant frequency of the accelerometer-foam assembly was estimated to be above 5kKz, hence the accuracy of the measurements was not affected. The structure was excited by hitting the side of the bulb at approximately 10% of its chord length from the leading edge. This configuration was aimed at detecting mainly the torsion of the keel.

Finally in configuration "C" the sensors were placed at l_{fin} and $0.5l_{fin}$, two on the leading edge with sensitive axis aligned with Y_k and two at 50% of the chord with sensitive axis aligned with Z_k. The structure was excited by hitting the nose of the bulb as shown in figure 6.7. The aim of this configuration was to detect mainly longitudinal oscillation of the keel. A fifth accelerometer was placed inside the hull on a keel floor in order to check if the supporting structure of the keel showed any significant movement; in configurations "A" and "B", it was mounted at 25% of the chord length from the leading edge with the sensitive axis aligned with Z_k, while in configuration "C" it was placed at the leading edge with the sensitive aligned with Y_k.

The accelerometers used were ICSensors 3140 type with a measuring range of $\pm 5g$, a sensitivity of $400mV/g$, a bandwidth of 0-500Hz and a weight of 10 grams. The output from the sensors was amplified with a gain of 4 (maximum value allowed by the recording equipment), hence, with a resolution of the logging unit of 12bit over a $0 - 5V$ input range, the resolution of the measured signal was $0.76mg$. To avoid aliasing, each signal was first filtered with a 5-pole Butterworth lowpass filter with a cutoff frequency of $250Hz$, and then sampled at $1kHz$.

The measurements were carried out with the boat out of the water, resting on two steel cradles based on a solid concrete ground. The keel was partly lodged into a pit sufficiently wide for a person to operate around it. The keel structure was set into vibration by hitting the bulb with a 10kg hammer. In order to avoid denting the bulb, the head of the hammer was covered with a 5mm thick sheet of hard industrial rubber. The acquisitions were started manually and continued for at least 30 seconds after the hammer impact. The acquired time histories of the accelerations were then analysed both in the time domain and in the frequency domain in order to estimate the first natural frequencies of the structure and the corresponding mode shapes and modal damping ratios.

Power spectra of the signals were calculated by "Fast Fourier Transform" and natural frequencies were identified as the values corresponding to the significant peaks

in the spectra. The accuracy of these values could be estimated to be equal to the frequency resolution of the power spectra, which, with recording lengths between 30 and 45 seconds, was between 0.02 and 0.03 Hz. Secondly modal shapes and modal damping ratios were estimated by examining the signals in the time domain: in particular each mode was analysed by successively band-pass filtering the original signal around each of the identified natural frequencies. Figures 6.8, 6.9 and 6.10 illustrate this process.

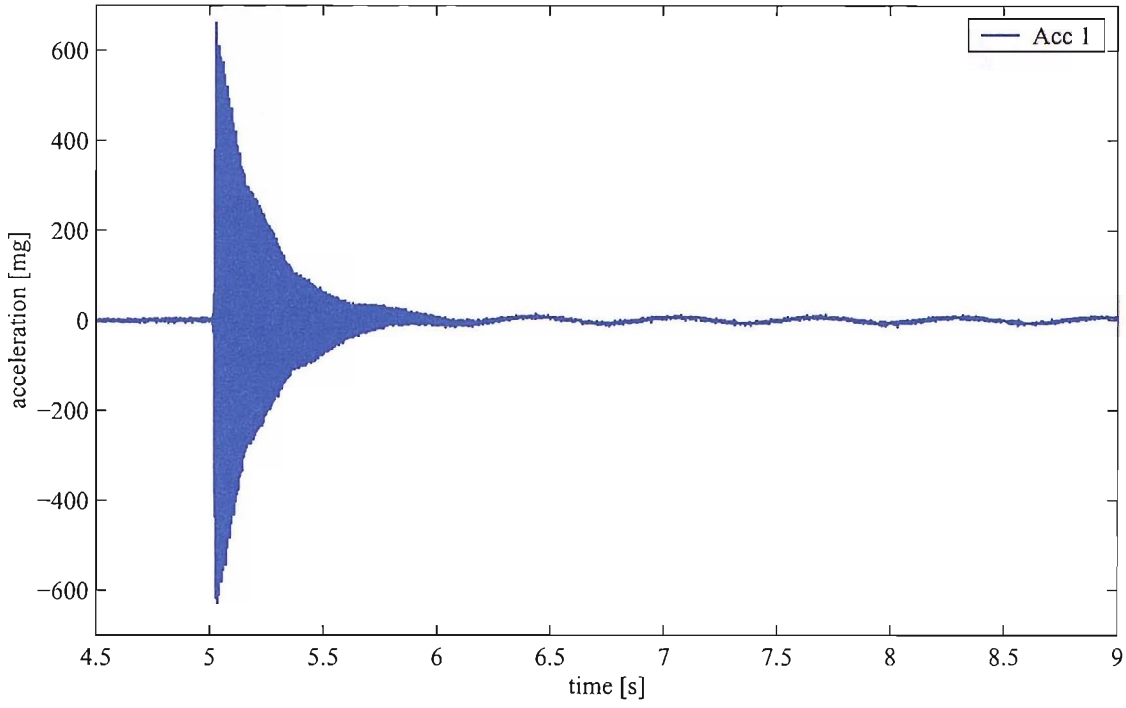

Figure 6.8: Keel structure test: detail of signal recorded from accelerometer 1 during impact in configuration "A".

In particular, figure 6.8 shows a typical recorded acceleration from accelerometer 1 when performing measurements in configuration "A". The initial phase of the response is dominated by high frequency vibration associated with higher modes. Then, gradually the higher frequencies die out to reveal the acceleration associated with the first mode.

Figure 6.9 shows the frequency spectrum of the signals recorded from all five mounted accelerometers during a test with configuration "A". The peaks associated with lateral bending modes can be identified, as pointed out in the graph. The frequency spectrum is obtained by performing a fast Fourier transform of all the signals over a period of 30 seconds: thus the amplitude of the peaks is a function of

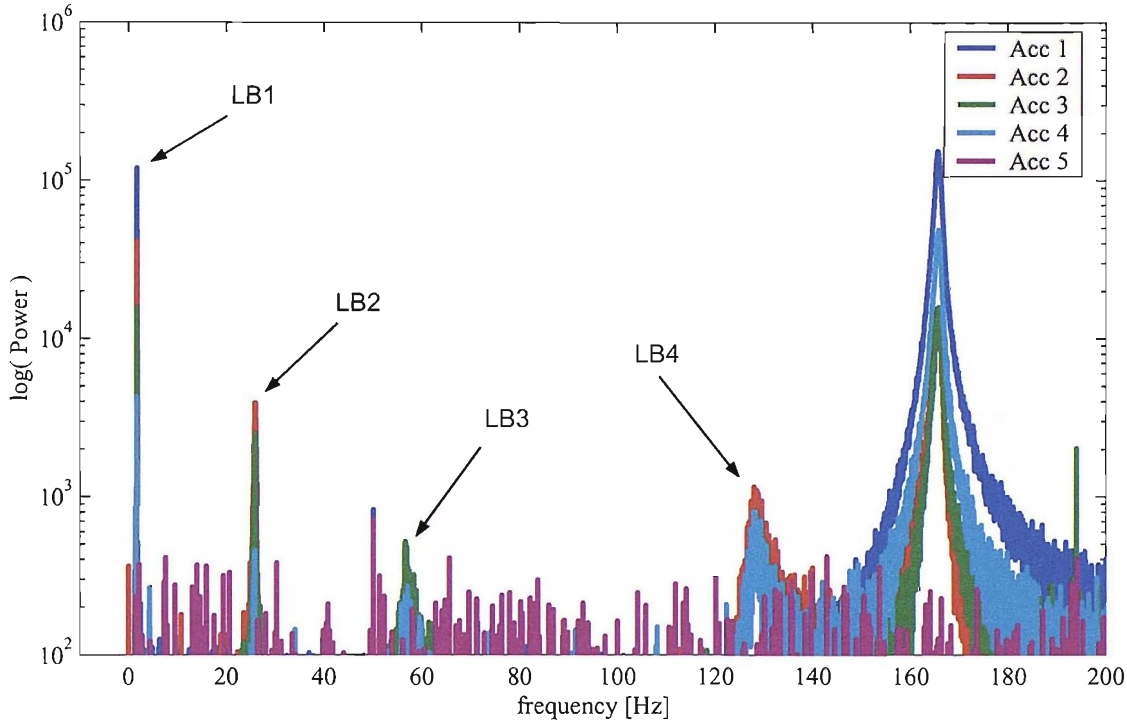

Figure 6.9: Keel structure test: power spectrum of all five mounted accelerometers. Arrows indicate the peaks corresponding to the first lateral bending modes.

both the amplitude of the vibration and of its duration in time. In particular, by looking at the time history of the recorded signal (figure 6.8), it can be seen that the first peak at approximately 2Hz is associated with a vibration of very small amplitude (approximately 10mg) which decays very slowly. On the other hand, for example, the peak around 165Hz is generated by relatively large amplitude acceleration that follow the impact and die out very quickly. The spreading in frequency of this peak is also evidence of the short duration in time of the associated vibration. With respect to this power spectrum, the following can be pointed out:

- All signals from the accelerometers were affected by noise. The noise level was measured by recording a full 30 seconds time-history of the accelerations without impacting the keel. The rms values of the signals thus acquired were between 0.64mg and 0.83mg for accelerometers 1 to 4 and 3.22mg for accelerometer 5. While care was taken to adequately wire and screen the whole recording apparatus, the remarkably higher noise affecting the last sensor could be attributed to the large additional length of cable needed in order to connect the sensor inside the hull (to this purpose the cable was lead through an open seacock). Furthermore, peaks can be observed at exactly 50Hz for all the signals, which

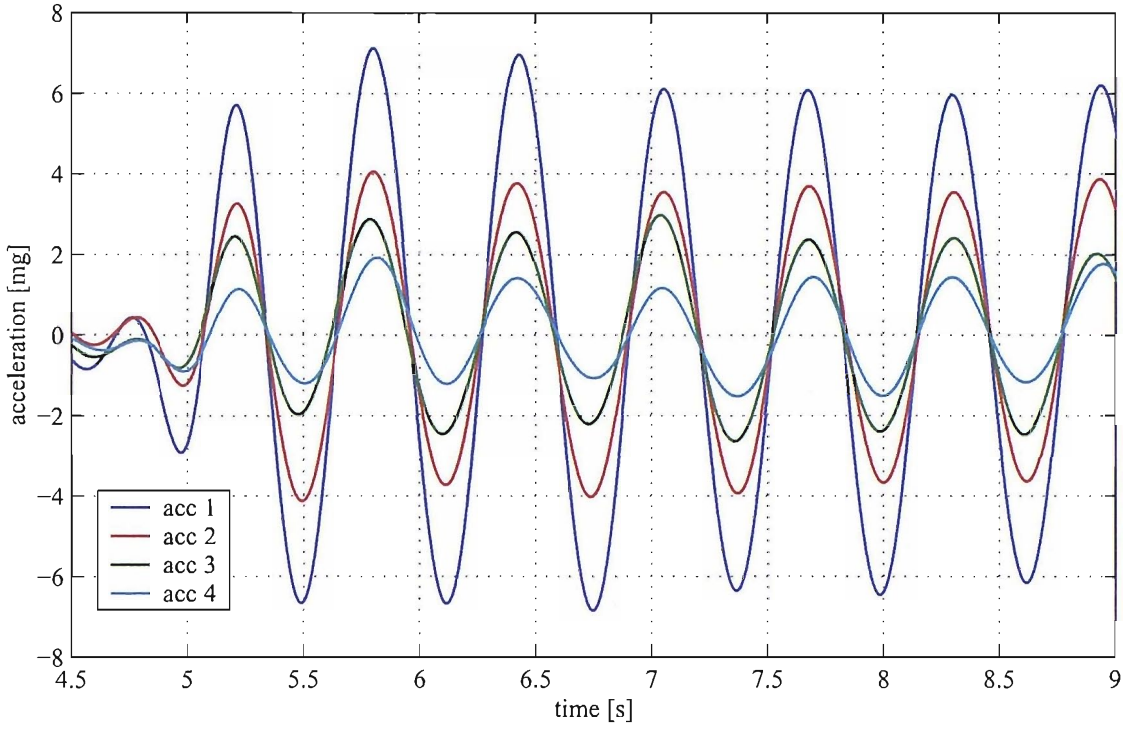

Figure 6.10: Keel structure test: low-pass filtered signals from the four accelerometers mounted on the fin (filter cut-off: $2.5Hz$). Relative amplitudes of acceleration due to the first lateral bending mode can be observed.

indicates that noise produced by the mains power supply still managed to find its way through the system.

- The relative amplitudes of the peaks from different sensors at a same frequency can be taken as an indication of the relative amplitudes of displacement at different positions along the fin, and hence of the modal shapes. However, due to the time averaging effect of the Fourier transform and to the relative influence of noise particularly on sensors that were close to nodes of vibration, a more accurate estimate of modal shapes could be obtained by analysing the band-pass filtered signals in the time domain as shown in figure 6.10. By this approach, some of the peaks appearing in the spectrum could safely be identified as the first lateral bending modes.

- While different natural modes were more or less easy to identify, depending on the configuration of the accelerometers and on the position of hammer impact, frequency components associated with torsional modes could be spotted in the spectra dominated by lateral bending and vice-versa.

Figure 6.10 shows the signals from the first four accelerometers, filtered so as to isolate the first natural frequency. The trace from accelerometer #5 has been omitted as it appeared to be largely dominated by noise and did not show any significant correlation with the others at any of the identified natural frequencies. It may be noted in figure 6.10 that, the oscillations following the hammer impact do not show a particularly clear exponential decay. Similarly, the ratios between the amplitudes of the peaks and troughs from different sensors seem to vary in time (this phenomenon being particularly evident for accelerometers 3 and 4). It is shown in Appendix F that the first phenomenon can be interpreted as amplitude modulation of the oscillations in one mode by those from other modes. Besides, when looking at oscillations with amplitude less than 5mg, the relative contribution of noise becomes apparent. This problem is particularly noticeable for the first natural frequencies, where it is practically very difficult to introduce enough energy to produce a large response by the structure. Yet, under the assumption that signal and noise are not correlated, a good estimate of the relative amplitudes can still be obtained by averaging the ratios over several peaks and troughs. In the same way, an estimate of modal damping ratios can be obtained by calculating the logarithmic decrements over several successive peaks, and then taking their average. Due to the insufficient level of definition of the signals in the frequency domain, this method has been preferred to the commonly used "half-power point" method.

Further time histories of the filtered signals showing the accelerations associated with different modes are reported in Appendix F.

All the natural frequencies that could be obtained by this method as well as the modal damping ratios and normalised amplitudes of deflection are reported in table 6.1. The following remarks can be made:

- Where an asterisk appears, it indicates that the adjacent value may not be reliable due to a poor signal-to-noise ratio (SNR). This may happen in three different conditions:
  - a low frequency mode for which it is difficult to produce a large enough response: this was typically the case of the first three modes where the SNR was particularly poor for the sensors located closer to the keel root.
  - a mode for which the point of hammer impact is a node: mode #4 (2-node lateral bending) falls under this category, where the combination of a low

Table 6.1: Natural frequencies, modal damping ratios and normalised amplitudes of motion obtained from the modal tests on the keel structure.

Mode #	Natural Frequency [Hz]	Critical Damping ratio (h)	Acc.1	Acc.2	Acc.3	Acc.4	Mode type	Config.
1	1.60	0.0073 ÷ 0.0110(*)	1	0.63	0.35	0.16(*)	1-node lateral bending	A,B
2	2.32	?	-	-	-	-	longitudinal oscillation	C
3	4.34	0.0033 ÷ 0.0037	-	-	-	-	1-node torsion	B,A
4	25.8	0.0057 ÷ 0.0065	0.37	1	0.79	0.31	2-node lateral bending	B,A
5	56.6	0.0054 ÷ 0.0056	-0.30	0.34	1	0.59	3-node lateral bending	A
6	113.2	0.0040 ÷ 0.0041	-	-	-	-	2-node torsion	B
7	128.4	0.0024 ÷ 0.0025	0.12(*)	1	-0.14	-0.70	4-node lateral bending	A
8	166.0	0.0008	1	-0.32	-0.32	0.56	bulb-fin joint deformation (?)	A

natural frequency and of a low excitation makes the SNR for accelerometers #1 and #4 particularly poor.

- a sensor is very close to a node of a natural mode of vibration: this, for instance, was the case of accelerometer #1 in mode #7 (4-node lateral bending).

- Amplitudes of motion for accelerometer #5 have not been reported as they never rise above the noise threshold. Except for the first three modes, the best signal-to-noise ratio for the accelerometer with the highest response (i.e. the one with respect to which other amplitudes are normalised) was always greater than 30; hence, assuming that accelerometer #5 did show a response and that this was completely masked by noise, its amplitude would have been less than 0.03 for 2-node lateral bending and even smaller for higher modes. While no conclusion can be drawn for the lower modes, the very good agreement between the measured frequencies and amplitudes and those obtained from the finite

element model described in the following section, suggests that the hypothesis of the keel root being always a node of the structure is altogether acceptable.

- Amplitudes of motion relative to modes dominated by torsion could not be safely defined. As a matter of fact, the number of sensors used was not sufficient to measure accurately the rotation of each section; besides, due to the rounded shape of the fin sections, it is practically very difficult to guarantee a good alignment between the sensitive axes of the accelerometers, and a small error in this sense can greatly affect the accuracy of the results.

- Mode #2 has been generically defined as "longitudinal oscillation" as it is not possible to obtain a reliable estimate of the mode shape, again due to poor SNR. Finite element analysis has later confirmed that this mode involves mainly an oscillation of the whole structure about the keel root and very little deformation of the fin.

- Mode #8 has been generically defined as "bulb-fin joint deformation": the analysis of the data from different test configurations suggests that this mode involves nearly only lateral deflections (i.e. it can be hardly detected in the spectra of the accelerations along Y_k). While the reduced number of sensors used in the tests does not allow the type of deformation involved with this mode to be defined accurately, the amplitudes of the measured accelerations are not compatible with a higher order lateral bending mode.

6.5 Comparison of results from modal tests and finite element analysis

As mentioned in section 6.3, the stiffness matrix $[K]$ has been defined as a function of the four parameters E_K, G_K, γ_y and γ_z representing respectively the equivalent Young's modulus and shear modulus of the fin material and the stiffnesses of the two rotary springs simulating the fin-hull joint (details about the formulation of [M] and $[K]$ are given in Appendix F).

The values of E_K and γ_y were obtained as the result of an optimisation process by which the finite element model was tuned to approximate as closely as possible the natural frequency and the mode shape of the first lateral bending mode as measured

through the modal tests described in section 6.4. In particular, a numerical algorithm was implemented in MATLAB to find the value of the $[E_K, \gamma_y]$ vector that minimises the difference between the measured and calculated first natural frequency, and the rms difference between the four relative amplitudes of displacement measured by the accelerometers and calculated at the corresponding location by the FE model.

This process requires the evaluation of the stiffness matrix and the solution of the eigenvalue problem to be performed several times; in order to limit computational time to an affordable level, the optimisation was carried out with a 50 elements model of the structure. Figure 6.11 shows that the value of the natural frequency obtained for the first mode with this number of elements is within 0.2% of the one obtained with a 200 elements model: this implies a possible error on the estimated frequency of 0.003Hz which is an order of magnitude lower than the accuracy of the experimental value. In the first optimisation process described above, estimated values were used in place of G_K and γ_z. Then, once E_K and γ_y were defined, the values of G_K and γ_z were found by having the FE model natural frequencies of respectively the first torsion and longitudinal bending mode match the measured ones. Finally the whole process was repeated until the values of the three first natural frequencies converged to within 0.01Hz of the measured ones. The final values of E_K, G_K, γ_y and γ_z are presented in table 6.2.

Table 6.2: Keel fin equivalent material properties.

E_K	G_K	γ_y	γ_z
77188 MPa	7996 MPa	$1.4432 \cdot 10^7 N \cdot m$	$1.3404 \cdot 10^7 N \cdot m$

The first twelve mode shapes and relative natural frequencies calculated with the finite element model are presented in figure 6.12. Each mode shape has been normalised with respect to the maximum displacement in the dominant type of deformation. For example, in the case of the first lateral bending mode, the deflection at the tip of the fin has been set to the unit value (figure 6.12.b) and the rotation θ_x scaled accordingly (figure 6.12.c). Coupling between bending and torsion is always present, but cannot be easily recognised on these graphs due to its very limited amplitude (e.g. for the 1-node lateral bending mode, a lateral deflection at the tip of 1m would involve a maximum rotation about X_k of 0.01 radians).

A comparison of the results of the FE analysis with the experimental data is

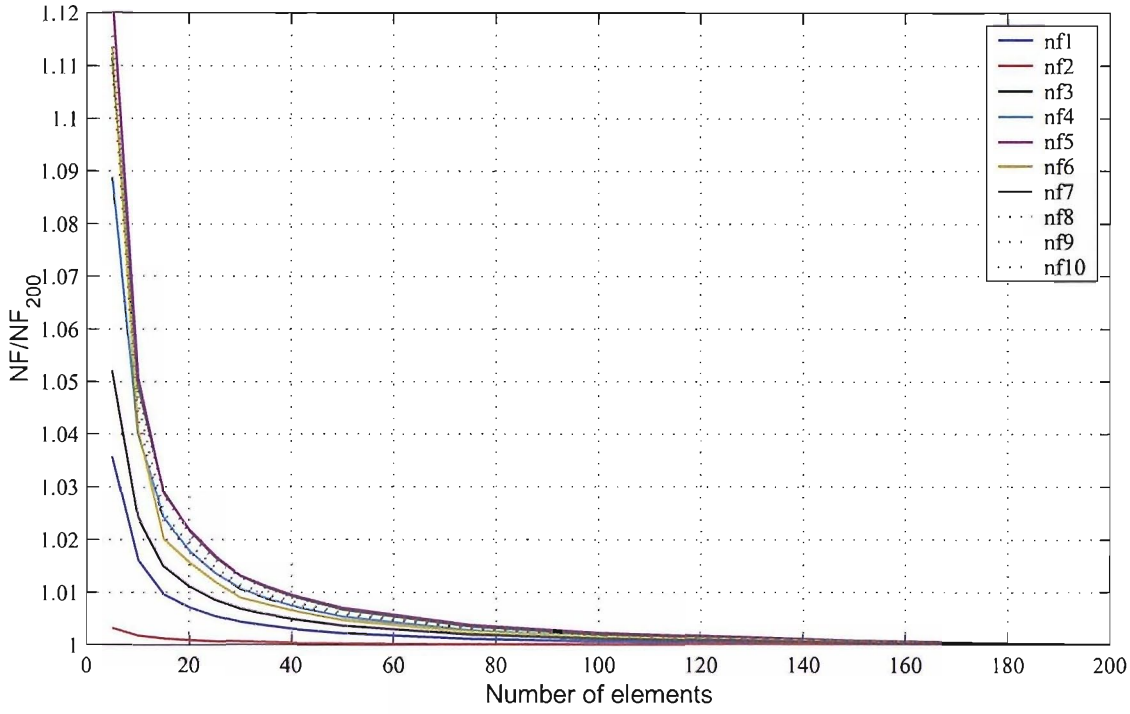

Figure 6.11: Convergence of natural frequency values calculated with finite elements model. NF/NF_{200} indicates the ratio of the natural frequency value obtained with a given number of elements to the value found with a 200 elements model. The lines labelled "nf1" to "nf10" correspond respectively to the first 10 natural modes.

presented in table 6.3 and figures 6.13. In particular, table 6.3 gives the measured natural frequencies and those calculated by FEA for the corresponding modes. For the modes for which modal amplitudes could be measured, the normalised rms error (NRE) is also given as an index of how well the calculated mode shapes agree with the measured data. The exact matching of the first three natural frequencies is a result of the adopted tuning process, hence it should not be regarded as an indication of the quality of the model. On the contrary, the closeness with which the following four natural frequencies are approximated does prove that the finite element model reproduces the behaviour of the structure with a good level of accuracy.

The natural frequency and the deflections associated with mode #8 do not find any match in the FEA results: this is most probably explained by the fact that this mode involves deformation of the bulb and/or of the bulb-fin joint which are not accounted for by the FE model. More generally, the FE model cannot be expected to reproduce accurately higher frequency modes; in fact these are most likely to involve deformation of the structure that cannot be described by a beam model approximation or that simply violate the conditions under which Euler-Bernoulli beam theory can

Table 6.3: Comparison of natural frequencies and mode shapes obtained from modal tests and finite element model.

Mode Type	**N.F.[Hz] (experimental)**	**N.F.[Hz] (FEA)**	**Mode shape NRE**
1-node lateral bending	1.60	1.60	0.012
longitudinal oscillation	2.42	2.42	-
1-node torsion	4.34	4.34	-
2-node lateral bending	25.8	24.9	0.078
3-node lateral bending	56.6	54.65	0.070
2-node torsion	113.2	101.1	-
4-node lateral bending	128.4	133.8	0.053
bulb-fin joint deformation	166.0	-	-

be applied.

The predicted mode shapes for lateral bending modes compare very well with the measured amplitudes as shown in figure 6.13: here it can be observed that the FE model appears to marginally overpredict the deflections in the vicinity of the fin root. This may be due to the influence of possibly inaccurate experimental data for the amplitude of deflection at the location of accelerometer #4. The overestimation of this amplitude would lead, through the tuning process, to the overprediction of E_K and to the underprediction of γ_y, and hence to the overestimation of the deflections close to the root. In order to avoid this possible error, the tuning process was repeated with the modal amplitude matching criterion based on the second mode of lateral bending and, alternatively, on the first mode with data from accelerometer #4 discarded. Both these approaches led to a better approximation of the mode shapes, but equally to a worse approximation of the natural frequencies. It was therefore concluded that the initially observed discrepancy is a consequence of the approximation introduced when considering the Young's modulus E_K constant throughout the fin and that it can be avoided only by building a more complex model of the structure.

With regard to the choice between privileging a better description of natural frequencies or a better approximation of modal shapes, it can be argued that each option has an influence on the precision with which the FE model predicts the response of the structure to a transient excitation. However it is believed that, in the absence of strong nonlinearities in the behaviour of the mechanical system, the errors potentially associated with the former option are easier to predict and to quantify than those carried by the second. Hence, the solutions given in table 6.2 have been retained for

the rest of the analysis.

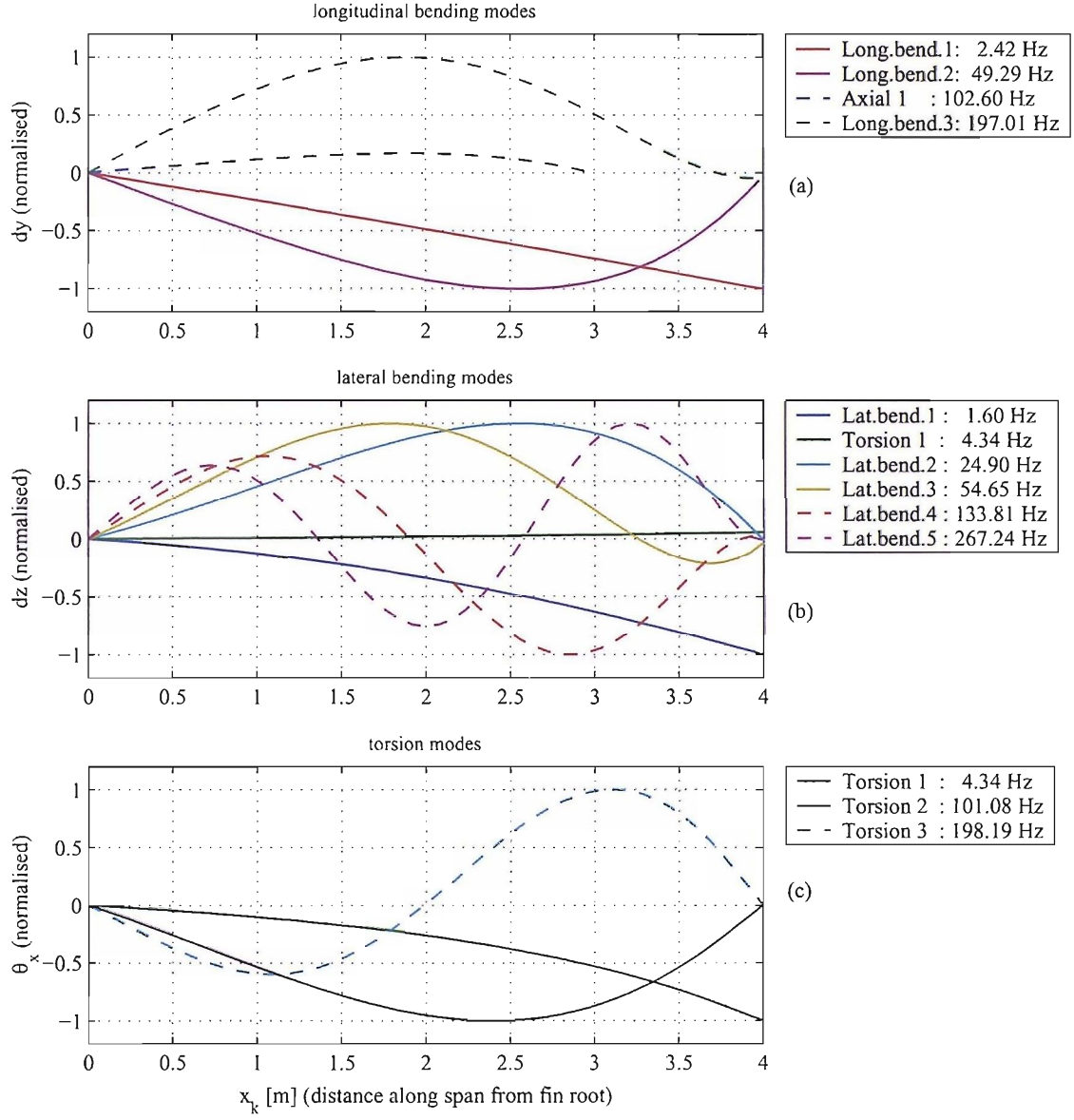

Figure 6.12: Mode shapes and relative natural frequencies of the finite element model ($N_{el} = 200$). All amplitudes are normalised with respect to the largest amplitude of the dominant type of deformation for each mode.

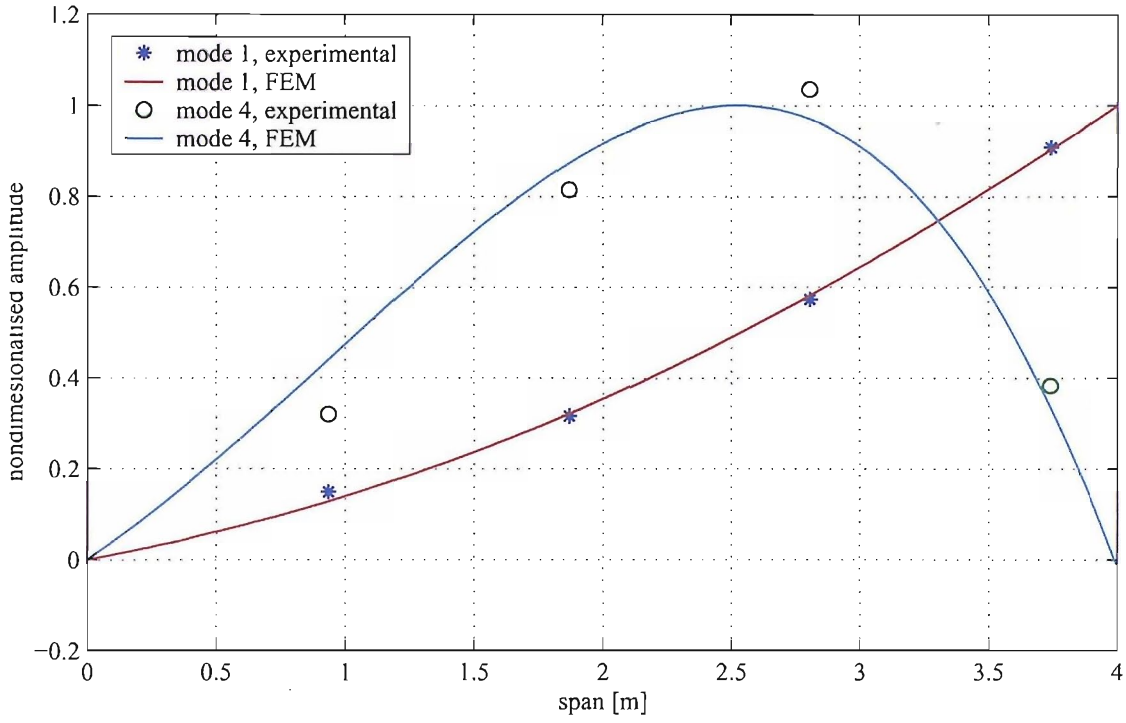

(a) First and second lateral bending mode

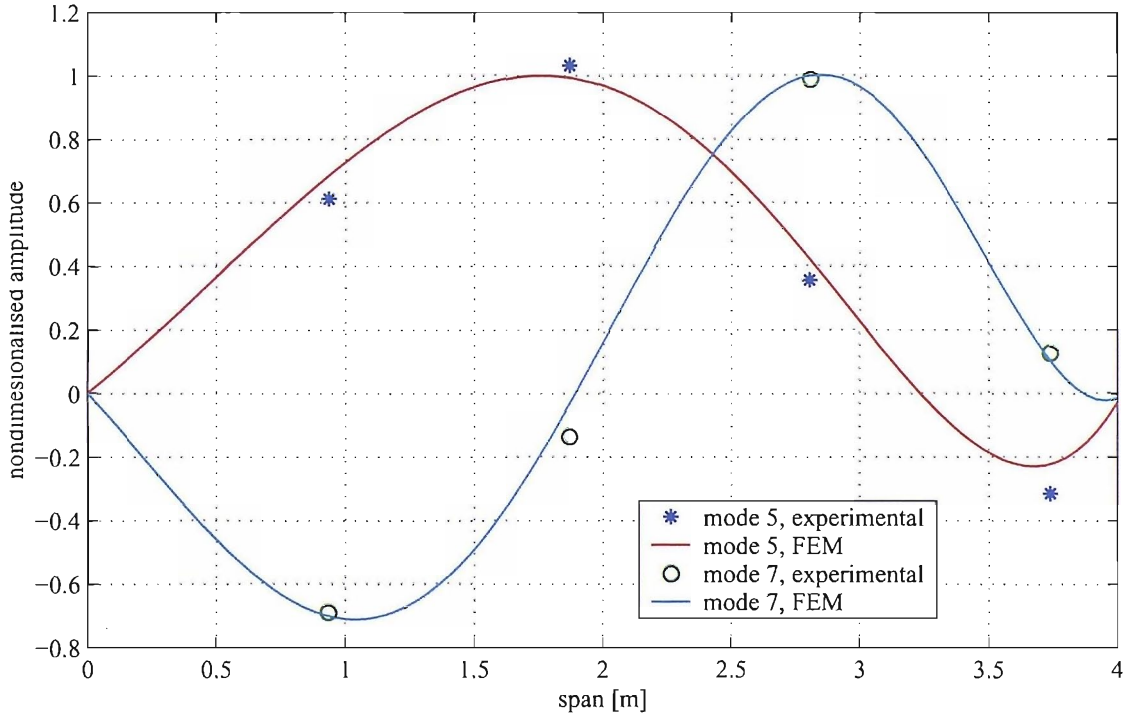

(b) Third and fourth lateral bending mode

Figure 6.13: Comparison of lateral bending mode shapes as measured and as calculated by FEM.

6.6 External Loads

The single most difficult task one is confronted with when trying to model the behaviour of the keel structure, is the description of the external loads that act upon it. These are schematically represented in figure 6.14 and may be generically subdivided into inertial and hydrodynamic forces. The former include the forces generated both by the acceleration of gravity and by the accelerations of the boat in a seaway. The latter can be split into the quasi-steady components associated with the relatively constant forward speed and leeway angle of the boat, and unsteady components related with the perturbation of the flow produced by the vibrations of the keel. They shall all be analysed in greater detail in the following sections.

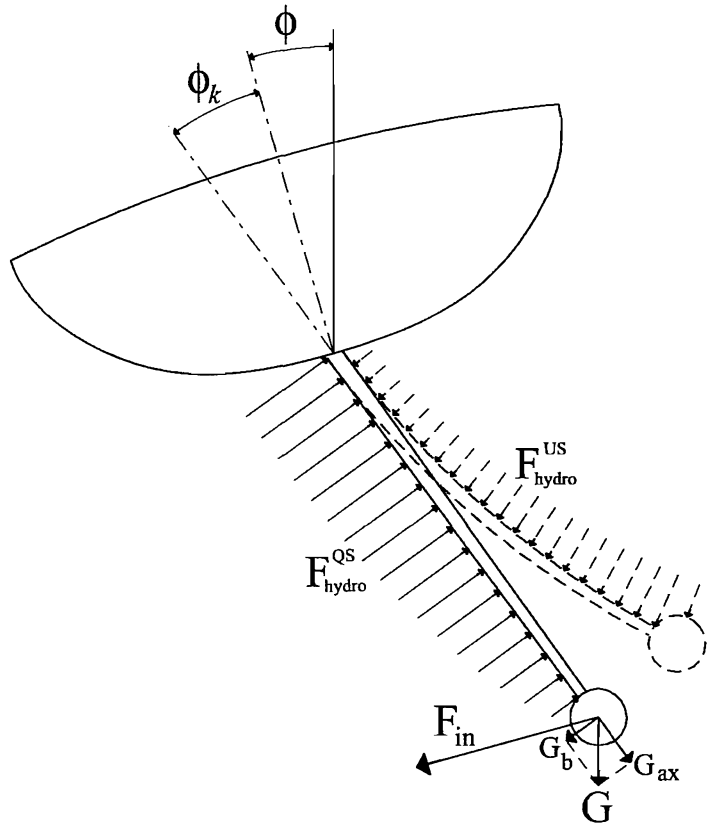

Figure 6.14: Schematic representation of the external loads acting on the keel.

6.6.1 Gravity force

The resultant of the gravity force acting on the keel is represented in figure 6.14 as "G". For the Open60' keels presently under examination, it may be considered to

act very close to the tip of the fin due to nearly 90% of the weight of the keel being concentrated in the bulb. As a consequence of the inclination of the keel relative to an earth-related vertical axis, the gravity force can be split into two components respectively perpendicular (G_b) and parallel (G_{ax}) to the spanwise direction. The former can result in significant shear forces and bending moments, particularly at large heel angles and when the keel is canted to windward. The axial component, on the other hand, normally loads the fin in tension and can be seen to increase the effective stiffness of the structure [30]. This particular effect is accounted for by additional terms in the stiffness matrix as shown in appendix F.

6.6.2 Inertial loads originated by motion in a seaway

It has been shown in section 6.2 that the keel structure can be regarded as an independent mechanical system subject to loading by inertial forces related to the motion of the boat. When the simplification used in the example of figure 6.4 is removed, it must first be considered that the non-inertial frame of reference (X_k, Y_k, Z_k) introduced to study the deformation of the keel is not only subjected to linear acceleration, but also to the angular motion corresponding to those of the boat. When analysing the structure with respect to this reference system then, the inertial force acting on a generic element of the structure with mass dm becomes:

$$\overrightarrow{F_{in}} = -dm\,\overrightarrow{a_k} - 2\,dm\,\overrightarrow{\omega} \times \overrightarrow{v} - dm\,\overrightarrow{\dot{\omega}} \times \overrightarrow{r} - dm\,\overrightarrow{\omega} \times (\overrightarrow{\omega} \times \overrightarrow{r}) \tag{6.5}$$

where $\overrightarrow{a_k}$ is the vector that describes the linear acceleration of the keel system, while $\overrightarrow{\omega}$ and $\overrightarrow{\dot{\omega}}$ indicate respectively the instantaneous angular velocity and angular acceleration vector; $\overrightarrow{r}$ and $\overrightarrow{v}$ define the position and velocity of dm relative to the origin of the X_k, Y_k, Z_k system. As a result of the different orientation of the keel axis system relative to the boat fixed system, $\overrightarrow{\omega}$ can be written as:

$$\overrightarrow{\omega} = \overrightarrow{i_k}\omega_z - \overrightarrow{j_k}\omega_x - \overrightarrow{k_k}\omega_y \tag{6.6}$$

with $\overrightarrow{i_k}, \overrightarrow{j_k}, \overrightarrow{k_k}$ equal to the three unit vectors aligned with the keel axis system, and ω_x, ω_y and ω_z the components of the angular velocity of the boat defined in the boat fixed reference system.

Considering the different terms in equation 6.5, the first and the third play the most significant role. In particular, it is expected that the vertical and lateral acceleration produced by slamming, may, by their magnitude and typical duration, lead

to a considerable dynamic response. On the other hand, the second term, commonly referred to as the Coriolis force, can be shown to be extremely small when compared to the others and is thus neglected in the rest of the study. Finally the last term, the centrifugal force, can result in an axial loading smaller by one order of magnitude than the gravity related force.

6.6.3 Quasi-steady hydrodynamic loads

When a yacht is sailing in a steady condition, the transverse component of the aerodynamic force generated by the sails is opposed by the hull adopting a leeway angle β [29]. The keel can then be considered as a foil placed in a flow with velocity equal to the boat speed relative to the water, and angle of attack:

$$\alpha_{k_0} = \arcsin\left(\sin(\beta)\cos(\phi + \phi_k)\right) \simeq \beta\cos(\phi + \phi_k) \tag{6.7}$$

The resulting hydrodynamic lift and drag are written as

$$L = \frac{1}{2}\rho U^2 S C_L \tag{6.8}$$

$$D = \frac{1}{2}\rho U^2 S C_D \tag{6.9}$$

where approximate values of the lift and drag coefficients C_L and C_D may be obtained by the lifting line theory or by empirical formulae such as the ones proposed by Gerritsma et al. [49]. The contribution of the bulb to the overall lift, can be estimated by considering an equivalent increase in span and aspect ratio as proposed by Hoerner [62]: the resulting C_L slope then becomes:

$$\frac{dC_L}{d\alpha} = C_{L,2D}\frac{AR_0(1+\frac{d_b}{T_k})(1+\frac{d_b}{2T_k})}{AR_0(1+\frac{d_b}{T_k})+2\cdot(1+\frac{d_b}{2T_k})} \tag{6.10}$$

where AR_0 represents the effective aspect ratio of the fin alone and d_b is the maximum diameter of the bulb. Similarly the contribution of the bulb to the total drag can be obtained by considering the induced drag reduction associated with the increase in equivalent aspect ratio, the frictional drag of the bulb and the interference drag generated by the junction of the fin and the bulb.

Equations 6.8 and 6.9 constitute a first approximation which, for instance, neglects free-surface effects and the influence of the interference between the flows over the canoe body and over the keel fin. More accurate predictions of steady-state forces

can be obtained by computational fluid dynamics (CFD) methods, however, such refinements are beyond the scope of the present study.

If a yacht is assumed to be sailing at a constant speed and on a steady course, the leeward-pointing sideforce produced by the sails is balanced by the hydrodynamic force generated mainly by the keel and the rudder. The boat can then be considered to be in static equilibrium and the hydrodynamic lift and drag produced by the appendages can be calculated by knowing the boat speed, its leeway angle (which commonly equates to the angle of attack of the keel), and the rudder angle.

When looking at a yacht sailing in waves, this static equilibrium becomes a dynamic one, whereby the aerodynamic and hydrodynamic forces can be found to be momentarily out of balance, but generally always tending to restore an equilibrium (unless the yacht is not naturally stable in course, a possible, but generally unwanted configuration). As a consequence, variations of leeway angle, and, hence, of lift and drag from the keel, can be observed, although constantly limited by the natural behaviour of the yacht and by the correcting action of the helm. Such variations, being substantially related to wave-induced motion, can be considered to happen at the normal frequencies of wave-encounter, i.e. typically $0 \div 1.3 rad/s$. As will be discussed in the next section, in these conditions, the steady-state formulae remain valid and the hydrodynamic forces can be calculated on the basis of the instantaneous velocity and angle of attack (i.e leeway angle).

6.6.4 Unsteady hydrodynamic loads

Unsteady hydrodynamic forces act on the keel as the result of rapid variations of its angle of attack. Such variations typically originate from fluctuations of the incoming flow, rigid-body motion and vibration of the keel associated with the motion of the yacht in waves. When attempting to model the dynamic behaviour of the keel structure immersed in water, it is important to model accurately these transient forces as they can translate into exciting, damping and added mass terms. From a hydrodynamic point of view, this problem is treated as the definition of the loads acting on a foil arbitrarily oscillating and deforming in an incompressible flow.

Commenting on the difficulty of this task, Blispinghoff wrote: "A complete solution calls for calculating the pressure distribution due to sudden displacements of all degrees of freedom, including whatever vibration modes are needed to describe

aeroelastic effects. In the light of existing theory, this is a practically impossible task. It is easy to understand why such loadings have been determined almost exclusively by two-dimensional strip methods." [15]. While it may be argued that, since Blispinghoff's comments, considerable progress has been made in the field of computational fluid dynamics and that, for the present case, numerical tools such as finite-volume RANS methods may for example yield very accurate solutions, the computational resources and the time required for the obtainment of these solutions make such methods inadequate for the present study. Instead, a strip method, based on the discretisation of keel fin into a series of "2D" profiles, remains computationally affordable and has therefore been applied. The following paragraphs discuss its advantages and limitations together with the details of its implementation.

A complete solution of the forces acting on a two-dimensional foil oscillating in a flow with harmonic motion, was first published by Theodorsen [125]. The schematic representation of the "2d" section adopted by this author together with the variables chosen to describe its motion are reproduced in figure 6.15 and followed in the present document. The foil is assumed to have a chord length equal to $2b$ and to be rotating about an axis placed at a distance ba aft from the mid-chord point (in the case of the keel fin sections presently under examination, this axis is actually located forward of the mid-chord point at approximately 45% of the chord length from the leading edge, thus a has a negative value).

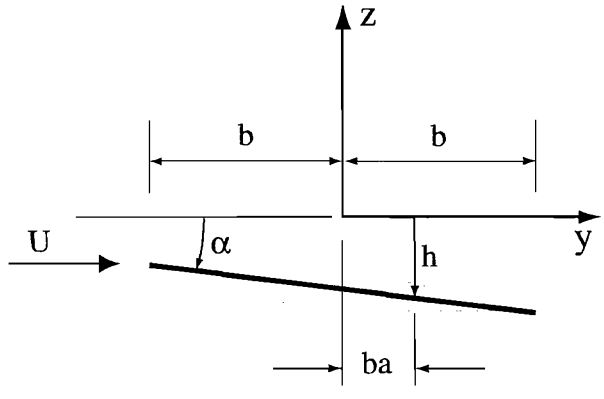

Figure 6.15: Mean line of a chordwise-rigid foil oscillating and pitching in a flow. $h(t)$ is the downward displacement of the axis ($x = ba$) of rotation, $\alpha(t)$. All quantities positive as shown. [15]

According to Theodorsen, the lift and moment acting on a two-dimensional thin foil undergoing harmonic vertical and pitching oscillations can be written as:

$$L = \pi\rho b^2 \left[\ddot{h} + U\dot{\alpha} - ba\ddot{\alpha}\right] + 2\pi\rho U\, C(k) \left[\dot{h} + U\alpha + b\,(1/2 - a)\,\dot{\alpha}\right] \tag{6.11}$$

$$M_x = \pi\rho b^2 \left[ba\ddot{h} - Ub(1/2 - a)\dot{\alpha} - b^2(1/8 + a^2)\ddot{\alpha}\right] + \\ + 2\pi\rho U b^2 (a + 1/2)\, C(k) \left[\dot{h} + U\alpha + b(1/2 - a)\dot{\alpha}\right] \tag{6.12}$$

where U is the velocity of the undisturbed incoming flow, k is the reduced frequency, defined as $\frac{\omega b}{U}$ and $C(k)$ is a complex function known as the Theodorsen function. Equation 6.11 can also be written as:

$$L = L_{QS}^{NC} + C(k) \cdot L_{QS}^{C} \tag{6.13}$$

where L_{QS}^{NC} and L_{QS}^{C} represent respectively the non-circulatory and the circulatory part of the quasi-steady lift obtained when the influence of the wake vortices is neglected.

In physical terms, the reduced frequency can be interpreted as a measure of the unsteadiness of the flow as it is proportional to the ratio of the time taken by a fluid particle to travel over the entire chord length, to the period of oscillation. L_{QS}^{NC} may be compared to an added mass term, while L_{QS}^{C} can be regarded as a damping force that tends to alter the oscillation of the foil in the fluid. Hence the Theodorsen function may be considered as a measure of how much damping is affected by the unsteadiness of the flow. This concept is further illustrated by figure 6.16 where the absolute value and the phase of $C(k)$ are plotted against the reduced frequency.

It can be noted that, for very low values of k, the Theodorsen function tends to 1, hence at small frequencies of oscillation, equation 6.11 tends to the definition of the quasi-steady lift. Conversely, as k increases, $C(k)$ gradually tends to 0.5, meaning that the hydrodynamic damping forces for high frequency vibration are reduced by a factor of two in comparison to those obtained by a quasi-steady approximation. Furthermore, for values of k greater than 0.1, the Theodorsen function can be seen to introduce a noticeable phase shift of hydrodynamic forces relative to the motion. Since the amount of energy extracted from or added to the motion is very sensitive to this phase shift, it becomes evident that unsteady effects can play a important role in altering the response of the structure.

A scale of cyclic frequencies has been plotted in figure 6.16, calculated on the basis of a forward speed of 5m/s and a half-chord length of 0.3m. These values represent

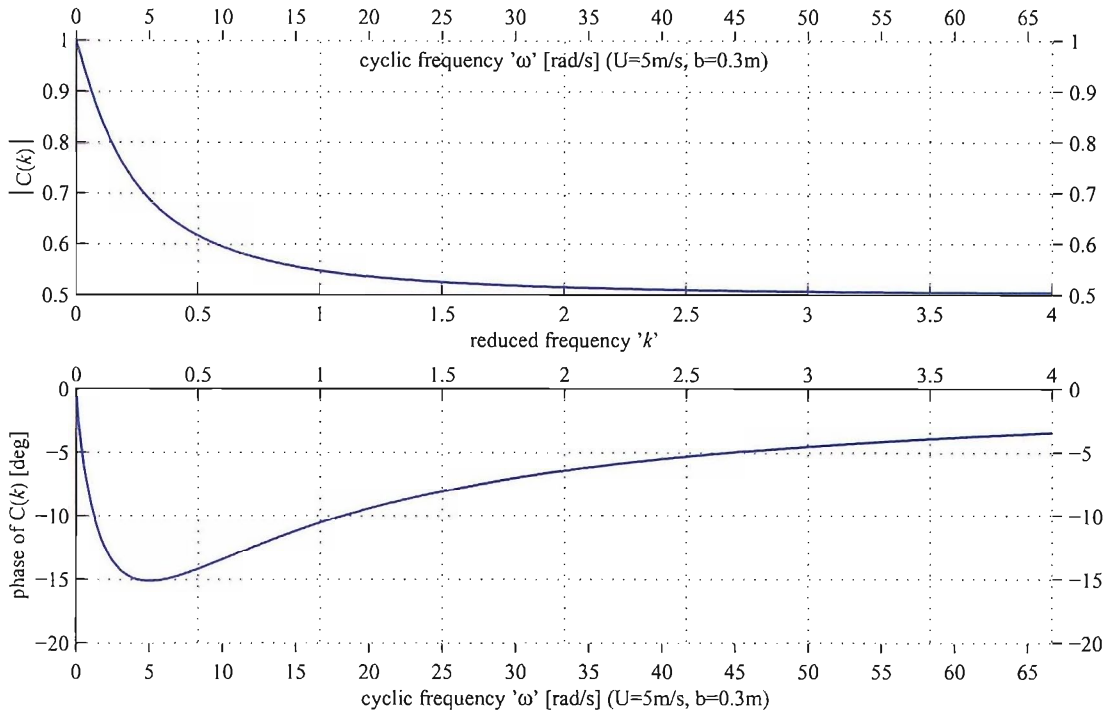

Figure 6.16: Absolute value and phase of the Theodorsen function $C(k)$. The scale of cyclic frequencies ω corresponding to reduced frequencies k is calculated on the basis of $U = 5m/s$ and $b = 0.3$.

respectively a typical upwind sailing speed and the dimensions of the section at the tip of the fin. It may be noted that, for the low-frequency components of motion typically associated with wave-encounter ($\omega = 0 \div 1.3 rad/s$), k is generally smaller than 0.08, the Theodorsen function is well approximated by one and the quasi-steady approximation is acceptable. On the other hand, at frequencies typical of the first dry bending mode of the keel ($\omega \simeq 10 rad/s$), k is equal to 0.6, the magnitude of the fluid-dynamic forces is reduced by 40% and their phase delayed by approximately 13 degrees, so the effects of unsteadiness must be accounted for.

The unsteady hydrodynamic forces acting on a two-dimensional foil undergoing arbitrary vertical and pitching oscillations, can be calculated by use of the Duhamel superposition integral. Thus, the expressions of lift and moment acting at the generic time "t" become:

$$L(t) = \pi \rho b^2 \left[\ddot{h}(t) + U\dot{\alpha}(t) - ba\ddot{\alpha}(t)\right] + L_C(t) \tag{6.14}$$

$$M(t) = \pi\rho b^2 \left[ba\ddot{h}(t) - Ub(1/2 - a)\dot{\alpha}(t) - b^2(1/8 + a^2)\ddot{\alpha}(t)\right] + b(a + 1/2)\, L_C(t) \tag{6.15}$$

with

$$L_C(t) = 2\,\pi\,\rho\,U\,b\left[\int_0^t \xi(\tau)\cdot\dot{h}(t-\tau)d\tau + U\int_0^t \xi(\tau)\cdot\alpha(t-\tau)d\tau + \right.$$
$$\left. + b(1/2-a)\int_0^t \xi(\tau)\cdot\dot{\alpha}(t-\tau)d\tau\right] \quad (6.16)$$

where $L_C(t)$ represents the instantaneous circulatory lift which is obtained by the summation of three convolution integrals. $\xi(\tau)$ is generally referred to as the impulse response function: it may be interpreted as the circulatory lift (normalised by $2\pi\rho Ub$) acting at time τ as the result of an impulse of unit magnitude of the transverse velocity $\dot{h}$ applied at time $\tau = 0$. $\xi(\tau)$ is strictly related to the Theodorsen function, and can be derived from it as shown in Appendix G.

The fundamental difference between quasi-steady approximation and the unsteady model of the fluid-dynamic loads is made apparent by equation 6.16. As a matter of fact, the former considers the loads acting at any given time to depend uniquely on the instantaneous attitude and motion of the foil at the same instant, whereas in the latter, the instantaneous loads are related to the present and past motion through the convolution integrals.

Results from equations 6.14 to 6.16 can be applied to the calculation of the unsteady hydrodynamic loads acting on the keel fin, through the use of a strip method. In particular, the fin is approximated by a series of strips in the spanwise direction: each strip is considered to have a constant chord and to be performing only a translational and angular motion (as shown in figure 6.15) resulting from the rigid-body motion and from the deformation of the whole keel.

The loads acting on the bulb are calculated separately, as if it was evolving in the flow in the absence of the rest of the keel. The bulb is treated as a non-lifting streamlined body: lift and moment are obtained from a linearised momentum method reported by [15] and they can be calculated as follows:

$$L_b = \rho K_V \nabla_b (U\dot{\alpha} + \ddot{h}) + \rho K_M \bar{M}\ddot{\alpha} \quad (6.17)$$

$$M_b = \rho U K_V \nabla_b (U\alpha + \dot{h}) - \rho K_M \bar{M}\ddot{h} - \rho K_J J_3 \ddot{\alpha} \quad (6.18)$$

where ∇_b indicates the volume of the bulb, $\bar{M}$ the volume static unbalance and J_3 the volume moment of inertia about the axis of polar symmetry. K_V, K_M and K_J. in this case, are reduction factors introduced to account for the "non-perfectly-two-dimensional"nature of the flow around the bulb when it performs translational and

rotational motion about its centre of gravity. They have been calculated on the basis of the formulae given by [12] for prolate ellipsoids; in particular, the factors have been evaluated for an ellipsoid with the same volume and maximum radius as the bulb.

The fundamental assumption behind the use of strip methods is that the loads over each strip are determined uniquely by the angle of attack and by the motion of the strip and are not influenced by the pressure distribution over the rest of the foil. This hypothesis is not verified in the limit of low reduced frequencies (i.e. quasi-steady conditions) where finite aspect ratio effects are known to affect the pressure distribution over the entire fin. With respect to the problem of the calculation of the response of the keel structure vibrating in the flow, this means that the damping associated with low-frequency components of motion is likely to be overestimated and, consequently, the amplitude of the response will be under-estimated, leading to unconservative predictions of the dynamic stresses.

A comprehensive investigation on the influence of finite span effects on the unsteady fluid-dynamic loads has been conducted by Reissner and Stevens. Their study concentrated on different types of harmonic motion, including rigid-body displacements, bending and torsion [111]. The result was a set of formulae describing the spanwise distribution of forces and moments, where the effect of three-dimensionality appears as a correction factor to the basic Theodorsen function. This correction factor is mainly a function of the aspect ratio, the reduced frequency, the location along the span and the spanwise variation of deflection (i.e. the mode shape). Reissner and Steven concluded that for large enough values of the reduced frequency, the results of two-dimensional theory could be retained as accurate: thus, as an approximative guideline, for foils with aspect ratio equal to or greater than 6, the finite span effect may be neglected for reduced frequencies larger than 1. On the other hand, for lower frequencies, the introduction of the correction factor would make the calculated lift distribution converge towards the one obtained by a steady-state lifting line theory.

With respect to the keel fin presently under study, Hoerner has shown that, in the steady-state case, the effect of wing-tip streamlined bodies such as the bulb is to modify the lift distribution, so that it may be compared with the one found on a foil with aspect ratio:

$$AR = AR_0 \left(1 + 1.9 \cdot \frac{d}{2s}\right) \tag{6.19}$$

where s and AR_0 are respectively the span and the aspect ratio of the foil with no wing-tip body, and d is the maximum diameter of the wing-tip body. For the Open60'

fins, this leads to an equivalent effective aspect ratio of 10.0 for an initial effective aspect ratio equal to 8.8. This correction translates the fact that the bulb acts to some extent as an end-plate, shifting the wing-tip vortex further away from the fin. Hence, at the tip of the fin, the flow is made closer to the two-dimensional case and the lift does not die to zero. Although no reference is made by Hoerner to unsteady conditions, Reissner and Stevens do state that in the case of harmonic oscillations, the two-dimensional nature of the flow is generally reinforced with increasing reduced frequency. Therefore it seems reasonable to assume that the lift distribution on the fin due to uniform translating and pitching motion, will always lie between the one suggested by Hoerner (for a steady-state condition where $k = 0$) and the one obtained by a two-dimensional approximation (for large values of k).

Finally, it may be noted that, if the Reissner and Stevens method is to be applied, a different correction factor should be evaluated for each mode shape and at each strip, thus requiring an extremely large number of calculations. However, it can be argued that, with an aspect ratio of 10, all the correction factors die out for reduced frequencies greater than 0.6. This implies that the unsteady loads associated with all the components of motion with frequency larger than approximately 1.2Hz, may be calculated on the basis of the original Theodorsen function and that three-dimensional corrections are relevant only for the lower frequency components of motion. These can be expected to be largely dominated by the rigid-body motions and by the first lateral bending mode. For all these modes, the correction factors are extremely close and, in particular, applying the ones associated with parabolic symmetrical bending to all modes leads to the most conservative estimates of the structural response.

In view of all the former remarks, the full procedure for the calculation of the unsteady hydrodynamic loads on the keel structure at a generic time t, may be outlined as follows:

1. Divide the fin into N strips of equal width along the span.

2. Obtain the history of the translation ($h(t) = -z(t)$) and rotation ($\alpha(t) = \theta_x(t)$) at the centre of each strip.

3. Calculate the modified Theodorsen function at each strip as from the method given by Reissner and Stevens, on the basis of the flow velocity U, the average chord of the strip $2b$, the location of the strip along the span and a parabolic symmetrical bending mode shape.

4. Calculate the impulse response functions for the hydrodynamic loads, using the method outlined in Appendix G and the modified Theodorsen functions obtained at the previous point.

5. Calculate the loads on each strip from equations 6.14, 6.15 and 6.16.

6. Calculate the loads on the bulb from equations 6.17 and 6.18.

6.7 Numerical method

The equations of motion describing the behaviour of the finite element model presented in section 6.3, may be written as:

$$[\mathbf{M}]\ddot{\mathbf{X}} + [\mathbf{R_s}]\dot{\mathbf{X}} + [\mathbf{K}_\phi]\mathbf{X} = \mathbf{F_G} + \mathbf{F_{H_s}} + \mathbf{F_{In}} + \mathbf{F_{H_{us}}} \tag{6.20}$$

where $\mathbf{X}$ indicates the vector of the nodal displacements relative to the (X_k, Y_k, Z_k) reference system, written as:

$$\begin{aligned} \mathbf{X} &= [\mathbf{X_1}, \mathbf{X_2}, \ldots, \mathbf{X_n}]^T \\ \text{with } \mathbf{X_i} &= [x_i, y_i, z_i, \theta_{x_i}, \theta_{y_i}, \theta_{z_i}] \end{aligned} \tag{6.21}$$

$[\mathbf{M}]$ represents the mass matrix, $[\mathbf{R_s}]$ the structural damping matrix, and $[\mathbf{K}_\phi]$ the stiffness matrix including the stiffening terms associated with axial pre-constraint.

$\mathbf{F_G}$ indicates the vector of the nodal loads due to the gravity force, which is obtained by multiplying the mass matrix$[\mathbf{M}]$ by a vector of nodal accelerations:

$$\begin{aligned} \mathbf{a_g} &= [\mathbf{a_{g_1}}, \mathbf{a_{g_2}}, \ldots, \mathbf{a_{g_n}}]^T \\ \text{with } \mathbf{a_{g_i}} &= [g\cos(\phi + \phi_k), 0, -g\sin(\phi + \phi_k), 0, 0, 0] \end{aligned} \tag{6.22}$$

$\mathbf{F_{H_s}}$ indicates the vector of steady (or quasi-steady) hydrodynamic forces. Considering the typical lengths of time for which the response of the keel is calculated, both the gravity and the steady hydrodynamic forces can be regarded as constant. Hence, under the assumption that keel structure behaves like a linear mechanical system, its response can be written as the sum of a static term originated by the constant external loads and of a variable term produced by the inertial force and the unsteady hydrodynamic forces. Consequently, the vector of the nodal displacements can be rewritten as:

$$\mathbf{X} = \mathbf{X_S} + \mathbf{X_D} \tag{6.23}$$

and equation 6.20 can be split as follows:

$$[\mathbf{M}]\ddot{\mathbf{X}}_\mathbf{D} + [\mathbf{R_s}]\dot{\mathbf{X}}_\mathbf{D} + [\mathbf{K}_\phi]\mathbf{X_D} = \mathbf{F_{In}} + \mathbf{F_{H_{us}}} \tag{6.24}$$

$$[\mathbf{K}_\phi]\mathbf{X_S} = \mathbf{F_G} + \mathbf{F_{H_s}} \tag{6.25}$$

For simplicity, in the following part of this discussion the vector of the nodal displacements including the static and dynamic terms will be referred to as "$\mathbf{X_T}$" and the dynamic response will be indicated simply by "$\mathbf{X}$".

The vector of the nodal loads due to the inertial forces $\mathbf{F_{In}}$ according to equation 6.5 can be obtained by multiplying the mass matrix $[\mathbf{M}]$ by a vector of nodal accelerations :

$$\begin{aligned}
\mathbf{a_{in}} &= [\mathbf{a_{in_1}}, \mathbf{a_{in_2}}, \ldots, \mathbf{a_{in_n}}]^T \\
\text{with } \mathbf{a_{in_i}} &= \mathbf{a_0} + \mathbf{a_{T_i}} + \mathbf{a_{C_i}} \\
\text{and } \mathbf{a_0} &= [a_{x_0}, a_{y_0}, a_{z_0}, \dot{\omega}_{x_0}, \dot{\omega}_{y_0}, \dot{\omega}_{z_0}] \\
\mathbf{a_{T_i}} &= [0, \dot{\omega}_{y_0}, -\dot{\omega}_{x_0}, 0, 0, 0] \times \mathbf{nc_i} \\
\mathbf{a_{C_i}} &= \left[\omega_{x_0}^2 + \omega_{y_0}^2, 0, 0, 0, 0, 0\right] \times \mathbf{nc_i}
\end{aligned} \tag{6.26}$$

where $\mathbf{a_0}$ indicates the vector of the acceleration of the boat fixed reference system relative to an earth fixed reference system and $\mathbf{nc_i}$ represents the vector of nodal coordinates relative to the (X_k, Y_k, Z_k) frame.

The vector of the unsteady hydrodynamic force $\mathbf{F_{H_{us}}}$ may also be written as $\mathbf{F_{H_{us}}}(\mathbf{X} + \mathbf{X_0}, \dot{\mathbf{X}} + \dot{\mathbf{X}}_\mathbf{0}, \ddot{\mathbf{X}} + \ddot{\mathbf{X}}_\mathbf{0}, \mathbf{U})$ where $\mathbf{X_0}$ represents the vector of the displacements of the yacht relative to the fixed axes reference system. It can be seen from equations 6.14 and 6.15 that the terms depending on acceleration, are only a function of the instantaneous values of $\ddot{h}$ and $\ddot{\alpha}$, hence it is customary to consider these components of the hydrodynamic forces as added mass terms and to lump them with the mass matrix and with the inertial forces vector. An added mass matrix M_A can be formed accordingly as shown in appendix F.2. Similarly, the terms of equations 6.14 and 6.15 which depend only on the instantaneous values of the lateral and angular velocities $\dot{h}$ and $\dot{\alpha}$ can be regarded as linear damping terms and are thus condensed into an hydrodynamic damping matrix $[\mathbf{R_H}]$. Further details about the way $[\mathbf{R_S}]$ and $[\mathbf{R_H}]$ are assembled, are given in appendix F.2. Equation 6.24 can then be rewritten

as:

$$([\mathbf{M}] + [\mathbf{M_A}])\ddot{\mathbf{X}} + ([\mathbf{R_S}] + [\mathbf{R_H}])\dot{\mathbf{X}} + [\mathbf{K}_\phi]\mathbf{X} = ([\mathbf{M}] + [\mathbf{M_A}])\mathbf{a_{in}} + \tilde{\mathbf{F}}_{\mathbf{H_{us}}}(\mathbf{X} + \mathbf{X_0}, \dot{\mathbf{X}} + \dot{\mathbf{X}}_\mathbf{0}, U) \quad (6.27)$$

where the remaining components of the unsteady force $\tilde{\mathbf{F}}_{\mathbf{H_{us}}}(\mathbf{X} + \mathbf{X_0}, \dot{\mathbf{X}} + \dot{\mathbf{X}}_\mathbf{0}, U)$ are calculated by the procedure outlined at the end of section 6.6.4. In particular, the fin is divided into strips centred on each node and the resulting forces and moments are considered to be applied at the nodes.

Equation 6.27 may be rewritten in terms of the modal coordinates $\mathbf{Q}$ which can be expressed as:

$$\mathbf{Q} = [\Phi]\,\mathbf{X} \quad (6.28)$$

where $[\Phi]$ represents the matrix of the modal shapes obtained by solving the eigenvalue problem:

$$-\omega^2([\mathbf{M}] + [\mathbf{M_A}]) + [\mathbf{K}_\phi]\mathbf{X} = [0] \quad (6.29)$$

By introducing respectively the generalised mass, damping and stiffness matrices $[\hat{\mathbf{M}}] = [\mathbf{\Phi}]^\mathbf{T}[\mathbf{M} + \mathbf{M_A}][\mathbf{\Phi}]$, $[\hat{\mathbf{R}}] = [\mathbf{\Phi}]^\mathbf{T}[\mathbf{R_S} + \mathbf{R_H}][\mathbf{\Phi}]$ and $[\hat{\mathbf{K}}] = [\mathbf{\Phi}]^\mathbf{T}[\mathbf{K}_\phi][\mathbf{\Phi}]$, equation 6.27 becomes:

$$[\hat{\mathbf{M}}]\ddot{\mathbf{Q}} + [\hat{\mathbf{R}}]\dot{\mathbf{Q}} + [\hat{\mathbf{K}}]\mathbf{Q} = [\mathbf{\Phi}]^\mathbf{T}\left(([\mathbf{M}] + [\mathbf{M_A}])\,\mathbf{a_{in}} + \tilde{\mathbf{F}}_{\mathbf{H_{us}}}([\mathbf{\Phi}]^{-1}\mathbf{Q} + \mathbf{X_0}, [\mathbf{\Phi}]^{-1}\dot{\mathbf{Q}} + \dot{\mathbf{X}}_\mathbf{0}, \mathbf{U})\right) \quad (6.30)$$

It may be noted that, while $[\hat{\mathbf{M}}]$ and $[\hat{\mathbf{K}}]$ are diagonal matrices, $[\hat{\mathbf{R}}]$ is not, hence the modal equations expressed by 6.30 are coupled by the generalised damping forces. Moreover, the unsteady hydrodynamic forces $\tilde{\mathbf{F}}_{\mathbf{H_{us}}}$ can be regarded as a combination of nonlinear coupled damping and restoring terms. Consequently, the response of the system must be obtained by integrating equation 6.30 through a numerical time stepping method. To this end, a new variable is introduced in the form of:

$$\mathbf{Y(t)} = \begin{bmatrix} \dot{\mathbf{Q}}(\mathbf{t}) \\ \hline \mathbf{Q(t)} \end{bmatrix} \quad (6.31)$$

Equation 6.30 can then be rewritten as:

$$\dot{\mathbf{Y}}(\mathbf{t}) + [\mathbf{G}]\mathbf{Y}(\mathbf{t}) = \mathbf{H}(\mathbf{t}) \quad (6.32)$$

with:

$$[\mathbf{G}] = \left[\begin{array}{c|c} [\hat{\mathbf{M}}]^{-1}[\hat{\mathbf{R}}] & [\hat{\mathbf{M}}]^{-1}[\hat{\mathbf{K}}] \\ \hline -[\mathbf{I}] & [\mathbf{0}] \end{array}\right] \quad \text{and} \quad \mathbf{H(t)} = \left[\begin{array}{c} [\hat{\mathbf{M}}]^{-1}\hat{\mathbf{F}}(\mathbf{t}) \\ \hline [\mathbf{0}] \end{array}\right] \tag{6.33}$$

and:

$$\hat{\mathbf{F}}(\mathbf{t}) = [\mathbf{\Phi}]^{\mathbf{T}} \left(([\mathbf{M}] + [\mathbf{M_A}])\, \mathbf{a_{in}(t)} + \tilde{\mathbf{F}}_{\mathbf{H_{us}}}([\mathbf{\Phi}]^{-1}\mathbf{Q(t)} + \mathbf{X_0(t)}, [\mathbf{\Phi}]^{-1}\dot{\mathbf{Q}}(\mathbf{t}) + \dot{\mathbf{X}}_{\mathbf{0}}(\mathbf{t}), \mathbf{U}) \right) \tag{6.34}$$

Equation 6.32 can be regarded as an initial value problem of the form:

$$\begin{cases} x' = f(t, x) \\ x(t_0) = x_0 \end{cases} \tag{6.35}$$

which in the present study has been solved by a fourth order Adams-Moulton method. Further details about the implementation of this standard numerical algorithm can be found in [79] and [82].

6.8 Theoretical Shock Spectra for the keel of an Open60'

The graphs in figure 6.17 and 6.18 represent the theoretical shock spectra of the keel of an Open60' for a transient lateral load. More precisely, the load consists of a single localised force acting at the centre of gravity of the bulb along a direction perpendicular to the neutral axis of the keel fin. Its magnitude varies in time like a "half-cycle sine" wave (cf. inset of figure 6.17).

The maximum magnitude F_0 is fixed and equivalent to the weight force of the bulb (i.e. $m_{bulb} \cdot g$, $32362N$ in the present case). The different curves are obtained by calculating the ratio of the maximum amplitude of the response (i.e. $maximax F_z^{dyn}$) for transient loads of different duration t_1, to the amplitude of the response for a static load of magnitude F_0 (i.e. $max F_z^{QS}$).

The response of the keel structure is considered respectively in terms of the resultant lateral shear force (F_z) and lateral bending moment (M_y) acting at the root of the keel fin. Effectively, $max F_z^{QS}$ has magnitude F_0 and $max M_y^{QS}$ has magnitude $F_0 \cdot l_{fin}$ where l_{fin} indicates the distance between the root of the fin and the axis of symmetry of the bulb.

Different configurations are considered:

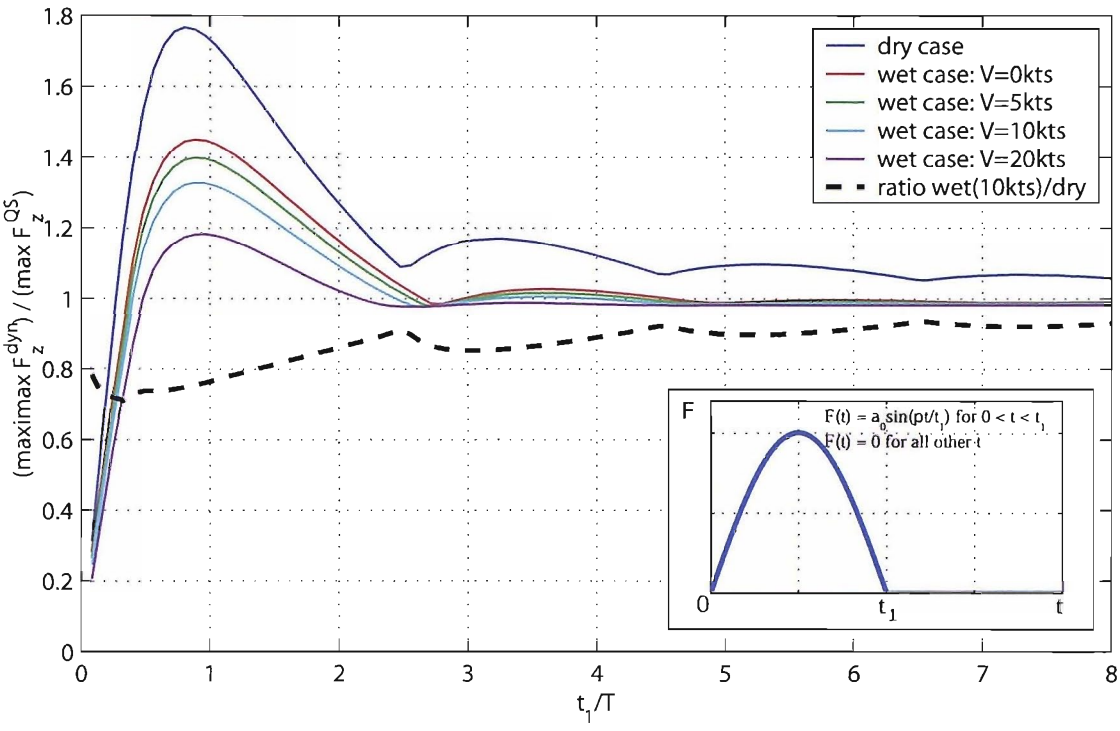

Figure 6.17: Open60' keel theoretical shock spectra: shear force at fin root.

- the "dry" case corresponds to the keel vibrating "in vacuo" (only structural damping applies);
- the "wet" cases correspond to the keel vibrating in water with different inflow velocities (0, 5, 10, 20 kts). In these configurations, hydrodynamic added mass and damping effects both alter the phase and the magnitude of the dynamic response.

A further curve (black dotted line) indicates the ratio of the shock spectrum for the $10kts$ wet case to the one for the dry case. It can be regarded as an example of the attenuation factor linked with the hydrodynamic effects.

It can be noted that:

- the curves are obtained with a linear finite element model (6dof/node Euler beam elements); only rotation around the boat longitudinal and transversal axes are allowed at the node representing the root of the fin; the constraint applied by the keel-hull joint is then modelled through two rotary springs. Results are obtained by modal decomposition and only the first 6 natural modes of the structure are retained for the calculations

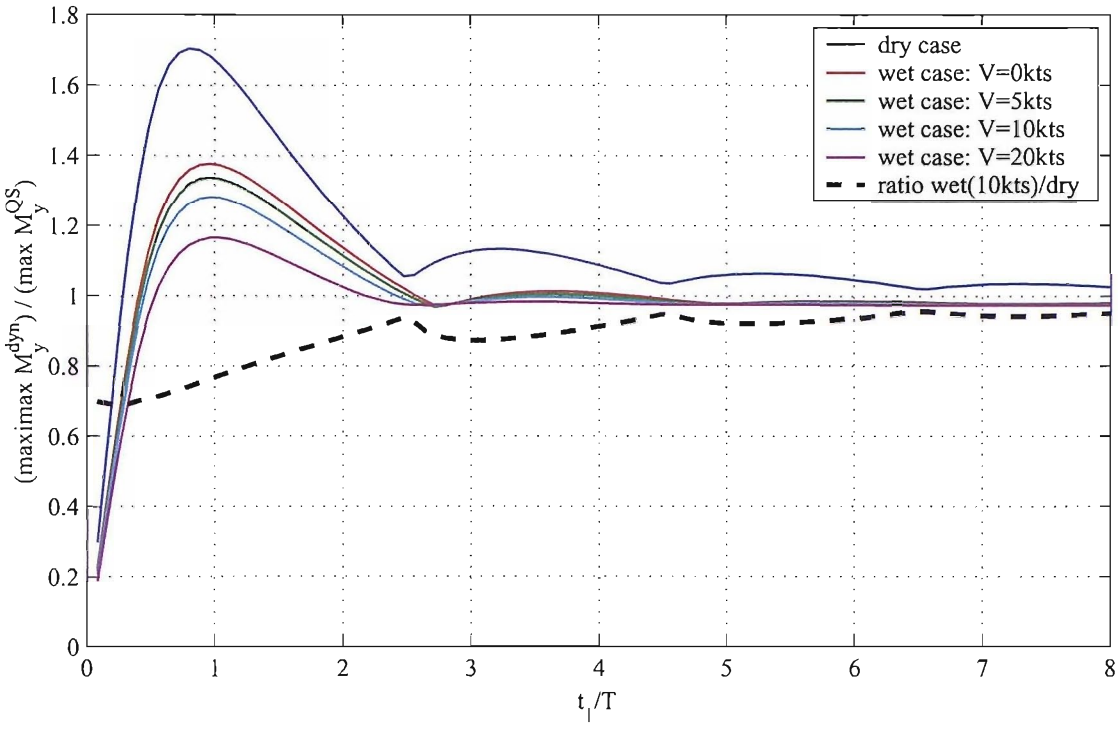

Figure 6.18: Open60' keel theoretical shock spectra: bending moment at fin root.

- on the horizontal axis, the pulse duration t1 is non-dimensionalised by the natural period T of the 1st dry lateral bending mode of the keel (i.e. $1.60Hz$ in vacuo). It appears then that the highest dynamic amplification occurs for pulse durations between 0.8 and 1 times the dry natural period.

- It has been shown (cf. [53]) that for $t_1 < T$, the curve of the maximax response is relatively insensitive to the pulse shape, that is, the same dynamic amplification occurs for rectangular and "versed-sine" pulses.

6.9 Summary

A numerical model has been implemented to evaluate the amplitude of the dynamic response of the keel of a yacht subject to transient inertial and hydrodynamic loads. The structural deformations and internal stresses of the keel of an Open60' have been calculated by a finite element model, which has been calibrated against the results of full scale modal tests. The different components of the transient forces normally acting on a keel have been considered, and particular attention has been given to the modelling of the unsteady hydrodynamic loads associated with the keel vibration in

water.

Theoretical shock spectra have been calculated for the keel of an Open60' sailing at a range of different speeds. These have shown that dynamic amplification factors of up to 1.45 may be observed for the response to a transient excitation with a typical "half-cycle sine" profile.

Finally, the method has been used successfully to calculate the internal forces and moments and the deflections of the keel of an Open60' from recorded time histories of motion (cf. 3.6).

Chapter 7

Conclusion

In a landscape of constantly increasing performance, with sailing boats now able to maintain average speeds which a few years ago were achieved only by high-performance power craft, dynamic loads have become a subject of both concern and great interest for the yacht design community. Articles can often be found in the specialised press quoting structural failures which - they claim - may possibly be avoided if dynamic phenomena were better understood. For lack of reliable alternatives, structural designers, while equipped with very powerful computational tools and better and better understanding of the behaviour of advanced composite materials, still tend to rely on the laws of statics and on outdated empirical data when studying problems that are of a fundamentally dynamic nature.

With this situation in mind, the aim of the present study was to help make some progress in the knowledge of both dynamic loads and how sailing yacht structures may respond to them. In particular, in collaboration of Groupe Finot Naval Architects, a design office with an outstanding record in the field of offshore racing yachts, two key areas of investigation were identified: hydrodynamic slamming loads and the response of the keel structure to transient inertial loads.

Having identified the lack of pertinent experimental data as one the major issues to be addressed, the first part of the study focused on producing a data acquisition system that could be used to carry out measurements on offshore racing yachts while they are subject to the most severe loadings. The system was later successfully implemented and used to make recordings on several boats during long oceanic passages. A multitude of data were gathered describing both the spectra of encountered conditions and the resulting motion of the vessels. In particular, values of acceleration were

accurately measured. These data proved extremely useful in evaluating the magnitude of inertial loads which can be critical for the keel structure. Measurements of the vessel attitude and motion velocity while undergoing hydrodynamic impact could equally be obtained in a large number of occasions, thus providing a solid statistical base for studying both the magnitude and frequency of occurrence of slamming loads.

While experimental data were being gathered autonomously by data acquisition systems fitted on different boats, a better understanding of the hydro-elastic phenomena involved with slamming was equally sought. For this, scaled models of offshore sailing yachts were used to carry out investigations in controlled laboratory conditions. Pressures affecting hull panels and the factors that influence them were measured by use of "slam patches". This provided not only a better understanding of the physical phenomena involved with water impact, but also a reliable reference for testing predictions from analytical models.

With the new knowledge acquired from both full scale and model scale tests, an attempt was made at devising a method for predicting structural response to slamming loads, that would be sufficiently simple for being used as a design tool and yet still capable of accounting for complex features like hydro-elastic phenomena. The result of this work has been presented in chapter 5. While the outlined method relies on many important simplifying hypotheses, it achieves particularly good correlation with experimental data measured for some standard water impact problems. With respect to being implemented as a design tool, it is felt that results from the method may not be trusted to be quantitatively accurate, partly due the uncertainties that affect some of the input parameters. However, thanks to its capacity to correctly model the influence of different parameters affecting slamming loads and response, it may safely be used for comparing the ability of different structures to perform when subject to slamming.

Finally, the last part of the study concentrated on the response of keel structures to inertial loads initiated by slamming. Again, an analytical model was developed and validated by performing experimental measurements on an Open60' type yacht. The model was then implemented to derive estimates of the internal loads seen by the keel structure of the same yacht during a round-the-world race. This provided the author with extremely valuable insight into the load levels experienced by this item and, more generally, into the ways in which standard design parameters may affect its dynamic behaviour.

In conclusion, it is believed that, while considerable progress in the knowledge of complex dynamic phenomena affecting sailing yacht structures still remains to be made (and indeed should be pursued), the present investigation has been successful in advancing the understanding of some of the main issues involved. The extremely large quantity of experimental data gathered has not only allowed to validate some new hypotheses, but it will remain as a very valuable reference for many further studies on this most interesting subject.

7.1 Further Work

With the data acquisition system having been validated as a reliable and useful tool, it is believed that further series of measurements should be performed on a wider variety of boats. The aim should be to obtain a wider data base that could allow empirical relations between environmental conditions and yacht characteristics and slamming to be more easily identified. Besides, measurements on more common cruising yachts would allow to clearly define the implications of different service characteristics.

Since the data acquisition has been designed and assembled, technology has considerably improved. As a result, it is envisaged that, for the same updated cost of the initial system, new equipment could be used now that would allow better accuracy to be obtained, and virtually continuous time-history acquisition of several variables to be performed for several weeks in a row.

Slam patch tests have equally proven to be a reliable and cost effective tool for acquiring knowledge of slamming pressures. The present study has left questions relating to the scaling of air-cushioning effects open for further investigation. Further verifications of the analytical model outlined in chapter 5 should be performed by experimenting with different types of slam patches (e.g. variable mass, stiffness, geometry, etc.). A more realistic scaled version of a hull panel may be built on larger scale models, which are becoming more and more common in high-profile applications like the America's Cup and the Volvo Ocean Race.

Considerable progress remains to be made in terms of understanding the statistical nature of slamming events and of the associated loads. Better knowledge of the probability of occurrence of given slamming loads would allow not only safety factors to be more clearly evaluated but also the fatigue life of structures exposed to slamming to be estimated.

The work performed on the keel response may be improved by adopting a more accurate (and more complex) hydrodynamic model. Besides, direct measurements of internal loads may be performed to validate the approach. The model should be validated for canting keel configurations. Together with the above mentioned study on the statistics of slamming, this part of the work could then be applied to further full scale measurements to investigate long term fatigue problems.

APPENDICES

Appendix A

Design and implementation of a data acquisition system for full-scale measurements

A.1 Overview

A data acquisition system has been designed and implemented with the aim of performing measurements that help improve the knowledge of dynamic loads experienced by Open60' yachts. The present report describes its main characteristics as well as the considerations involved with its design.

A.2 Approaches to the measurement of slamming loads

The hydrodynamic loads acting on the hull as the result of slamming are the main subject of the present study. Different approaches can be taken to the measurement of slamming loads. To each approach, correspond different physical variables to be recorded and hence different sensors and data logging equipment. This concept is further illustrated by figure A.1. Direct measurement of the hydrodynamic loads can be obtained only through pressure measurement devices (usually pressure transducers). Yet, for practical reasons, it is rarely possible to use these sensors. Hence, slamming loads are most often obtained by "indirect" measurement, that is, by recording either

the cause of loads or their effect.

The former approach, requires accurate knowledge of the water impact phenomenon: slamming loads are then normally deduced from such variables as the attitude and the velocity of the hull relative to the water at the time of impact.

The latter approach consists of determining the slamming pressures by observing either the deflections, the strains or the acceleration they induce in the structure of the boat. In particular, it relies on the assumption that there is a biunivocal correspondence between the loads and their effects. In general, this is not verified as, for instance, the same maximum hull panel deflection can be produced by different pressure distributions. However, the loads obtained by this approach can be regarded as equivalent loads (i.e. loads that have the same effect as the actual ones) and thus represent useful information for design purposes.

From a scientific point of view, the best option would be indeed to record all the variables shown in figure A.1. However, the choice is almost always limited by practical considerations. The implications related with the use of different types of sensors are reviewed in detail in the following sections.

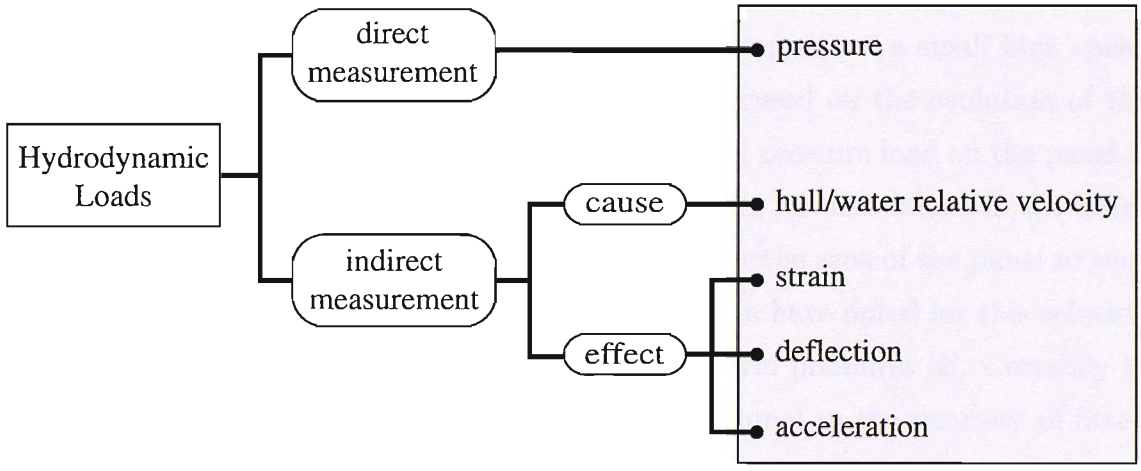

Figure A.1: Approaches to the measurement of slamming loads

A.3 Review of available technical solutions

Different types of sensors in different combinations can be used to investigate slamming loads. The aspects involved with their application are discussed in the following sections.

A.3.1 Pressure transducers

Pressure transducers are the only sensors that can provide a direct measurement of the hydrodynamic pressures acting on the hull of a vessel. Several experiments have reported using them on different types of vessels with differing results. The main aspects related to their use appear to be:

- The need for a dense array of sensors: during a slam the pressure distribution on the wetted part of the hull is highly non-uniform. Since pressure transducers provide a very local measurement (the size of their sensing element usually being of the order of a few square millimetres), the profile of the pressure distribution over a hull panel or a structural reinforcement can only be obtained by interpolating simultaneous readings from several sensors distributed over its surface. Heller and Jasper have reported results from experiments on a motor torpedo boat where four pressure transducers were placed along a girth of 2.43 metres at several stations [59]. From these, transversal and longitudinal pressure distributions have been deduced at different time steps. More recently, Rosen et al. obtained a better definition of the evolution of the pressure front by mounting the sensors with a spacing of only $250mm$ on one panel of a small high speed craft [114, 115]. Whether attention should be focused on the evolution of the pressure front or whether knowledge of the overall pressure load on the panel is sufficient for design purposes is a subject still open for discussion. In the latter case the sensors need to be evenly distributed over the area of the panel so that a spatial average can be deduced. Allen and Jones have opted for this solution in their experiments to calculate equivalent uniform pressures [2]. Certainly in both cases the precision of the results is proportional to the quantity of fitted transducers. However, as there generally is a practical limit to the number of sensors that can be installed and monitored, a compromise always needs to be found between the density of the measurement points and the size of the area to be examined.

- The variability of the measurements: for a given vessel sailing at a constant speed with a constant heading through an irregular sea, every slam produces a slightly different pressure distribution. This is due to the infinite number of combinations of hull attitudes (i.e. heel, trim and yaw), hull instantaneous velocities and wave profiles that a slam can result from. Hence, pressure at

a given position on the hull can only be measured in terms of a statistical distribution. For a sailing yacht, this distribution will depend on the sea state, on the sailing conditions and particularly on the heel angle. Therefore, if a representative sample is to be obtained, measurements need to be taken over long periods of time .

- The large quantity of data: the extremely fast nature of the pressure variations during a slam requires high sampling rates to be used. Recently Rosen et al. have used a sampling frequency of $2kHz$ in their full scale tests, but tests performed by Wraith on a model [137] have shown that this may not be sufficient, as pressure rise times can be shorter than 1 millisecond [1]. Such high sampling frequencies call for large data storage capacities and automatically triggered acquisitions on systems using a buffer memory. This solution allows data to be recorded from the time preceding the triggering event (pressure going above a set threshold) and avoids the problems typical of continuous or manually triggered acquisitions.

- The limited availability of boats for testing: due to the fact that holes have to be made through the hull for the pressure transducers, it is generally difficult to find boats available for these sensors to be fitted. Only two cases have been found in the literature of researchers instrumenting sailing yachts with pressure transducers (Reichard [110] and Hentinen et al. [61]). In both cases the tests were carried out on laboratory boats specially made in view of the measurements.

  Pressure transducers are used most often in conjunction with other types of sensors (generally accelerometers). It is very difficult to characterise a slam by examining only pressure recordings; in fact, since the measurements are generally taken over a limited area, a slam can even occur without any significant pressure rise over the instrumented portion.

[1] Wraith used a sampling frequency of 100KHz. It should be noted that, effectively, a pressure transducer provides an average value of the pressure over its sensing element. Thus, except in the ideal case of the free surface being perfectly parallel to the sensing element, the rise time is always inversely proportional to the area of the sensing element.

A.3.2 Strain gauges

Strain gauges can provide an indication of the response of the structure to exterior loads. The loads may be determined if their relation to the deformations is known, either through analytical models or as the result of an experimental calibration process. This is for instance the case of rigging screws which are subject to a pure tension load: a measurement of the axial deformation will give a rather precise indication of the load, provided the material properties are known. The problem is a lot more complex when considering the hull and distributed loads such as hydrostatic and hydrodynamic pressures. In practice, it is impossible to determine the pressure distribution over a hull panel by measuring only its deformation. Nevertheless, an equivalent pressure distribution can be identified which would generate a deformation similar to the one measured. This is typically the case with slamming loads (i.e. transient hydrodynamic loads): given the complexity and the variety of pressure distributions that result from slamming, researchers tend to define equivalent uniform static pressures which, if applied in a static or quasi-static way to the panel, will produce the same stresses or deformations that are experienced in reality. In this respect, strain measurements can provide useful information for the study of the response to dynamic loads on the hull and, indeed, some researchers have adopted this technique (cf. [45, 56, 108, 115]). Besides, the comparison of the measured deformation with the maximum allowable ones can always provide an indication of the performance of the structure under examination relative to given operational conditions.

With respect to hydrodynamic loads, strain gauges of different types have been used to investigate the response of primary and secondary structural elements. On large vessels, long-base strain gauges have been adopted to measure main girder and deck deformation [66]: these particular sensors are based on displacement transducers, measuring the relative displacement of two points belonging to the same structural element. More common electrical resistance strain gauges are generally used to investigate deformation of elements such as pillars, frames, stringers and hull panels. This type of measurements is more typical of small craft like common offshore sailing yachts, where secondary stresses are the main area of concern.

Like pressure transducers, strain gauges provide a very local measurement, therefore several sensors are needed to measure the deformation of an entire structural element. For a hull panel, for example, an external pressure load gives rise to a

combination of in-plane and bending stresses. The exact distribution of strain is a function of the boundary conditions: depending on the amount of rotation that is allowed at the edges, the highest bending moments appear in the middle of or close to the edges of the panel. As, in general, the boundary conditions are difficult to determine a priori, strain gauges must be fitted both at the edges and at mid-span of the panel. Besides, it is important to have them fitted on both sides of the panel in order to be able to determine the proportion of strain attributable to bending and that to membrane stresses [22]. From a practical point of view this constitutes a problem, as electrical wires need to be lead through the hull to the gauges on the exterior side. Indeed, of all the authors that reported strain measurements on hull panels of small craft, only Hayman et al. [57] appear to have performed tests with gauges on both sides. Their measurements were taken on a coastal rescue craft with a GRP sandwich hull. In the same occasion shear gages were mounted in the core to investigate core shear deformation. To the best of the author's knowledge, only Reichard [110] and Hentinen et al. [61] have published details about measurements of strain on sailing yacht hulls. Reichard instrumented one panel with four strain gauges, all placed on the inner side: the data shown appear to be very noisy with a dominant frequency that the author interpreted as the first natural frequency of the panel. Hentinen et al. also reported having fitted strain gauges on panels in the bow, but no results where presented from these measurements. Interestingly they also obtained the total force on a stringer by subtracting the shear forces measured with two shear gauges fitted at each end of the web laminate.

The use of electrical resistance strain gauges onboard sailing yachts may be found to be impractical due to the following issues:

- Complexity of the wiring: every strain gauge needs a dedicated amplifier which must be placed in the vicinity of the gauge itself.

- Sensitivity to electro-magnetic interference: a large number of sources of electro-magnetic interference can be found on board common vessels (e.g. VHF and SSB radio transmitters, radars, long unscreened electric wires, computers, etc.). Every gauge then needs to be carefully screened together with its wiring.

- Sensitivity to temperature changes: the temperature of the hull is likely to change in relation with the temperature of the water. For long term measurements, where considerable changes in sea water temperature can be expected.

additional gauges must be put in contact with the structure to provide temperature compensation.

- Fragility and susceptibility to humidity: particular care needs to be taken in protecting and water-proofing the gauges and their wiring, specially when the area where they are placed is directly exposed to contact with sea water or movable objects (both conditions being often verified in the case of hull bottoms).

Electrical resistance strain gauges are more commonly used on sailing yachts to measure local deformations of components like rudder stocks, keel attachments, rigging and deck hardware. Details from these measurements, however, are nearly always kept confidential. The only published results that could be found were obtained by Keuning et al. [77] who successfully instrumented rigging screws to obtain measurements of the average and transient loads in the lower shrouds.

A.3.3 Alternative sensors for strain and deflection measurements

Two main alternatives can be considered for strain and deflection measurements.

The first has been proposed by Campbell [22] and it involves the use of displacement transducers to measure the inward deflection of hull panels. These sensors can be extremely reliable and accurate and they present the main advantage of not requiring any holes to be made in the hull. The problem persists, however, of finding a suitable reference point for the measurements. In this respect, it could be envisaged to support the transducers with a rigid structure anchored to stiffer structural elements like bulkheads, ring frames and longitudinal stiffeners. While this structure could be built to be sufficiently stiff in order not to deform under the effect of inertial loads, it is arguable that the deflection of the main structural components to which it is attached may not be neglected. Besides, due to its weight and to its distance from the centre of gravity of the boat, this arrangement would not be accepted onboard a yacht during a race.

From the point of view of assessing the external pressure loads, there are some difficulties which make this solution not suitable to be applied on and Open60'. To begin with, external loads can be deduced either by comparing the measured deflections with predictions from structural calculations or by calibrating the displacements

against known pressures. In the first case, the quality of the results would be subject to the ability of the analytical model to accurately reproduce the behaviour of the actual structure and the nature of the loads. In the second, it would be necessary to build a device that could allow uniform pressures to be statically applied to the hull on an area at least as wide as one panel. This would be quite a complex and expensive task considering the magnitude of the forces that a similar test would have to produce.

Furthermore, it should be noted that the amplitude of deflection of hull panels cannot be expected to be a function of the external pressure only. As a matter of fact, in so far as external pressure loads are reacted to by membrane (in-plane) forces, deflections will be a function of the pre-stress in the panels (i.e. of the traction/compression generated by variable rig loads and global hydrodynamic loads) as well as of the actual perpendicular load.

The second alternative to electrical strain gauges is the use of Bragg grating strain sensors. These present the advantage of being totally immune to electromagnetic interference and corrosion. As a relatively young technology, Bragg gratings have only started to be applied in the marine field in the last five years. Recently Wang et al. [134] and Jensen et al. [71] have shown promising results in relation to monitoring strains in the primary and secondary structure of an FRP fast patrol boat. So far, the main limitations in view of an application on sailing yachts appear to be the size and the cost of the electronic equipment that is needed to process and acquire the optic signals from the sensors. Both elements though can be expected to improve significantly in the next years, making this technology a very good candidate for application in the near future.

A.3.4 Accelerometers

Accelerometers can be used to measure the acceleration related to the rigid-body motion of a boat as well as to the vibration induced by transient loads.

Heller et al. [59] and Allen et al. [2] have proposed semi-empirical methods to derive slamming pressures from maximum values of acceleration measured at the centre of gravity of the vessel. These have been widely used for designing the internal structure of planing craft and, in fact, served as a basis for the rules published by several different classification societies (cf. for instance [4, 34, 35, 38, 54, 70, 89]). As

a result, several authors have attempted to measure rigid-body acceleration on all kinds of vessels, primarily to verify that their actual behaviour was compatible with the assumptions made at the design stage (cf. [61,66,87,110,115]).

On power boats, most researchers have performed acceleration measurements with only two accelerometers, placed respectively at the vessel longitudinal centre of gravity, and in the bow area, and measuring along the vessel vertical axis z: theoretically, this configuration allows the heave (linear) and pitching (rotary) acceleration to be obtained, since power craft usually have small running roll and trim angles.

On sailing vessels, slamming can induce large transversal and longitudinal acceleration, hence measurements are to be carried out along all six degrees of freedom. This requires at least six accelerometers to be fitted around the vessel as shown for instance in figure A.2.

An accelerometer fixed to the boat structure will respond to the deceleration of the whole vessel as well as to the vibrations induced by each slam. Furthermore, "dc" type sensors react to changes of heel and trim of the vessel [22]. When analysing acceleration recordings it is then extremely important to separate the components of the signals associated with linear and rotational rigid-body motion from those related to deformation of the structure. This can be done by examining the frequency spectra of the recordings and by comparing the response of several sensors placed at different locations within the vessel.

Finally, the full set of data describing the motion of a boat in six degrees of freedom can be obtained by the use of accelerometers [86,92,99]. When studying slamming, this is particularly interesting as it provides information about the attitude of the yacht at the time of impact (e.g. heel and trim angle) and about its velocity.

From a practical point of view, accelerometers are reliable instruments and straight forward to install. They can be obtained from several manufacturers in a variety of configurations, including water-proof and ruggedised versions. Also, many piezo-resistive type sensors offer integral thermal compensation and signal amplification, which reduce considerably the need for frequent re-calibration and the number of different components in the data acquisition system.

A.4 Design brief for the data acquisition system

The design brief for a data acquisition system has been established by considering the requirements of Groupe Finot Naval Architects and of the skippers likely to accept the system on their yacht, and by analysing the environmental conditions typically present onboard offshore sailing yachts.

Groupe Finot has required an investigation of the dynamic loads experienced by offshore sailing yachts in the long term. Particular importance has been attached to the measurement of slamming loads. It has been agreed that a data acquisition system should be implemented to measure the magnitude and the frequency of these loads. Ideally the areas of the hull that are affected the most by slamming loads should also be identified.

The data acquisition system should be suitable for a series of measurements to be performed over long offshore passages and, ultimately, during the Vendée Globe Challenge, a non-stop single-handed race around the world for Open'50 and Open'60 class boats.

As a result, the following characteristics were required for all the components of the system:

- **Reliability** - The system should be able to work continuously for up to 2500 hours. Over this length of time, no human intervention should be required neither for re-calibration nor for repair.
- **Ruggedness** - The system should not be affected by the following elements:
  - **Humidity** - All the components that would not be installed in the main compartment of the boat, would be waterproof. The others would need to be splash-proof and resistant to condensation. All the cables and connectors would be waterproof.
  - **Mechanical loads** - The system should tolerate single acceleration of up to 15g (10 ms half sine) and vibration of 1g RMS at 1000Hz. These limits were established to be in excess of the maximum possible impact acceleration experienced by the main structural components of the boat and of the largest vibration generated by the engine. All connectors should be designed to avoid unintentional disconnection through shock, vibration and cable pull.

  - **Power supply instability** - The system should tolerate power supply failures of up to two hours. During these interruptions, it should reduce or suspend its activity. All functions should be resumed to a normal state after every power supply failure.
  - **Temperature changes** The system should function normally in ambient temperatures ranging between -10^0C and $+40^0$C.
  - **Electro-magnetic interference** - Neither the system nor the quality of the recorded data should be affected by interference from any of the on-board radio-transmitters (VHF radio, single-side band radio, satellite communication devices, radar antenna) or from any other electronic device. This condition would result in the system being completely screened and would then also ensure that the system itself would not affect the performance of the above mentioned devices.

- **Weight** - The weight of the system should be kept down to a minimum in order not to affect the performance of the host boat during races. A weight limit of 3kg was established.

- **Power consumption** - Open class boats mainly rely on the onboard diesel engine or on dedicated generators to produce electric power (which is stored in 12V or 24V batteries). Electric power consumption then translates into diesel fuel that needs to be carried onboard to produce it and should therefore be minimised. As a criterion, it was established that the power consumption of the data acquisition system should not be greater than 2% of the average total power consumption of all the onboard instruments.

- **Data storage capacity** - Permanent data storage capacity should be sufficient to allow recordings to be taken over 100 days.

- **Autonomy** - The system should not require any attention by any of the onboard crew while the boat is sailing. The acquisition should therefore be programmed and started before the boat leaves port and it should be carried out until the boat comes back to port. No manual triggering, calibration, system check or data download would be required while the boat is at sea.

Finally, Groupe Finot asked for the cost of the data acquisition system to be less than 100.000 French Francs.

A.4.1 Description of the equipment

In view of the requirements outlined in the previous section, the choice has been made to implement a data acquisition system made of an autonomous programmable logging unit and of seven accelerometers.

The chosen accelerometers are brand "IC Sensors" model #3140: these are piezoresistive type sensors, with internal temperature compensation, signal conditioning and very low long-term zero-level drift. Although, piezoelectric type sensors are often preferred for applications involving impacts, piezoresistive sensors have been adopted for their ability to measure constant and extremely low frequency accelerations. With resonant frequencies above 850 Hz, their linear response bandwidth was considered to be sufficiently wide for the projected application. Internal temperature compensation and low drift are extremely important to avoid the need for frequent calibration. Internal signal amplification allows the number of components in the system to be reduced by avoiding the need for external amplifiers, and guarantees an acceptable signal-to-noise ratio, even with considerable lengths of cable. Three different manufacturers were found offering sensors with equivalent specifications: the final choice was based on the best compromise between cost and performance. Two different ranges of measurement are used: $\pm 5g$ and $\pm 10g$. The detailed specifications of the sensors are listed in table A.1.

Table A.1: Specifications of the accelerometers

Parameter	**Range**	
	$\pm 5g$	$\pm 10g$
Mounted resonant frequency	850 Hz	1200 Hz
Sensitivity	400mV/g	200mV/g
	Typical (all ranges)	
Damping Ratio	0.7	
Accuracy	$\pm 0.2\% span$	
Transverse sensitivity	1%	
Zero drift due to temperature changes $(5 - 40°C)$	$< 0.1\% span$	
Output Noise	0.5 mV peak to peak	
Supply Voltage	8-30 Volts	
Supply current @12 Volts	5 mA	
Weight	13 grams	

The sensors are mounted inside water-proof boxes (IP67) directly attached to the

structure. Figure A.2 shows their typical locations inside the boat. Accelerometers #1 and #2 are mounted on the collision bulkhead, measuring accelerations along the Z and Y axes respectively. Accelerometers #3,#4,#5 and #6 are mounted on the main bulkhead: the first two, close to the deck edge, measure acceleration along the Z axis; #5 and #6, on the centre line, measure along the Y and X axis respectively. This configuration allows the six components (three linear and three angular) of rigid-body acceleration to be measured. During some of the tests, a seventh and an eighth accelerometer (#7 and #8) have been placed respectively on the aftermost water-tight bulkhead inside the boat and on the main bulkhead, both over the centre-line and both measuring along the Z axis. This introduces redundancy in the measurement of heave and pitch acceleration and equally allows potential components of acceleration due to vertical bending to be identified.

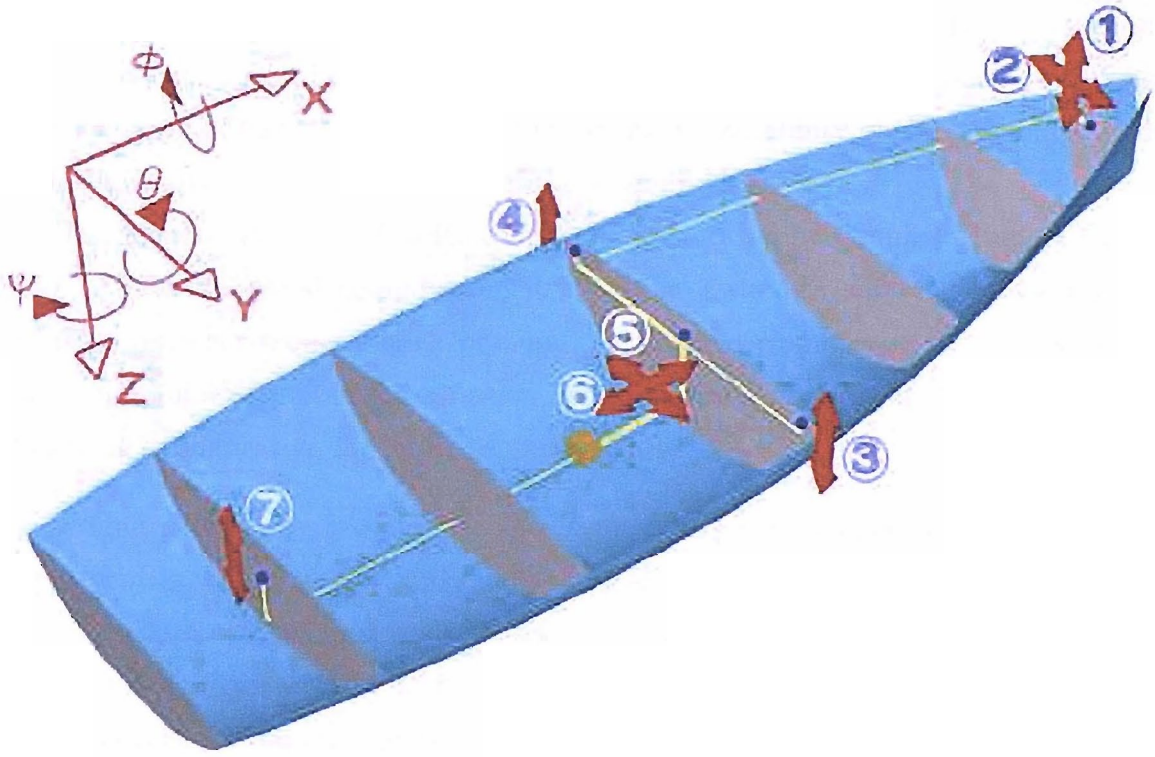

Figure A.2: Locations of the accelerometers and orientation of the sensitive axes. Accelerometer #8, not shown here, has been placed on the frame closest to the LCG.

Multi-conductor shielded cables are used to supply power and to collect the signals from the sensors. Although heavier, $0.22mm^2$ core section cables have been preferred over $0.055mm^2$ for better conductivity and robustness. Where possible, the cables

have been lead through bulkheads together with instrument cables and power supply cables for navigation lights. This avoids the need for drilling additional holes that may affect the watertightness of the bulkheads. It equally increases the chances of electromagnetic interference affecting the signals, particularly from the navigation lights cables which are usually unscreened and carry relatively high currents (approximately 2A). Tests performed in harbour have shown that the screen of the sensors cables is effective in eliminating this possible interference.

Connections between the logging unit and the cables and between the cables and the accelerometers is insured by high quality connectors. For the first series of measurements, circular connectors from "Framatome Connectors International" conforming to MIL-C-26482 standard have been used. They were chosen particularly for their ruggedness and for the quality of their latching system. However, it has later appeared that their size and the particular configuration of their solder connections make them rather impractical for the present application. For all following measurements series, Lemo self-latching "0B type" connectors have been used. They were chosen because of the quality of the contacts, reliability of the latching system, screening capability and simplicity of the assembly system.

The logging unit is a "CardCorder 3" manufactured by Cranfield Impact Centre Ltd. Made of several components, its modular structure allows it to be tailored to meet different requirements for number of logged channels, type of sensors and maximum allowed power consumption. For measurements during offshore races, the following configuration has been adopted:

- One power supply module: specifically designed to operate directly from a vehicle battery supply, this module contains a high efficiency switching regulator that can accept input voltages between 9 and 35 Volts (thus allowing the logging unit to be powered of both 12V and 24V supplies, the two typical ratings found on offshore sailing yachts). Integral protection and EMI filtering are equally ensured by this component.

- One signal acquisition and processing module: this component features 8 single-ended analog input channels, one 8-bit digital input channel, integral 5^{th} order Butterworth low-pass filters with programmable cut-off frequency and a 12-bit analog/digital converter. A maximum 30000 samples-per-second rate is allowed on the analog channels. This module has been customised for the

present application to include a stable 9V (maximum 1W output) supply for the accelerometers.

- One CPU module: it mainly contains a 16bit processor (supported by fixed memory and a real time calendar clock) and a removable "CompactFlash" card for non-volatile data storage. Two RS-232 serial ports are available: one is dedicated to communications with a personal computer for data transfer and real-time calibration, while the other is used for retrieving data from onboard instruments via a NMEA-0183 interface. Specific software has been developed in collaboration with the Cranfield Impact Centre to be able to read and interpret standard NMEA-0183 sentences. Details about this internal software and about the programming of the data acquisition can be found in section A.6.

A.5 Preliminary testing and calibration

The sensors and the logging unit have been tested in a laboratory before the first full-scale tests. In particular, the specifications of the sensors have been verified and checks performed to investigate the influence of power supply failures and of temperature variations (details about theses tests can be found in Appendix B).

For every series of measurements, the whole system is calibrated on land just before being installed onboard. Gain and zero are set for every channel by performing a typical "0-2g" test on a suitably chosen horizontal reference surface. Calibration values are then saved on the CompactFlash card and backed-up on a laptop computer. A post-calibration is performed with the same procedure after the measurements to check for eventual changes in the system behaviour.

Table A.2 shows an example of the values obtained for a series of measurements over a transatlantic crossing (17 days elapsed between pre- and post-calibration): as the resolution of the Cardcorder is limited to $1.22mV$ (the A/D converter having a 12bit resolution), these values are the result of a 5 seconds average. It can be seen that, for this example, sensitivity did not change significantly while, for some sensors. the output corresponding to zero g drifted slightly. Table A.2 also shows the error generated by the drift in the signals of accelerometers 5 and 6 when the average of their signals is used to calculate heel and trim angles. In general, over all the series of measurements performed, both sensitivity changes and "zero" drifts have remained

within acceptable limits: only in one occasion (acquisition on Gartmore during the Vendee Globe Challenge 2000), one sensor has shown considerable drift (equivalent to 0.55 g) and corrections have had to be applied during data processing.

Table A.2: Typical Pre- and Post-calibration data

	Pre-CALIBRATION				Post-CALIBRATION			
Accel.#	"+1g" [mV]	"-1g" [mV]	sensitivity [mV/g]	zero [mV]	"+1g" [mV]	"-1g" [mV]	sensitivity [mV/g]	zero [mV]
1	2675.7	2278.6	198.6	2477.2	2678.8	2280.9	199.0	2479.9
2	2678.6	2281.7	198.4	2480.2	2677.9	2281.0	198.5	2479.4
3	2669.0	2273.6	197.7	2471.3	2662.3	2268.1	197.1	2465.2
4	2686.3	2287.8	199.2	2487.1	2686.5	2287.3	199.6	2486.9
5	2865.1	2071.4	396.8	2468.3	2868.6	2075.0	396.8	2471.8
6	2876.3	2062.7	406.8	2469.5	2876.0	2062.2	406.9	2469.1
7	2657.7	2260.9	198.4	2459.3	2654.7	2258.2	198.2	2456.5
8	2817.8	2413.0	202.4	2615.4	2823.3	2418.1	202.6	2620.7

Accel.#	Sensitivity change [mV/g]	Zero drift [mV]	Zero drift [g]	Equivalent angle [deg]
1	0.4	2.7	0.01	-
2	0.0	-0.7	0.00	-
3	-0.6	-6.1	-0.03	-
4	0.4	-0.2	0.00	-
5	-0.1	3.6	0.01	0.57
6	0.0	-0.4	0.00	0.00
7	-0.2	-2.8	-0.01	-
8	0.2	5.3	0.03	-

A.6 Data acquisition

The majority of the measurements has been performed during single-handed offshore races. As the skipper is not to be given the additional burden of running or overseeing the data acquisition, the logging unit is programmed before the start of every trip to perform a number of tasks autonomously. This is done by using the internal software of the Cardcorder and by pre-programming a number of parameters via a laptop computer connected to the unit through a serial link. Three different types of acquisition are typically run simultaneously:

Continuous Time History acquisition

The continuous time history acquisition mode has been used mainly to store

data from the onboard instruments through the whole trip in order to build a logbook with information about the sailing conditions. Stored data include boat speed, apparent wind speed, apparent wind angle, magnetic heading and position given by GPS receiver (latitude/longitude). Most of these data are time averaged by the onboard instruments before being output through the NMEA interface and their update rate is generally 1Hz. From these parameters it is possible to calculate "a posteriori" the true wind speed, true wind angle, speed and course over the ground. For the purpose of compiling a logbook and in order to limit the required storage capacity for this acquisition mode, the full set of parameters is typically recorded at 5 to 20 seconds intervals.

When an operator can be onboard to trigger manually the acquisition, this mode can be used to record long time histories (up to 24 hours) of the acceleration signals with sampling rates of up to 200 Hz.

Triggered Time History acquisition

A short time history of all the signals from the accelerometers is saved every time a "slam" is detected.

The triggering condition is defined as either the vertical acceleration at the bow exceeding $2g$ or the one at the centre of gravity exceeding $1g$. These values have been fixed after the first series of measurements: they were chosen in order to maximise the number of recorded "slams" without exceeding the storage capacity of the logging unit. It should also be noted that they are strictly a function of the filtering frequency, the implications of which are discussed in section A.6.1.

The circular buffer memory of the Cardcorder allows not only data following the trigger event to be stored but also those preceding it. Thus, it is possible to analyse the motion of the boat preceding as well as following the slam. The recorded time histories are typically 20 to 60 seconds long and centred around the trigger event. Each short recording is automatically tagged with the time and date of the recording and with a "snapshot" (single value) of all the data from the onboard instruments (i.e. boat speed, apparent wind speed and angle, position, etc.) taken at the time of the trigger event.

During the round-the-world trips, the unit is also programmed to record 120 seconds long histories of all the accelerations twice a day, using time data from

the GPS as triggers.

Peak Values acquisition

The "peak values" acquisition mode involves an histogramming method. A range of interest is defined and then divided into a number of equally spaced bins. The logging unit detects relative minima and maxima ("valleys" and "peaks") in the input signals: every time a peak is detected within one of the defined bins, that bin is incremented.

To prevent peaks of the signal generated by minor oscillations (e.g. linked to structural vibration) from being counted, a threshold value is specified: as shown in figure A.3, the histogram is not updated unless the difference between the peak value and the last relative minimum is greater than the threshold value. Multi-dimensional histograms can be built, where the first dimension corresponds to the channel for which peaks are to be counted (defined as primary channel) and the others represent the instantaneous levels of other channels (defined as secondary channels) at the time when the primary channel peak is detected (e.g. peaks of vertical acceleration are counted together with instantaneous values of lateral acceleration and boat speed). The appropriate value for the threshold parameter depends strictly on the filter cut-off frequency and on the range of the histograms: in general, the higher the cut-off frequency, the larger the amplitude of the oscillations of the signals following a slam.

Due to the limited roll-off of the available filters (5^{th}order Butterworth) and to the relatively low frequency of the structural vibration produced by slamming on the tested yachts, it is difficult to filter out completely the higher frequency components of the signals while preserving those associated with rigid-body motion (the delicate issue of filtering is dealt with in greater detail in section A.6.1). Equally, it is extremely important that only one peak is counted for each slam. Therefore, during the first series of measurements, several tests have been performed to identify the most suitable threshold value: long time histories have been acquired and, from these, histograms of peak values created with different methods including the one used by the logging unit. By comparing both, the most appropriate value of the threshold value has determined for the following measurements.

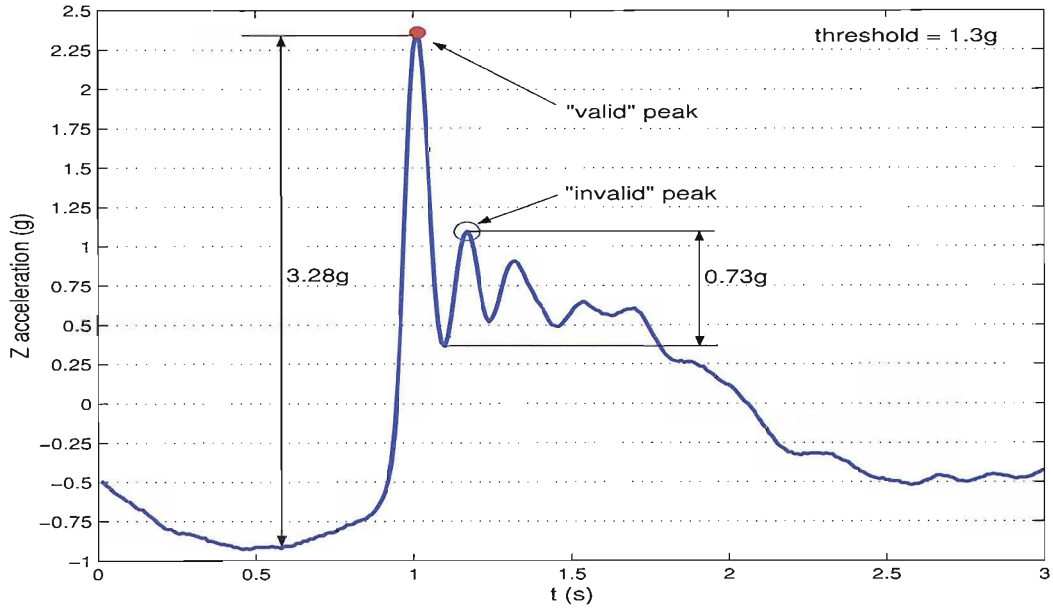

Figure A.3: The effect of the threshold value

A.6.1 Filtering

Low-pass filtering of the signals from the accelerometers is always required to avoid the risk of aliasing. During the full-scale tests, however, filtering is mainly justified by the necessity to isolate the frequency components of the signals associated with rigid-body motion form the ones generated by structural vibration.

Two types of vibrations have been considered: those produced by the onboard engine and those resulting from slamming. Figure A.4 shows typical frequency spectra of the signals from accelerometers *hvb* and *hv1* obtained while recording with the boat on a mooring and the engine running at the speed normally used to charge batteries. The dominant component and the one with the lowest frequency corresponds to a one-per-cycle excitation (at 23.9 Hz i.e. 1434rpm). Engine vibration appears to be picked up mainly by the accelerometers measuring along the z axis (corresponding to the axis of translation of the pistons), the highest amplitude signal being recorded from accelerometer *hvb* with an r.m.s value of 0.014g. Considering 700rpm as the lowest possible speed the engine can run at, a filter cut-off frequency lower than $10Hz$ must be adopted in order to exclude any contribution from engine vibration in the recorded signals.

The implications of filtering accelerometer signals with respect to accurately measuring the rigid body acceleration of a vessel are illustrated in figures A.5 and A.6. When trying to measure the rigid body acceleration of a vessel, one should not forget

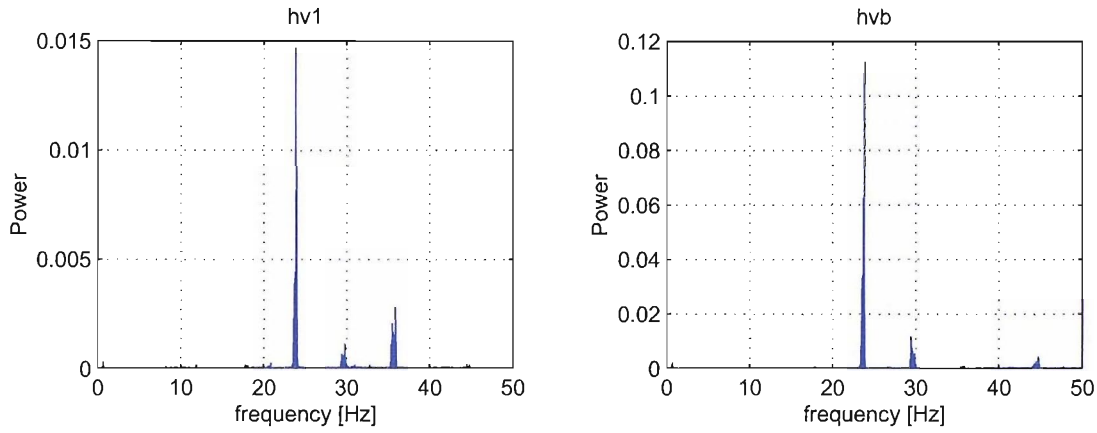

Figure A.4: Frequency spectra of the signals from accelerometers *hv1* (left) and *hvb* (right) with engine running at approximately 1400 rpm

that the vessel is never infinitely rigid and will always respond to transient wave excitation by vibrating. As a result, an accelerometer placed at the vessel LCG typically will pick up the acceleration resulting from vessel flexural vibration on top of the rigid-body acceleration (i.e. the acceleration of the vessel centre of gravity). The difference between the measured acceleration (a_{LCG}) and the actual rigid body acceleration (a^{rb}_{LCG}) then depends on the relative amplitude of the vessel transient flexural response. Since the components of acceleration associated with flexural vibration all occur at frequencies equal or higher than the first flexural natural frequency T_1, in order to discard them, one is tempted to low-pass filter the recorded signals with a filter cut-off frequency that is below $1/T_1$. However, because the rigid-body component of the vessel response has as wide a spectrum as the exciting force, lowpass filtering will invariably lead to part of the "rigid-body signal" also being decimated.

This is illustrated by figure A.5. Here, the vessel has been modelled as a non-uniform beam subject to an impulsive load applied at a distance from its centre of gravity. For very short impulse durations, the acceleration picked up by the accelerometer at the LCG will be lower than the actual rigid body value. This may be understood by considering that very short loads tend to produce high accelerations near their point of application, but not necessarily in the rest of the vessel. Conversely, as the impulse duration becomes higher relative to the vessel first natural period, the response at the LCG in terms of acceleration may actually be higher than the actual rigid body value. Figure A.5 shows that lowpass filtering the signal from

an accelerometer at the vessel LCG will bring the measured value closer to the actual rigid body value for impulse durations higher than the first natural period. For shorter impulse durations, filtering will actually mask the largest part of response of the structure, including its rigid body component, even more so as the filter cut-off frequency is low relative to the first natural frequency.

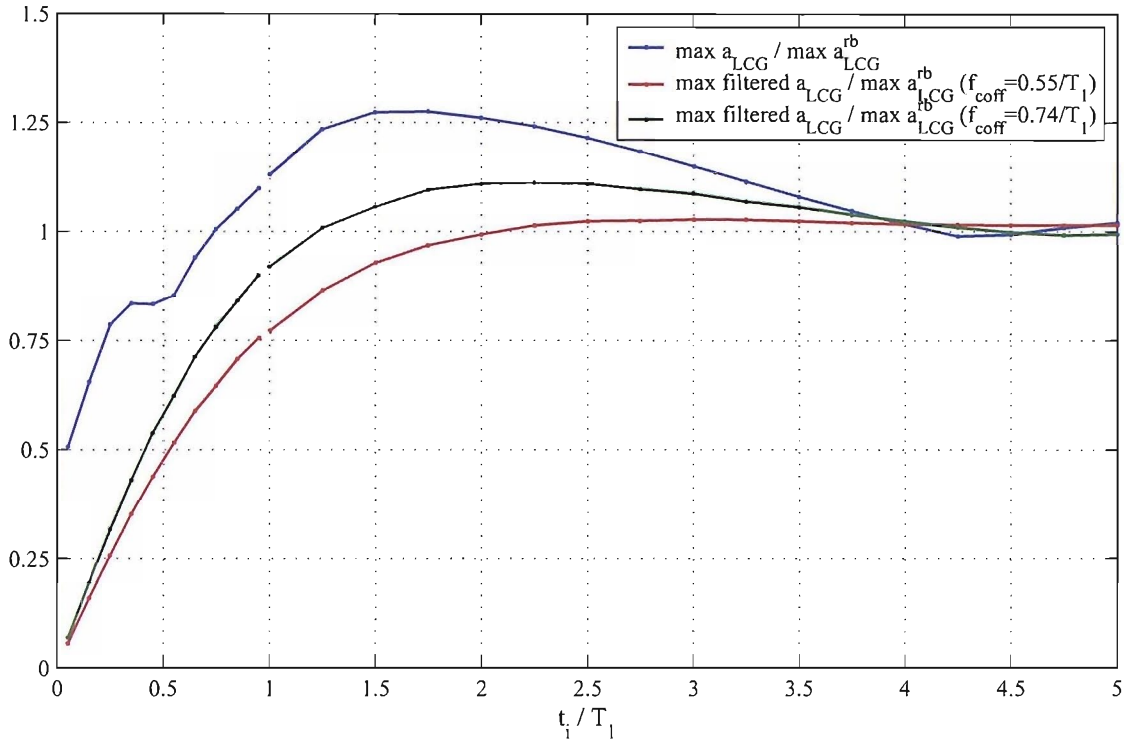

Figure A.5: Ratio of acceleration at the vessel LCG to actual rigid-body acceleration.

Figure A.6 gives an indication of how the error in estimating the vessel rigid body acceleration depends not only on the duration of the excitation and on the filtering, but also on the point of application of the load along the length of the vessel. In particular, it may be noticed that, as the force is applied further away from the LCG, the amplitude of response of the lower flexural modes tends to increase, and, with it the error on the estimate of the rigid body acceleration. Conversely, as the point of application is moved towards the LCG, the higher errors will be found for very short excitations, where the response of the structure is dominated by vibrations along the higher modes. Again it can be observed that filtering is beneficial if the impulse duration is relatively high, but results in larger errors for short excitations.

With respect to the study of slamming loads this leads us to conclude that one can hardly obtain a measure of the very short pressure peak acting on the hull bottom by

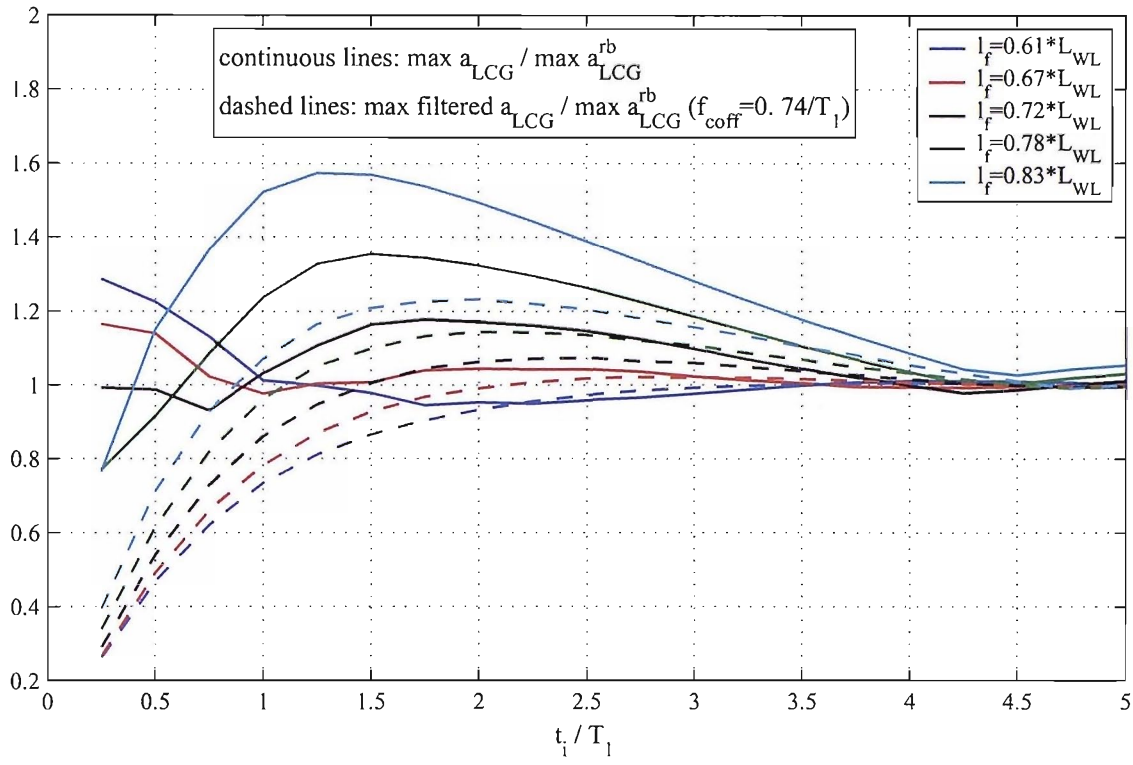

Figure A.6: Influence of the position of force application on the ratio of acceleration at the vessel LCG to actual rigid-body acceleration.

measuring accelerations at the vessel's LCG. Indeed, while the rigid body acceleration is proportional to these pressures, it cannot be properly measured by a limited number of accelerometers along the span of the vessel. On the other hand, when attempting to measure the hydrodynamic impulse associated with the full immersion of the hull sections following the first contact with water, it may be argued that its duration should be generally higher than the vessel's first natural period. An accelerometer placed at the LCG would then respond to this excitation and lowpass filtering should be beneficial in improving the accuracy of the rigid body acceleration estimate.

Appendix B

Data acquisition système: preliminary test report

The following report was issued in November 1999 for Groupe Finot. It contains elements gathered during preliminary tests of the Cardcorder3 IRAAM système, in view of its use for onboard data acquisition.

B.1 Rapport sur les premiers essais de la centrale d'acquisition Cardcorder3

Ce rapport décrit les résultats des premiers tests d'une centrale d'acquisition Cardcorder3 IRAAM, prêtée par le Cranfield Impact Centre du 8/11/1999 au 19/11/1999. Ces tests ont été effectués par moi même dans les laboratoires de la "Wolfson Unit for Marine Technologies and Industrial Aeronautics". Leur but était de vérifier principalement:

- la consommation d'énergie électrique.
- le bon fonctionnement du système suite à des instabilités d'alimentation électrique (chutes de tension, surcharges, interruptions d'alimentation courtes et prolongées, etc.).
- la capacité d'alimenter directement six accéléromètres IC Sensors 3140.
- les caractéristiques physiques (poids et encombrement) et la possibilité de rendre l'appareil étanche.

- les performances annoncées par le constructeur et, en particulier, l'aptitude à accomplir les taches prévues pour la chaîne de mesures embarquée.
- la fiabilité, dans la limite du temps disponible pour les test.
- la qualité du signal fourni par les accéléromètres (présence de bruit, précision,etc.) ainsi que sa stabilité dans le temps

B.1.1 Consommation d'énergie électrique

Pendant les tests l'unité était alimentée par un transformateur AC/DC 240V-0/30V: celui-ci permet de faire varier la tension d'alimentation entre 0 et 30 Volt et de lire le courant absorbé par les appareils connectés. Ainsi on a mesuré:

Tension d'alimentation	Courant max.
12.8V	260 mA
12V	280 mA
11V	305 mA

De manière générale le courant absorbé varie en fonction de la tension d'alimentation (qui peut varier entre 7.5V et 24V) et engendre une consommation a peu près constante de 3.3W. Ces mesures on étés effectuées avec les six accéléromètres alimentés par la centrale: *la consommation de 3.3W correspond donc à la consommation totale de la chaîne de mesure.* Finalement le taux d'activité de la centrale n'affecte le niveau de consommation que très marginalement: avec alimentation à 12.8V, on observe un différence de courant absorbé inférieure à 10mA (i.e. moins de 4%) entre la condition de "stand-by" (aucune acquisition en cours) et celle de "pleine charge" (haute fréquence d'acquisition et accès fréquents à la carte mémoire).

B.1.2 Influence des instabilités d'alimentation

On a vérifié les cas suivants:

1. **Chute de tension de durée inférieure à une seconde**: la centrale semble interrompre sont fonctionnement dès lors que la tension d'alimentation est inférieure à 7.5V. Le transformateur que j'ai utilisé ne me permettait pas des interruptions suffisamment courtes (quelques centièmes de seconde) pour

éviter ce phénomène. Si la centrale était en train d'acquérir des données avant l'interruption, l'acquisition redémarre toujours moins de 2 secondes après l'interruption. Lorsque l'interruption a lieu pendant l'enregistrement d'une "histoire temporelle", les informations sont réparties en 2 fichiers (avant/après interruption). On a constaté que dans ce cas la date et l'heure d'enregistrement montrés par le premier fichier étaient fausses: ce problème a été communiqué à CIC et déjà corrigé.

2. **Chute de tension prolongée**: de manière générale, à partir du moment ou la tension d'alimentation descend en dessous de 7.5V, la durée de l'interruption ne semble faire aucune différence. Le fonctionnement reprend toujours normalement moins de 2 secondes après que l'alimentation est rétablie. En aucun cas, pendant les deux semaines de test, on a constaté des pertes de données où des changements du mode de fonctionnement faisant suite à des coupure d'alimentation.

3. **Instabilités, chutes de tension, sur-tensions**: lorsque la tension d'alimentation varie à l'intérieur de la fourchette admise (7.5V-24V)[1], toute variation ne semble affecter ni la qualité des données enregistrées, ni le bon fonctionnement de la centrale. La tension d'alimentation fournie aux accéléromètres reste dans tous les cas stable à 9V (à 1% près).

B.1.3 Alimentation des accéléromètres

La centrale Cardcorder étant capable d'alimenter correctement les accéléromètres, cette solution me parait la meilleure: elle permet en effet de ne pas devoir utiliser un transformateur supplémentaire et donc de réduire la consommation totale et d'augmenter la fiabilité.

[1] Celle-ci devrait inclure notamment les surtensions dues à l'entrée en marche du générateur. La centrale d'acquisition est équipée d'un fusible de protection contre les surcharges, mais il faut la démonter pour y accéder

B.1.4 Caractéristiques physiques

Les dimensions et les poids des différents éléments testés sont:

composant	poids(kg)	dimensions(mm)
centrale d'acquisition	0.85	$105 \times 96 \times 75$
boîtier accéléromètres	0.2	$64 \times 58 \times 36$
câble	0.05 (par mètre)	5 (diamètre)

Poids total (avec 4 boîtiers accéléromètres et 36 mètres de câble): 3.5 kg.
Du point de vue de l'étanchéité, la centrale présente un volet pour le chargement de la carte de mémoire qui n'est pas prévu pour être étanche. La modification de se détail, bien que possible, engendrerait à ce stade une augmentation sensible du prix: elle pourrait par contre faire l'objet d'une négociation lors d'un éventuel futur achat de plusieurs unités. Pour le moment et pour les premiers tests en mer la solution meilleure me parait de loger la centrale dans un boîtier étanche de dimension légèrement supérieure ($150 \times 150 \times 150mm$).

B.1.5 Test des performances, configuration pour mesures en navigation

J'ai programmé la centrale d'acquisition pour une série de mesures très similaire à celle que nous allons adopter pour les tests en mer. La seule différence était l'absence de connexion aux instruments de bord: l'interface NMEA est en effet en train d'être développée pour notre application et n'était donc pas présente dans le prototype testé. Je considère cependant que, de part la très faible fréquence d'échantillonnage que nous allons adopter pour les données NMEA (1/30s à 1/min), ceci ne devrait alourdir que très marginalement la tache de la centrale d'acquisition. La centrale était programmée pour accomplir les opérations suivantes en même temps:

1. enregistrement des signaux des six accéléromètres sur 3 secondes à chaque fois qu'un impact est détecté (1 sec avant impact et 2 sec après). Fréquence d'échantillonage par canal: 200 Hz. Fréquence de filtrage: 20 Hz. Pour les conditions de détection d'impact voir ci dessous.

2. enregistrement des signaux des six accéléromètres sur 70 secondes à chaque fois

que l'angle de gîte dépasse 70 deg pendant plus de 1 seconde (10 secondes avant dépassement angle et 60 secondes après). Fréquence d'échantillonnage: 20 Hz.

3. enregistrement d'histogramme (en deux dimensions) des accélérations à l'étrave: on compte le nombre d'accélérations verticales dans dix tranches entre 2g et 6g et, parallèlement, le nombre d'accélérations latérales en dix tranches de -1.0 à 1.0 g. Voir graphique.

4. enregistrement d'histogramme des accélérations au centre de gravité: on compte le nombre d'accélérations verticales au centre de gravité dans dix tranches de 0.5 à 2 g.

La centrale était programmée pour détecter un impact à chaque fois que:

- l'accélération verticale à l'étrave dépasse 1g ou bien
- l'accélération latérale à l'étrave dépasse 0.5g ou bien
- l'accélération au centre de gravité dépasse 0.8g

Les graphiques qui suivent montrent les enregistrements typiques obtenus dans cette configuration. Ces résultats correspondent à des simulations en laboratoire: ils ne sont pas nécessairement représentatifs des tracés que nous obtiendrons en mer; aussi les seuils et les durées d'enregistrement devront être mieux définis après les premiers tests en mer: un seuil d'accélération trop bas pourrait déclencher un grand nombre d'enregistrements en très peu de temps et remplir la mémoire très vite de manière inutile. Un seuil trop haut, au contraire, ne déclenchera que trop peu d'enregistrements et nous ferait perdre des informations intéressantes.

Bien qu'ils ne soient pas affichés ci-dessus, on peut de manière égale produire des histogrammes pour les accélérations longitudinales, des tracés de l'angle d'assiette, etc. La qualité des résultats a été vérifiée en enregistrant en même temps des histoires temporelles et des histogrammes et en vérifiant que les deux soient cohérents: aucune erreur n'est apparue. Au cours de certains enregistrements j'ai augmenté la fréquence d'échantillonnage jusqu'à 1kHz, cependant le processeur n'a pas montré de signes de surcharge (on voyant lumineux s'allume à chaque fois que le processeur n'arrive plus à suivre). De façon générale la fréquence d'échantillonnage ne semble pas affecter la charge du micro-processeur autant que d'autres facteurs. En une seule occasion j'ai réussi à surcharger la centrale, ceci en doublant le nombre de conditions de détection

d'impact et en multipliant par trois la taille des histogrammes à enregistrer: l'intérêt de cette configuration était purement de trouver les limites de la centrale d'acquisition. Je n'envisage pas de l'adopter pour les campagnes en mer et j'estime que la centrale est suffisamment puissante pour effectuer les mesures dont nous avons besoin.

B.1.6 Fiabilité

Deux semaines de tests en laboratoire ne sont sûrement pas suffisantes pour évaluer la fiabilité d'un système qui est sensé fonctionner pendant cent jours sur un bateau de course au large. De ce point de vue le véritable test ne pourra être fait que en mer et il est prudent de prévoir autant d'essais en mer que possible avant le départ du Vendée-Globe 2000. Au cours des tests, j'ai laissé volontairement la centrale et les accéléromètres sous tension pendant huit jours d'affilée (i.e. un peu moins de 200 heures): aucune irrégularité de fonctionnement n'a été observée. J'ai également essayé d'évaluer les effets des défauts d'alimentation (voir chapitre ci-dessus) et les dérives du signal des accéléromètres suite à des changements de température: dans cette optique deux accéléromètres ont été placés pendant 1 heure dans un réfrigérateur à 4^o C (ce qui représente une différence de température de 15^oC par rapport à la température ambiante du laboratoire. Aucune dérive n'a pu être observée.

B.1.7 Qualité du signal et précision

Les signaux enregistrés au cours des test présentent un bruit typiquement de l'ordre de 1.55 mV r.m.s. Cette valeur descend à moins de 0.5 mV lorsque le signal est filtré à 20Hz. Ces valeurs induisent une marge de précision de 0.008 g (et 0.002 pour le signal filtré; les accéléromètres ayant une sensibilité de 200mV/g). D'autre part, elles sont bien compatibles avec la résolution à 12 bit de la centrale d'acquisition qui interdit une précision supérieure à 0.006 g. Lorsque on considère la mesure d'angles d'inclinaison effectuée avec les accéléromètres, les valeurs indiquées engendrent une marge de précision de 0.6 degrés. Il faut enfin remarquer qu'il est optimiste de s'attendre à de tels niveaux de précision pour les mesures en navigation: en effet la qualité du montage a bord (surtout en ce qui concerne le bon alignement des accéléromètres avec les axes du bateau), bien que très bonne, peut facilement engendrer des erreurs du même ordre. De même le processus de filtrage nécessaire pour

extraire les mesures d'angles introduit des petites erreurs (essentiellement des retards). Il est donc plus sage d'envisager pour les mesures en navigation une précision de 0.05 g pour les accélérations et de 1-2 degrés pour les angles.

B.1.8 Conclusions

Le résultat de ces premiers tests est globalement très positif. La centrale d'acquisition répond bien à notre cahier des charges en ce qui concerne ses performances, sa fiabilité, sa consommation, son poids et ses dimensions.Il est regrettable que des difficultés logistiques ne m'aient pas permis les mesures en navigation que j'avais initialement prévu pour le dernier jour de tests. Celles-ci seront donc la première priorité dès lors que la centrale que nous avons commandé sera livrée (actuellement CIC prévoit la livraison pour la troisième semaine de Janvier). Les principaux objectifs pour les prochaines semaines sont:

- Tester le bon fonctionnement de l'interface NMEA.
- Effectuer plusieurs campagnes de mesures en mer, si possible sur différents bateaux.
- Construire dans les laboratoires de la Wolfson Unit un petit circuit imprimé pour réduire le nombre de connections électriques et augmenter la fiabilité.

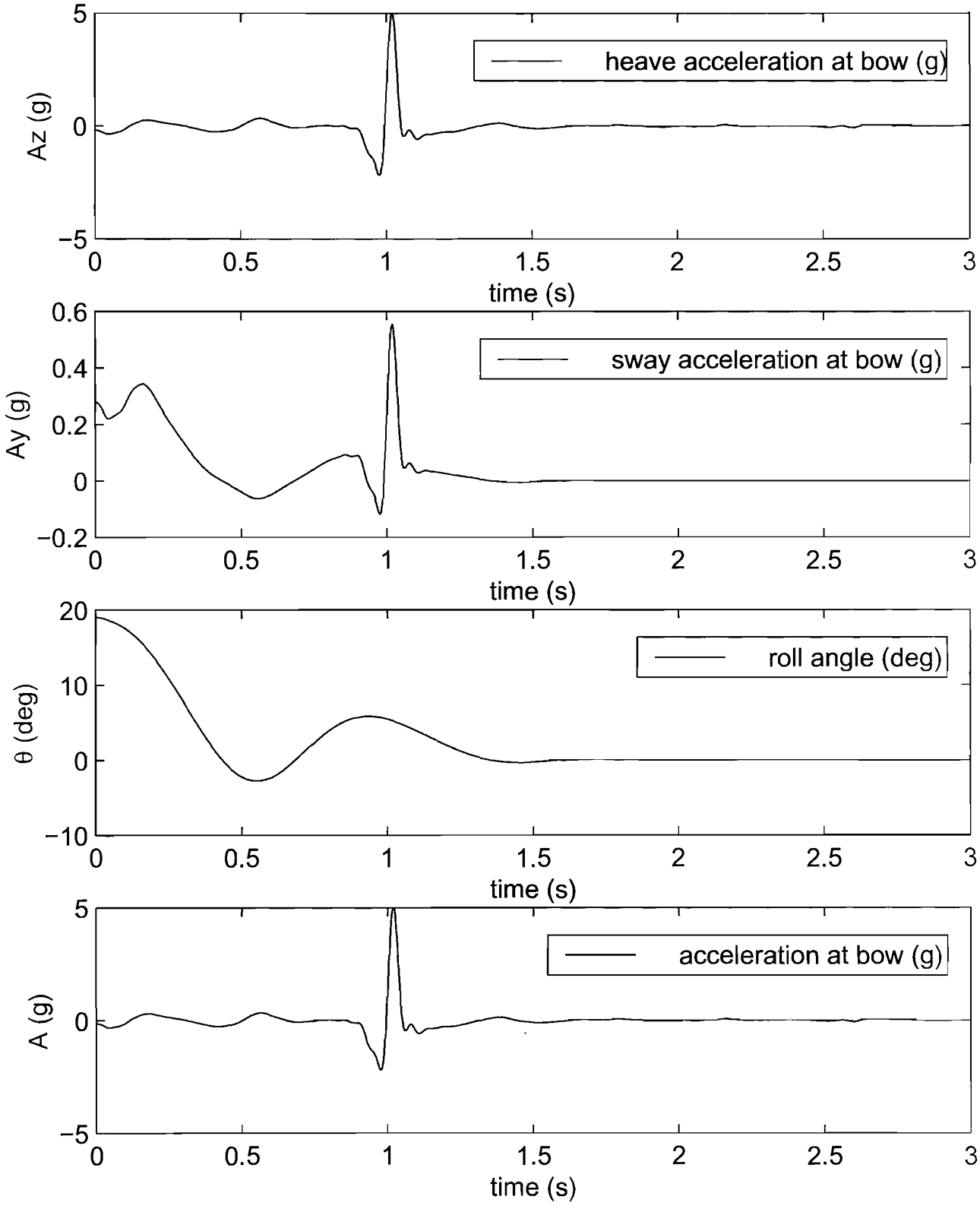

Figure B.1: Enregistrement d'impact (**simulation**): composante verticale et transversale de l'accélération à l'étrave, angle de gîte et accélération résultante à l'étrave

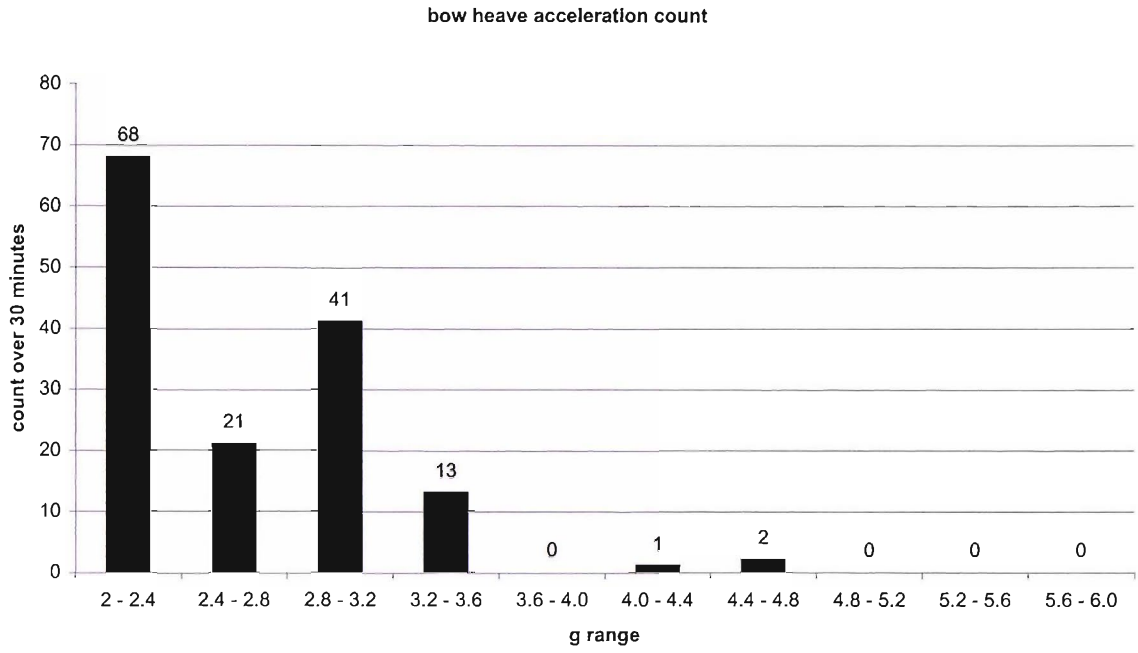

Figure B.2: Histogramme des accélérations verticales à l'étrave pendant 30 minutes (**simulation**)

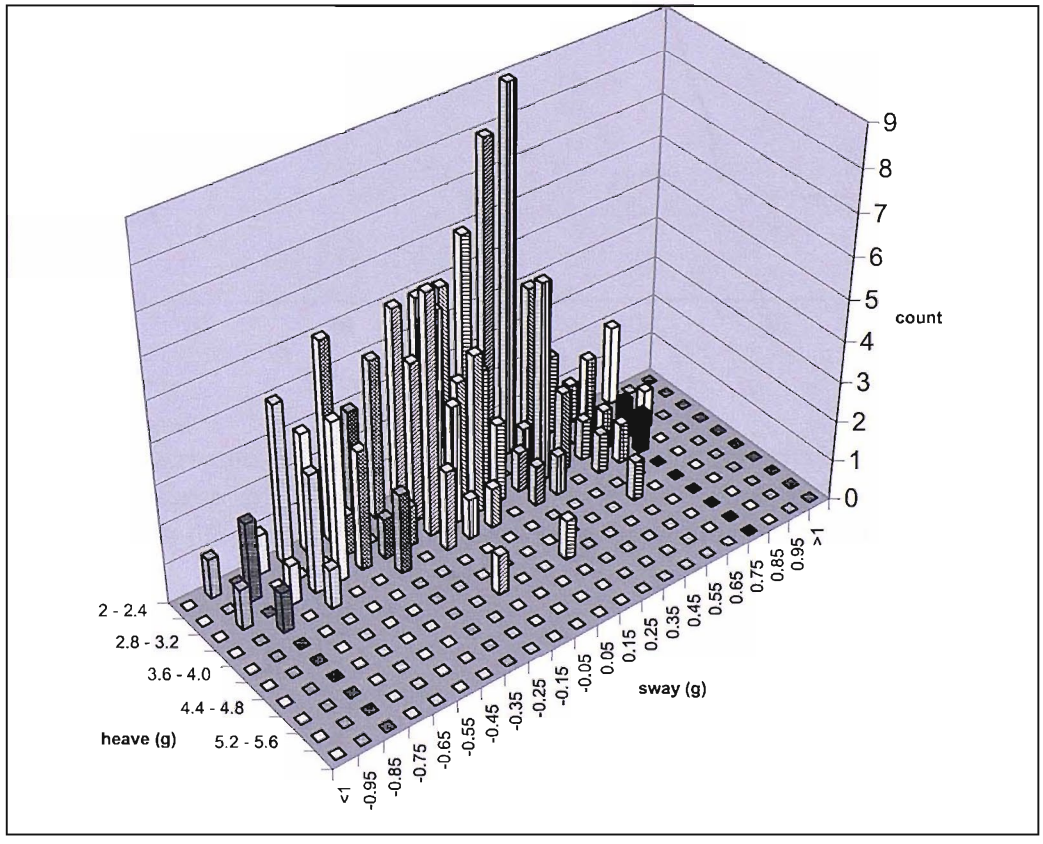

Figure B.3: Histogramme des accélérations verticales et transversales à l'étrave pendant 30 minutes (**simulation**)

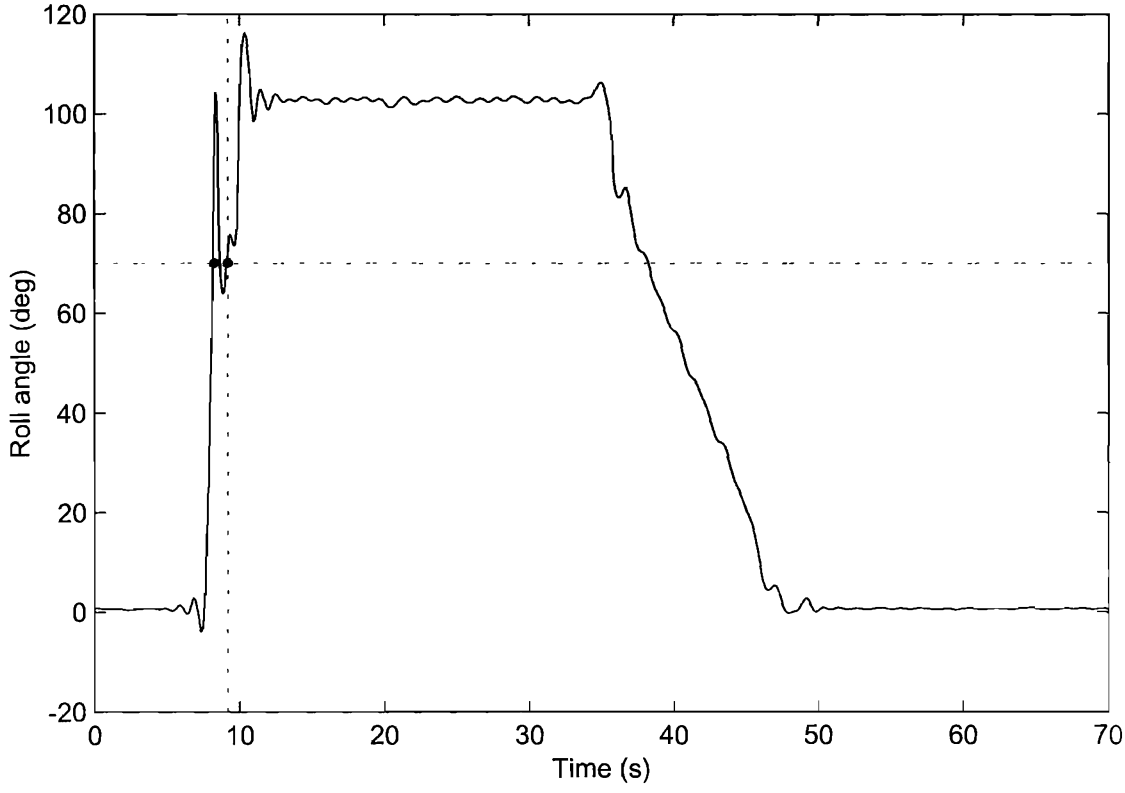

Figure B.4: Enregistrement de l'angle de gîte pendant chavirage (**simulation**): l'enregistrement est déclenche quand l'angle de gîte dépasse 70 deg pendant plus de 1 seconde; les dix secondes précédentes sont également sauvegardées

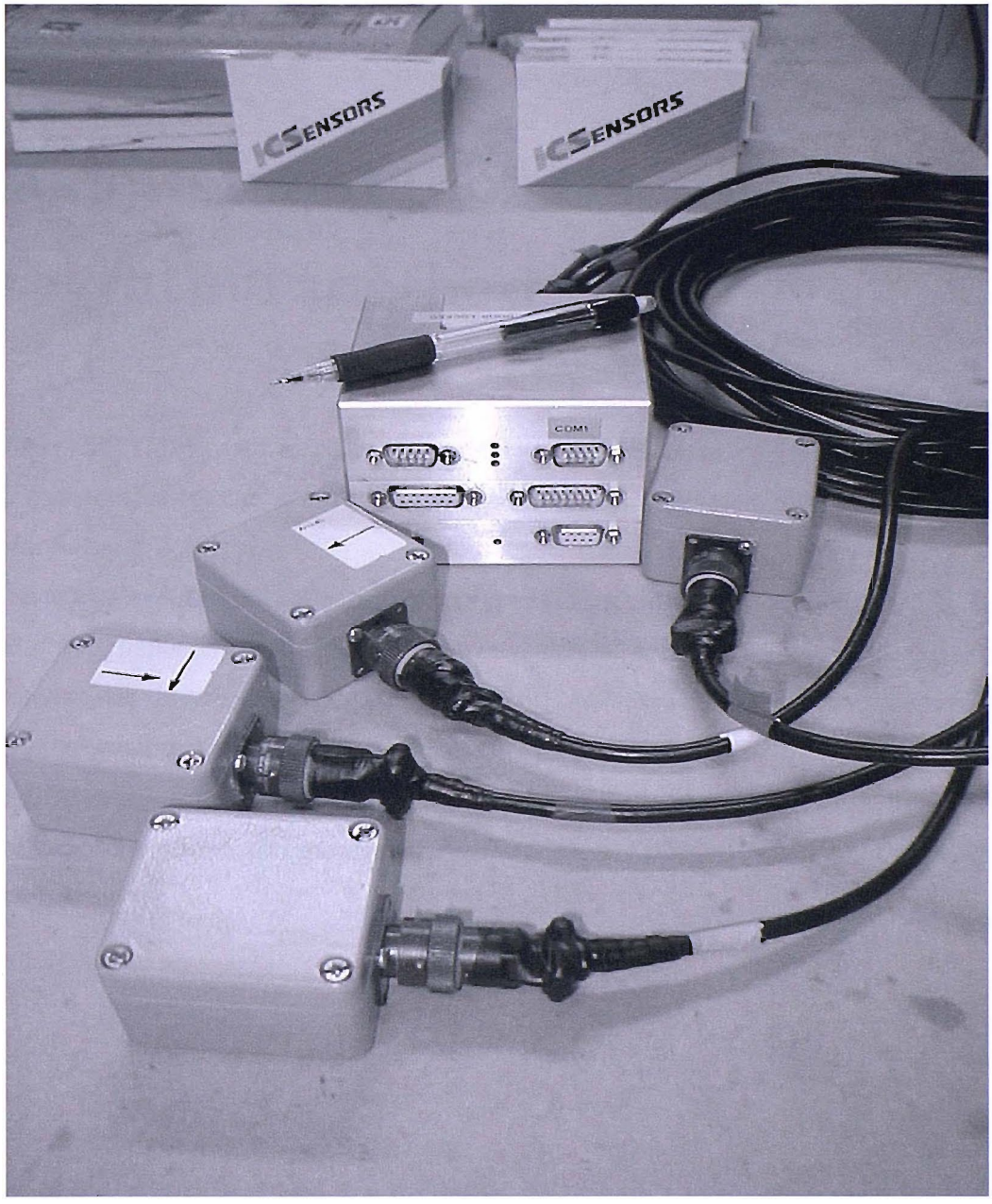

Figure B.5: Centrale Cardcorder et quatre boîtiers accéléromètres

Appendix C

Validation data for the numerical integration method

The following tables contain the numerical details illustrating the influence of different parameters on the accuracy of the numerical integration method presented in sections 3.3 and 3.4.

The tables are divided into three parts containing values respectively for the linear and angular displacements (i.e. surge, sway, heave, roll, pitch, yaw), for their first derivatives (e.g. heave velocity, pitch rate, etc.), and for their second derivatives (e.g. heave acceleration, pitch acceleration, etc.). Each cell contains two values: the top one indicates the normalised RMS error (NRE) as defined in 3.32, while the bottom one, in brackets, shows the maximum relative error (MRE, cf. 3.33) for the same set of parameters.

Table C.1: Influence of signals recording length.

t_{rec}	x_0	y_0	z_0	ϕ_0	θ_0	ψ_0
$10s$	7.3	6.2	4.0	4.3	4.1	5.0
	(26.1)	(25.2)	(15.8)	(12.3)	(12.6)	(17.5)
$20s$	5.8	5.4	2.2	1.7	1.7	1.3
	(18.3)	(16.5)	(7.0)	(4.2)	(4.6)	(4.1)
$60s$	3.6	3.6	0.8	1.2	1.2	0.7
	(11.1)	(11.5)	(2.7)	(2.3)	(2.2)	(2.5)
$120s$	1.7	1.8	0.4	1.1	1.1	0.3
	(5.4)	(5.8)	(1.4)	(1.4)	(1.5)	(1.4)
$240s$	1.2	1.4	0.3	1.1	1.1	0.2
	(4.2)	(5.3)	(1.2)	(1.6)	(1.6)	(1.3)
t_{rec}	$\dot{x}_0$	$\dot{y}_0$	$\dot{z}_0$	$\dot{\phi}_0$	$\dot{\theta}_0$	$\dot{\psi}_0$
$10s$	3.4	3.1	1.9	1.4	1.3	1.5
	(13.0)	(12.9)	(7.9)	(4.9)	(5.0)	(5.4)
$20s$	1.9	1.7	0.7	1.0	1.0	1.0
	(5.8)	(5.4)	(2.7)	(3.1)	(2.8)	(3.1)
$60s$	0.9	1.0	0.3	0.8	0.8	0.8
	(3.1)	(3.3)	(1.2)	(2.4)	(2.4)	(2.5)
$120s$	0.5	0.5	0.2	0.8	0.8	0.8
	(1.9)	(2.0)	(0.9)	(2.6)	(2.6)	(2.7)
$240s$	0.4	0.4	0.2	0.8	0.8	0.9
	(1.6)	(1.9)	(0.9)	(2.7)	(2.7)	(3.0)
t_{rec}	$\ddot{x}_0$	$\ddot{y}_0$	$\ddot{z}_0$	$\ddot{\phi}_0$	$\ddot{\theta}_0$	$\ddot{\psi}_0$
$10s$	1.7	1.6	0.7	0.6	0.6	0.6
	(6.3)	(5.7)	(3.3)	(2.7)	(2.7)	(2.7)
$20s$	0.7	0.7	0.3	0.2	0.2	0.2
	(2.3)	(2.2)	(1.3)	(1.3)	(1.2)	(1.3)
$60s$	0.5	0.5	0.2	0.2	0.2	0.2
	(1.3)	(1.4)	(1.0)	(0.9)	(0.9)	(1.0)
$120s$	0.4	0.4	0.2	0.2	0.2	0.2
	(1.2)	(1.2)	(0.9)	(0.9)	(0.9)	(0.9)
$240s$	0.4	0.4	0.2	0.2	0.2	0.2
	(1.2)	(1.2)	(0.9)	(0.9)	(0.9)	(0.9)

Table C.2: Influence of average heel angle

$\bar{\phi}_0$	x_0	y_0	z_0	ϕ_0	θ_0	ψ_0
$0deg$	2.8	2.6	0.9	1.4	1.3	0.8
	(11.8)	(11.4)	(4.3)	(3.0)	(3.2)	(3.1)
$6deg$	5.2	4.8	1.1	1.5	1.4	1.0
	(19.9)	(18.5)	(4.5)	(3.5)	(3.7)	(3.6)
$12deg$	3.6	3.6	0.8	1.2	1.2	0.7
	(11.1)	(11.5)	(2.7)	(2.3)	(2.2)	(2.5)
$18deg$	5.3	5.5	1.1	1.4	1.4	0.8
	(20.3)	(20.9)	(4.5)	(3.8)	(3.6)	(3.1)
$24deg$	4.7	4.9	1.2	1.5	1.3	1.0
	(17.5)	(18.8)	(4.7)	(3.4)	(3.4)	(3.5)
$30deg$	4.7	4.5	1.2	1.4	1.3	0.9
	(17.8)	(17.1)	(4.5)	(3.3)	(3.2)	(3.6)
$\bar{\phi}_0$	$\dot{x}_0$	$\dot{y}_0$	$\dot{z}_0$	$\dot{\phi}_0$	$\dot{\theta}_0$	$\dot{\psi}_0$
$0deg$	0.9	0.8	0.4	0.9	0.8	0.9
	(3.7)	(3.6)	(1.7)	(2.9)	(2.8)	(3.1)
$6deg$	1.4	1.3	0.4	0.9	0.9	0.9
	(5.8)	(5.1)	(1.8)	(2.7)	(2.8)	(3.0)
$12deg$	0.9	1.0	0.3	0.8	0.8	0.8
	(3.1)	(3.3)	(1.2)	(2.4)	(2.4)	(2.5)
$18deg$	1.4	1.5	0.4	0.8	0.9	0.9
	(5.6)	(5.8)	(1.8)	(2.7)	(2.7)	(2.8)
$24deg$	1.3	1.3	0.4	0.8	0.8	0.8
	(5.6)	(5.5)	(1.8)	(2.6)	(2.7)	(2.6)
$30deg$	1.2	1.2	0.4	0.8	0.8	0.9
	(5.0)	(5.1)	(1.8)	(2.6)	(2.5)	(2.9)
$\bar{\phi}_0$	$\ddot{x}_0$	$\ddot{y}_0$	$\ddot{z}_0$	$\ddot{\phi}_0$	$\ddot{\theta}_0$	$\ddot{\psi}_0$
$0deg$	0.5	0.5	0.2	0.2	0.2	0.2
	(1.7)	(1.7)	(1.2)	(1.0)	(1.1)	(1.1)
$6deg$	0.6	0.6	0.2	0.2	0.2	0.2
	(2.0)	(1.8)	(1.3)	(1.1)	(1.1)	(1.2)
$12deg$	0.5	0.5	0.2	0.2	0.2	0.2
	(1.3)	(1.4)	(1.0)	(0.9)	(0.9)	(1.0)
$18deg$	0.5	0.5	0.2	0.2	0.2	0.2
	(1.9)	(2.0)	(1.3)	(1.1)	(1.0)	(1.1)
$24deg$	0.5	0.6	0.2	0.2	0.2	0.2
	(1.9)	(2.0)	(1.3)	(1.1)	(1.1)	(1.1)
$30deg$	0.5	0.5	0.2	0.2	0.2	0.2
	(1.7)	(1.8)	(1.2)	(1.0)	(1.0)	(1.1)

Table C.3: Influence of significant wave height

$h_{1/3}$	x_0	y_0	z_0	ϕ_0	θ_0	ψ_0
$0.4m$	2.1	2.2	1.3	0.8	0.3	1.1
	(7.6)	(7.8)	(4.5)	(2.7)	(2.9)	(3.5)
$1m$	2.0	1.9	1.2	0.8	0.5	0.9
	(7.0)	(6.9)	(4.2)	(2.5)	(2.5)	(3.2)
$2m$	2.7	2.5	0.9	0.9	0.8	0.9
	(10.4)	(9.7)	(3.5)	(2.7)	(2.9)	(3.0)
$4m$	3.6	3.6	0.8	1.2	1.2	0.7
	(11.1)	(11.5)	(2.7)	(2.3)	(2.2)	(2.5)
$8m$	4.2	5.1	1.8	2.7	2.7	1.5
	(17.5)	(21.0)	(8.4)	(7.6)	(7.5)	(7.6)
$h_{1/3}$	$\dot{x}_0$	$\dot{y}_0$	$\dot{z}_0$	$\dot{\phi}_0$	$\dot{\theta}_0$	$\dot{\psi}_0$
$0.4m$	0.8	0.9	0.5	0.2	0.3	0.2
	(2.9)	(3.1)	(1.7)	(0.8)	(0.9)	(0.7)
$1m$	0.8	0.8	0.4	0.3	0.3	0.3
	(2.7)	(2.8)	(1.6)	(1.1)	(1.1)	(1.1)
$2m$	0.9	0.8	0.3	0.5	0.5	0.5
	(3.2)	(3.1)	(1.2)	(1.6)	(1.7)	(1.6)
$4m$	0.9	1.0	0.3	0.8	0.8	0.8
	(3.1)	(3.3)	(1.2)	(2.4)	(2.4)	(2.5)
$8m$	1.6	2.0	1.0	1.7	1.9	2.0
	(7.1)	(8.4)	(5.0)	(7.0)	(7.7)	(8.9)
$h_{1/3}$	$\ddot{x}_0$	$\ddot{y}_0$	$\ddot{z}_0$	$\ddot{\phi}_0$	$\ddot{\theta}_0$	$\ddot{\psi}_0$
$0.4m$	0.3	0.3	0.0	0.1	0.1	0.0
	(1.1)	(1.0)	(0.1)	(0.2)	(0.2)	(0.2)
$1m$	0.3	0.3	0.0	0.1	0.1	0.1
	(0.9)	(0.9)	(0.2)	(0.2)	(0.2)	(0.3)
$2m$	0.3	0.3	0.1	0.1	0.1	0.1
	(1.2)	(1.1)	(0.4)	(0.4)	(0.4)	(0.4)
$4m$	0.5	0.5	0.2	0.2	0.2	0.2
	(1.3)	(1.4)	(1.0)	(0.9)	(0.9)	(1.0)
$8m$	1.2	1.2	0.9	0.8	0.7	0.8
	(5.0)	(5.7)	(4.8)	(5.6)	(4.7)	(6.5)

Table C.4: Influence of wave encounter angle

μ	x_0	y_0	z_0	ϕ_0	θ_0	ψ_0
$180deg$	2.6	2.7	0.8	1.7	1.5	0.8
	(11.4)	(11.7)	(3.9)	(3.1)	(3.1)	(3.1)
$135deg$	3.6	3.6	0.8	1.2	1.2	0.7
	(11.1)	(11.5)	(2.7)	(2.3)	(2.2)	(2.5)
$90deg$	3.6	3.4	1.1	1.0	1.0	1.2
	(15.9)	(15.0)	(5.4)	(4.1)	(4.4)	(4.0)
$45deg$	6.7	7.7	3.2	2.4	1.7	3.7
	(28.0)	(31.5)	(14.5)	(10.9)	(9.4)	(14.0)
$0deg$	15.6	15.0	9.5	4.6	3.7	7.4
	(58.5)	(57.3)	(39.6)	(16.2)	(16.8)	(23.7)
μ	$\dot{x}_0$	$\dot{y}_0$	$\dot{z}_0$	$\dot{\phi}_0$	$\dot{\theta}_0$	$\dot{\psi}_0$
$180deg$	0.8	0.8	0.4	1.0	1.0	1.0
	(3.4)	(3.4)	(1.7)	(3.4)	(3.4)	(3.5)
$135deg$	0.9	1.0	0.3	0.8	0.8	0.8
	(3.1)	(3.3)	(1.2)	(2.4)	(2.4)	(2.5)
$90deg$	1.6	1.5	0.5	0.8	0.8	0.8
	(6.5)	(5.8)	(2.2)	(2.9)	(2.9)	(2.8)
$45deg$	4.5	5.5	1.7	1.8	1.6	1.7
	(18.8)	(21.5)	(8.3)	(7.8)	(6.8)	(7.4)
$0deg$	9.5	9.0	4.4	1.0	0.9	1.0
	(28.5)	(27.8)	(15.0)	(3.6)	(3.4)	(3.4)
μ	$\ddot{x}_0$	$\ddot{y}_0$	$\ddot{z}_0$	$\ddot{\phi}_0$	$\ddot{\theta}_0$	$\ddot{\psi}_0$
$180deg$	0.5	0.6	0.3	0.2	0.3	0.3
	(1.6)	(1.7)	(1.4)	(1.4)	(1.4)	(1.4)
$135deg$	0.5	0.5	0.2	0.2	0.2	0.2
	(1.3)	(1.4)	(1.0)	(0.9)	(0.9)	(1.0)
$90deg$	0.8	0.7	0.1	0.1	0.1	0.1
	(3.1)	(2.9)	(0.9)	(0.9)	(0.8)	(0.7)
$45deg$	5.4	6.2	0.2	0.8	0.7	0.8
	(24.3)	(27.5)	(1.1)	(4.0)	(3.4)	(3.6)
$0deg$	4.9	4.9	0.3	0.2	0.2	0.3
	(17.1)	(16.7)	(1.8)	(1.4)	(1.4)	(1.5)

Table C.5: Influence of noise affecting the accelerometer signals

noise rms	x_0	y_0	z_0	ϕ_0	θ_0	ψ_0
$0.025m/s^2$	2.9	2.9	0.9	1.4	1.3	0.9
	(12.5)	(12.3)	(4.0)	(3.4)	(3.0)	(3.4)
$0.05m/s^2$	2.9	3.5	1.0	1.3	1.2	0.8
	(12.2)	(13.8)	(4.6)	(3.9)	(3.3)	(3.2)
$0.1m/s^2$	3.4	5.6	1.0	2.0	1.3	1.2
	(13.6)	(19.7)	(4.4)	(5.3)	(3.6)	(4.5)
$0.2m/s^2$	4.3	9.9	1.3	3.2	1.6	1.7
	(16.5)	(34.5)	(5.6)	(10.1)	(5.1)	(6.5)
$0.4m/s^2$	6.8	18.7	1.9	5.3	2.2	2.9
	(24.7)	(63.2)	(7.7)	(19.0)	(7.8)	(11.3)
$0.8m/s^2$	14.5	35.4	3.3	10.2	4.2	5.6
	(50.1)	(118.9)	(13.2)	(36.9)	(17.3)	(21.7)
noise rms	$\dot{x}_0$	$\dot{y}_0$	$\dot{z}_0$	$\dot{\phi}_0$	$\dot{\theta}_0$	$\dot{\psi}_0$
$0.025m/s^2$	0.9	1.0	0.3	0.9	0.9	1.0
	(3.9)	(4.0)	(1.6)	(3.0)	(3.0)	(3.3)
$0.05m/s^2$	0.9	1.2	0.4	0.9	0.9	0.9
	(3.8)	(4.6)	(1.7)	(3.2)	(3.2)	(3.1)
$0.1m/s^2$	1.1	1.9	0.4	1.0	0.9	0.9
	(4.5)	(6.6)	(1.9)	(3.6)	(3.2)	(3.5)
$0.2m/s^2$	1.6	3.6	0.6	1.3	1.0	1.2
	(6.0)	(12.6)	(2.9)	(5.3)	(4.1)	(4.8)
$0.4m/s^2$	2.5	6.7	0.9	2.1	1.2	1.6
	(9.5)	(23.0)	(4.7)	(8.9)	(5.4)	(7.1)
$0.8m/s^2$	5.3	12.8	1.8	3.9	2.0	2.7
	(19.8)	(45.7)	(8.9)	(16.3)	(9.9)	(12.5)
noise rms	$\ddot{x}_0$	$\ddot{y}_0$	$\ddot{z}_0$	$\ddot{\phi}_0$	$\ddot{\theta}_0$	$\ddot{\psi}_0$
$0.025m/s^2$	0.6	0.5	0.2	0.3	0.2	0.2
	(1.8)	(1.9)	(1.3)	(1.4)	(1.1)	(1.3)
$0.05m/s^2$	0.5	0.6	0.2	0.4	0.2	0.3
	(2.1)	(2.4)	(1.3)	(1.9)	(1.2)	(1.5)
$0.1m/s^2$	0.6	0.9	0.3	0.7	0.3	0.4
	(2.6)	(3.6)	(2.0)	(3.3)	(1.8)	(2.3)
$0.2m/s^2$	0.9	1.4	0.6	1.3	0.5	0.8
	(4.4)	(6.6)	(3.2)	(6.5)	(2.9)	(4.2)
$0.4m/s^2$	1.6	2.5	1.1	2.5	1.0	1.5
	(8.4)	(13.0)	(5.8)	(12.8)	(5.4)	(7.8)
$0.8m/s^2$	3.2	4.9	2.1	5.0	1.9	2.9
	(16.4)	(25.3)	(11.7)	(24.5)	(10.5)	(15.1)

Table C.6: Influence of zero-offset error in the accelerometer data

ϵ_{offset}	x_0	y_0	z_0	ϕ_0	θ_0	ψ_0
$0.05m/s^2$	3.0	2.8	1.0	1.8	1.6	0.9
	(12.8)	(12.1)	(4.4)	(3.1)	(3.4)	(3.4)
$0.1m/s^2$	2.6	3.0	1.0	2.9	2.3	0.9
	(10.8)	(13.4)	(4.3)	(3.7)	(3.3)	(3.3)
$0.2m/s^2$	3.1	2.9	1.3	5.1	4.7	1.0
	(13.1)	(12.7)	(5.7)	(4.1)	(4.2)	(4.3)
$0.4m/s^2$	3.4	3.3	2.2	10.8	9.0	1.5
	(14.7)	(14.2)	(8.9)	(5.8)	(6.2)	(6.5)
$0.8m/s^2$	4.0	4.5	3.8	21.4	18.2	2.5
	(17.2)	(19.0)	(16.0)	(10.0)	(11.0)	(11.5)
ϵ_{offset}	$\dot{x}_0$	$\dot{y}_0$	$\dot{z}_0$	$\dot{\phi}_0$	$\dot{\theta}_0$	$\dot{\psi}_0$
$0.05m/s^2$	1.0	0.9	0.4	1.0	0.9	1.0
	(4.1)	(3.7)	(2.0)	(3.1)	(3.1)	(3.3)
$0.1m/s^2$	0.9	1.0	0.6	0.9	0.9	0.9
	(3.6)	(4.2)	(2.5)	(3.2)	(3.4)	(3.5)
$0.2m/s^2$	1.2	1.1	0.9	1.0	1.1	1.1
	(5.0)	(5.0)	(3.7)	(4.1)	(4.1)	(4.4)
$0.4m/s^2$	1.6	1.6	1.8	1.4	1.5	1.5
	(6.8)	(7.1)	(7.4)	(6.3)	(6.7)	(6.7)
$0.8m/s^2$	2.6	2.9	3.5	2.3	2.5	2.6
	(11.3)	(12.4)	(14.8)	(10.2)	(11.0)	(11.2)
ϵ_{offset}	$\ddot{x}_0$	$\ddot{y}_0$	$\ddot{z}_0$	$\ddot{\phi}_0$	$\ddot{\theta}_0$	$\ddot{\psi}_0$
$0.05m/s^2$	0.6	0.5	0.4	0.2	0.2	0.2
	(2.0)	(1.7)	(1.5)	(1.3)	(1.2)	(1.4)
$0.1m/s^2$	0.6	0.6	0.6	0.3	0.3	0.4
	(1.9)	(2.3)	(2.1)	(1.5)	(1.8)	(1.8)
$0.2m/s^2$	0.8	0.8	1.4	0.6	0.6	0.6
	(2.9)	(3.0)	(3.5)	(2.7)	(2.7)	(2.8)
$0.4m/s^2$	1.3	1.3	2.4	1.1	1.2	1.2
	(4.9)	(5.6)	(7.0)	(5.5)	(5.8)	(6.0)
$0.8m/s^2$	2.4	2.6	4.9	2.2	2.3	2.4
	(9.9)	(10.7)	(13.6)	(10.3)	(11.2)	(11.5)

Table C.7: Influence of linearity error in the accelerometer data

ϵ_{nonlin}	x_0	y_0	z_0	ϕ_0	θ_0	ψ_0
1%	3.0	3.3	1.0	1.6	1.3	1.1
	(12.3)	(12.8)	(4.2)	(5.1)	(3.7)	(4.6)
2.5%	4.8	5.1	1.3	2.5	1.9	2.1
	(18.3)	(20.3)	(5.7)	(9.1)	(6.3)	(8.4)
5%	7.1	7.7	1.8	3.9	2.8	3.4
	(26.5)	(31.1)	(8.3)	(14.7)	(10.6)	(14.0)
ϵ_{nonlin}	$\dot{x}_0$	$\dot{y}_0$	$\dot{z}_0$	$\dot{\phi}_0$	$\dot{\theta}_0$	$\dot{\psi}_0$
1%	1.1	1.2	0.4	1.1	0.9	1.0
	(4.2)	(5.1)	(2.0)	(4.1)	(3.4)	(3.9)
2.5%	1.8	2.2	0.7	1.7	1.2	1.6
	(7.2)	(8.7)	(3.2)	(6.8)	(4.7)	(6.7)
5%	3.1	3.6	1.2	2.7	1.8	2.4
	(12.2)	(15.3)	(5.5)	(10.8)	(7.5)	(10.4)
ϵ_{nonlin}	$\ddot{x}_0$	$\ddot{y}_0$	$\ddot{z}_0$	$\ddot{\phi}_0$	$\ddot{\theta}_0$	$\ddot{\psi}_0$
1%	0.6	0.7	0.3	0.5	0.3	0.4
	(2.3)	(2.9)	(1.6)	(2.2)	(1.5)	(2.0)
2.5%	1.0	1.3	0.6	1.1	0.7	1.0
	(4.4)	(5.7)	(2.9)	(4.7)	(3.0)	(4.6)
5%	1.8	2.2	1.1	2.0	1.3	1.8
	(7.8)	(10.5)	(5.4)	(8.7)	(5.7)	(8.0)

Table C.8: Influence of accelerometers transverse sensitivity

Xsens	x_0	y_0	z_0	ϕ_0	θ_0	ψ_0
1%	3.9	6.8	1.1	2.5	1.6	1.5
	(15.3)	(22.7)	(4.5)	(6.8)	(4.0)	(5.8)
2%	6.0	11.2	1.5	4.0	2.7	2.6
	(21.0)	(38.1)	(6.8)	(12.5)	(7.4)	(9.9)
3%	8.4	18.1	1.9	6.6	3.7	3.7
	(30.5)	(64.2)	(8.9)	(21.2)	(11.4)	(14.2)
5%	11.7	22.8	2.8	8.6	5.5	5.5
	(43.1)	(80.5)	(12.6)	(26.7)	(14.7)	(21.5)
Xsens	$\dot{x}_0$	$\dot{y}_0$	$\dot{z}_0$	$\dot{\phi}_0$	$\dot{\theta}_0$	$\dot{\psi}_0$
1%	1.3	2.4	0.5	1.1	0.9	1.0
	(5.1)	(8.4)	(2.3)	(3.8)	(3.5)	(4.1)
2%	2.2	4.2	0.8	1.5	1.2	1.4
	(7.9)	(14.7)	(4.1)	(6.1)	(5.0)	(5.5)
3%	3.1	6.8	1.1	2.2	1.5	1.8
	(11.4)	(23.8)	(6.2)	(9.1)	(6.8)	(8.3)
5%	4.5	8.5	1.6	2.7	1.8	2.4
	(16.3)	(30.7)	(8.5)	(11.1)	(8.8)	(11.0)
Xsens	$\ddot{x}_0$	$\ddot{y}_0$	$\ddot{z}_0$	$\ddot{\phi}_0$	$\ddot{\theta}_0$	$\ddot{\psi}_0$
1%	0.6	0.9	0.4	0.4	0.3	0.4
	(2.2)	(3.7)	(2.1)	(2.0)	(1.9)	(2.2)
2%	0.9	1.5	0.7	0.7	0.5	0.6
	(3.9)	(6.3)	(3.9)	(3.7)	(3.3)	(3.8)
3%	1.2	2.3	1.1	1.1	0.8	1.0
	(5.7)	(10.1)	(6.3)	(6.0)	(5.3)	(6.5)
5%	1.8	2.9	1.8	1.6	1.2	1.4
	(8.2)	(13.7)	(8.9)	(8.2)	(7.2)	(9.0)

Appendix D

Wave height data comparison

The figures in this appendix illustrate the results of the comparison between NWW3 and GAPS data over the period of time corresponding to the 2000-01 edition of the Vendée Globe Race.

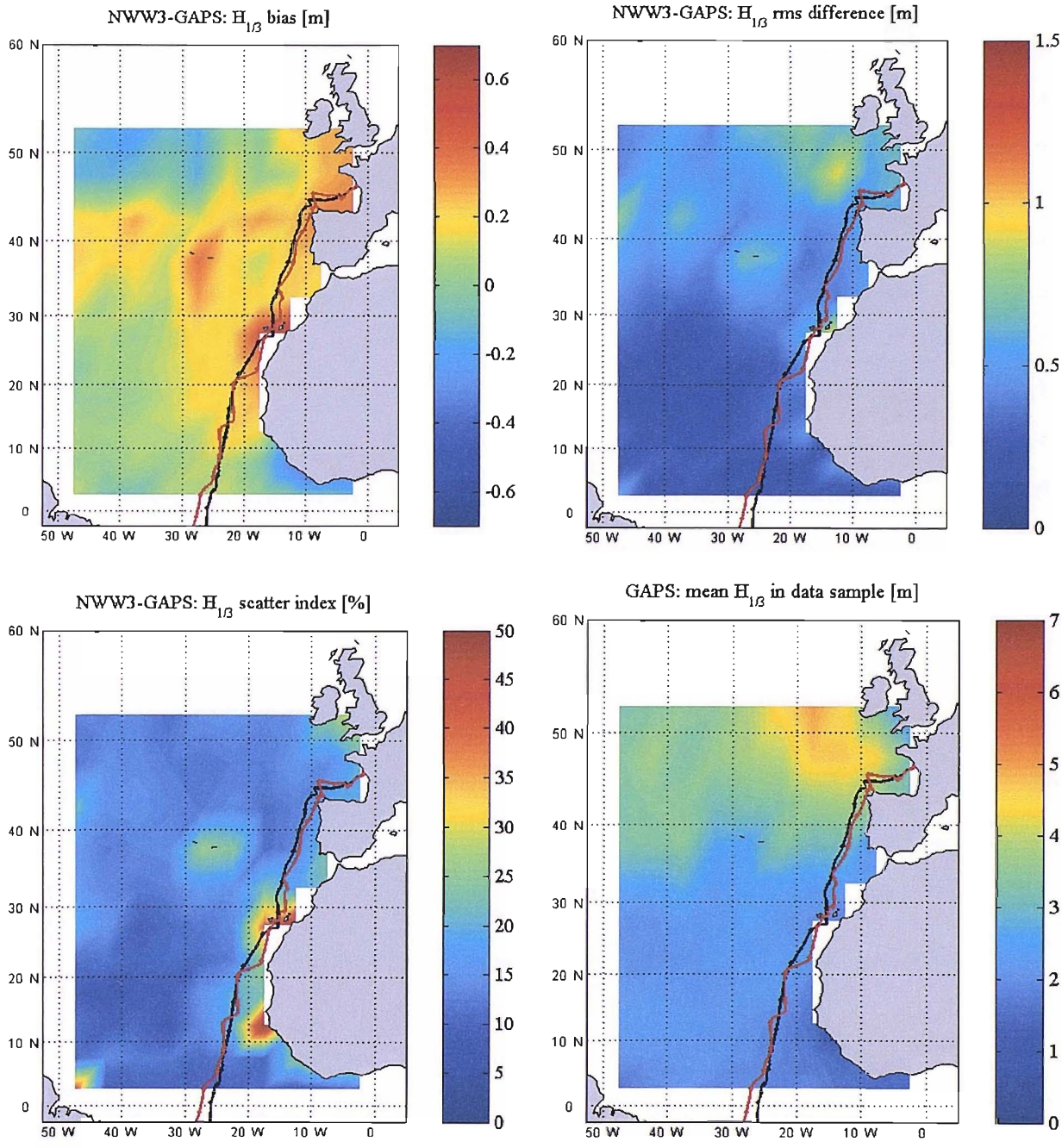

Figure D.1: Comparison of NWW3 and GAPS $H_{1/3}$ data: North Atlantic, 1 - 30 November 2000 (9583 co-located data points)

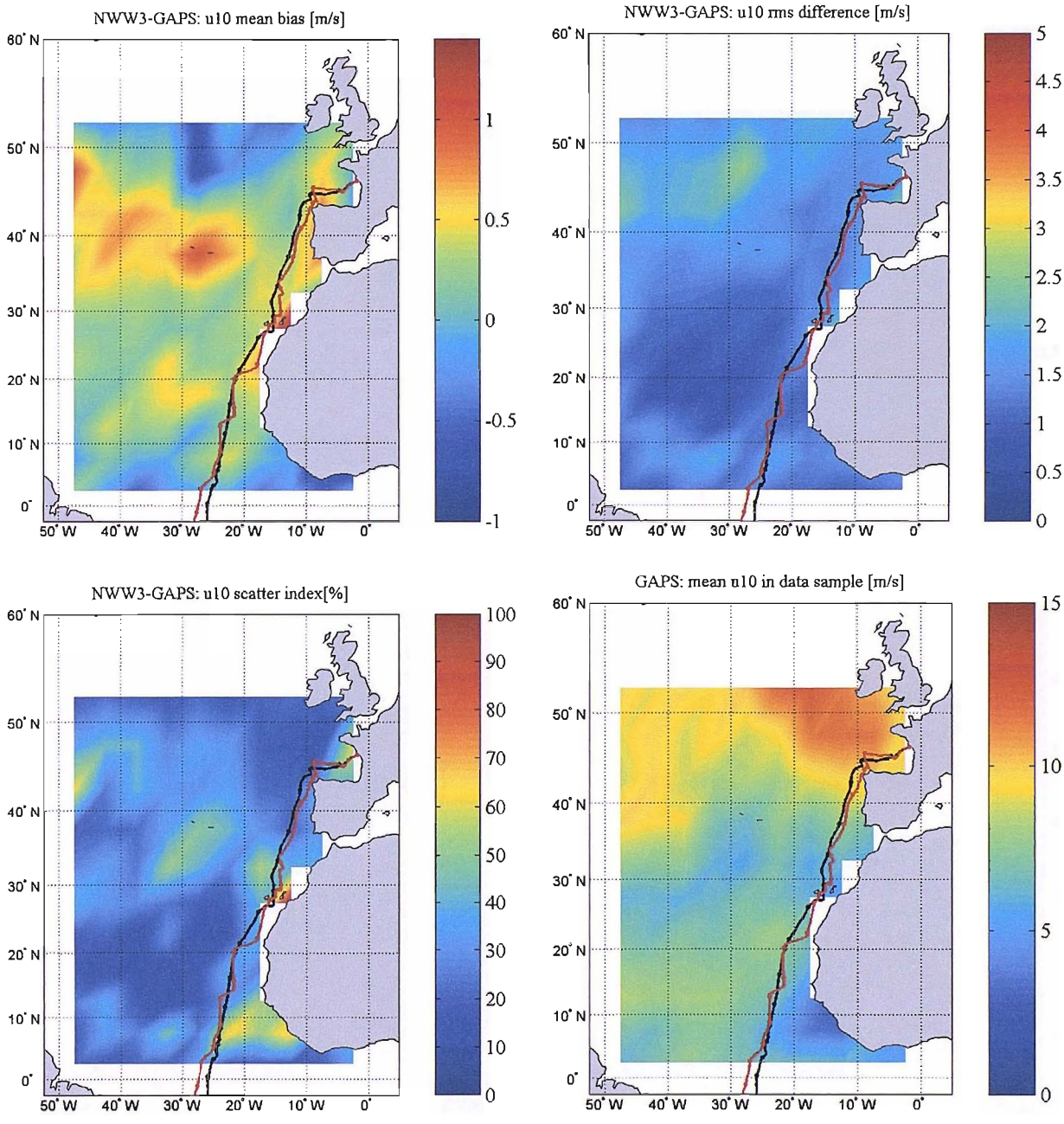

Figure D.2: Comparison of NWW3 and GAPS $u10$ data: North Atlantic, 1 - 30 November 2000 (9583 co-located data points)

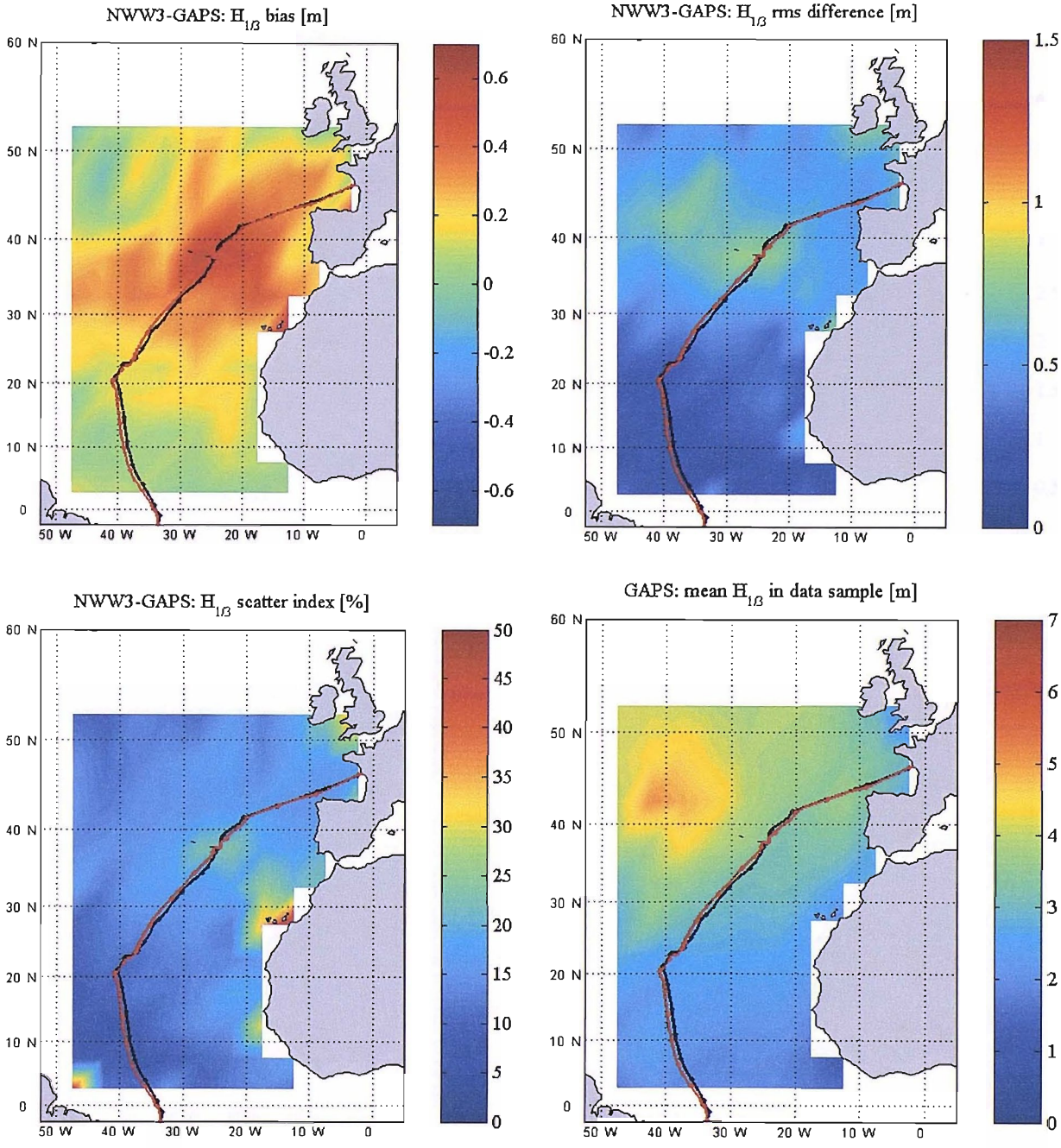

Figure D.3: Comparison of NWW3 and GAPS $H_{1/3}$ data: North Atlantic, 20 February - 31 March 2001 (7281 co-located data points)

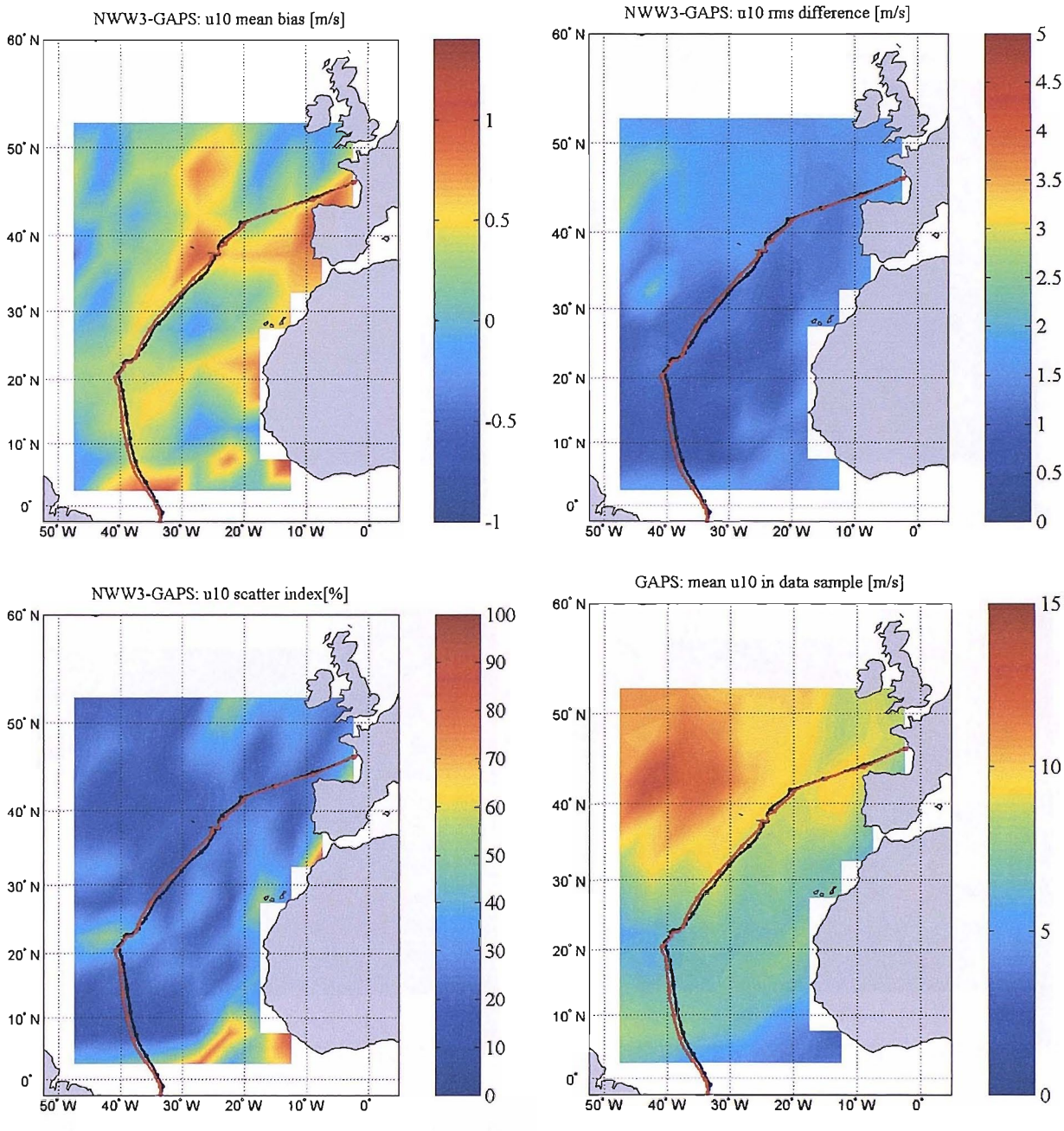

Figure D.4: Comparison of NWW3 and GAPS $u10$ data: North Atlantic, 20 February - 31 March 2001 (7281 co-located data points)

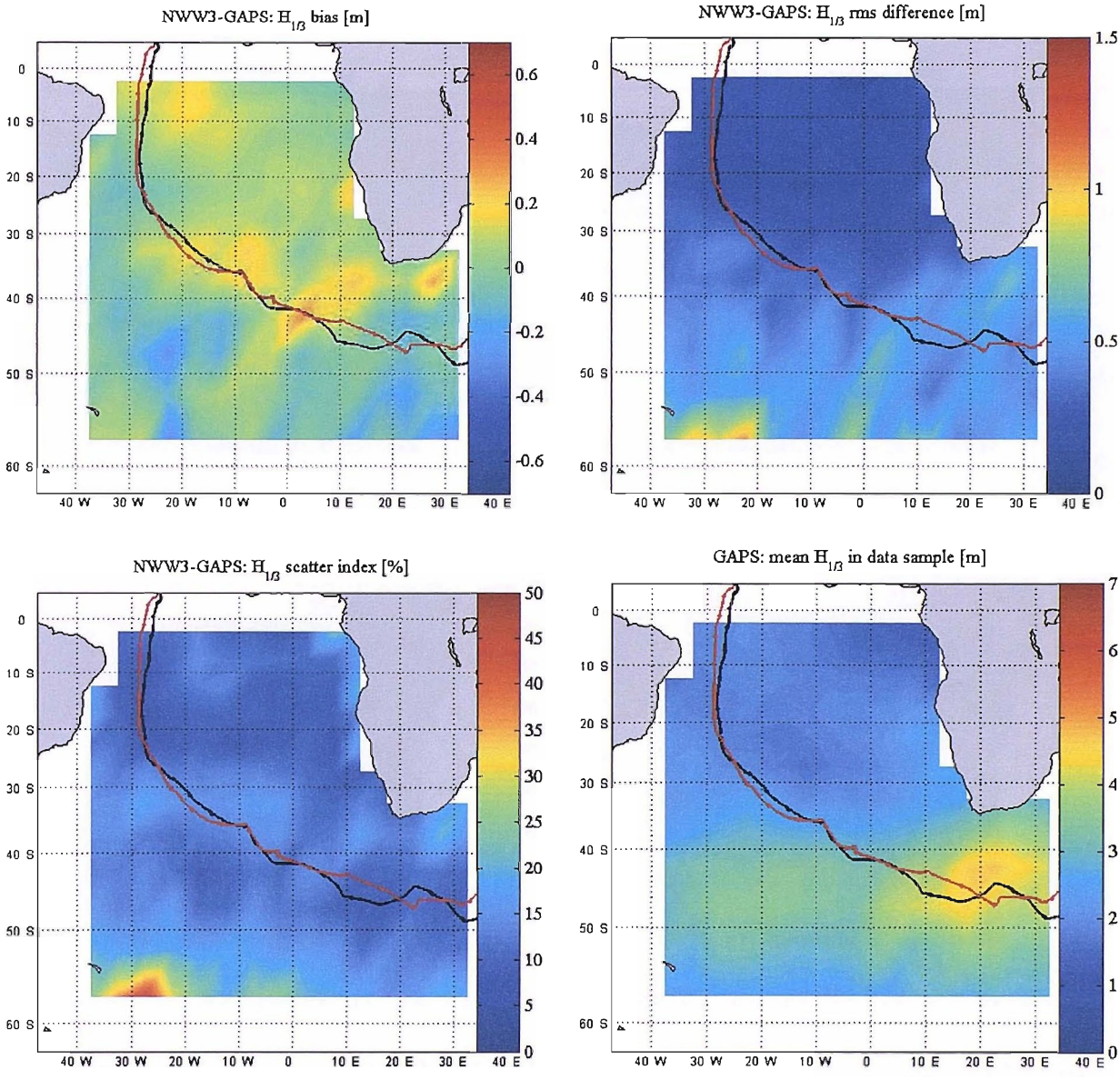

Figure D.5: Comparison of NWW3 and GAPS $H_{1/3}$ data: South Atlantic, 20 November - 20 December 2000 (17204 co-located data points)

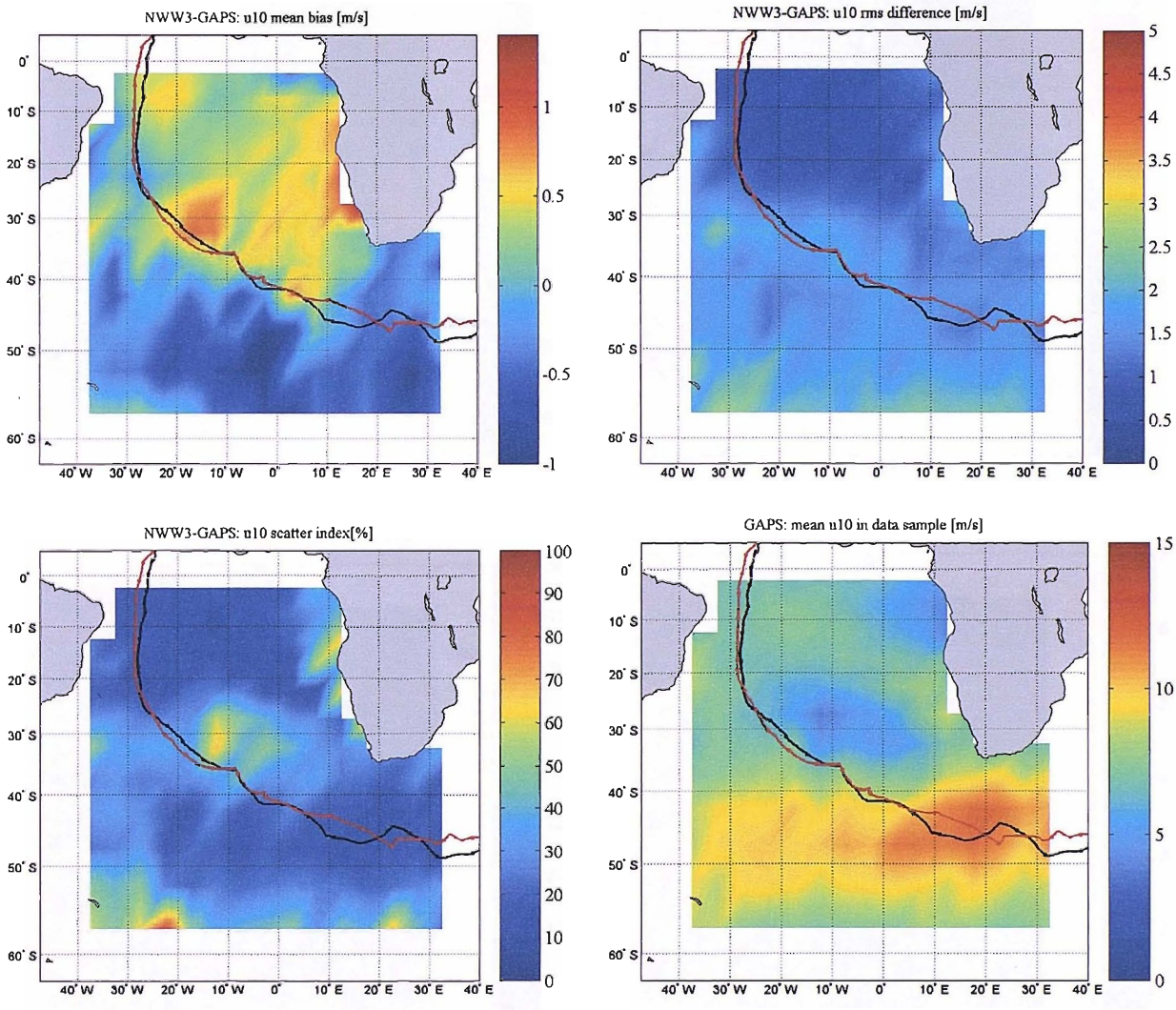

Figure D.6: Comparison of NWW3 and GAPS $u10$ data: South Atlantic, 20 November - 20 December 2000 (17204 co-located data points)

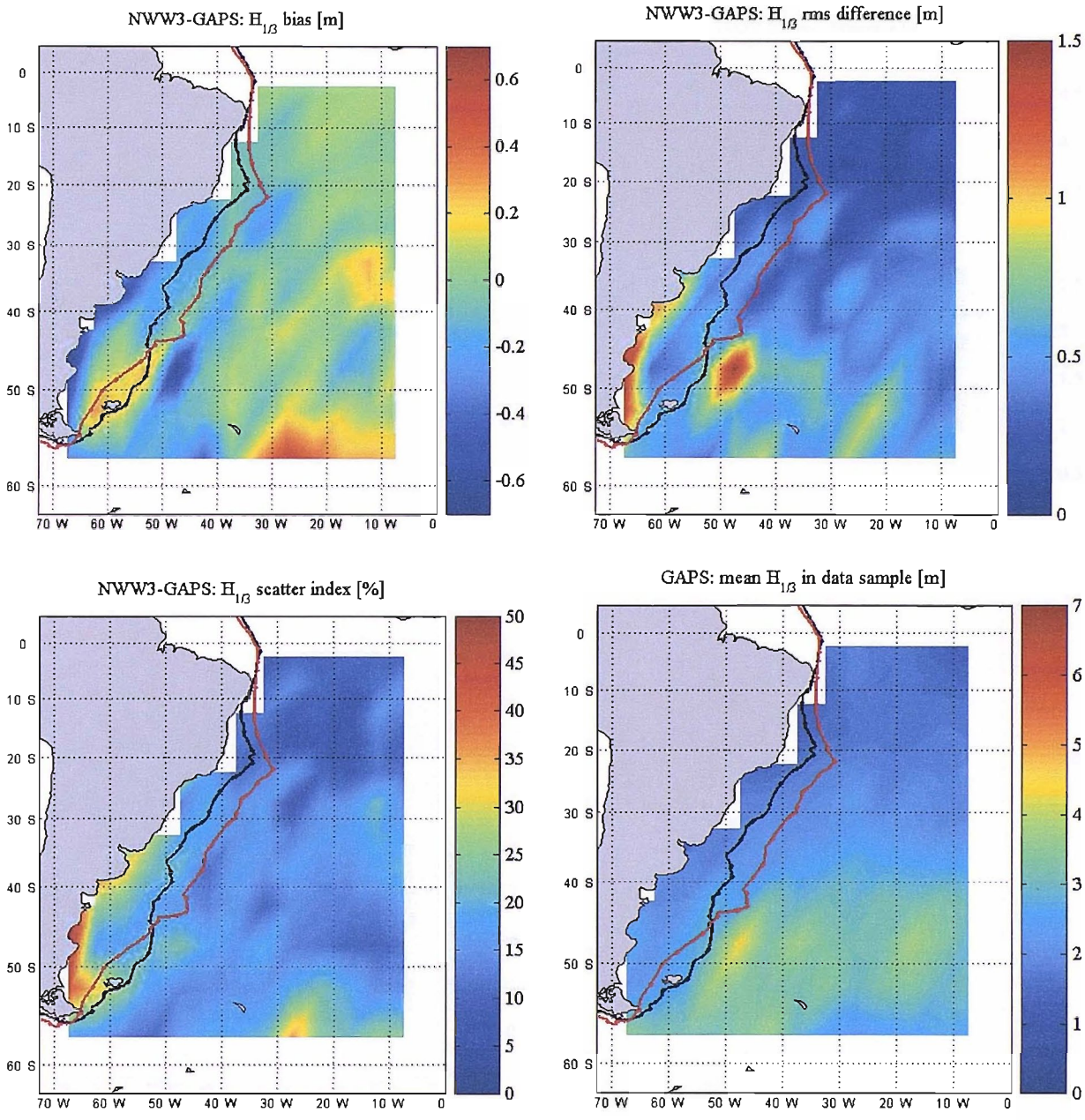

Figure D.7: Comparison of NWW3 and GAPS $H_{1/3}$ data: South Atlantic, 1 - 28 February 2001 (6654 co-located data points)

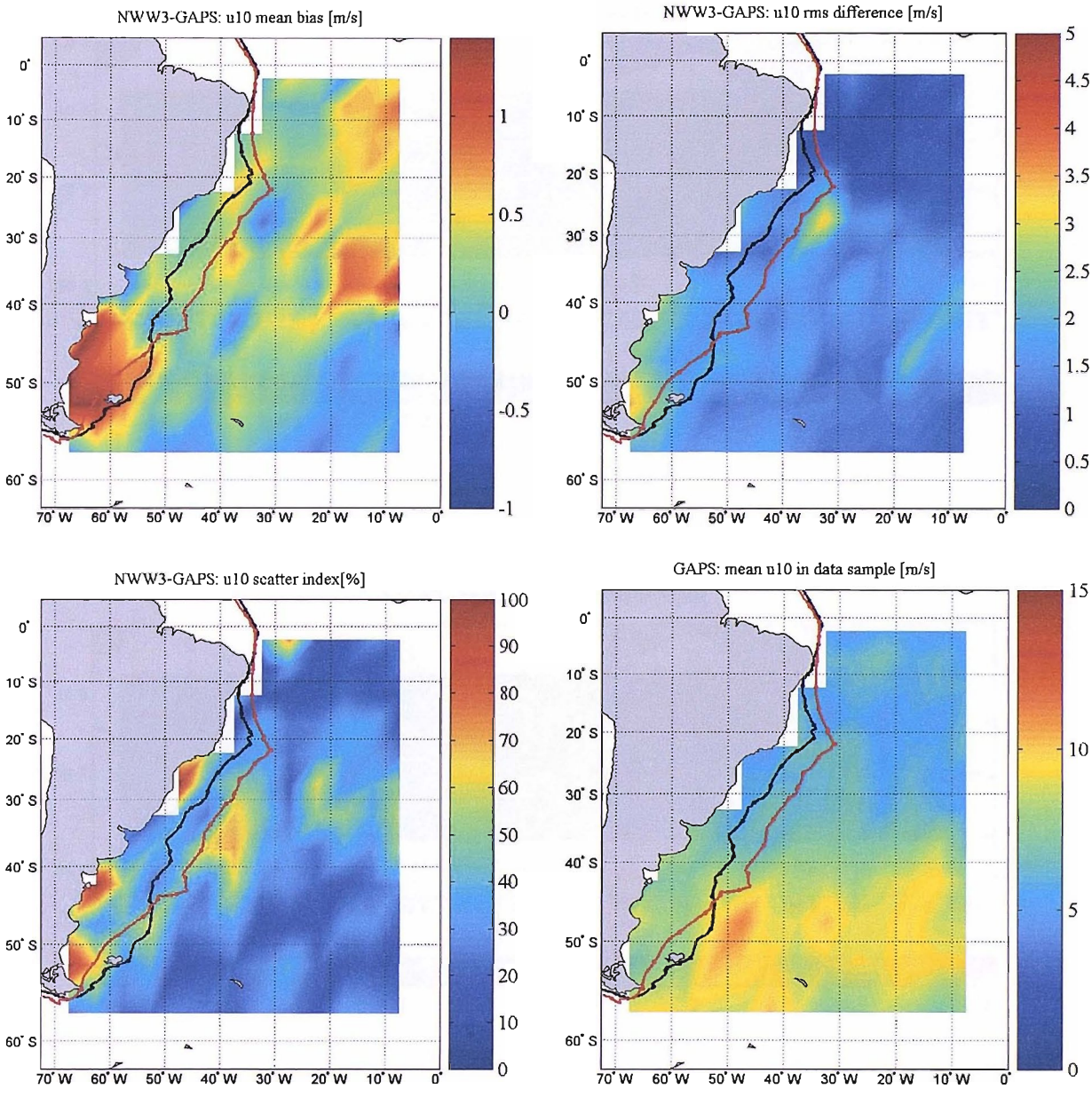

Figure D.8: Comparison of NWW3 and GAPS $u10$ data: South Atlantic, 1 - 28 February 2001 (6654 co-located data points)

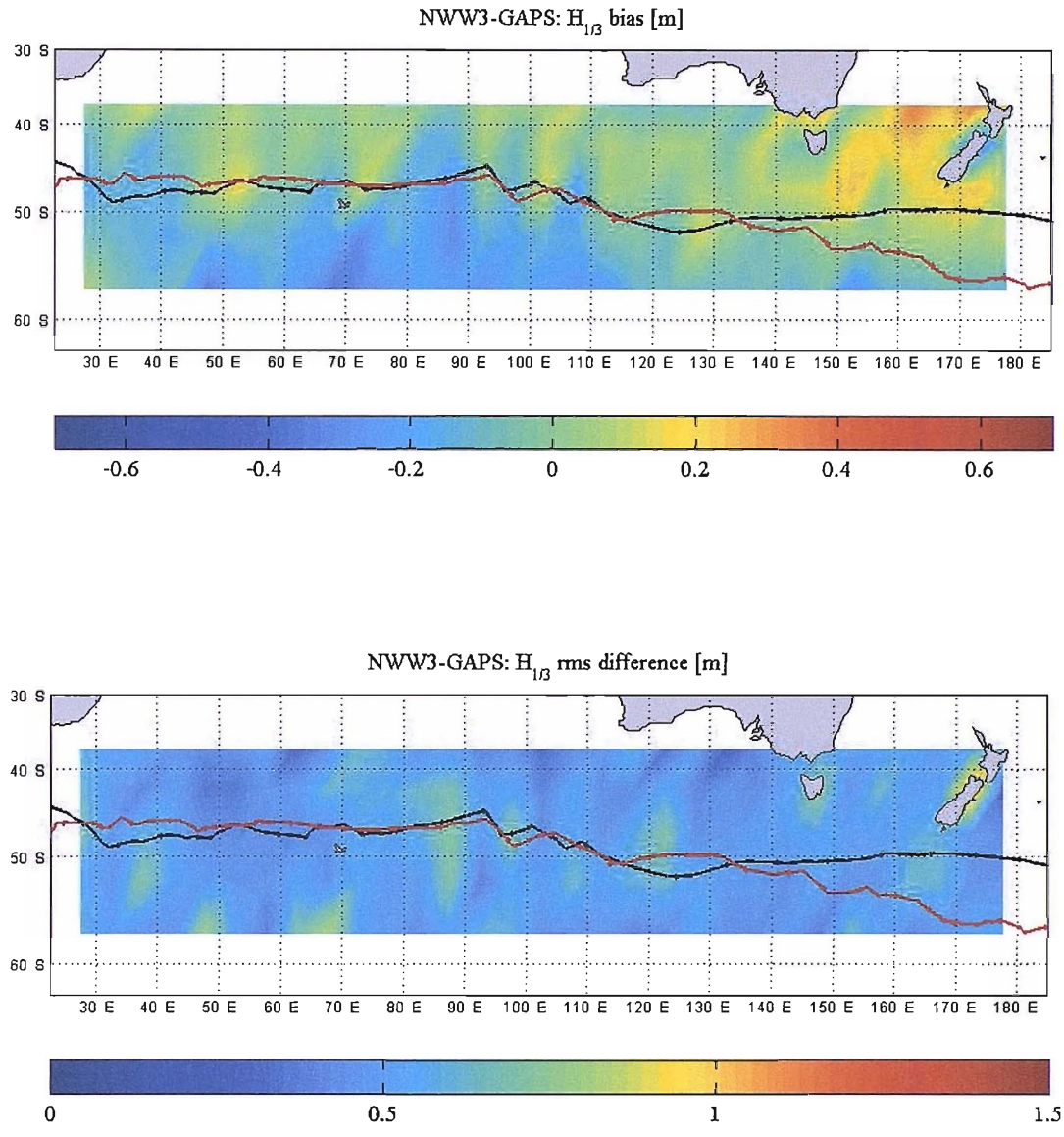

Figure D.9: Comparison of NWW3 and GAPS $H_{1/3}$ data: Indian Ocean, 15 December - 15 January 2000-1 (20633 co-located data points)

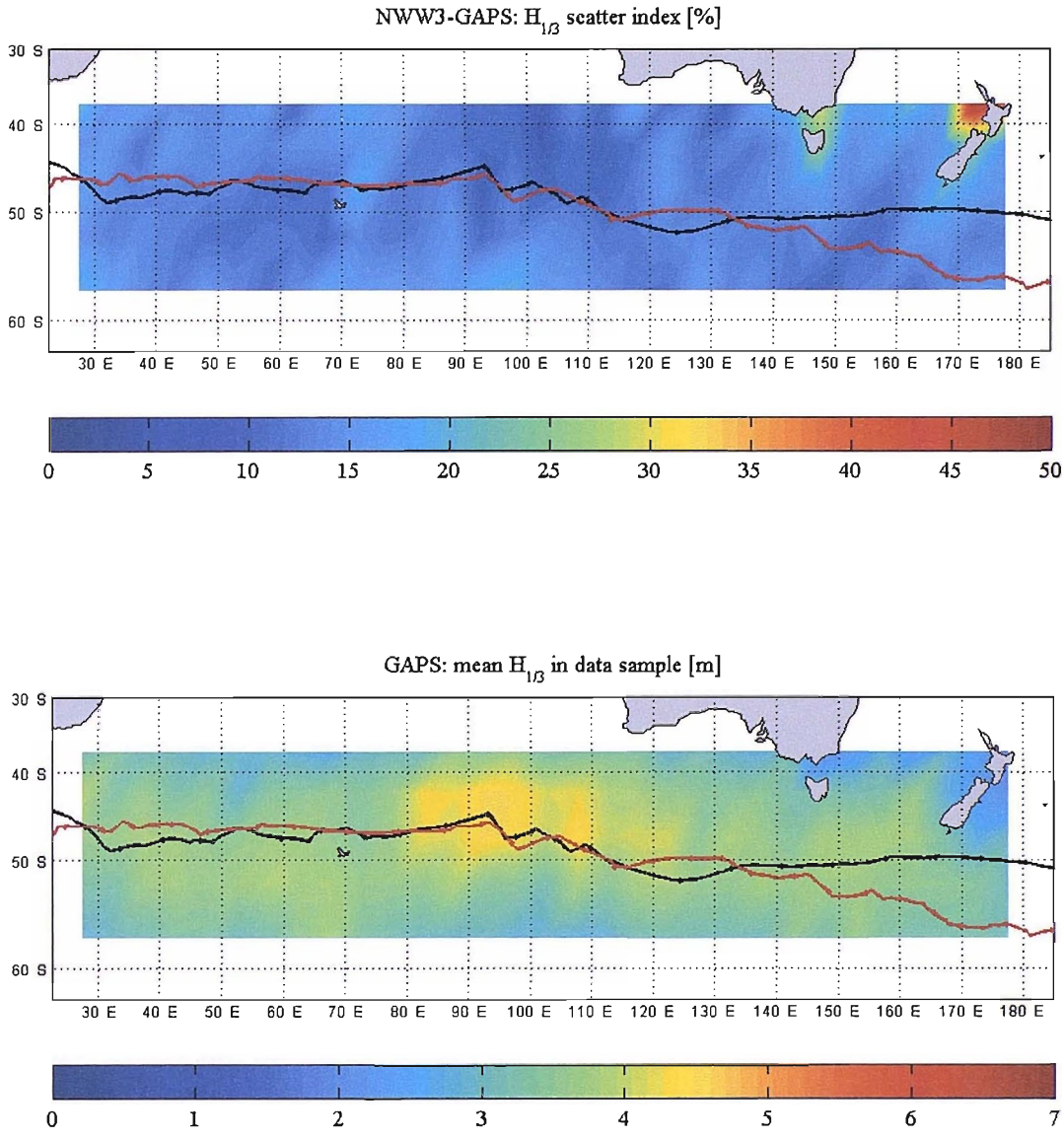

Figure D.10: Comparison of NWW3 and GAPS $H_{1/3}$ data: Indian Ocean, 15 December - 15 January 2000-1 (20633 co-located data points)

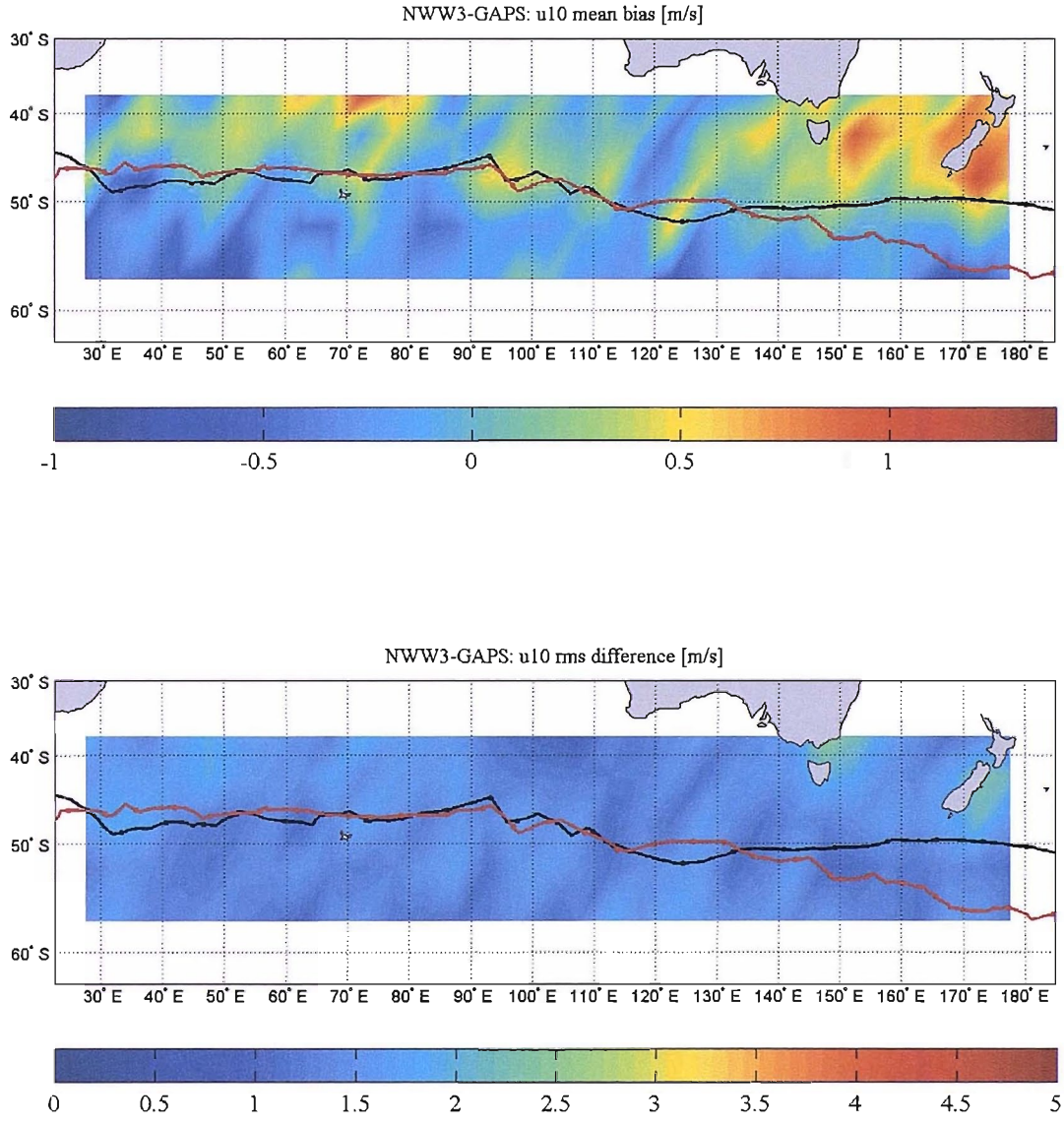

Figure D.11: Comparison of NWW3 and GAPS $u10$ data: Indian Ocean, 15 December - 15 January 2000-1 (20633 co-located data points)

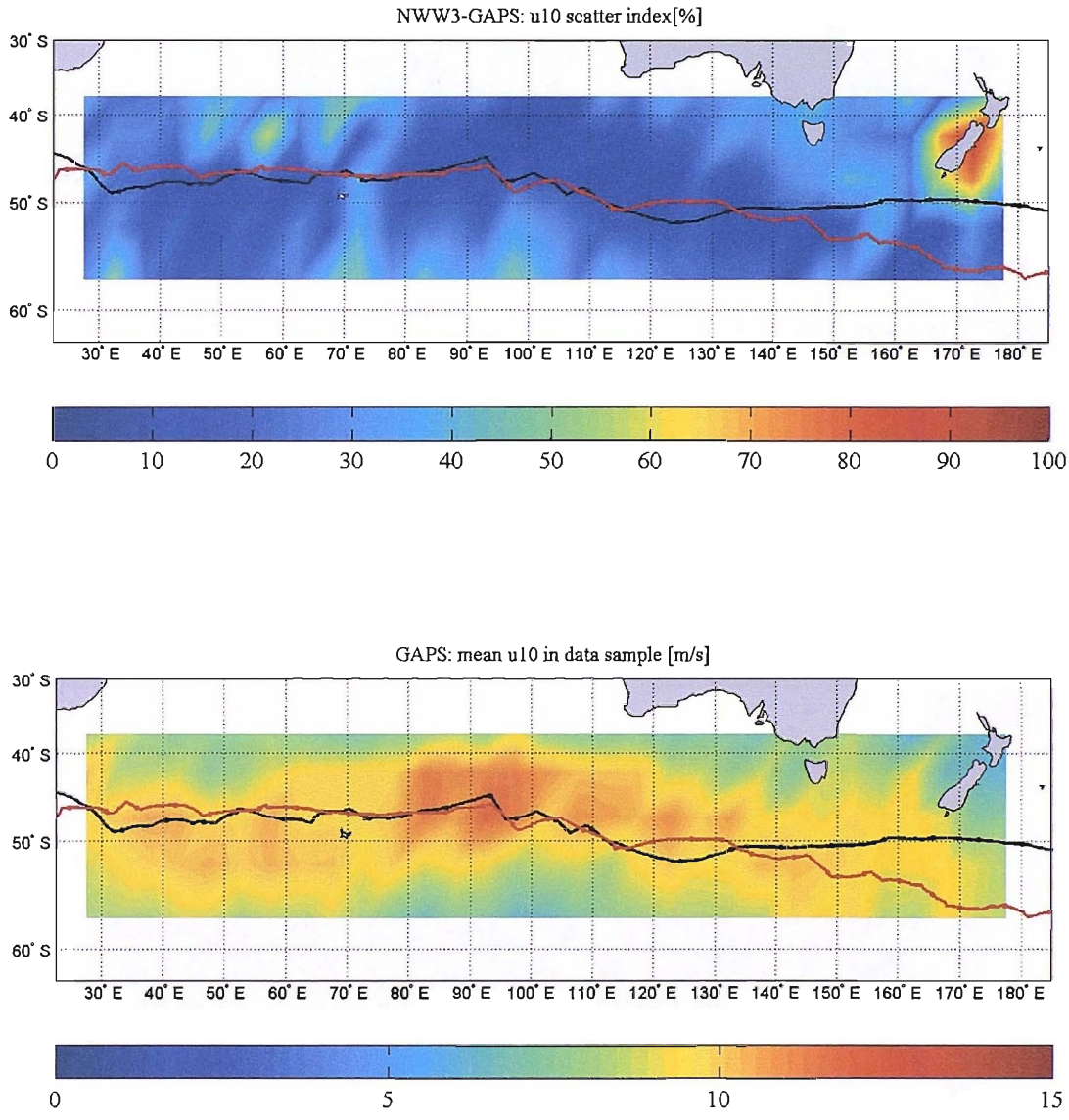

Figure D.12: Comparison of NWW3 and GAPS $u10$ data: Indian Ocean, 15 December - 15 January 2000-1 (20633 co-located data points)

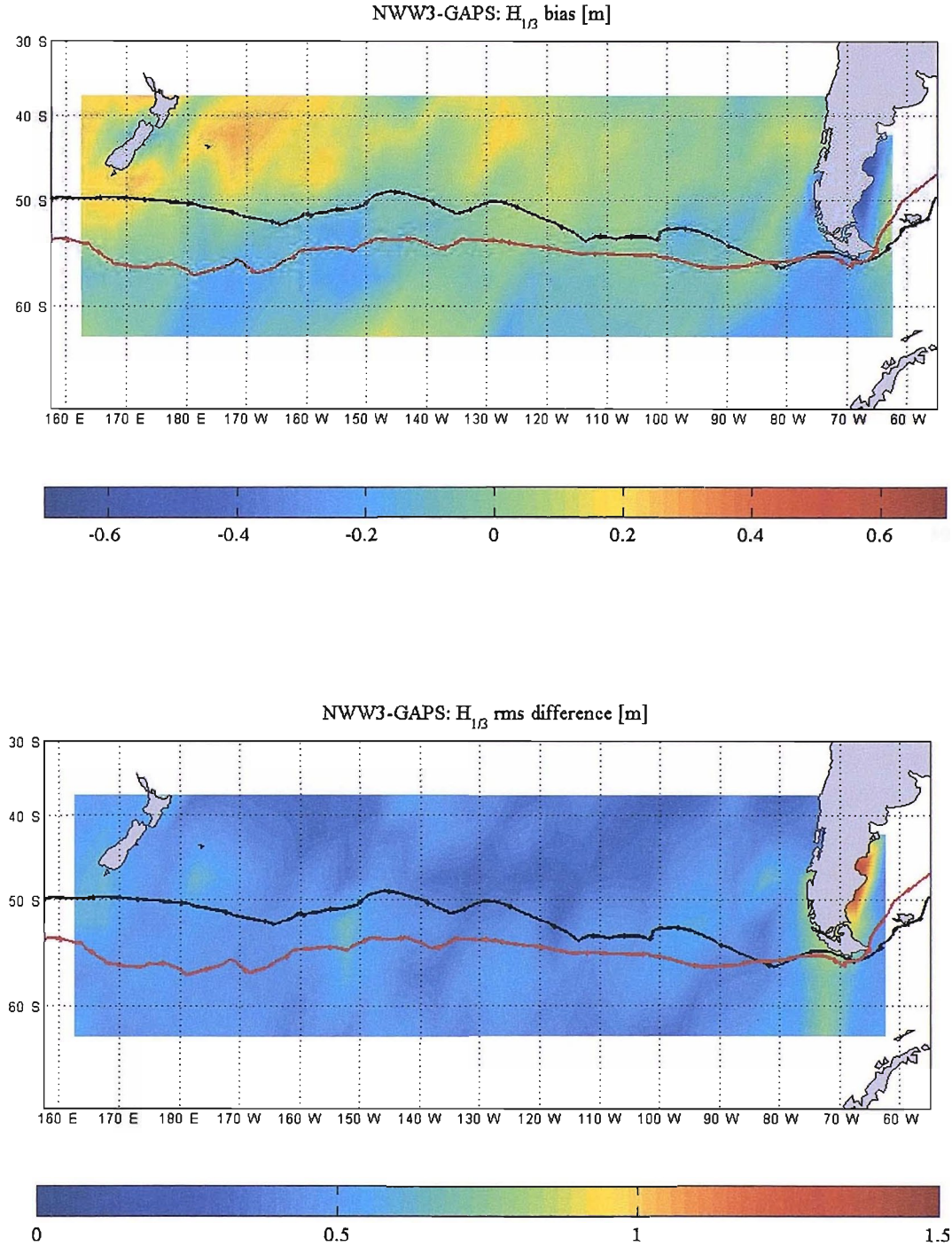

Figure D.13: Comparison of NWW3 and GAPS $H_{1/3}$ data: South Pacific, 20 December - 9 February 2000-1 (40085 co-located data points)

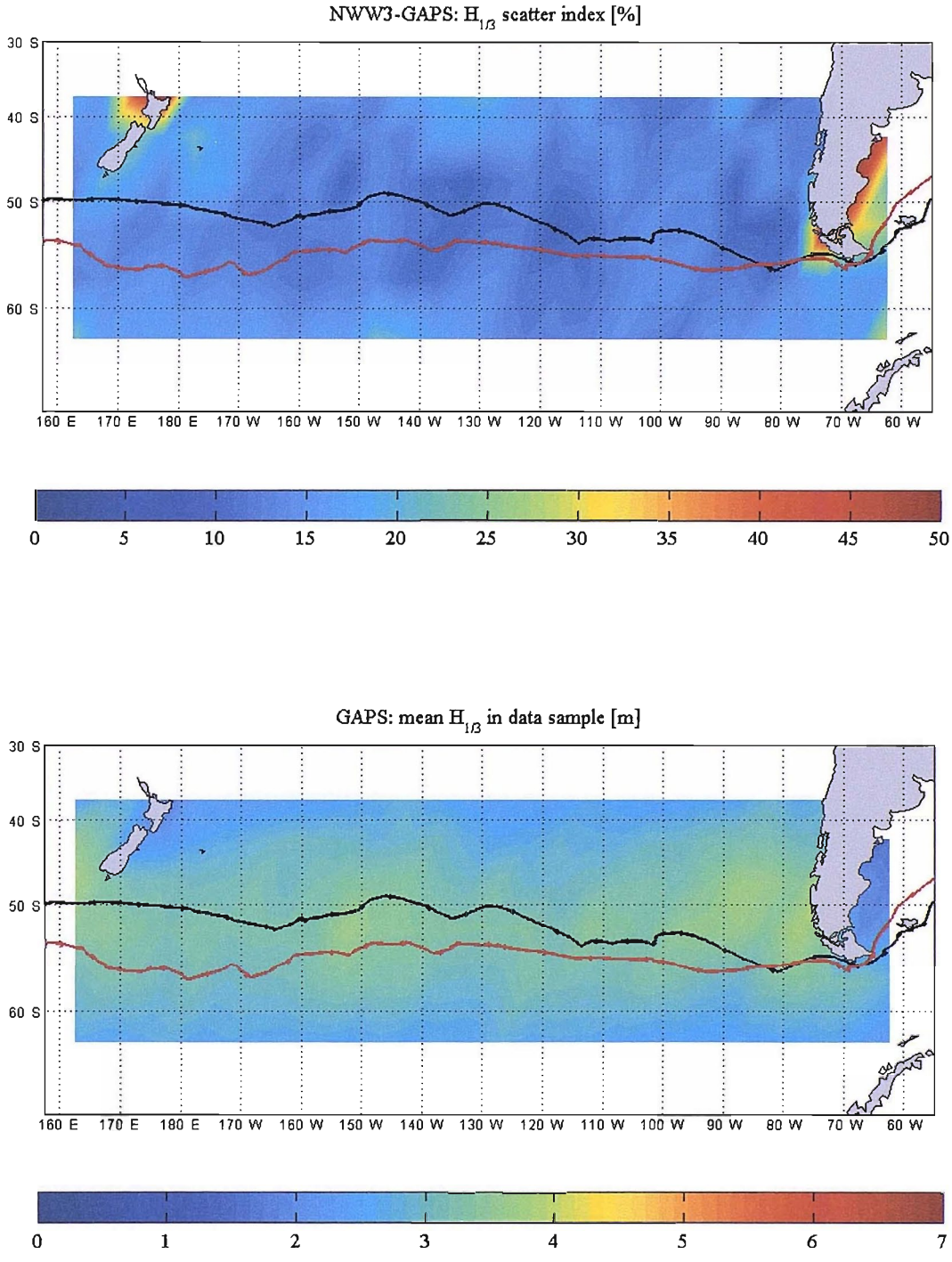

Figure D.14: Comparison of NWW3 and GAPS $H_{1/3}$ data: South Pacific, 20 December - 9 February 2000-1 (40085 co-located data points)

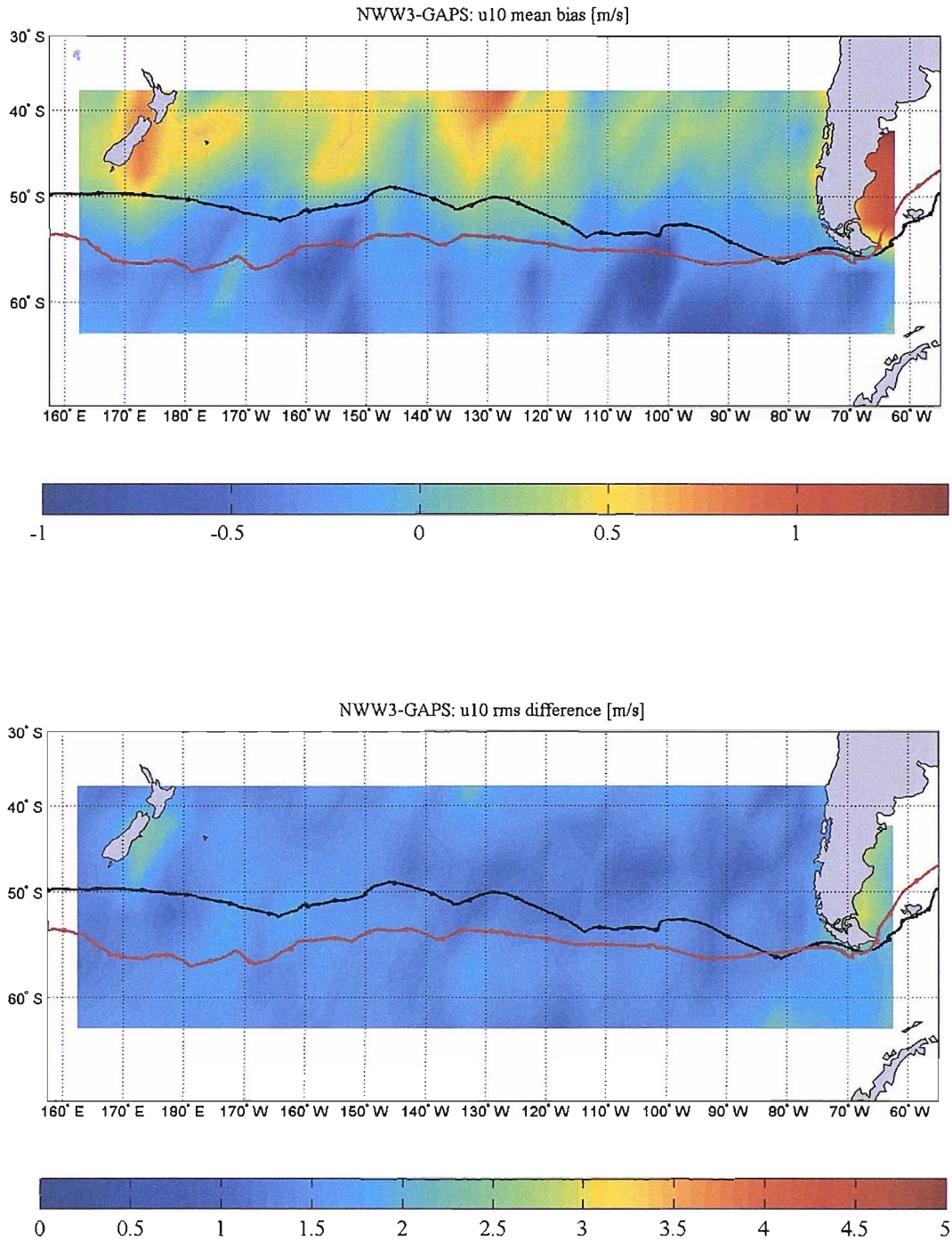

Figure D.15: Comparison of NWW3 and GAPS $u10$ data: South Pacific, 20 December - 9 February 2000-1 (40085 co-located data points)

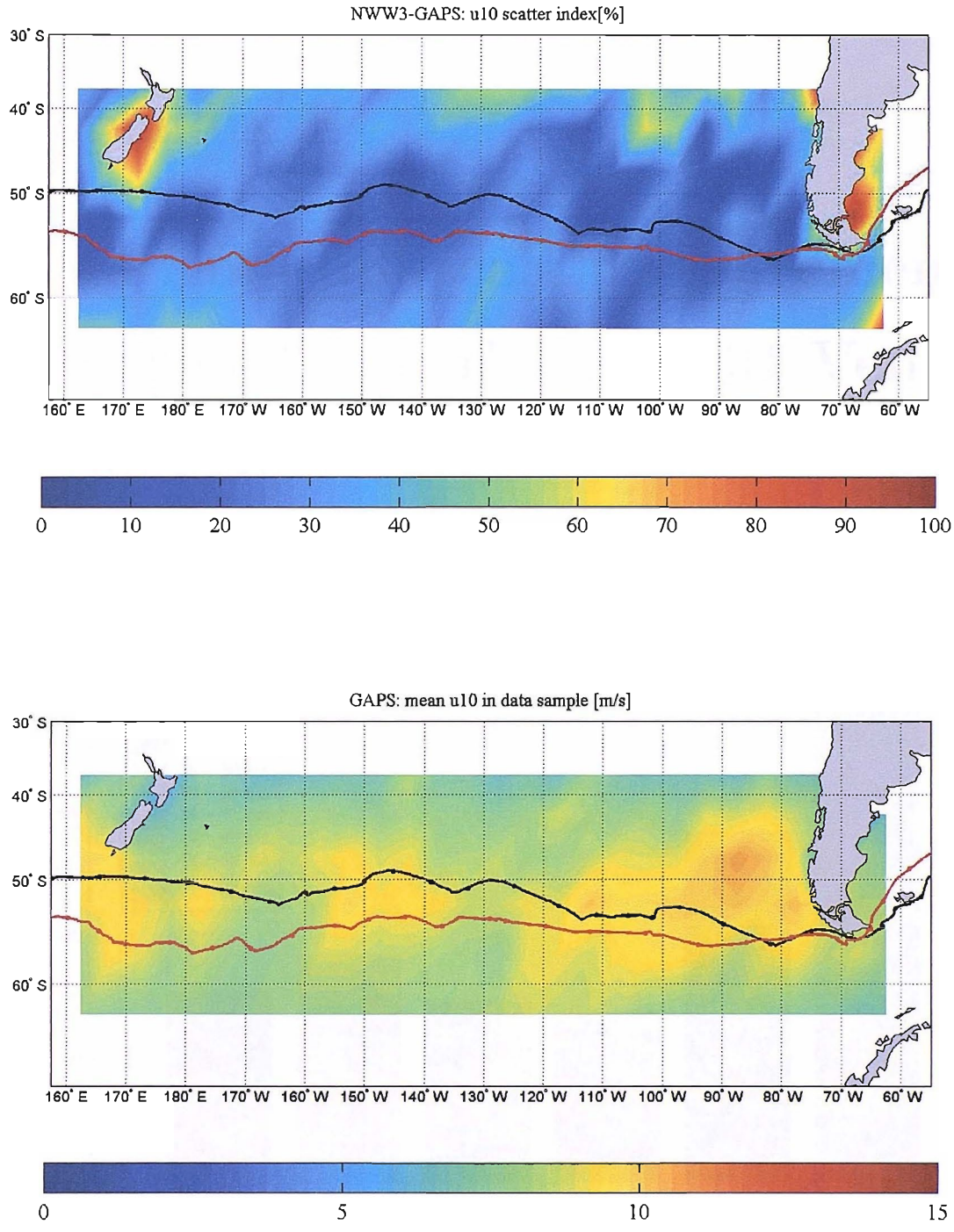

Figure D.16: Comparison of NWW3 and GAPS $u10$ data: South Pacific, 20 December - 9 February 2000-1 (40085 co-located data points)

Appendix E

Data from full scale measurements performed over the 2000-01 Vendée Globe Race

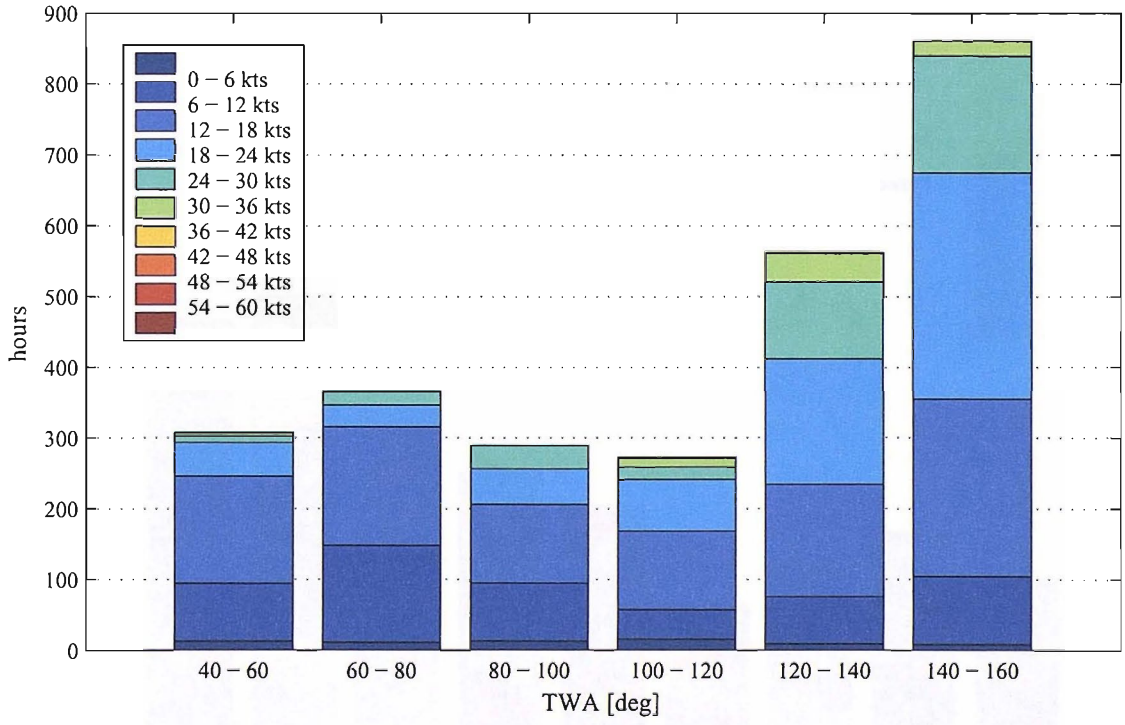

Figure E.1: Boat#1: summary of measured true wind angle and true wind speed.

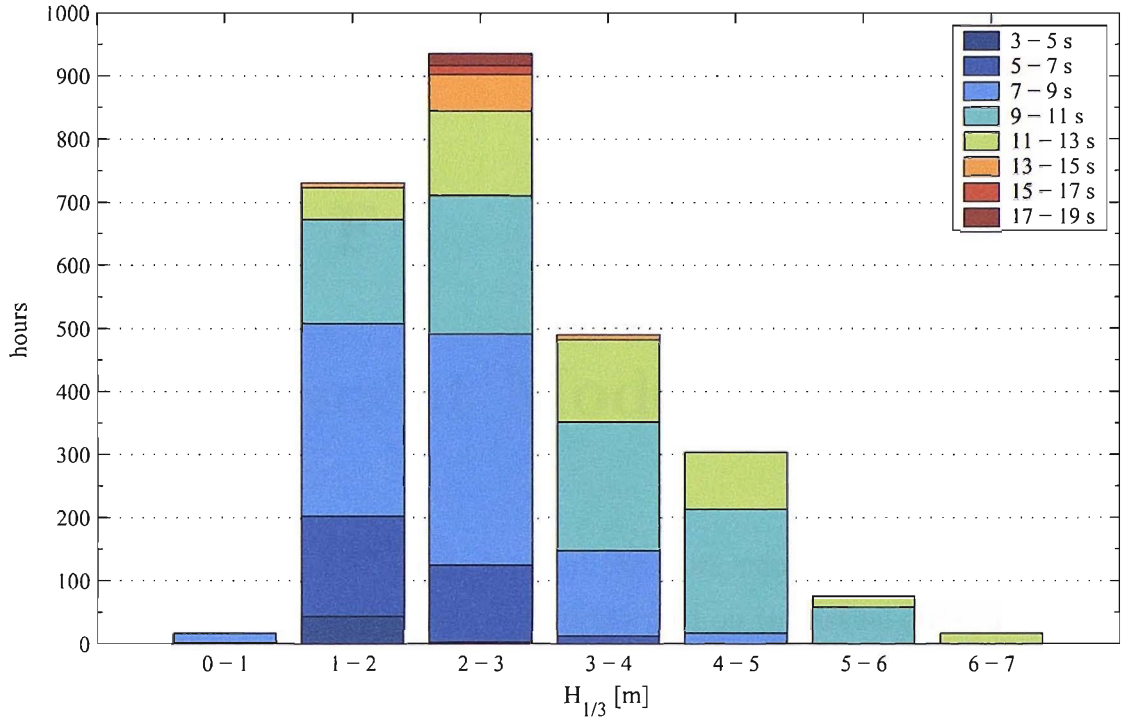

Figure E.2: Boat#1: summary of encountered significant wave height and wave peak period.

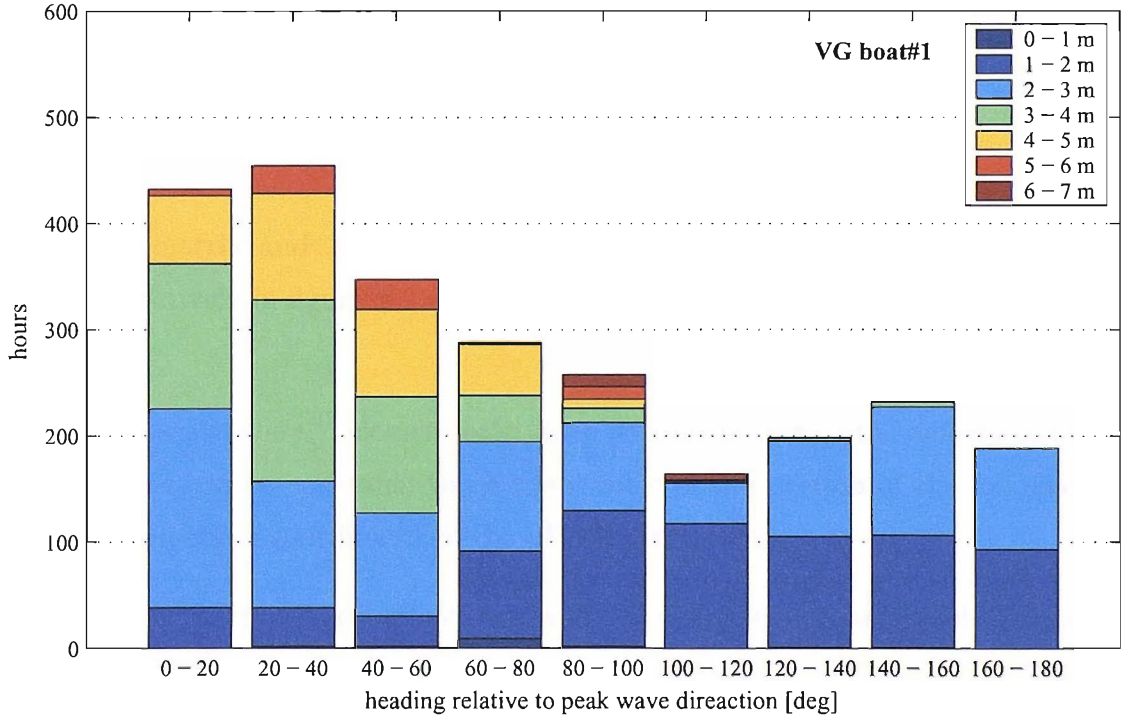

Figure E.3: Boat#1: summary of heading relative to the peak wave direction and significant wave height.

Appendix F

Finite Element Model of the Keel

The present appendix contains details about the finite element model used to analyse the keel and results from the modal tests performed on the actual structure.

F.1 The Mass and Stiffness Matrix

The finite element model has been developed in MATLAB through a group of ad hoc functions. The keel fin is described through Euler-Bernoulli beam elements. Each element has two nodes and six degrees of freedom per node. The generic vector of the nodal displacements for element n is written in the form:

$$\underline{v}_n^T = [u_1, v_1, w_1, \theta_{u_1}, \theta_{v_1}, \theta_{w_1}, u_2, v_2, w_2, \theta_{u_2}, \theta_{v_2}, \theta_{w_2}]$$

The mass matrix and stiffness matrix for the generic n^{th} element are defined as shown respectively in figure F.1 and figure F.2. The following terms are used in their definition:

- m_n: mass of the n^{th} element calculated as the product of the density of the foil (assumed to be constant) times the volume of the portion of the foil spanning between the x coordinates of the n^{th} element nodes
- I_{u_n},I_{v_n},$I_{\dot{w}_n}$: mass moment of inertia of the n^{th} element respectively around the local axes $\mathcal{U}$,$\mathcal{V}$,$\mathcal{W}$.
- l: length of the element (all elements have the same length)

- E_K and G_K: respectively the equivalent elastic modulus and shear modulus of the material of the fin. The fin is considered to be made of uniform isotropic material.

- J_{u_n} and J_{v_n}: area moment of inertia of the n^{th} element respectively about its longitudinal axis $\mathcal{U}$ and transversal axis $\mathcal{V}$. Although the dimensions of the section of the fin vary linearly along the span, the beam elements used for this analysis are assumed to have a constant section corresponding to the section of the fin at midspan between the x coordinates of the element's nodes.

- S_n: axial pre-constraint on the n^{th} element resulting from the weight force acting on the bulb and on the fin. This force is calculated by taking into account the average heel angle of the boat and eventually the swing angle of the keel. It can be shown that the effect of the variation of heel angle over the time-scales typically under exam in this study is negligible, thus justifying the use of a constant average value and avoiding the need for re-evaluating the stiffness matrix at different time steps.

The effects of the mass of the bulb are accounted for by adding the following matrix to the mass matrix of the element corresponding to the tip of the fin:

$$\left[\begin{array}{c|cccccc} [0] & \multicolumn{6}{c}{[0]} \\ \hline & m_b & 0 & 0 & 0 & 0 & -m_b \cdot d_b \\ & 0 & m_b & 0 & 0 & 0 & 0 \\ & 0 & 0 & m_b & m_b \cdot d_b & 0 & 0 \\ [0] & 0 & 0 & m_b \cdot d_b & I_{u_b} + m_b \cdot d_b^2 & 0 & 0 \\ & 0 & 0 & 0 & 0 & I_{v_b} & 0 \\ & -m_b \cdot d_b & 0 & 0 & 0 & 0 & I_{u_b + m_b \cdot d_b^2} \end{array}\right]$$

where m_b is the mass of the bulb, I_{v_b} and I_{u_b} are respectively the mass moment of inertia of the bulb around its axis of symmetry and around any axis perpendicular to it and passing through its centre of gravity, and d_b is the longitudinal distance (i.e. along the $\mathcal{Y}_k$ axis) between the centre of gravity of the bulb and the node at the tip of the fin. The non-diagonal terms $m_b \cdot d_b$ are introduced in order to model the coupling between lateral bending and torsion due to the longitudinal separation between the shear centre of the fin and the centre of gravity of the bulb.

The constraints imposed by the keel to hull joint on the rotation about $\mathcal{Y}_k$ and $\mathcal{Z}_k$ at the root are modelled by setting the fifth and sixth diagonal terms of the stiffness matrix of the element at the fin root equal respectively to the stiffnesses of rotary springs γ_y and γ_z (cf. table 6.2).

$$
M_n = \begin{bmatrix}
\frac{1}{3}m_n & & & & & & & & & & & & \\
0 & \frac{13}{35}m_n + \frac{6I_{w_n}}{5l} & & & & & & & & & & & \\
0 & 0 & \frac{13}{35}m_n + \frac{6I_{v_n}}{5l} & & & & & & & & & & \\
0 & 0 & 0 & \frac{1}{3}I_{u_n}\, l & & & & & & & & & \\
0 & 0 & -\frac{11l}{210}m_n - \frac{I_{v_n}}{10} & 0 & \frac{l^2}{105}m_n + \frac{2I_{v_n}\, l}{15} & & & & & & & & \\
0 & \frac{11l}{210}m_n + \frac{I_{w_n}}{10} & 0 & 0 & 0 & \frac{l^2}{105}m_n + \frac{2I_{w_n}\, l}{15} & & & & & & & \\
\frac{1}{6}m_n & 0 & 0 & 0 & 0 & 0 & \frac{1}{3}m_n & & & & & & \\
0 & \frac{9}{70}m_n - \frac{6I_{w_n}}{5l} & 0 & 0 & 0 & -\frac{13l}{420}m_n - \frac{I_{w_n}}{10} & 0 & \frac{13}{35}m_n + \frac{6I_{w_n}}{5l} & & & & & \\
0 & 0 & \frac{9}{70}m_n - \frac{6I_{v_n}}{5l} & 0 & -\frac{13l}{420}m_n + \frac{I_{v_n}}{10} & 0 & 0 & 0 & \frac{13}{35}m_n + \frac{6I_{v_n}}{5l} & & & & \\
0 & 0 & 0 & \frac{1}{6}I_{u_n}\, l & 0 & 0 & 0 & 0 & 0 & \frac{1}{3}I_{u_n}\, l & & & \\
0 & 0 & \frac{13l}{420}m_n - \frac{I_{v_n}}{10} & 0 & -\frac{l^2}{140}m_n - \frac{I_{v_n}\, l}{30} & 0 & 0 & 0 & \frac{11l}{210}m_n + \frac{I_{v_n}}{10} & 0 & \frac{l^2}{105}m_n + \frac{2I_{v_n}\, l}{15} & & \\
0 & -\frac{13l}{420}m_n + \frac{I_{w_n}}{10} & 0 & 0 & 0 & -\frac{l^2}{140}m_n - \frac{I_{w_n}\, l}{30} & 0 & -\frac{11l}{210}m_n - \frac{I_{w_n}}{10} & 0 & 0 & 0 & \frac{l^2}{105}m_n + \frac{2I_{w_n}\, l}{15}
\end{bmatrix}
\qquad (SYM)
$$

Figure F.1: Mass matrix for an Euler-Bernoulli beam element.

$$
K_n = \begin{bmatrix}
\frac{EA_n}{l} & & & & & & & & & & & & & & \\
0 & \frac{12EJ_{w_n}}{l^3} + \frac{6S_n}{5l} & & & & & & & & & & & & & \\
0 & 0 & \frac{12EJ_{v_n}}{l^3} + \frac{6S_n}{5l} & & & & & & & & & & & & \\
0 & 0 & 0 & \frac{GJ_{u_n}}{l} & & & & & & & & & & & \\
0 & 0 & -\frac{6EJ_{v_n}}{l^2} - \frac{S_n}{10} & 0 & \frac{4EJ_{v_n}}{l} + \frac{2lS_n}{15} & & & & & & & & & & \\
0 & \frac{6EJ_{w_n}}{l^2} + \frac{S_n}{10} & 0 & 0 & 0 & \frac{4EJ_{w_n}}{l} + \frac{2lS_n}{15} & & & & & & & & & \\
-\frac{EA_n}{l} & 0 & 0 & 0 & 0 & 0 & \frac{EA_n}{l} & & & & & & & & \\
0 & -\frac{12EJ_{w_n}}{l^3} - \frac{6S_n}{5l} & 0 & 0 & 0 & -\frac{6EJ_{w_n}}{l^2} - \frac{S_n}{10} & 0 & \frac{12EJ_{v_n}}{l^3} + \frac{6S_n}{5l} & & & & & & & \\
0 & 0 & -\frac{12EJ_{v_n}}{l^3} - \frac{6S_n}{5l} & 0 & \frac{6EJ_{v_n}}{l^2} - \frac{S_n}{10} & 0 & 0 & 0 & \frac{12EJ_{v_n}}{l^3} + \frac{6S_n}{5l} & & & & & & \\
0 & 0 & 0 & -\frac{GJ_{u_n}}{l} & 0 & 0 & 0 & 0 & 0 & \frac{GJ_{u_n}}{l} & & & & & \\
0 & 0 & -\frac{6EJ_{v_n}}{l^2} - \frac{S_n}{10} & 0 & \frac{2EJ_{v_n}}{l} - \frac{lS_n}{30} & 0 & 0 & 0 & \frac{6EJ_{v_n}}{l^2} + \frac{S_n}{10} & 0 & \frac{4EJ_{v_n}}{l} + \frac{2lS_n}{15} & & & \\
0 & \frac{6EJ_{w_n}}{l^2} + \frac{S_n}{10} & 0 & 0 & 0 & \frac{2EJ_{w_n}}{l} - \frac{lS_n}{30} & 0 & -\frac{6EJ_{w_n}}{l^2} - \frac{S_n}{10} & 0 & 0 & 0 & \frac{4EJ_{w_n}}{l} + \frac{2lS_n}{15} &
\end{bmatrix}
$$

(SYM)

Figure F.2: Stiffness matrix for an Euler-Bernoulli beam element.

F.2 The added mass matrix

The consistent hydrodynamic added mass matrix for the generic element n is written as:

$$M_{A_n} = \pi \rho b_n^2 l \begin{bmatrix} 0 & & & & & & & & & & & \\ 0 & 0 & & & & & & & & & & \\ 0 & 0 & \frac{13}{35} & & & & & & & & & \\ 0 & 0 & \frac{-a_p b_n}{3} & \frac{b_n^2(.125+a_p^2)}{3} & & & & & & (\underline{SYM}) & & \\ 0 & 0 & \frac{-11}{210} l & 0 & \frac{l^2}{105} & & & & & & & \\ 0 & 0 & 0 & 0 & 0 & 0 & & & & & & \\ 0 & 0 & 0 & 0 & 0 & 0 & 0 & & & & & \\ 0 & 0 & 0 & 0 & 0 & 0 & 0 & 0 & & & & \\ 0 & 0 & \frac{9}{70} & 0 & \frac{-13}{420} l & 0 & 0 & 0 & \frac{13}{35} & & & \\ 0 & 0 & \frac{-a_p b_n}{6} & \frac{b_n^2(.125+a_p^2)}{6} & 0 & 0 & 0 & 0 & \frac{-a_p b_n}{3} & \frac{b_n^2(.125+a_p^2)}{3} & & \\ 0 & 0 & \frac{13}{420} l & 0 & \frac{-l^2}{140} & 0 & 0 & 0 & \frac{11}{210} l & 0 & \frac{l^2}{105} & \\ 0 & 0 & 0 & 0 & 0 & 0 & 0 & 0 & 0 & 0 & 0 & 0 \end{bmatrix} \tag{F.1}$$

where b_n indicates the mean half-chord of the part of the fin described by the element and a_p is a distance expressed as a ratio of b_n between the X_k axis and the mid-chord point of the foil (see figure 6.15).

F.3 Results from keel structure modal tests

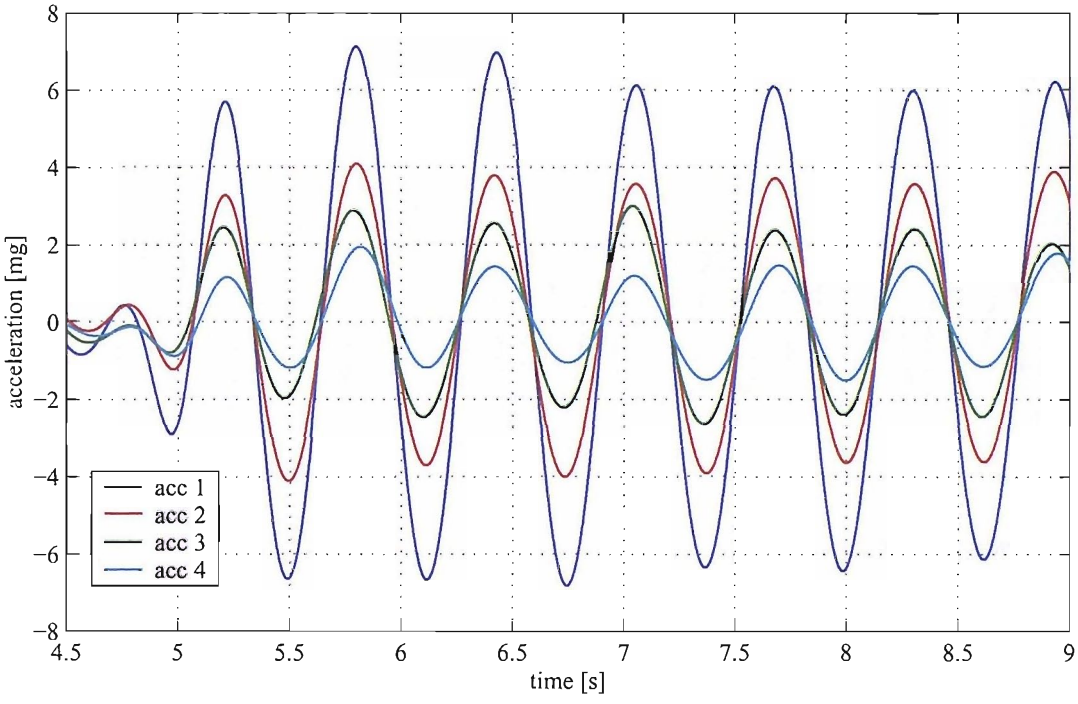

Figure F.3: Keel structure test: lateral accelerations at l_{fin}, $0.75l_{fin}$, $0.5l_{fin}$ and $0.25l_{fin}$, associated with first lateral bending mode ($nf_1 = 1.60Hz$). Curves obtained by applying to the recorded signals a "0 phase shift" digital 8^{th} order Butterworth low-pass filter with filter cut-off frequency $2.5Hz$.

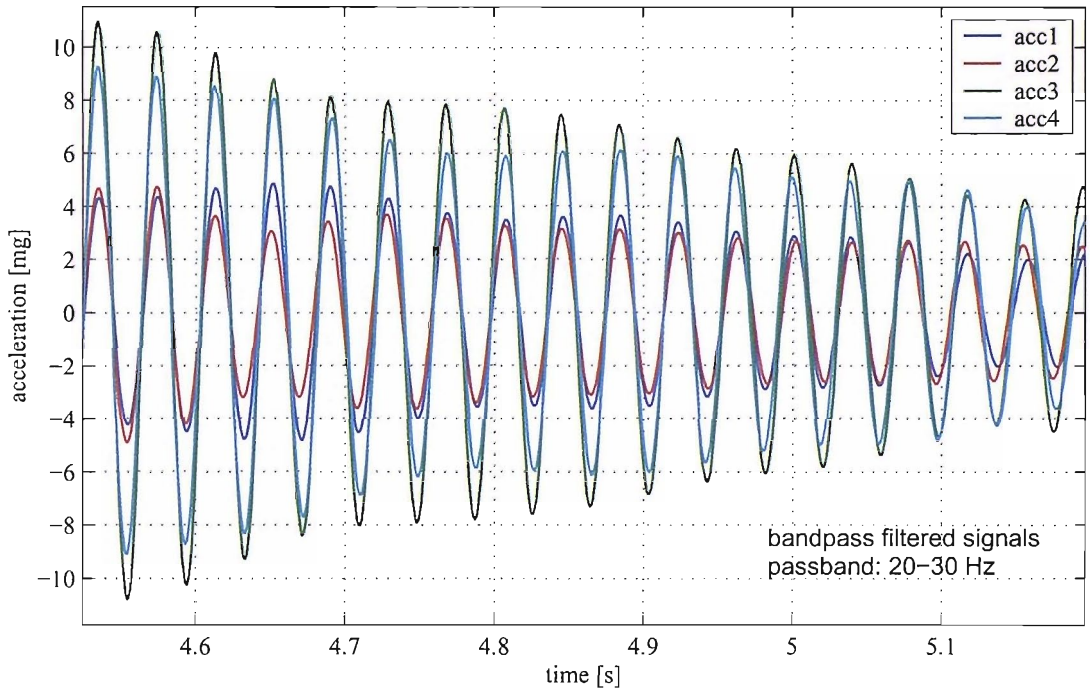

Figure F.4: Keel structure test: lateral accelerations at l_{fin}, $0.75l_{fin}$, $0.5l_{fin}$ and $0.25l_{fin}$, associated with second lateral bending mode ($nf_4 = 25.8Hz$). Curves obtained by applying to the recorded signals a "0 phase shift" digital 8^{th} order Butterworth band-pass filter with passband $20 - 30Hz$.

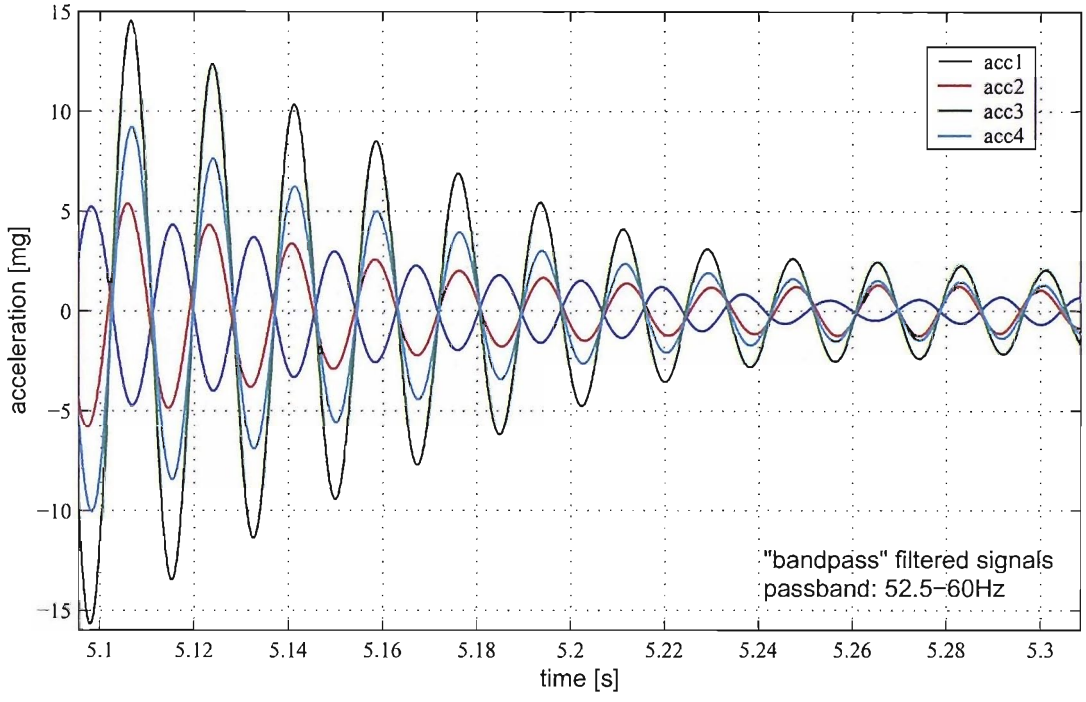

Figure F.5: Keel structure test: lateral accelerations at l_{fin}, $0.75l_{fin}$, $0.5l_{fin}$ and $0.25l_{fin}$, associated with third lateral bending mode ($nf_5 = 56.5Hz$). Curves obtained by applying to the recorded signals a "0 phase shift" digital 8^{th} order Butterworth band-pass filter with passband $52.5 - 60Hz$.

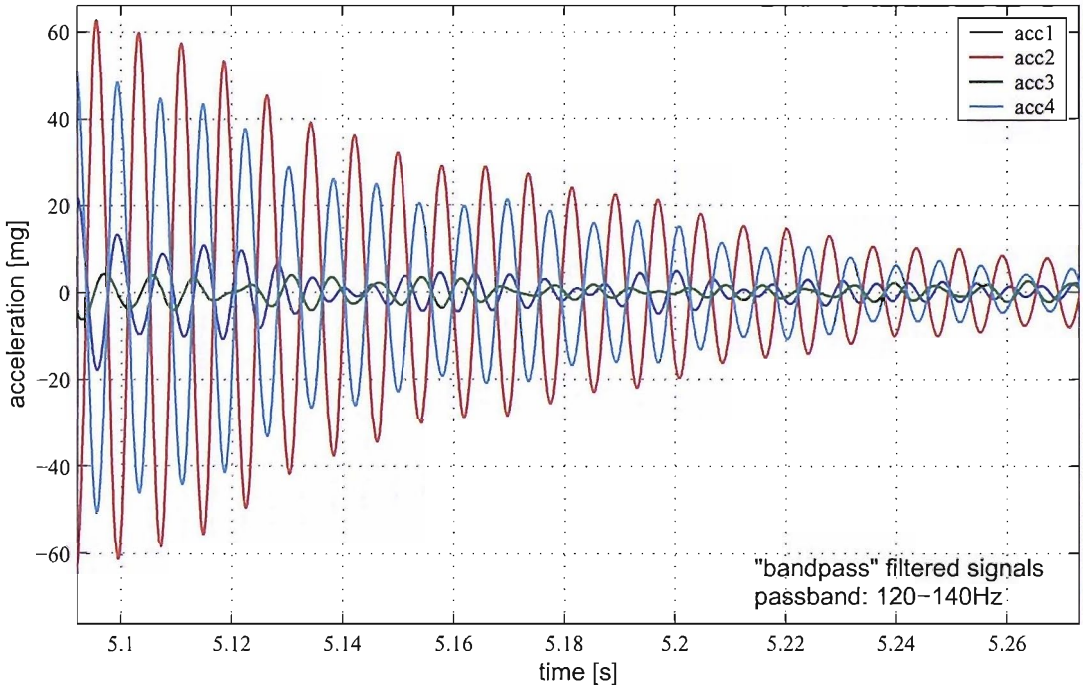

Figure F.6: Keel structure test: lateral accelerations at l_{fin}, $0.75l_{fin}$, $0.5l_{fin}$ and $0.25l_{fin}$, associated with fourth lateral bending mode ($nf_7 = 128.4Hz$). Curves obtained by applying to the recorded signals a "0 phase shift" digital 8^{th} order Butterworth band-pass filter with passband $120 - 140Hz$.

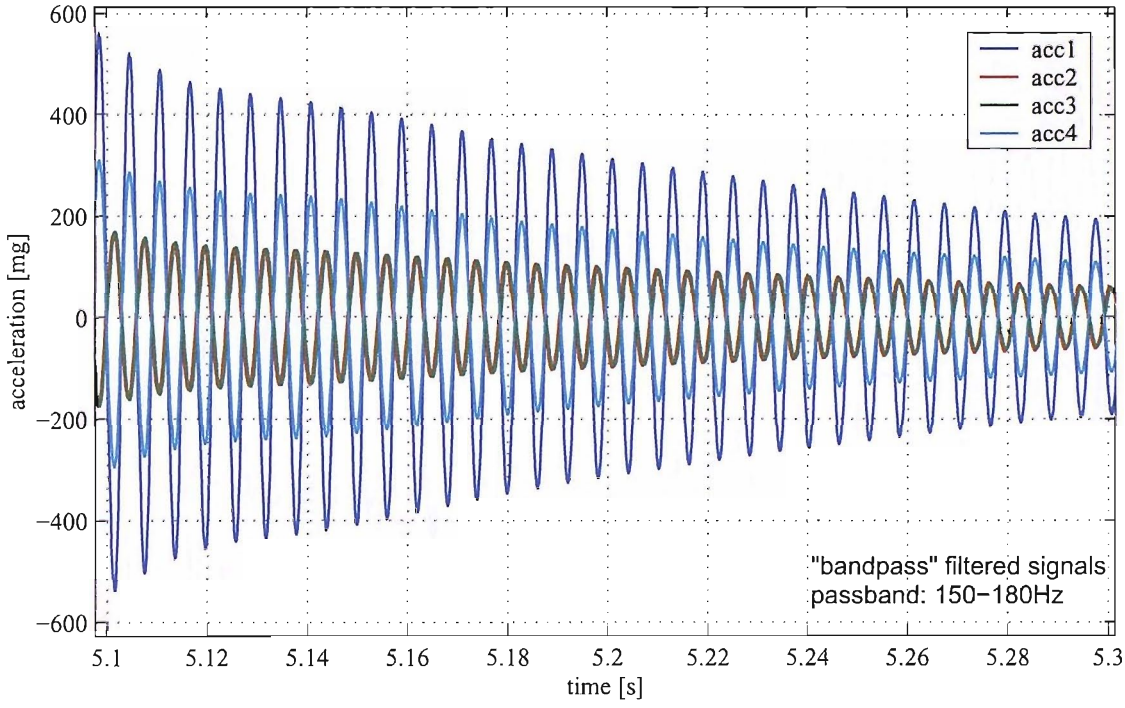

Figure F.7: Keel structure test: lateral accelerations at l_{fin}, $0.75l_{fin}$, $0.5l_{fin}$ and $0.25l_{fin}$, associated with fifth lateral bending mode ($nf_8 = 166.0Hz$). Curves obtained by applying to the recorded signals a "0 phase shift" digital 8^{th} order Butterworth band-pass filter with passband $150 - 180Hz$.

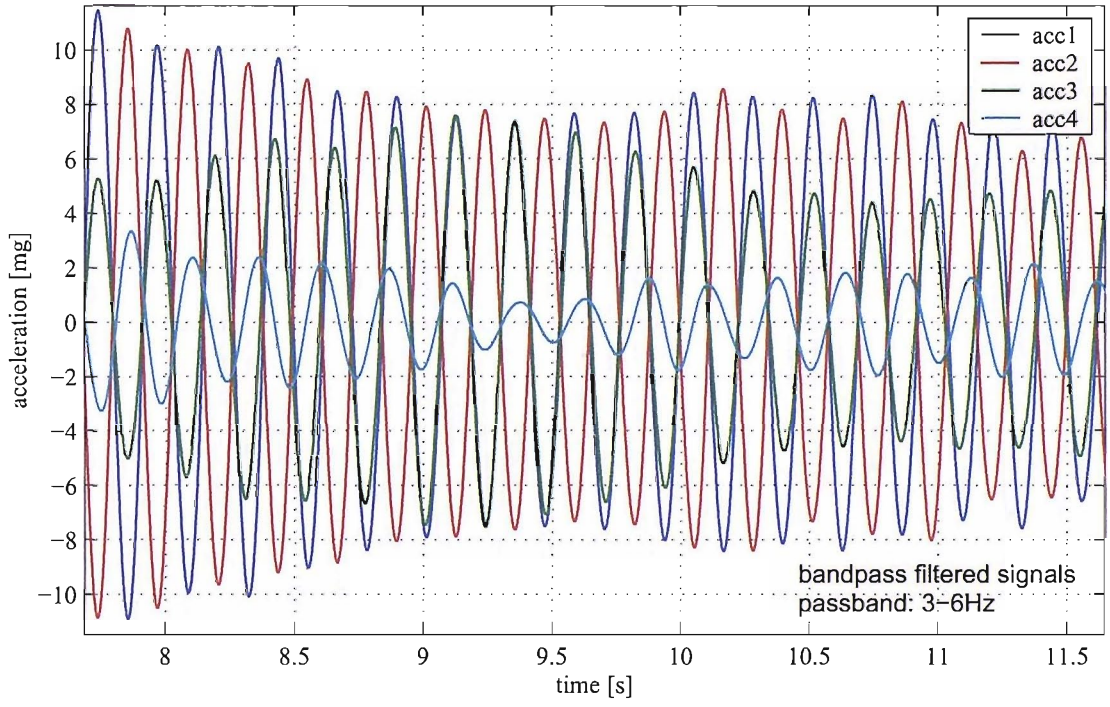

Figure F.8: Keel structure test: lateral accelerations at l_{fin} and $0.5l_{fin}$, associated with first torsion mode ($nf_3 = 4.34Hz$). Curves obtained by applying to the recorded signals a "0 phase shift" digital 8^{th} order Butterworth band-pass filter with passband $3 - 6Hz$.

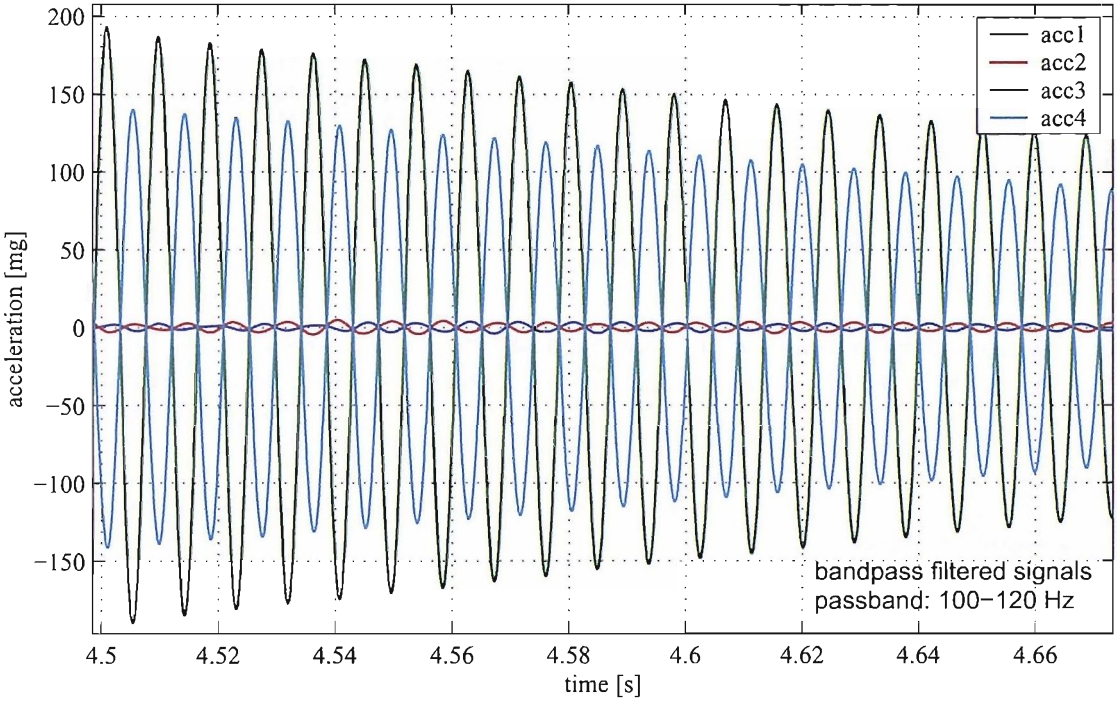

Figure F.9: Keel structure test: lateral accelerations at l_{fin} and $0.5l_{fin}$, associated with second torsion mode ($nf_6 = 113.2Hz$). Curves obtained by applying to the recorded signals a "0 phase shift" digital 8^{th} order Butterworth band-pass filter with passband $100 - 120Hz$.

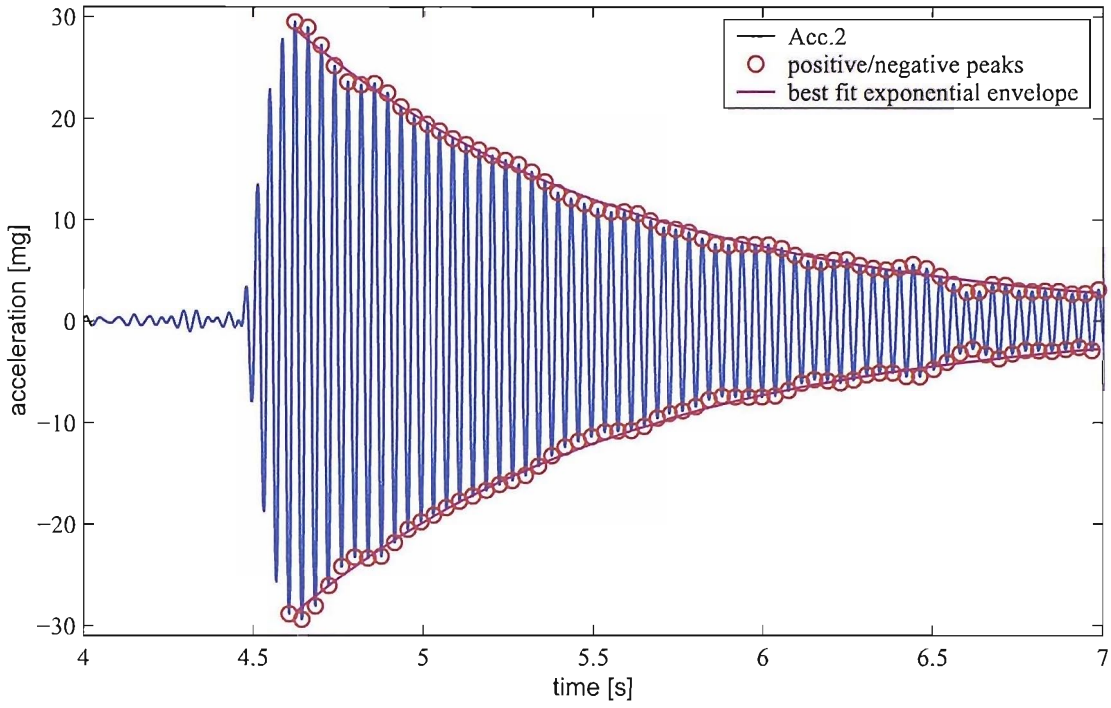

Figure F.10: Keel structure test: lateral accelerations associated with second lateral bending mode ($nf_4 = 25.8Hz$). Analysis of the nature of the decay of the oscillations following the hammer impact.

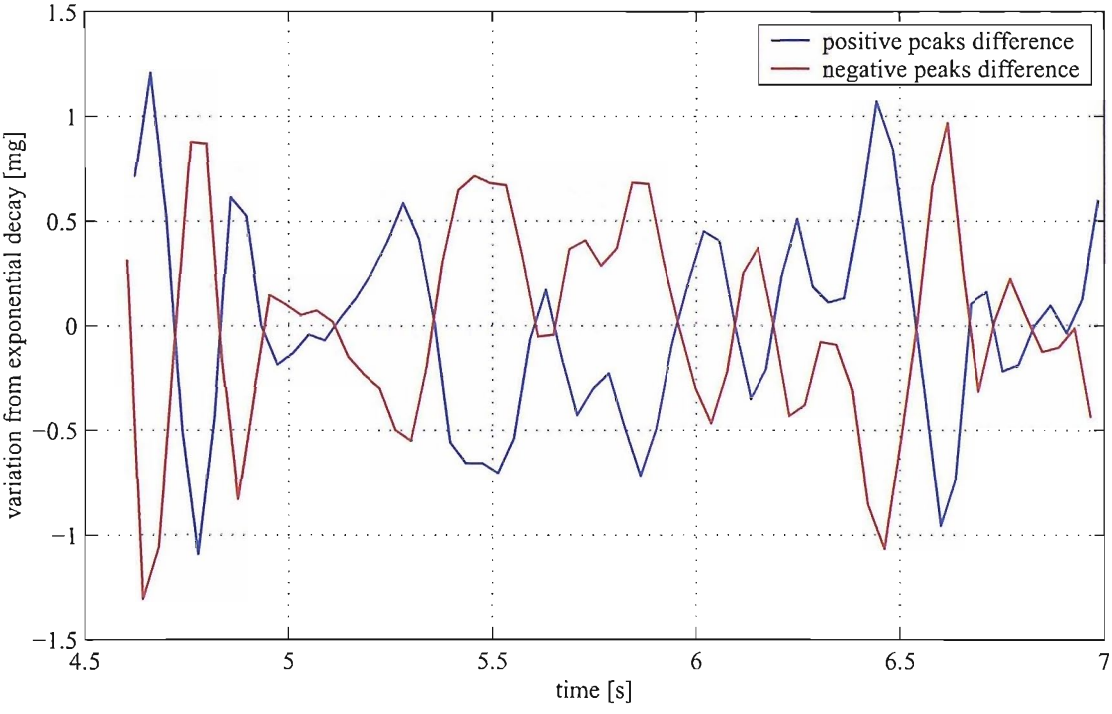

Figure F.11: Keel structure test: analysis of the nature of the decay of the oscillations following the hammer impact.

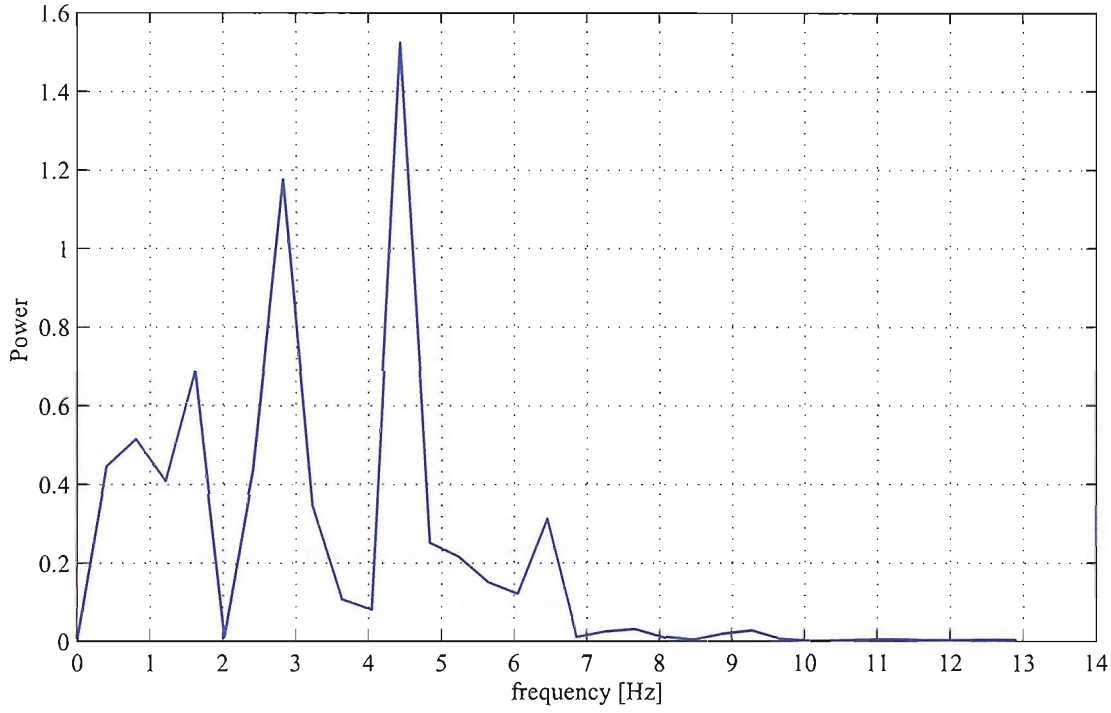

Figure F.12: Power Spectrum

Appendix G

Derivation of the hydrodynamic impulse response function.

It has been shown in chapter 6.6.4 that the loads acting on a two-dimensional foil harmonically oscillating in a flow, can be expressed as a function of the motion and, through the Theodorsen function $\mathcal{C}(k)$, of the reduced frequency k. For illustrative purposes, consider the motion to be a pure harmonic transverse oscillation, which can be described in complex form as:

$$\dot{h}(t) = H_0(\omega)\, e^{i\omega t} \tag{G.1}$$

where $\dot{h}(t)$ is the instantaneous velocity of the foil in the direction perpendicular to the flow and $H_0(\omega)$ is a vector in the complex plane describing both the amplitude and the phase of the oscillation. The resulting circulatory lift is of the form:

$$L(t) = L_0(\omega)\, e^{i\omega t} = 2\,\pi\,\rho\,U\,b\,\mathcal{C}(k)\,\dot{h}(t) \tag{G.2}$$

where $L_0(\omega)$ is also a complex vector. In order to simplify the following equations, a normalised lift is introduced in the form of:

$$\bar{L}(t) = \bar{L}_0(\omega)\, e^{i\omega t} = \frac{L(t)}{2\,\pi\,\rho\,U\,b} = \mathcal{C}(k)\,\dot{h}(t) \tag{G.3}$$

Considering $\dot{h}(t)$ as the input of a linear system and $\bar{L}(t)$ as the output, they can be related as follows:

$$\bar{L}_0(\omega) = \Xi(\omega)\, H_0(\omega) \tag{G.4}$$

where

$$\Xi(\omega) = \frac{\bar{L}_0(\omega)}{H_0(\omega)} \tag{G.5}$$

is the complex transfer function of the system. From equations G.2 and G.4, it follows that $\Xi(\omega)$ is equal to the Theodorsen function $\mathcal{C}(k)$, which, by considering U and b as fixed parameters, may be written as:

$$\Xi(\omega) = \mathcal{C}(\frac{\omega b}{U}) = \mathcal{C}_{U,b}(\omega) \tag{G.6}$$

Regarding the circulatory lift associated with an arbitrary transverse oscillation, this has been defined in equation 6.16 by using a convolution integral as:

$$L_C(t) = 2\,\pi\,\rho\,U\,b \int_{-\infty}^{t} \xi(\tau) \cdot \dot{h}(t-\tau) d\tau \tag{G.7}$$

Since the Fourier transform of a convolution integral is the product of the Fourier transforms of the convoluted variables, it follows from equation G.7 that:

$$\begin{aligned} \mathcal{F}\{L_C(t)\} &= \mathcal{F}\left\{2\,\pi\,\rho\,U\,b \int_{-\infty}^{t} \xi(\tau) \cdot \dot{h}(t-\tau) d\tau\right\} \\ \text{i.e. } L_C(\omega) &= 2\,\pi\,\rho\,U\,b \cdot \Xi(\omega) \cdot H(\omega) \end{aligned} \tag{G.8}$$

where it appears that the Fourier transform of the impulse response function $\xi(\tau)$ is the complex transfer function $\Xi(\omega) = \mathcal{C}(k)$. By splitting $\Xi(\omega)$ into its real and imaginary part $\Xi^R(\omega)$ and $\Xi^I(\omega)$, it can be shown that:

$$\xi(\tau) = \frac{-2}{\pi} \int_0^{\infty} \Xi^I(\omega) \sin(\omega\tau)\, d\omega \tag{G.9}$$

$$= \frac{2}{\pi} \int_0^{\infty} \Xi^R(\omega) \cos(\omega\tau)\, d\omega \qquad \text{for } \tau > 0 \tag{G.10}$$

which indicates that, if the real and imaginary parts of the transfer function $\Xi(\omega)$ are known, the impulse response function can be obtained for all $\tau > 0$ from either equation G.9 or G.10. The complex transfer function has been shown in equation G.6 to be equal to the Theodorsen function, the exact expression of which is:

$$\mathcal{C}(k) = F(k) + iG(k) = \frac{K_1(ik)}{K_0(ik) + K_1(ik)} \tag{G.11}$$

where $K_0(ik)$ and $K_1(ik)$ are modified Bessel functions of the second kind which can be evaluated numerically by an algorithm available in MATLAB. Functions $F(k)$ and $G(k)$ (corresponding to $\Xi^R(\omega)$ and $\Xi^I(\omega)$) are plotted and tabulated in [47], where it can be noted that, when k (and thus ω) tends to infinity, the real part of the Theodorsen function tends to 1/2 while the imaginary part tends to zero. Hence, the integral in equation G.9 is easier to evaluate than the one in equation G.10. In

particular, an efficient and accurate method for the numerical solution of this type of integral can be found in [7] and is used herein. Bailey shows that equation G.9 can be reduced to:

$$\xi(\tau) \approx \frac{-2}{\pi} \sum_{n=1}^{N-1} \left(G(k_n) - G(k_{n+1})\right) \Omega_n \left\{ \frac{1}{\Omega_n \tau} - \frac{\cos(\Omega_n \tau)}{\Omega_n \tau} \frac{\sin(\Delta_n \tau)}{\Delta_n \tau} \right\} \tag{G.12}$$

where

$$k_n = \frac{\omega_n\, b}{U} \quad , \quad \Omega_n = \frac{\omega_{n+1} + \omega_n}{2} \quad \text{and} \quad \Delta_n = \frac{\omega_{n+1} - \omega_n}{2}$$

and where N and ω_N (i.e. the upper frequency to which the integrations are taken) are chosen so that it can be sensibly ensured that the integrations have converged.

Finally, it should be noted that the impulse response function $\xi(\tau)$ depends on the ratio U/b through the Theodorsen function. Hence, for example, for given a fixed chord length $2b$, equation G.12 would need to be re-evaluated for each different flow velocity U. This can be avoided, by noting that equation G.9 may be re-written as:

$$\xi_{U/b}(\tau) = \frac{-2}{\pi} \int_0^\infty G(\frac{\omega\, b}{U}) \sin(\omega\tau)\, d\omega \tag{G.13}$$

which, through a variable substitution $k = \omega\, b/U$ and by defining $\bar{\tau} = \frac{U}{b}\tau$, becomes:

$$\xi_{U/b}(\tau) = \frac{-2}{\pi} \frac{U}{b} \int_0^\infty G(k) \sin(k\frac{U}{b}\tau)\, dk \tag{G.14}$$

$$= \frac{U}{b}\, \xi_1(\bar{\tau}) \tag{G.15}$$

Thus it is only necessary to evaluate $\xi_1(\bar{\tau})$ once and any impulse response function $\xi_{U/b}(\tau)$ can be obtained by substituting the time variable and by carrying out a simple multiplication.

The same procedures apply to the calculation of impulse response functions derived from modified Theodorsen functions, as from the Reissner and Stevens method.

Appendix H

Paper presented at the 15^{th} Chesapeake Sailing Yacht Symposium

Annapolis, USA, January 26^{th} 2001

An experimental investigation of slamming on ocean racing yachts.

Paolo Manganelli, Ship Science, School of Engineering Sciences, Southampton, UK
Philip A. Wilson, Ship Science, School of Engineering Sciences, Southampton, UK

ABSTRACT

Groupe Finot Naval Architects and the School of Engineering Sciences, Ship Science of the University of Southampton have started a joint research project to carry out an experimental investigation concerning the effects of slamming on offshore sailing yachts.
A reliable autonomous data acquisition system was designed that allowed measurements to be taken during long offshore races. The details of the design and implementation of this system are presented together with some sample results from the first measurement campaigns.

NOTATION

A_{cg}	Acceleration at the centre of gravity
B_{MAX}	Maximum beam
B_{WL}	Beam at waterline
DSA	Downwind sail area
$H_{1/3}$	Significant wave height
LCG	Longitudinal centre of gravity
L_{OA}	Length overall
L_{WL}	Length at waterline
nre	Normalised rms error
T	Draft
TWA	True wind angle
USA	Upwind sail area
Δ	Displacement
ε	Angle between the boat vertical axis and the direction of acceleration
∇	Volume displacement

INTRODUCTION

The lighter the structure the higher the loads. This is one of the most interesting (and difficult) challenges in the structural design of racing yachts. In reality, with all the other characteristics of the boat remaining the same, lighter structures allow higher ballast-to-weight ratios and thus higher righting moments. These in turn translate into larger sideforces, larger driving forces and better speed through the water or, in other words, larger aerodynamic and hydrodynamic loads.
This challenge has been met in the past thanks to constant progress in material properties and more and more efficient design. However, the challenge is always open and lighter structures and faster boats are still to be built.
One of the conditions to carry structural optimisation to a further stage is certainly a better definition of the external loads. In this respect, while structural analysis of sailing yachts has relied for years on a static or quasi-static approach, there is an increasing necessity for trying to evaluate dynamic loads and their effect in a more precise way.
High hydrodynamic loads act during a slam in the form of a localised pressure pulse rapidly travelling over a limited part of the hull. Typically, as the forward sections of the boat strike the water surface, the hull panels in the slamming area are affected by a highly non-uniform pressure distribution with peak values that can reach a thousand times the order of magnitude of the hydrostatic pressure. These peaks only act on a very limited area (smaller than the average panel size) and for a very short time (typical recorded pulse durations are between 15 and 50 ms).
For design purposes, the tendency has always been to represent these loads by an equivalent static pressure uniformly distributed over the panels. When the duration of the pressure pulse is considerably longer than the natural periods of the panels, this pressure can simply be taken as the spatial average of the real hydrodynamic load. Alternatively, if the panel is expected to show a non negligible dynamic response, the equivalent pressure would be defined as that pressure which, if applied to the panel, will result in the same deformation and same maximum stress produced by the actual loading (Heller and Jasper, 1961; Allen and Jones, 1978).
Most of the published research about slamming on sailing yachts has concentrated on the definition of suitable

values for an equivalent pressure. Several authors have contributed with theoretical and experimental investigations on this subject. Joubert (1982), Brown, Joubert and Yan Ping (1996) and Brown, Wraith and Joubert (1999) have carried out an extensive analysis of local pressure loads on hull plating and the associated structural response. They concluded in most instances that the rules in the American Bureau of Shipping "Guide for building and classing Offshore Racing Yachts" might lead to inadequate scantlings.

Reichard (1984) and Hentinen and Holm (1994), carried out some full-scale measurements by instrumenting sailing boats with pressure transducers. The latter also deduced that actual pressures are higher than the ones recommended by the ABS guide and that the unaccounted nonlinear mechanical behaviour of the hull panels combined with design safety-factors would explain the relative absence of damage on most sailing vessels. Their conclusion then was that *"there is a lot to learn about slamming loads, and the mechanisms of the structures are yet by no means fully understood"*.

Indeed the question about the correct definition of design pressures for modern sailing yachts remains an open problem. Brown et al. (1999) suggest that, because every impact produces a different impact pressure, what is needed is an estimate of worst case loading. This would certainly be valuable information for design purposes, but it would not be sufficient. In fact if slamming loads are to produce a structural failure, it is more likely to happen because of fatigue rather than because of maximum stress exceedance. For example, this was probably the case with the numerous sandwich core failures observed at the end of leg 5 of the 1993-94 Whitbread race: as Bowler commented (Jeffrey, 1998) failures only started to appear on yachts after they had sailed 20000 miles and most of them had already survived conditions similar to or heavier than those encountered during leg 5 without damage. Hence, ideally materials and scantling definition should also take into account non-maximum slamming loads and their frequency of occurrence.

EXPERIMENTAL INVESTIGATION

The investigation focused on Open'50 and Open'60 class boats. These are ocean racing yachts designed primarily for single-handed sailing. Several aspects make them very suitable for this type of study: their high beam-to-length ratio and relatively low equivalent deadrise angles favour large impact loads. Their steering relies for more than 95% of the time on auto-pilot systems: such devices, while trying to keep a constant heading or a constant apparent wind angle, are "blind" with respect to the incoming waves and do not take any action to avoid or reduce slamming. Finally, Open'60 are currently among the fastest sailing monohulls, capable of sustaining steady speeds of more than 20 knots while sailing in rough seas.

In choosing a way of investigating slamming loads, a solution had to be determined that was compatible with this type of boat. In addition, it was considered that measurements should be taken during races as in these conditions voluntary speed reduction is minimal and the highest loads are likely to appear. This would sensibly narrow down the possible choices regarding the sensors and the data acquisition system to be used. Pressure transducers, although being the only devices that allow direct measurement of hydrodynamic loads, were ruled out. There were two main reasons for this choice: firstly, to resolve the pressure distribution over the hull and its evolution in time, a relatively dense array of sensors must be employed (Allen and Jones, 1978, Rosen and Garme, 1999). This, together with the necessity of sampling the signals at high frequencies (i.e. more than 1 KHz), involves using data acquisition systems that are capable of processing and storing large quantities of data, but are not suitable to be installed on board an offshore sailing yacht during a race. Secondly, from a purely practical point of view, pressure transducers potentially affect the water-tightness of the boat, as they need to be fitted through the hull and no skipper would accept it.

Using displacement transducers and strain gauges was considered as an alternative. These devices allow the measurement of the structural deformation that is induced by slamming loads. Displacement transducers, in particular, may give an indication of the inward deflection of hull panels whilst strain gauges would provide useful data about the relative amount of bending and membrane deformation. Unfortunately, both type of sensors would be difficult to fit on our test boats and their use appeared incompatible with long-term unattended measurement campaigns.

The best solution was to use accelerometers. If they are mounted on the primary structure (bulkheads and girders) they allow rigid-body accelerations to be recorded and the global dynamic structural behaviour to be identified while, if fixed directly onto the hull plating and on secondary reinforcements (i.e. stringers and frames), they give an indication about the local structural response. Indeed, through double integration of their signal in the time domain, it is also possible to calculate their displacement and hence amplitudes of rigid-body motion and of structural deformation.

It is arguable that the magnitude of the rigid body acceleration following an impact is proportional to the hydrodynamic load acting on the hull. This is one of the main conclusions of the theory of Heller and Jasper (1961), from which formulae for the definition of design pressures are generally derived (see DNV Tentative Rules for classification of High Speed and Light craft, 1991, A.B.S. Rules for building and classing High Speed Craft, 1997, and Draft ISO Standard 12215 for Small Craft Hull Construction/Scantlings, 2000). However, their model relied on the assumptions that *"the time variation of the load has only a small amount of high-frequency content"* and that the hull acts *"nearly"* as a rigid body during the water impact. Although using accelerometers would not allow us to verify the validity of the first assumption, it would give us a good indication of the relative amount of energy present in the flexible modes or, in other words, of

how accurate it is to consider the boat "rigid" through the impact. The next section will concentrate on the details of how these sensors and the data acquisition system were set up.

Experimental setup

For measurements during long offshore races, seven accelerometers and a programmable data-logging unit were used. The position and the orientation of the sensitive axes of the accelerometers are shown in figure 1. Two sensors were mounted on the collision bulkhead (which is approximately at 13% of L_{OA} on Open'50s and at 5% of L_{OA} on Open 60's) measuring acceleration along the Y and Z axes (respectively 1 and 2 in the figure). Four were fixed to the bulkhead closest to the centre of gravity (approximately at 50 % of L_{OA}), two on the sides (3 and 4) measuring acceleration along the Z axis and two on the centreline measuring along the X and Y axes (6 and 5). Finally, one accelerometer was mounted on a bulkhead in the aft area (approximately at 90% of L_{OA}) measuring along the Z axis (7). Although six accelerometers would be sufficient to measure the six components of rigid-body motion, seven were used in order to have some redundancy on the measurement of heave and pitch acceleration and to identify the amplitude of longitudinal bending vibration.

For two reasons *IC Sensors 3140* accelerometers were chosen: internal signal amplification allowed a very good signal-to-noise ratio to be achieved despite the long lengths of cable, while built-in temperature compensation guaranteed very small drift over time (typically less than ±0.01g), avoiding the need for constant recalibration. All had a ±10g measurement range except for 5 and 6 where a ±5g range was chosen to give a better resolution. Their linear bandwidth extends from 0Hz to 500Hz.

With respect to rigid-body motion measurement, the use of inertial measurement units was considered: these devices generally include three angular rate sensors and three accelerometers to measure oscillatory motion in six degrees of freedom. The main advantage over strap-down accelerometer systems is that one less stage of integration is needed to calculate angular motions, so dynamic accuracy is better. Besides, their reliability and their weight have been sensibly improved in the recent years thanks to the introduction of vibrating quartz and laser ring gyros in place of traditional spinning mass units. However, cost and power consumption are still considerably higher than those of systems using only accelerometers, and these factors were of primary importance for us.

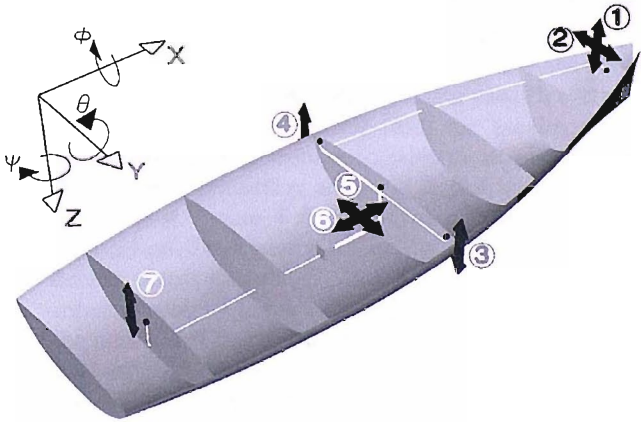

Fig. 1 Position and sensitive axes of the accelerometers

For the data acquisition, a customised logging unit supplied by the Cranfield Impact Centre was used. Up to eight analogue signals could be logged through an A/D converter equipped with programmable filters. Data from the boat instruments could equally be recorded through a standard NMEA interface. The maximum allowed sampling frequency per channel was 2 KHz.

The unit was programmed to perform all the following tasks at the same time:

Logbook acquisition: a single sample of boat speed, boat heading, true wind speed, true wind angle and GPS position was stored at regular intervals (typically 20 seconds). This provided a useful reference about the sailing conditions.

Short time-histories recording: whenever the vertical acceleration at the bow or at the centre of gravity exceeded preset threshold values, a short time-history of all the accelerometer signals was recorded. In particular, the logging unit had a circular memory buffer that allowed it to store not only the data following a triggering event, but also those that preceded it. Hence, typically, the five seconds preceding a "slam" and the five following are recorded. The analogue channels are normally sampled at 100Hz while a single sample of boat speed, true wind angle, true wind speed and GPS position is attached to the time-history. The unit has a permanent internal clock so that every acquisition is time-stamped.

Data reduction: multi-dimensional histograms were continuously built up. Figure 2 shows an example: peak values of acceleration at the centre of gravity (A_{cg}) are counted and separated in different bins depending on their magnitude and on the value of the apparent wind angle (TWA) at the time of impact. Along the axes are shown the central values of each bin. Note that the graph in this example was built over a period of several days where downwind sailing conditions were predominant. This explains the large number of impacts in the 70 –90 degrees category. Similar histograms were recorded relating acceleration at the centre of gravity and at the bow to boat speed and to wind speed.

The priorities in the design of the data acquisition system were to minimise weight and power consumption, and to maximise ruggedness and autonomy. As a result the logging unit only weighted 750g and it absorbed a maximum current of 225mA from a 12V supply. All the parameters of the acquisition were programmed before the boat would leave port: when sailing, the acquisition would stop only in case of a major power supply failure (i.e. voltage of the batteries dropping below 7V) and it would resume as soon as the supply was re-established. Data were constantly saved to permanent memory and they

were retrieved when the boat arrived to port. No user intervention was ever required during the voyage. The whole system was waterproof and particular attention was paid to protecting every component from electro-magnetic interference.

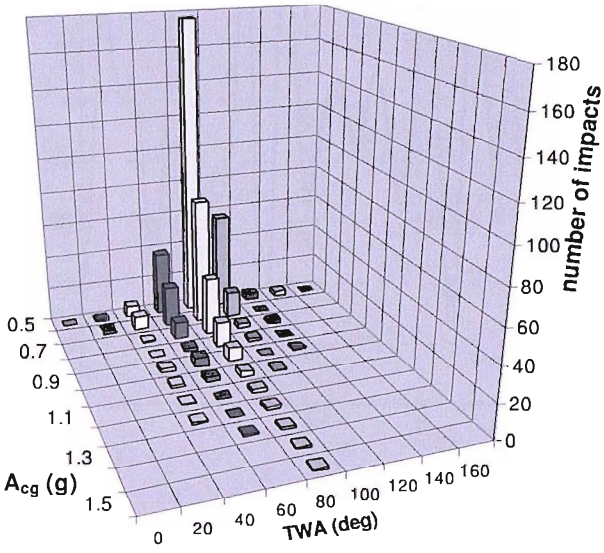

Fig. 2 Bi-dimensional histogram of A_{cg} and TWA

MOTION MEASUREMENT

All DC type accelerometers respond to the component of the acceleration of gravity aligned with their sensitive axis, thus before the measurements can be examined, they must be corrected for the effects of heel and trim changes. This can be done by implementing an iterative analysis procedure proposed by Miles (1986). The technique uses integration in the frequency domain to solve the full non-linear differential equations for the linear and angular displacements.

The method was validated by applying it to a model running in a towing tank. Accelerometers were fitted on the model in the same positions where they are on a real boat. The longitudinal separation between accelerometers 1 and 7 was 1440mm; the lateral separation between 3 and 4 was 470 mm. The model was towed at a fixed speed in regular and irregular waves. It was free to heave and pitch and constrained in sway, surge, roll and yaw. Heave and pitch displacements obtained from the accelerometer measurements were compared with those given by a displacement transducer and by a potentiometer on the towing post. Figure 4 shows a typical example of this comparison. Tests were made at four different angles of heel to assess the possible presence of coupling in the measurements of heave and sway. As shown in figure 3 the normalised rms errors expectedly increased with the heel angle. The error on heave measurement was less than 6% even at large angles, while the error on pitch measurement remained under 4%. Finally measurements of sway roll and yaw from the accelerometers, gave negligible values, which were well within the play in the towing structure.

These results proved the analysis procedure to be very accurate and gave us confidence to apply it to full-scale measurements.

DETERMINATION OF ENCOUNTERED SEAWAY

Among all the factors that determine the magnitude and the frequency of occurrence of slamming, sea state is certainly one of the most relevant. In order to give a better interpretation of our results, it was then extremely important to obtain information about the encountered seaway. Normally, during seakeeping tests, wave buoys are used to measure the main wave characteristics. Otherwise, on-board wave radars have proved to give good estimates of significant wave height and main period in most cases. None of these devices however, can be used for long-term measurement campaigns, so an alternative source of information had to be defined. Through the Southampton Oceanographic Centre, it was possible to access measurements of significant wave height and zero up-crossing period taken by satellite altimeters. Data about local wave height and period were equally provided by a computational wave model based on winds and currents and run by the Ocean Modelling Branch (OMB) of the U.S. National Oceanic and Atmospheric Administration (NOAA). Satellite altimeters are regarded as the most accurate source of information, however, as they orbit around the globe, their ground footprint is very often too distant from the actual position of the boat to give useful information. On the other hand, computational models can be less reliable, but they always provide values very close to the position of the boat (typical data grid densities are 1 deg latitude by 1 deg longitude). Whenever it was possible to compare them the two sources were generally in good agreement: figure 5 illustrates the statistical distribution of the difference between the measurements of $H_{1/3}$ by the two methods over the month of March 2000 (when the first campaign

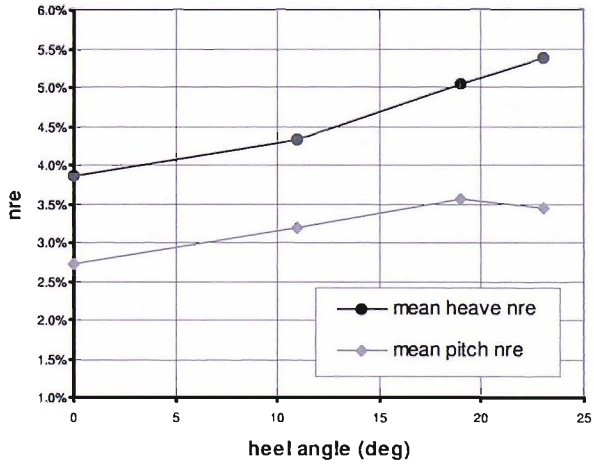

Fig. 3 Normalised RMS errors between real and estimated motion

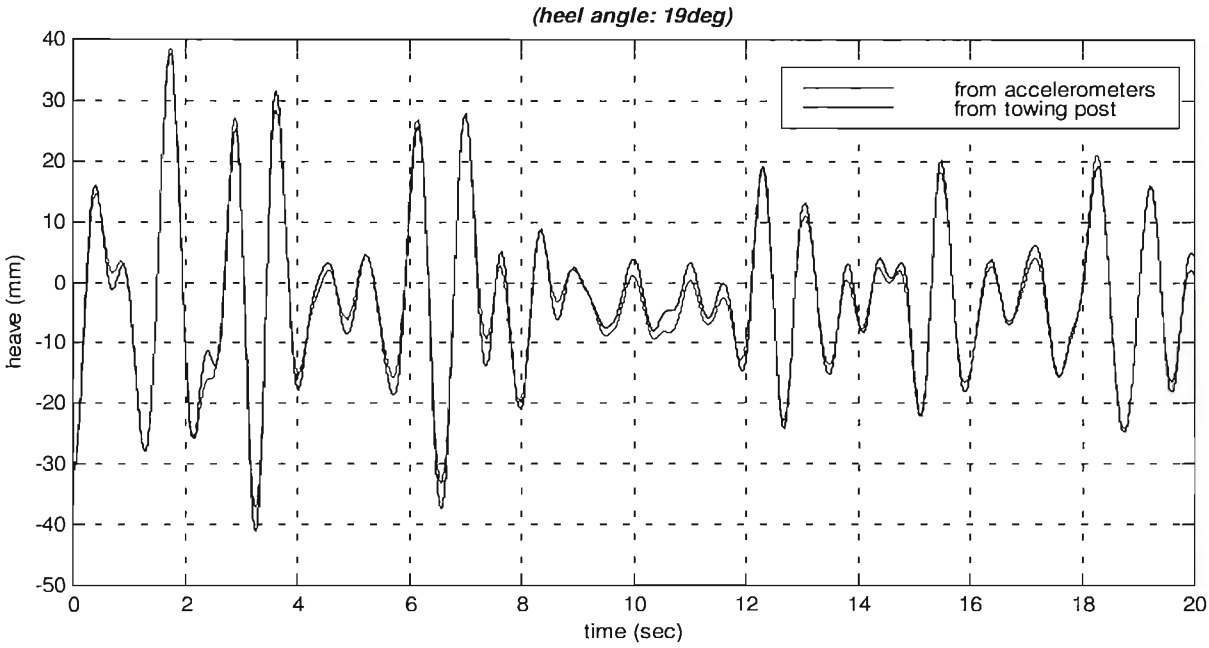

Fig. 4 Comparison of heave measurements

was carried out). These data are closely matched by a gaussian distribution with a 0.057 average and 0.134 standard deviation, suggesting that the value given by the computational model approximates the satellite observation with better than 19% accuracy in 70%of the cases.

In view of these results, it seemed justified to use data from the computational wave model in our analysis and integrate them with satellite altimeter measurements whenever these were available.

SAMPLE RESULTS FROM THE FIRST MEASUREMENT CAMPAIGNS

At the time of writing, three main measurement campaigns have been carried out, two during delivery trips across the Atlantic Ocean on Open'60s and one during a single-handed transatlantic race on an Open'50. The main characteristics of these boats are listed in table 1. Although when not racing, the constraints about weight and power consumption are less strict, the system has always been used in its "racing" configuration i.e. with only seven accelerometers. The reason for this was the necessity to test the system thoroughly in view of its use during the Vendee Globe Challenge 2000, a non-stop round-the-world race. So far, recordings have been taken over 51 days and 9650 sailed miles.

During our first campaign across the Atlantic, one of the authors could be on board: this was particularly useful, not only to identify and solve initial problems, but also to perform several different types of acquisition during the same trip. Typically, the two main problems in the beginning were to identify suitable triggering conditions for the time-history recordings and cut-off frequencies for the low-pass filters.

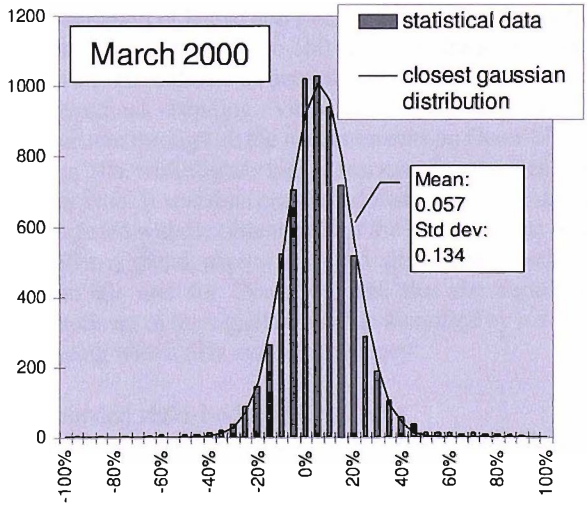

Fig. 5 Percentage difference between significant wave heights estimated by computational model and measured by satellite altimeter.

	Gartmore	Group4	sailthatdream.com
Class	Open'60	Open'60	Open'50
L_{OA}	18.28m	18.28m	15.24m
B_{MAX}	5.60m	5.60m	4.95m
L_{WL}	18.28m	18.28m	15.24m
B_{WL}	3.50m	3.50m	2.93m
T	4.5m	4.5m	4.12m
Δ	9.4t	9.2t	5.2t
USA	280m^2	246m^2	192m^2
DSA	500m^2	500m^2	345m^2
$L/\nabla^{1/3}$	8.72	9	8.8
Material (hull)	Carbon fibre /nomex	Carbon fibre /nomex	Carbon fibre /nomex

Table 1 Main boat characteristics

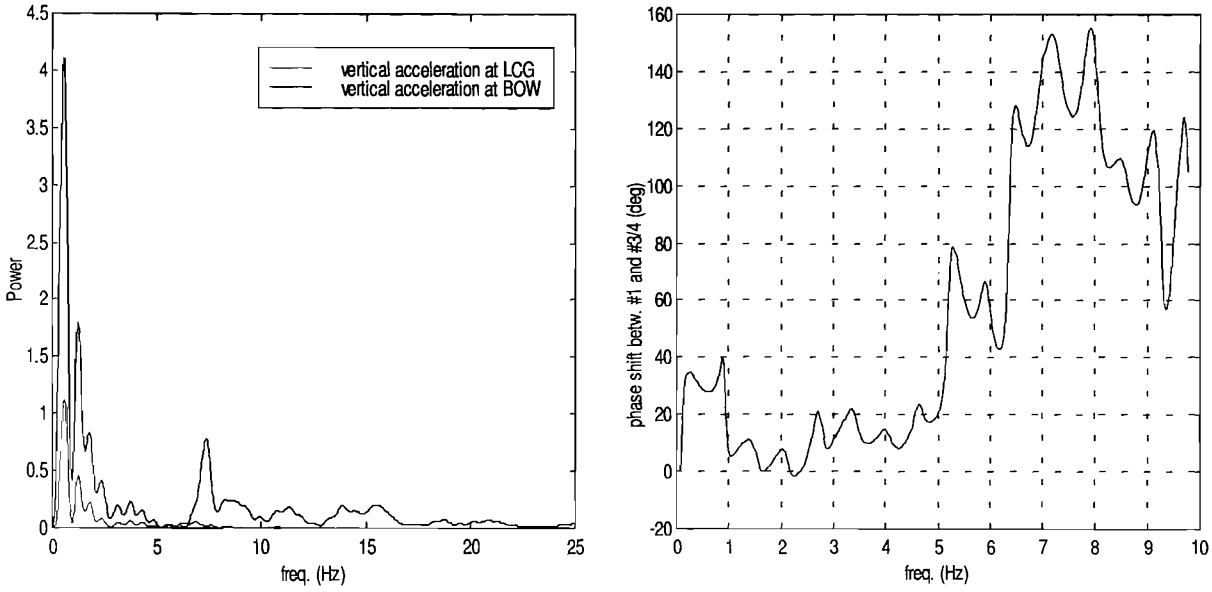

Fig. 6a Typical power spectra of signals from accelerometers mounted near the bow and near the LCG.
Fig. 6b Phase difference between the signals of accelerometers mounted at the bow and close to LCG.

Before being acquired, all the signals were low-pass filtered to avoid aliasing: initially the cut-off frequency was set to 40 Hz and the sampling frequency to 200Hz in order to check the frequency content of the signals. Figure 6a shows typical frequency spectra of the signals from accelerometers 1, 3 and 4. Most of the power is in the 0-1Hz band, corresponding to the wave encounter frequencies. Minor peaks can be distinguished particularly on the bow accelerometer at 7Hz, 12Hz, and 15 Hz: these correspond to resonance of flexible modes. In order to distinguish the frequency components of the signal related to rigid-body motion from those related to structural deformation, the phase of the signals were analysed. Figure 6b shows an example of the difference between the phase of the signals from accelerometers 1, 3 and 4. Non-zero values in the 0-1 Hz band are produced by the combination of heave and pitch rigid-body modes, while phase differences of up to 160 deg in the frequency range above 5 Hz indicate structural deformation (in this case longitudinal bending vibration). This pattern was consistent through all the measurements on Open'60s and Open'50s, with slightly higher resonant frequencies in the latter case. It was then concluded that most of the energy associated with flexible modes of the hull would be in the frequency band above 5Hz and 6Hz respectively for Open'60s and for Open'50s, and that the rigid-body component of the signals would be identified by low-pass filtering with a 5Hz cut-off frequency.

Recorded rigid-body accelerations

The highest accelerations were measured on the Open'50 Sailthatdream.com during the Europe1 Newman transatlantic race. As shown by figure 7, upwind sailing conditions were predominant in this event. The maximum recorded values of acceleration were 1.72g at the centre of gravity and 5.31g at the bow. These occurred while the boat was beating at approximately 8 knots in 5.1 metres estimated significant wave height. In the same circumstances several impacts produced accelerations greater than 1.5g at the centre of gravity and than 4g at the bow. Table 2 was constructed from the recordings made over the whole race: it indicates that, at closer wind angles, the average magnitude of the accelerations increased almost linearly with the wave height. Conversely, at all true wind angles, the frequency of the impacts appeared to be higher for significant wave heights between two and three metres. This is most likely to be explained by the wave encounter frequency being higher in this range of significant wave heights. The data in table 2 also show that no significant acceleration was recorded while sailing at true wind angles greater than 120 degrees, however the number of hours spent at this heading was too small to allow any conclusion to be drawn. In fact, the third measurement campaign proved that substantial accelerations can be experienced when sailing downwind. Here several severe "slams" were recorded at true wind angles higher than 120 degrees when wave height was greater than 4m. In particular, the highest recorded acceleration was 1.22g at the centre of gravity and it occurred while the boat was sailing at 22 knots with a true wind angle of 133 degrees.

At this point, it should be noted that, in several impacts, the transverse acceleration component was found to be of a similar magnitude to the vertical one, therefore suggesting that a considerable part of the hydrodynamic load was born by the hull topsides. As shown in figure 8 and 9, the actual orientation of the maximum acceleration expectedly depended both on the heel angle and on the true wind angle (which often corresponds to the heading relative to the waves).

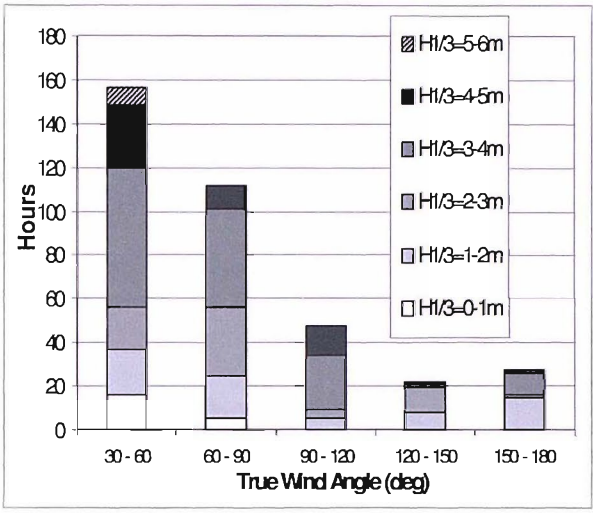

Fig.7 Distribution of time spent sailing at different true wind angles and in different significant wave heights

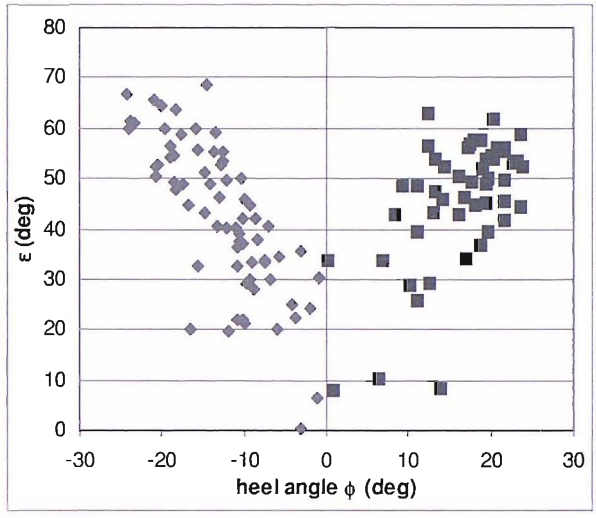

Fig.8 Measured angles of the acceleration vector at the bow relative to the vessel-related vertical axis as a function of heel angle.

	TWA				
	30 - 60	**60 - 90**	**90 - 120**	**120 - 150**	**150 - 180**
$H_{1/3}$= 0 - 1m	0	0			
$H_{1/3}$= 1 - 2m	0.33/h 0.73g	0.36/h 1.13g	0	0	0
$H_{1/3}$= 2 - 3m	1.93/h 0.82g	1.87/h 0.86g	1.67/h 0.84g	0	0
$H_{1/3}$= 3 - 4m	0.89/h 0.98g	0.09/h 0.79g	0	0	0
$H_{1/3}$= 4 - 5m	0.52/h 1.03g	0	0	0	
$H_{1/3}$= 5 - 6m	0				

Table 2 Example of impact characteristics as a function of true wind angle and significant wave height. The value in the top-left corner of each cell indicates the average number of impacts per hour that produce an acceleration greater than 2g at the bow. A value equal to 0 means that the 2g threshold was never exceeded. The number in the bottom-right corner represents the corresponding average acceleration at the centre of gravity. Cells are empty where the conditions were out of the spectrum met during the measurement campaign.

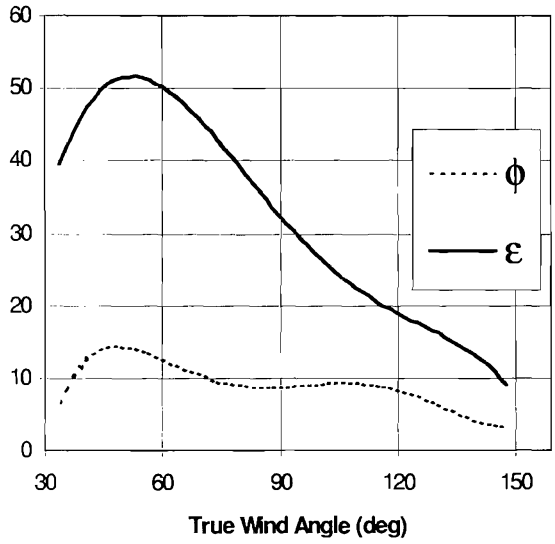

Fig.9 Example of relation between true wind angle, angle of acceleration at the bow (ε) and heel angle (ϕ). The curves represent the moving average of the measured values.

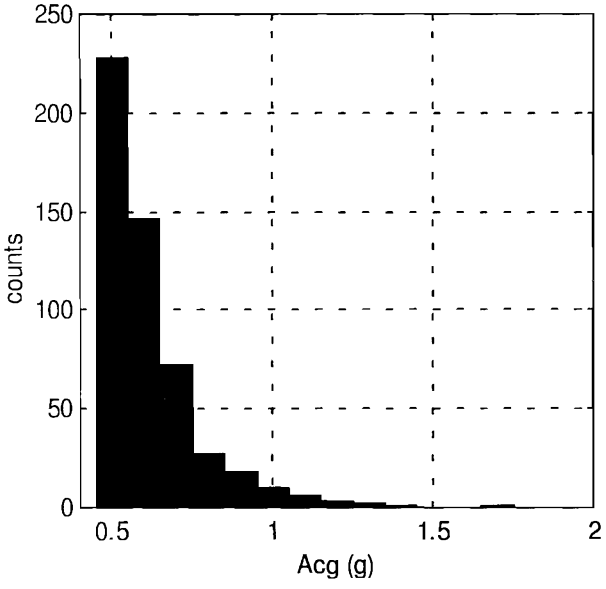

Fig.10 Example of relative frequency of acceleration at the centre of gravity.

Maximum values of rigid-body accelerations from each measurement campaign were analysed statistically. Figure 10 shows an example of the histograms of the peak accelerations at the centre of gravity, built during the measurement campaigns. By analysing these data in terms of cumulative distributions, it was observed that the recordings always matched very closely a Weibull probability distribution function. This had to be written in the form:

$$F_X(x) = 1 - e^{-\left(\frac{x-x_0}{k}\right)^r}$$

where x_0 was equal to 0.5g, the central value of the smallest bin in the recorded histograms. Parameters "k" and "r" were estimated by a linear least squares method. Figure 11 shows an example of the results from the tests on an Open'60. With k and r known, the probability of accelerations exceeding a given value x could be calculated as the joint probability $P_1[A_{cg} \geq 0.5g] \cdot P_2[A_{cg} > x]$ where:

$$P_1 = \frac{2\pi \cdot N_A}{T_R \cdot \overline{\omega}_e} \qquad \text{and}$$

$$P_2 = e^{-\left(\frac{x-x_0}{k}\right)^r}$$

with:

N_A : number of counted accelerations exceeding 0.5g

$\overline{\omega}_e$: average encounter frequency over the recording period (which could be estimated from acquired time histories)

T_R : recording time.

Similarly, the average of the $1/N^{th}$ highest accelerations could be obtained as:

$$\overline{x}_{\frac{1}{N}} = k \cdot M \cdot \left[\frac{(\ln M)^{1/r}}{M} + \frac{1}{r} \cdot \Gamma(1/r) \cdot \left(1 - P(1/r, \ln M)\right) \right]$$

with: $$M = N/P_1 = N \cdot \frac{T_R \cdot \overline{\omega}_e}{2\pi \cdot N_A}$$

and Γ and P respectively the complete and incomplete Gamma functions.

CONCLUSIONS

A data acquisition system has been designed and implemented to study slamming on ocean sailing yachts. Slamming events have been characterised by measuring the rigid-body accelerations and the vibration that they induce in the structure. Rigid-body accelerations have been measured in six degrees of freedom by means of seven strap-down accelerometers. An iterative analysis procedure that allows the calculation of linear and angular displacements from acceleration recordings has been experimentally validated.

Statistical analysis of the results from long measurement campaigns has shown that peak values of acceleration always tend to follow a Weibull probability distribution function. A method has been outlined that allows the calculation of the probability of exceedance of given thresholds and of averages of highest values.

Time histories of the accelerometer signals recorded

during slams have suggested that considerable bending and torsional vibrations are initiated by slamming. Further measurement campaigns are planned in which a larger number of sensors will be used to get a better definition of modal shapes and amplitudes.

ACKNOWLEDGEMENTS

This work would not have been possible without the support of Jean-Marie Finot and of all the people at Groupe Finot Naval Architects: to them we wish to express our deepest gratitude.
We would also like to thank the Wolfson Unit for Marine Technology and Industrial Aeronautics for their assistance throughout the project.
Special thanks go to Josh Hall, Alex Thomson, Mike Golding and Bernard Gallay for letting us install our equipment on their boats.

REFERENCES

Heller, S.R., Jasper, N.H., "On the structural design of planing craft", Transactions of the Royal Institution of Naval Architects, Vol.103, 1961, pp 49-65.

Allen, R.G., Jones, R.R., "A simplified method for determining structural design-limit pressures on high performance marine vehicles", American Institute of Aeronautics and Astronautics, 1978.

Joubert, P.N., "Strength of Bottom Plating of Yachts", Journal of Ship Research, Vol.26, No.1, March 1982, pp.45-49.

Brown, K.C., Joubert, P.N., Ping Yan, "Tests on Yacht Hull Plating", Marine Technology, Vol.33, No.2, April 1996, pp.130-140.

Brown, K.C., Wraith, R.G., Joubert, P.N., "Local Pressure on Hull Plating Due to Slamming", 5th International Conference on Fast Sea Transportation, Seattle, September 1999.

Reichard, R.P., "The Structural Response of Small Craft to Dynamic Loading", Proceedings of the Fourteenth AIAA Symposium on the Aero/Hydronautics of Sailing, Vol.30, Lay Beach, November 1984.

Hentinen, M., Holm, G., "Load measurement on the 9.4m sailing yacht 'Sail Lab'", 13th International Symposium on Yacht Design and Yacht Construction, Amsterdam, Nov.1994.

Jeffrey, T., "Core of the problems", Yachting World, No.146, July 1994, pp.76-77.

Rosen, A., Garme, K., "Slamming Studies on High-Speed Planing Craft through Full-Scale Trials and Simulations", 5th International Conference on Fast Sea Transportation, Seattle, September 1999.

Miles, M.D., "Measurement of six degree of freedom model motions using strapdown accelerometers", 21st ATTC, Washington D.C., 1986, pp369-375.

Det Norske Veritas, "Tentative rules for classification of High Speed and Light Craft", Part 3, Ch.1, January 1991.

American Bureau of Shipping, "Rules for building and classing High Speed Craft", 1997.

Draft ISO Standard 12215 for Small Craft – Hull Construction/Scantling, Part 5, June 2000.

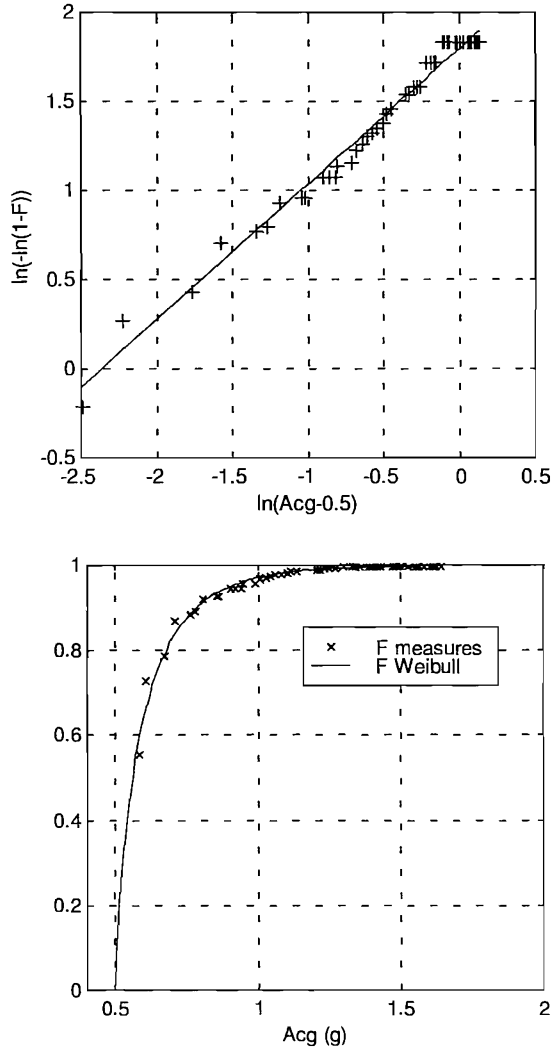

Fig.11 Example of measurements of peak acceleration at the centre of gravity fitting a Weibull probability distribution function.

Appendix I

Paper presented at the 17^{th} International Symposium on Yacht Design and Yacht Construction

Amsterdam, Netherlands, November 18^{th} and 19^{th} 2002.

17th International Symposium on "Yacht Design and Yacht Construction"

INVESTIGATION OF SLAMMING LOADS USING SLAM PATCHES ON A SCALE MODEL OF AN OPEN60' CLASS YACHT.

P. Manganelli*, B. Wagemakers*, P. A. Wilson*

ABSTRACT

A model of an Open60' class boat has been instrumented with slam patches in order to measure hydrodynamic forces acting on the bottom of the hull as a result of slamming. Drop tests and seakeeping tests have been performed to investigate the relative influence of different variables on the magnitude of slamming loads. Results are presented together with a discussion of the issues involved with this particular measurement technique.

INTRODUCTION

The past twenty years have witnessed a formidable progress of the performance of racing yachts. Advances can be ascribed in large part to the new possibilities opened up by the use of polymeric composite materials. The science of structural design has moved forward in parallel. Better understanding of the mechanical phenomena together with wider availability of powerful tools like finite element analysis and fast computers have contributed to this development. At present, many agree that the problem is not so much "how to design and build a structure to resist a given load", but rather "what loads should the structure be designed for?". As performance is continuously increased, new problems appear, need to be understood and then solved. A typical example of this was the extensive delamination of the front crossbeams experienced by three maxi catamarans competing in "the Race 2001": this problem, previously known to designers of fast ferry catamarans, was induced by the considerable loads associated with "wetdeck" slamming. It was only when yachts were built that could regularly sustain average speeds in excess of 30kts, that the problem became known in the world of sailing.

One of the challenges currently faced by designers is the difficulty of obtaining accurate predictions of dynamic loads and response. In this respect, the phenomenon of slamming and its effects on the structure present one of the areas of greatest interest. The problem has been known now for quite some time and the "solutions" found so far have often been the result of a successful empirical approach. This was due more to the tremendous complexity of the engineering problem to be solved than to a lack of technical knowledge. In the recent years, two problems have appeared which have made the need for scientific advances more strongly felt: firstly, it is believed that minor structural failures initiated by slamming loads are common. However, due to the lack of well-established structural monitoring procedures such as those commonly found in the field of aeronautics, these may go unnoticed for long periods and, when eventually discovered, be associated with the wrong cause. Besides financial considerations may induce builders, designers and even owners to keep these failures more or less secret, thus hindering the basic mechanism of empirical progress. Secondly, the constant demand for increasing performance, more and more often leads designers into "untrodden territories", where no previous experience can help.

With the aim of promoting the knowledge of the dynamic loads initiated by slamming on offshore sailing monohulls, a research project was started in 1998 in collaboration between the Department of Ship Science of the University of Southampton and Groupe Finot Naval Architects. As a result, a large amount of experimental data was collected through measurements performed on yachts engaged in long transoceanic passages [13]. In parallel, an experimental investigation of bottom slamming pressures based on model test was started in Southampton. The details of this particular study are presented in this paper.

* School of Engineering Sciences, Ship Science, University of Southampton

EXPERIMENTAL SET-UP

For the investigation of slamming loads a 1/7th scale model of an Open60' (see table 1 for details) was outfitted with "slam patches". The use of a similar method has already been reported by Kapsenberg et al. [10] and by Purcell et al. [14]. The principle of slam patches for the measurement of hydrodynamic bottom pressures is straightforward. A panel of a size representative of a full-scale hull panel (i.e. typically the portion of the hull delimited longitudinally by two bulkheads or ring frames and transversely by two girders or stringers) is cut out of the bottom of the model and replaced by a panel with a high specific stiffness, which does not touch the cutout sides. A load cell is fitted on top of this panel and supported by a rigid stud, which, in turn, is connected to the reinforced internal structure of the model (figure 1). By this arrangement, the external pressure loads acting on the panel are transmitted through and measured by the load cell.

Effectively, slam patches may be considered as pressure transducers with a very large diaphragm. By dividing the force measured by the load cell by the known surface of the scaled panel, the average pressure acting on the panel can be directly obtained.

Several authors have reported on experiments involving the measurement of slamming loads through the use of arrays of pressure transducers fitted on the hull of model and full-scale vessels [15],[14],[8],[1],[9]. It is generally observed that the pressure distribution following a slam is highly non-uniform. Hence, with diaphragm sizes typically in the order of 1-4 mm^2, pressure transducers provide a very local measurement and several sensors must be used if an estimate of the pressure distribution over a hull panel is sought. Conversely, slam patches allow the average pressure to be measured over a set area with only one transducer, while local peak pressures may only be inferred. Among the authors who have studied the problem, there is a rather wide agreement on the fact that the average pressure values offer a better starting point for understanding the structural behaviour of the hull panels exposed to slamming. Allen and Jones [1], for example, stated that the *"average uniformly distributed pressures should correlate much more closely with measured structural responses in plating, stiffeners and frames, than would the peak pressures as measured on individual gauges."* Two main considerations support this statement: firstly, measurements of local pressures performed on vessels in a seaway, tend to show considerable scatter as small variations of the impact angle and of the water surface state can produce very large differences. It is thus extremely difficult to repeat two identical slams even in a controlled laboratory environment. Secondly, the local pressure peaks tend to act for a very short time, (often smaller than the first natural period of the panel) and over a very limited area. The response of the first natural modes of deformation of the structure is then only marginally affected by these values and correlates more closely with the relatively slower variation of the average pressure.

Several aspects influenced the design and construction of the slam patches. The size was chosen to correspond to a full-scale panel of the Open60' yacht represented by the model, while a square shape was adopted in order to minimise the moments acting on the load cell. This produced a panel size of 80x80mm at model scale. Preliminary seakeeping tests [5] indicated the main slamming area to be comprised between 25% and 45% of the waterline length aft of the forward perpendicular. Six slam patches were then fitted in this portion of the hull, respectively three along the centreline and three on the starboard side, placed along the centreline of the wetted area corresponding to a 20 degrees heel angle. In order to ensure sufficient stiffness and strength of the model and to provide a firm point of attachment for the support stud connecting the panel to the model, additional stiffening members were laminated into the model, as shown by figure 1. All six panels were made of glass fibre and polyester resin, laminated in a female mould of the model. The thickness of the panels varied between 2.5 and 3mm. A small GRP bridge structure was then laminated on the upper side to allow an accelerometer to be mounted at the centre of the panel while providing an attachment point for the load cell. A 1.5mm gap was left between the panels and the hull cut-out: the reduced length of the support studs together with the stiff general construction ensured that the panel would never come in contact with the surrounding structure and that all the loads would be carried by the load cell.

Watertight integrity was guaranteed by a thin film of latex applied over the exterior side of the panels and attached only to the surrounding part of the hull. This method had been validated previously by Kapsenberg et al. [10] and offered the smallest interference with the panel movements under the applied loads.

Three piezoelectric load cells with a range of +/-500N and a natural frequency of 70kHz were used, allowing the force to be measured only on three of the six panels at each slam. Several different arrangements were adopted in order to investigate the evolution of the pressure, both in the longitudinal and transverse direction. It was initially planned to fit four pressure transducers at the corners of the aftmost centreline panel to provide an element for comparison with the slam patch measurements. However, at the time of performing the tests, only four sensors with a range of 13.5kPa could be sourced. Although not suitable for measuring the peak pressures, these transducers were used anyway to provide an indication of the evolution of the pressure front over the adjacent panel.

Two accelerometers with a range of +/-10G were fitted on the bow and at the LCG of the model, while piezo-electric accelerometers with a range of +/-1000G were placed on the instrumented panels to measure their inertial response.

Furthermore, during the rotational drop tests, a linear potentiometer attached between a fixed overhead point and the bow was used to obtain the vertical velocity of the model at the time of impact. During tests in waves with forward speed, this velocity was deduced from measurements of heave and pitch available from the transducers fitted on the towing post. All tests were filmed by using two video cameras (one under water an one just above the surface) to provide further visual information. The layout and numbering of the sensors is shown in figure 2.

The experiments were performed with the model held stationary and also attached to a towing tank carriage in the following series: rotational drop tests with zero forward speed, rotational drop tests with forward speed and towing tests in waves. Rotational drop tests were performed by supporting the model from the transom with a purpose built rig and by letting the bow fall freely into the water from variable heights. To ensure repeatability, a release mechanism based on an electromagnet was implemented. The point of first contact with the water and the trim angle at impact could be varied by adjusting the transom height. For drop tests with forward speed, the support rig was attached to the underside of the towing tank carriage and the model was released onto the calm water when the set speed was reached. Forward speed tests were performed in a way similar to standard seakeeping tests, by towing the model in regular waves: the model was allowed to heave and pitch freely and was restrained in sway, surge, roll and yaw. The tests were performed in regular waves rather than in a set of irregular waves because this would guarantee better repeatability of the measurements and allow a larger number of slams to be recorded at each run.

Where possible, a number of parameters were varied in isolation within each test series to investigate their influence. Thus, for the drop tests, impact velocity, forward velocity, displacement, longitudinal radius of gyration, point of initial impact/trim angle at impact and heel angle were varied. For the forward speed tests, displacement, forward velocity and wave height and slope were varied. A summary of the main test parameters can be found in table 2.

All signals from the sensors were collected through two 8-channel A/D converters and logged with a desktop PC. Sampling rates ranging between 2KHz and 10kHz were used, depending on the length of the acquisition and on the number of logged signals. Calibration of the pressure transducers was performed with a 1.2m tube filled with a column of water of known height, placed over the sensors with the hull turned upside down. Readings from the load cells were checked by forcing vertical oscillations of the model in water and by comparing measurements with the pressure transducers. The difference was generally smaller than 2%.

DYNAMIC BEHAVIOUR OF A SLAM PATCH

Before proceeding to analyse the results of the measurements, some aspects of the dynamics of slamming loads and of the ensuing structural response should be carefully considered.

The behaviour of a slam patch is more easily understood through the analysis of a mechanical analogue. Thus, to a first approximation, the slam patch assembly may be described as the one-degree-of-freedom system shown in figure 3. The force measured by the load cell is equivalent to the force exerted by the

spring (and the damper) onto the mass element (i.e. the panel) m_{sp} and is then proportional to its displacement relative to the support structure m_{mod}. It can be demonstrated that, depending on the time history of the external load, the phase and relative amplitude of the response may vary, or in other words, that the measured force may differ from the externally applied one [17]. On this point, Kapsenberg [10] commented that the slam patch behaves as a "mechanical filter", responding linearly to the slow variations of the pressure load and hardly reacting to the faster ones. The slamming load acting on the panel may then be known by measuring jointly the force applied to the load cell and the acceleration of the panel itself. In the present investigation, this was done by fitting high frequency accelerometers onto the panels that were supported by the load cells.

Preliminary tests performed with an impact hammer, proved that it was thus possible to measure the external transient load with accuracy greater than 5%. However, when the same method was applied during the drop tests, the results were unreliable: while the forces measured by the load cells showed very good repeatability, the acceleration data were totally uncorrelated. It is believed that this was due to water impact producing a larger response of the vibrational modes of the panel itself. Hence, the measured accelerations were not representative of the "rigid-body" motion of the panel. This fundamental problem is difficult to overcome as most solutions (e.g. fitting additional accelerometers on the panel, using a stiffer panel) would increase the weight of the panel and, thus, reduce the natural frequency of the slam patch. Therefore, when an exact measure of the external slamming load is sought, a dense array of conventional pressure transducers may offer a better solution than slam patches. On the other hand, it can be argued that, in view of structural design, the force measured by the load cell of a slam patch may represent a more useful piece of information than the external load. In fact, similarly to the slam patch, the structure of the full-scale boat does not respond linearly to the transient slamming load. For the purpose of structural design, it is then customary to refer to equivalent static pressures as the load which, if applied statically to the structure, will result in the same amount of deformation and stress as the ones produced by the actual dynamic loading [8]. *Provided the slam patch replicates the dynamic behaviour of the full-scale structure*, the force it measures should correspond exactly to the equivalent static load on the hull panel.

The natural frequencies of all the slam patches were measured in the dry condition by impact hammer tests and found to lie in the range between 425Hz and 610Hz, equivalent to a full-scale range of 160-230Hz. Table 3 reports the first bending mode natural frequency obtained by using analytical formulas [19] for the corresponding full-scale panel with different boundary conditions and different material properties. Similarly, finite element analysis carried out by Manganelli [13] indicates the first natural frequency of a typical rectangular panel of a modern Open60' (made of a monolithic carbon fibre-epoxy laminate) to be in the range of 185 to 300Hz, again depending on the boundary conditions. It was then concluded that the frequency response of the slam patches was representative of that of an actual full-scale hull panel.

HYDROELASTIC EFFECTS AND SCALING OF THE LOADS.

It is arguable that hydroelasticity plays an important role in the determination of slamming loads. Both Faltinsen [7] and Bereznitski [2] agree on the point that hydroelastic effects reduce the amplitude of the response of the structure subjected to slamming loads. Simply put, this may be explained by the fact that the deflection of the structure produced by the initial slamming force induces a drop of the velocity of the structure itself relative to the water: this drop, in turn, brings a reduction of the pressure exerted by the fluid on the impacting body and, hence, a lower maximum deformation. It appears then that, in order for the structural behaviour of the model to be representative, full-scale hydroelastic effects should be replicated correctly at model scale. This raises two main issues.

Firstly, it may be observed that the behaviour of the slam patches used in the present investigation does not reproduce exactly that of an actual hull panel. The first mode of deformation of the slam patch involves a nearly uniform vertical displacement of the panel as the load cell contracts and expands like a spring. Conversely, a hull panel has the vertical motion of its edges constrained by the surrounding structure and its first bending mode can involve a very different amount of deflection between the edges and the centre, depending on the boundary conditions. If then the first natural frequency of the slam patch and its stiffness are equivalent to those of the hull panel, the overall reduction of relative velocity following impact is expected to be more important for the slam patch panel (as the whole panel deflects upwards instead of just

the central portion). Hence, larger hydroelastic effects and consequently lower response may be observed for the slam patch. When scaling measurements from model to full-scale, this would lead to an underestimation of the actual response or, in other words, to a non conservative prediction of the equivalent loads.

Secondly, it can be demonstrated that, if the behaviour of the slam patch is to replicate that of a hull panel in terms of the bending stiffness (defined as the ratio of the force uniformly applied over the panel to the deflection at its centre), the stiffness k_{sp} of the patch should be equal to:

$$k_{sp} = \frac{1}{R^2} k_{fsp} \text{ with } k_{fsp} = \frac{E_{fs} \cdot t_{fs}^3}{\alpha \cdot b_{fs}^2}, \quad (1)$$

where R is the scale factor (7 in the present study), k_{fsp} is the equivalent bending stiffness of the full-scale panel and E_{fs}, t_{fs}, and b_{fs}, are respectively the modulus of elasticity, thickness and length of the full-scale panel. a is a coefficient whose value depends on the boundary conditions and on the length/width ratio of the panel and, in the present case, is comprised between 0.0138 (for all edges fully clamped) and 0.0444 (for all edges simply supported).
It has been suggested by Sellars that hydroelastic effects should be scaled on the basis of a constant Cauchy number [16], which is an expression of the relative magnitude of inertial forces to elastic forces, and can be expressed as:

$$C_n = \frac{\rho \cdot V^2}{E} \cong \frac{\rho \cdot V^2 \cdot \ell}{k} \quad (2)$$

with ρ being the density of the water, V the impact velocity and l a typical linear dimension of the structure. If the density of water is the same for model and full-scale conditions, equation (1) is compatible with a constant Cauchy number when velocities are scaled on the basis of constant Froude number.

Considering the slam patches used in the present study, table 3 shows that the ratio of the stiffness k_{sp} to the bending stiffness of a full-scale panel was of the order of 1/R and therefore too high. In relative terms, the attenuation of the structural response due to hydroelastic effects may then be expected to be lower at model scale.

It is important to note that, from a practical point of view, correcting this problem would be very difficult. Indeed, the stiffness k_{sp} of the slam patch is strictly dependent on the rigidity of the load cell, which, typically, is determined by manufacturing characteristics and cannot be easily altered. Besides, in the present case, the requirement for the natural frequency of the slam patch to be correctly scaled would also call for an extremely low panel weight, hardly achievable if sufficient stiffness is to be guaranteed.

Based on the conclusions drawn by Bereznitski [2], it appears that the effects of hydroelasticity depend mainly on the ratio of the impulse duration to the first natural period of the structure, and that they are not very sensitive to changes in stiffness. It seems preferable then to privilege a correct scaling of the natural frequencies than of the stiffness. Furthermore, a quantitative estimate of the error introduced by the incorrect scaling of hydroelastic effects may be obtained from the data presented by Bereznitski for a two dimensional beam. These indicate that an augmentation of the bending stiffness by a factor of 7.9 (i.e. close to the present case) would produce an increase of the structural response by approximately 35%. An error of the same magnitude may then be considered to affect the estimate of the full-scale equivalent slamming loads obtained from the measurements performed in the present study.

Finally, it has been noted by Sellars that the effects of air entrapment do not scale due to the velocity of sound in air being the same at model and full-scale. As a result, the attenuation of the slamming pressures induced by this phenomenon is expected to be more significant at full-scale. This may again contribute to render the load predictions obtained from model tests conservative [16]. However, drawing from a comparison between experimental data and analytical model predictions, Wraith [18] suggests that the cushioning effect of air entrapment is negligible for bodies with the curvature radii typically found in sailing yacht hulls. Hence, it may be concluded that the error introduced by the incorrect scaling of air entrapment effects in the present study was marginal.

EXPERIMENTAL RESULTS

The most relevant results obtained from all test series are discussed below. A more comprehensive description of all the acquired data may be found in [5] and [13]. All data are presented for the full-scale yacht. In conformity with the considerations on scaling set out in the previous section, Froude scaling has been applied. Pressures are reported as measured by the load cells and no correction from the acceleration of the panel has been included. As mentioned previously, the loads thus obtained correspond to the equivalent static loads normally referred to for design purposes.

The relation between impact velocity and maximum equivalent average pressure on the panels is shown in figures 4 and 5. In particular, figure 4 presents the pressures obtained from rotational drop tests with zero heel angle. Experimental data have been fitted by a least squares method with trend lines of the form: $P_n = \beta_n \cdot V_i^{\gamma_n}$, with P_n representing the maximum equivalent average pressure on panel "n" and V_i^{γ} the velocity recorded at the centre of the panel at the time of impact (although the accelerometers gave evidence of a small amplitude longitudinal bending vibration prior to impact, this effect was neglected and the model was considered to move like a rigid body for all the time preceding impact; a more comprehensive description of this phenomenon together with a justification of the rigid body assumption can be found in [13]). The parameters β_n and γ_n are given for all six panels in table 4. Normalised rms errors between experimental values and the theoretical fitting line are equally presented in table 4. Considering the large scatter that often affects experimental measurements of slamming pressures, the repeatability of these results was very satisfactory. Despite the tests being performed with a limited set of drop heights, it was extremely difficult to repeat impact velocities accurately: this was explained by the fact that differences in drop height of a few tenths of a millimetre would be sufficient to produce appreciable variations of the impact velocity. The data reported in figure 4 correspond to a series of drops carried out in the standard condition, i.e. with the standard displacement and mass moment of inertia (as indicated in table 2) and with the transom height set for a point of first contact between the hull and the water placed at 34.5% of the waterline length aft of the forward perpendicular. In this condition, panel 2 hit the water slightly before panel 1 and 3 in the upright tests, and similarly panel 5 preceded panel 4 and 6 in the heeled tests.

It can be noted that the values of the exponents are very consistent, possibly with the exception of panels 4 and 5, which also feature the smallest mean curvature radius. A qualitative justification for the observed values of γ may be presented as follows: on the basis of theoretical considerations founded on the principle of conservation of momentum, and in the absence of all factors that may limit the pressures acting on the panels (e.g. effects of the compressibility of water, cushioning by entrapped air, etc.), pressures would be expected to be proportional to the impact velocity squared. However, as the velocity increases, the pressure pulse duration and rise-time decrease proportionally: as the pressure rise and decay times become shorter than the first natural period of the panel, the ratio of the maximum response to the maximum excitation will equally decrease. Furthermore, hydroelastic effects and air entrapment are both expected to reduce the maximum load with increasing impact velocities. In this respect, it may be noticed from figure 4 that the pressures recorded at the highest impact velocities tend to lie below the trend line: this may be an indication of the fact that, at higher velocities, attenuating factors become even more important.

The effect of panel curvature may be observed by comparing the results for panel 2 and 5: as the curvature radius decreases from 6.2m to 1.94m, β shows a 52% reduction. On the contrary of what would be expected, in the same case, γ increases. This, however, may be explained by the fact that a lower number of data points was used for the calculation of γ_5.

The effect of the trim angle of the panel at the time of impact was investigated by performing rotational drop tests with different transom heights: as a result, the point of first contact with water was shifted fore and aft of the area where the slam patches were fitted. A summary of the results of these tests is presented in figure 6. It was noted that small changes in trim (i.e. of the order of 1 deg) did not have a significant effect on the values of γ while they altered β by as much as 50%.

Figure 7 gives evidence of the decay of maximum pressures along the girth: the indicated pressures were recorded by instrumenting both panel 2 and panel 5 during the same test. Rotational drops were carried out at zero heel angle and the maximum pressures have been plotted with respect to the impact velocity of panel 2. It may be noted that the values measured for panel 5 could be ascribed almost entirely to hydrostatic pressure. This was certainly the combined result the high average deadrise angle of the side panel (≈37deg) and of the considerable deceleration happening between the time of impact of panel 2 and the first contact of panel 5.

The detailed analysis of panel response times and of vertical displacement time histories obtained from the linear potentiometer, indicated that no sensible change in the vertical velocity of the model happens between the time of impact and the instant when the maximum force is measured by the load cells. This was further investigated by performing tests with increasing mass moments of inertia (the equivalent of increasing displacement for standard translational drop tests) and constant impact velocity. Figure 8 shows that no consistent variation of the maximum pressure on panel 2 could be observed for an increase of the inertia of up to 80%. This supports the thesis that, for relatively small hull panels, maximum pressures depend mainly on the impact velocity and are not affected by displacement.

Results obtained with the model towed in waves are shown in figures 9 to 11. All tests were performed in regular waves in the towing tank of the Southampton Institute for Higher Education. The standard testing condition included the same displacement Δ_0 adopted for the drop tests and a boat speed of 8.8kts (F_n=0.35 is considered to be representative of an Open 60' sailing upwind in rough seas). Due to the size limits of the towing tank, tests were only performed in bow waves (μ= 180deg). In order to maximise the occurrence of slamming, the wavelength was adjusted to produce the encounter frequency corresponding to the maximum value of the pitch RAO [5]. A wave height variation of 0.075m to 0.18m at model scale (i.e. 0.525÷1.26 m at full-scale) was initially planned. It was later found that heights lower than 0.09m would not produce any slamming while waves higher than 0.16m would cause the bow of the model to hit the underside of the towing carriage. Between four and eight slamming events could be recorder at each run. In spite of all efforts made to guarantee good repeatability, impact velocities, and consequently impact loads, were still affected by noticeable scatter. Typically a normalised rms scatter of 5% could be observed for impact velocities and of up to 35% for impact pressures, within the same run. Nevertheless, some clear trends could be identified in the acquired data.

Figure 9 shows the pressure-velocity relation obtained for panels 1 to 3 from tests in the upright condition with standard boat speed and increasing wave height. The mean values and standard deviations of impact speed and impact pressure were calculated for all slams in each run. This resulted in the data points and the error bars represented in figure 9. It will be noticed that, for the same impact velocities, the equivalent average pressures generated by impacts in waves were almost always lower than those observed in the drop tests. Several factors were responsible for this reduction: first of all, the average trim angle of the panels at the time of impact ranged from –2 to +6 degrees; results from the drop tests series proved that smaller variations of the trim angle were sufficient to substantially decrease the maximum pressures. Also, footage obtained from both the underwater and above-water camera, confirmed that a considerable amount of water remained attached to the bottom of the hull in the phase between emersion and re-entry, and that the associated dripping altered the state of the free surface prior to each slam. The effects of these irregularities were not covered by drop test investigations, however results published in [3] and [4] for cylinders with circular section indicate that, specially at small trim angles, they may reduce the maximum amplitude of response by up to 20%. More importantly, figure 10 illustrates that, while average pressures are generally lower for the tests in waves, occasionally some slams could produce loads equal or even marginally higher than those measured in the drop tests. It seems then reasonable to conclude that the drop tests results may be retained as a close indication of the maximum equivalent slamming loads experienced by the hull of a yacht in a seaway.

Finally, the effects of displacement variation were analysed as shown in figure 11. In particular, tests were performed with three different displacements, by adding weights at the LCG of the model (thus leaving the moment of inertia virtually unchanged), equivalent to the mass of the water ballast taken onboard by some Open 60s'. The wave encounter frequency was always kept the same as in the standard test conditions. Hence, the relative amplitude and phase of the motion would be expected to change for different

displacements. The common perception that increased displacement makes a boat more sea kindly, was confirmed by the measurements: indeed, in the higher ballast configurations, slamming was not observed on panel 2 and 3 for wave heights lower than 1 metre. A comparison of the loads on panel 1 showed that these remained approximately constant in the intermediate ballast condition and eventually decreased at the highest displacement. This latter phenomenon was most probably produced by the boat slamming "earlier" on the back of the wave and, consequently, with higher trim angles.

Although an investigation of the effects of forward speed variation was planned, due to a failure of the data acquisition system, a representative quantity of data could not be obtained.

Rotational drop tests with forward speed in the upright and heeled condition, reproduced closely the results observed for the zero speed homologues, to the only exception of the pressures measured on panel 4. This showed a marginal increase of the loads at the highest speeds. It was then concluded that slamming loads were only dependent on the component of flow velocity perpendicular to the panel surface, and that the increase shown by panel 4 was due to its normal vector being oriented slightly towards the bow.

CONCLUSIONS

A simple and reliable method for the measurement of equivalent "static" slamming loads has been established. The importance of scaling issues has been underlined. It is the authors' belief that some of the discrepancies observed in the published data about slamming pressures, may be due to such issues being overlooked.
The results of rotational drop tests in calm water and with no forward speed have confirmed the strong dependency of the structural response on the impact velocity. Formulas that describe this relation have been outlined. Due to a lack of experimental validation, their scope cannot be extended to hull forms and structures different from those examined in the present study. They may however offer a valid reference for qualitative considerations applied to similar yachts.

Maximum panel loads were found to be insensitive to the inertia of the model. However, displacement may play a significant role in the decay of pressures away from the point of first impact. For the presently examined yachts, the low length-volume ratio certainly contributes to a very fast decay.

Measurements of equivalent slamming loads performed in waves with forward speed showed considerable scatter. Small changes of the trim angle at impact and the variable effects of the disturbance produced by the motion of the hull on the free surface were considered as the main causes for this dispersion. While loads originated by slams in waves were generally lower than those observed in the drop tests, equal impact velocities could occasionally induce similar pressures. For the purpose of design, reference should therefore be made to the results obtained from drop tests.

No comparison of the measured loads has been carried out with the design pressures recommended by classification societies and other design standards. For this to be possible, a criterion for the definition of impact velocities should first be established. In this respect, measurements performed by Manganelli on full-scale Open'60 suggest that impact velocities greater than 2.5 m/s may be observed regularly in heavy slamming conditions [13][12]. Even allowing for the pressures indicated by the drop tests data to be somewhat conservative, the resulting loads would still seem to be dangerously close to the design limits currently adopted for these structures. It may then be concluded that, through different ways, the structural designers of the boats examined here have come to reduce safety margins to very low levels and that any step towards further structural optimisation should be taken with the greatest caution.

ACKNOWLEDGMENTS

The present work was largely based on the experimental results obtained by Messrs. Jeremy Elliott, David Grant, Dan Holman, Stuart Woodger, and Bob Wagemakers, as part of their M.Eng. Group Design Project carried out in Ship Science, School of Engineering Sciences, University of Southampton.

The authors would like to express their gratitude to:

Dr Jan Alexander Keuning for providing the yacht models that were used in the present study and Groupe Finot Naval Architects for giving access to all the needed technical information.

Geert Kapsenberg for sharing with them his extensive knowledge and experience.

REFERENCES

[1] Allen, R.G. and Jones, R.R. "A simplified method for determining structural design-limit pressures on high performance marine vehicles", AIAA/SNAME Advanced Marine Vehicle Conference, April 1978.

[2] Bereznitski, A., "Slamming: the role of Hydroelasticity", Intl. Shipbuild. Progr., vol.48, no.4, 2001, pp. 333-351

[3] Campbell, I.M.C., Wellicome, J.F., Weynberg, P.A., "An Investigation into Wave Slamming Loads on Cylinders (OSFLAG 2A)", Wolfson Marine Craft Unit, Report No.317, 1977

[4] Campbell, I.M.C., Weynberg, P.A., "Measurement of parameters affecting slamming", Wolfson Unit for Marine Technology and Industrial Aeronautics, Report No. 440, 1980

[5] Elliot, J.P, Grant, D.S., Holman, D.C., Wagemakers, B., Woodger, S.J., "An Investigation of the Influence of Slamming Impact on the Design of Offshore Sailing Yachts", M.Eng (Hons) Group Design Project, Ship Science, School of Engineering Sciences, University of Southampton, 2002

[6] Faltinsen, O.M., "Sea Loads on Ships and Offshore Structures", Cambridge University Press, 1990

[7] Faltinsen, O.M., Kvålsvold, J., Aarsnes, J.V., "Wave Impact on a horizontal elastic plate", Journal of Marine Science and Technology, No.2, 1997, pp.87-100

[8] Heller, S.R., Jasper, N.H., "On the Structural Design of Planing Craft", Transactions of the Royal Institution of Naval Architects, Vol.103, 1961, pp 49-65.

[9] Hentinen, M., Holm, G., "Load measurement on the 9.4m sailing yacht 'Sail Lab'", 13th International Symposium on Yacht Design and Yacht Construction, Amsterdam, November 1994.

[10] Kapsenberg, G.K. and Brizzolara, S. "Hydro-elastic effects of bow flare slamming on a fast monohull." Fifth International Conference on Fast Sea Transportation (FAST'99), Seattle, August 1999.

[11] Kapsenberg, G.K., various verbal and written communications between April and December 2001

[12] Manganelli, P., Wilson, P.A.W., "An Experimental Investigation of Slamming on Ocean Racing Yachts", Proceedings of the 15th Chesapeake Sailing Yacht Symposium, Annapolis, January 2001

[13] Manganelli, P., "Experimental Investigation of Slamming Loads on Offshore Sailing Yachts", Internal Report, Ship Science, School of Engineering Sciences, University of Southampton , 2002

[14] Purcell, E.S., Allen, S.J and Walker, R.T. "Structural Analysis of the U.S. Coast Guard Island Class Patrol Boat." SNAME Transactions, Vol.96, 1988, pp.221- 246.

[15] Rosen, A.R. and Rutgersson, O., "Full-scale trials on a small high speed naval craft with focus on slamming", 17th International Conference on Offshore Mechanics and Arctic Engineering, 1998.

[16] Sellars, F.H., "Water Impact Loads", Marine Technology, Vol. 13, No. 1, Jan 1976, pp. 46-58

[17] Snowdon, J.C., "Vibration and shock in damped mechanical systems", John Wiley&Sons, 1968

[18] Wraith, R., "Pressure Loads on Ship Hull Plating Caused by Slamming", PhD Thesis, University of Melbourne, 1998

[19] Young, W.C., "Roark's formulas for stress and strain", 6th edition, McGraw-Hill, 1989

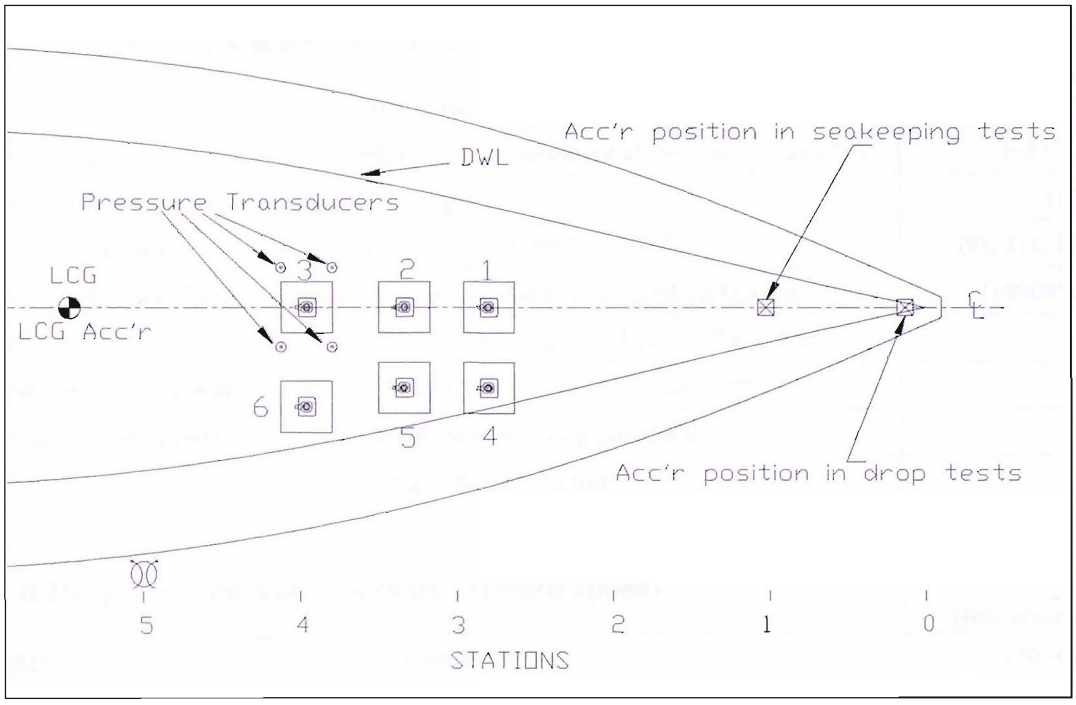

Figure 2 – Layout of the sensors in the scale model

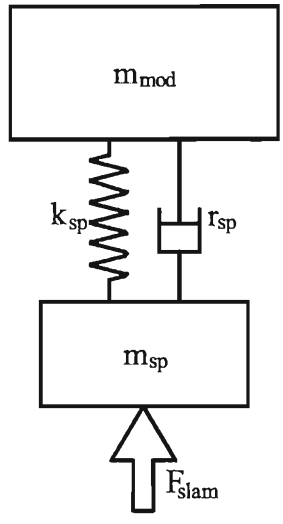

Figure 3 – Mechanical analogue of a slam patch: m_{mod} indicates the mass of the model excluding one slam patch, m_{sp} represents the mass of the panel plus accelerometer, fastening parts (nut, screw and washer) and half the mass of the load cell, k_{sp} indicates the rigidity of the slam patch and r_{sp} describes the total structural damping. F_{slam} indicates the integrated pressure over the slam patch panel. Typical values found in the present study were: m_{sp}=0.053 kg; k_{sp}= 392180÷807950 N·m; r_{sp}= 0.005 r_c (r_c: critical damping ratio)

- Table 2 -

Rotational Drop Tests Parameters (zero forward speed)

		(full-scale equivalent)
Drop Height:	**10÷70mm**	**(70÷490mm)**
Vertical velocity at impact:	**~0.4÷1.3 m/s (measured at the centre of panel 2)**	**(~1÷3.5 m/s)**
Displacement (Standard condition): (Δ_0=32.13kg)		**(11t)**
Displacement variations:	**$0.8\cdot\Delta_0$, Δ_0 , $1.19\cdot\Delta_0$, $1.4\cdot\Delta_0$**	**(9t, 11t, 13.5t, 15.9t)**
Mass moment of inertia about pivot point (Standard condition): I_0=64.893 kg·m^2		**(1090657 kg·m^2)**
Mass moment of inertia variations:	**$0.82\cdot I_0$, $0.9\cdot I_0$, I_0 , $1.13\cdot I_0$, $1.27\cdot I_0$, $1.45\cdot I_0$**	
Point of first contact with water:	**13.4 , 34.5 , 57.2 % of L_{WL} aft of FP**	
Trim angle at time of impact:	**-0.775 deg , -0.4 deg , -0.125 deg**	
Heel angles:	**0 deg , 10 deg , 20 deg**	

Rotational Drop Tests Parameters (with forward speed)

		(full-scale equivalent)
Drop Height:	**10÷60mm**	**(70÷420mm)**
Vertical velocity at impact:	**~0.4÷1.2 m/s (measured at the centre of panel 2)**	**(~1÷3.2 m/s)**
Forward speed:	**0.97÷3.5 m/s**	**(2.57÷9.26 m/s i.e. 5÷18kts)**
Displacement:	**Δ=32.13kg**	**(11.02t)**
Mass moment of inertia:	**I_0=64.893 kg·m^2 (about pivot point)**	**(1090657 kg·m^2)**
Point of first contact with water:	**34.5 % of L_{WL} aft of FP**	
Trim angle at time of impact:	**-0.4 deg**	
Heel angle:	**0 deg**	

Tests in regular waves (with forward speed)

		(full-scale equivalent)
Displacement:	**Δ , $1.18\cdot\Delta$, $1.33\cdot\Delta$ (Δ=32.13kg)**	**(11t , 13t, 14.7t)**
Mass moment of inertia (about LCG):	**$I_{cg,0}$, $1.23\ I_{cg,0}$, $1.85\ I_{cg,0}$ ($I_{cg,0}$=12.67 kg·m^2)**	**($I_{cg,0}$=212945 kg·m^2)**
Wave encounter frequency:	**6.787 rad/s**	**(2.565 rad/s)**
Forward speed:	**1.711 m/s (F_n=0.35)**	**(4.53 m/s i.e. 8.8kts)**
Wave Height (H):	**0.075÷0.16 m**	**(0.525÷1.26 m)**
Wave Slope (H/λ)	**2.19% ÷ 4.67%**	
Heel angle:	**0 deg, 20 deg**	

- Table 3 -

			all edges simply supported		all edges fixed	
Material	**Weight / unit area [kg/m²]**	**Flexural rigidity [N·m]**	**1st natural frequency [Hz]**	**Bending stiffness [N/m]**	**1st natural frequency [Hz]**	**Bending stiffness [N/m]**
E-Glass/Epoxy	**22.769**	**2917.7**	**113.4**	**2472072**	**207.2**	**7953624**
Kevlar/Epoxy	**15.440**	**2925.7**	**137.9**	**2472072**	**252.0**	**7953624**
Carbon/Epoxy	**12.479**	**2874.2**	**152.0**	**2472072**	**277.8**	**7953624**
Carbon/PVC/Epoxy Sandwich	**8.075**	**3042.0**	**194.4**	**2472072**	**355.3**	**7953624**

Natural frequencies are calculated as follows:

$$f = \frac{K_1}{2\pi}\sqrt{\frac{D}{m_a \cdot b^4}}$$

(D: flexural rigidity; m_a weight per unit area; b: length of the panel)
all edges simply supported : $K_1 = 19.7$
all edges fixed: $K_1 = 36.0$ (ref. [19])

Bending stiffness is defined as:

$$k = \frac{E \cdot t^3}{\alpha \cdot b^2}$$

(E: equivalent elastic modulus; t: overall thickness of laminate; b: panel length)
all edges simply supported : $\alpha = 0.0444$
all edges fixed: $\alpha = 0.0138$ (ref. [19])

All data are calculated for a 560x560mm panel. Thicknesses vary for different materials in order to achieve a constant bending stiffness equivalent to that of a typical hull bottom laminate found in the Open 60' yacht under study.

For comparison:		
Slam patch nat. frequencies:	**425Hz ÷ 610 Hz**	**(full-scale equivalent: 161Hz ÷ 231Hz)**
Slam patch stiffness (k_{sp}):	**392180 N·m ÷ 807950 N·m**	

- Table 4 -

Panel #	β_n	γ_n	**n.r.e. %**	**mean curvature radius [m]**	**trim @ impact [deg]**
1	**52631**	**1.6511**	**10.1**	**3.541**	**-0.27**
2	**81397**	**1.5920**	**8.3**	**6.208**	**0**
3	**66796**	**1.625**	**10.3**	**8.201**	**0.37**
4	**21584**	**1.7173**	**5.3**	**1.785**	**-2.07**
5	**39199**	**1.7867**	**3.0**	**1.941**	**0**
6	**45591**	**1.6534**	**4.7**	**2.207**	**2.48**

The panel mean curvature has been defined here as:

$$r_m = \frac{r_1 \cdot r_2}{r_1 + r_2}$$

r_1 and r_2 are the curvature radii of the arcs passing through the centre of the panel and the midpoints of respectively the longitudinal and transversal edges of the panel

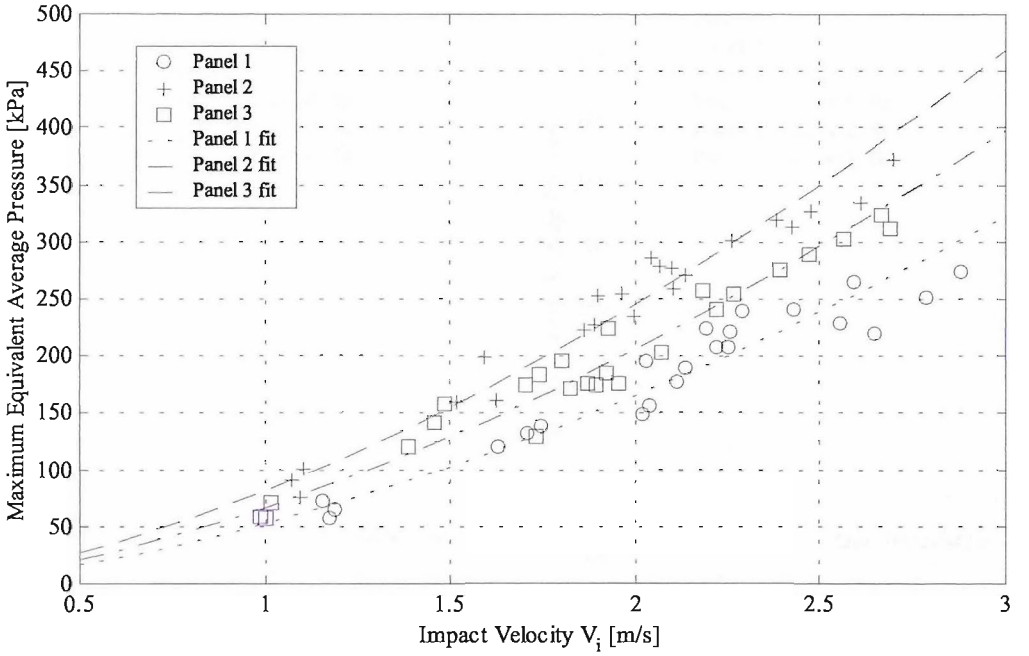

Figure 4 – Maximum equivalent panel pressures obtained from tests in standard condition (base displacement, zero heel, intermediate transom height). Parameters defining the trend lines are given in table 4.

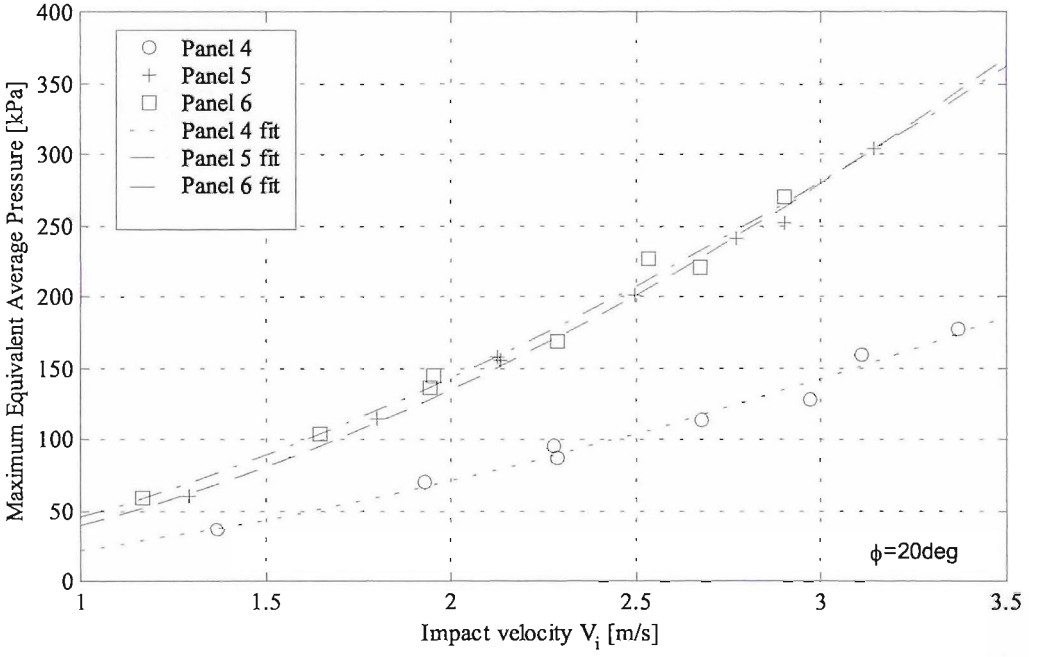

Figure 5 – Maximum equivalent panel pressures obtained from tests in standard heeled condition (base displacement, twenty degrees heel to stbd, intermediate transom height). Parameters defining the trend lines are given in table 4.

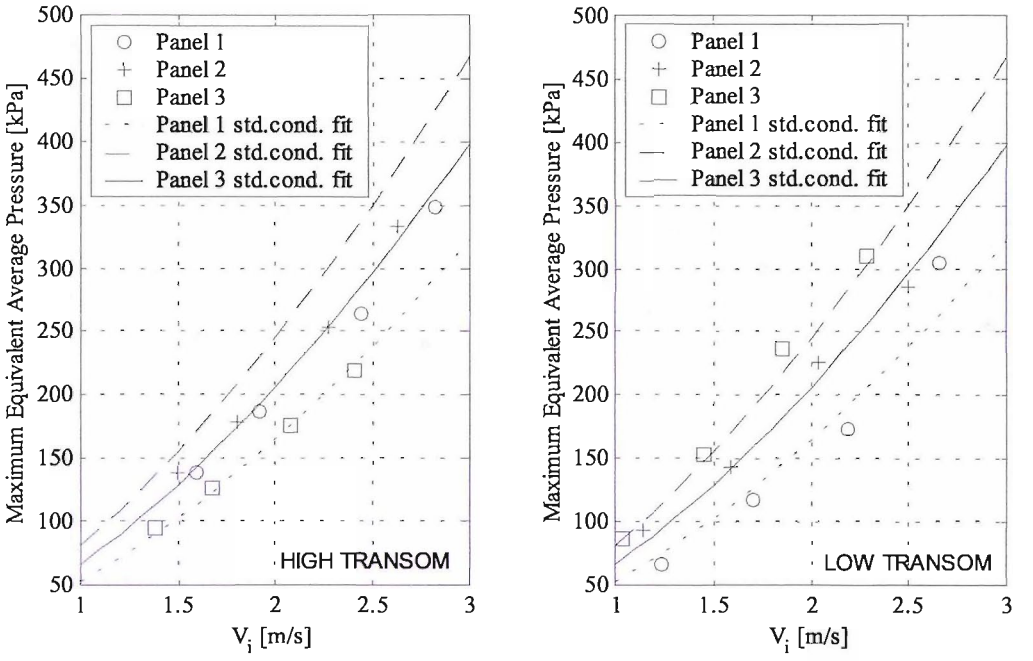

Figure 6 – Effect of the change of longitudinal position of first contact with water. The reported lines are the trend lines fitting the standard condition data (intermediate transom height, point of first contact on panel 2): they are plotted here for the sake of comparison. In the "high transom" condition, relative to the standard condition, P1 loads increased by an average of 19.3%, P2 loads decreased by an average of 13.2% and P3 loads decreased by an average of 19%. In the "low transom" condition, relative to the standard condition, P1 loads decreased by an average of 8.6%, P2 loads decreased by an average of 10.5% and P3 loads increased by an average of 28.5%.

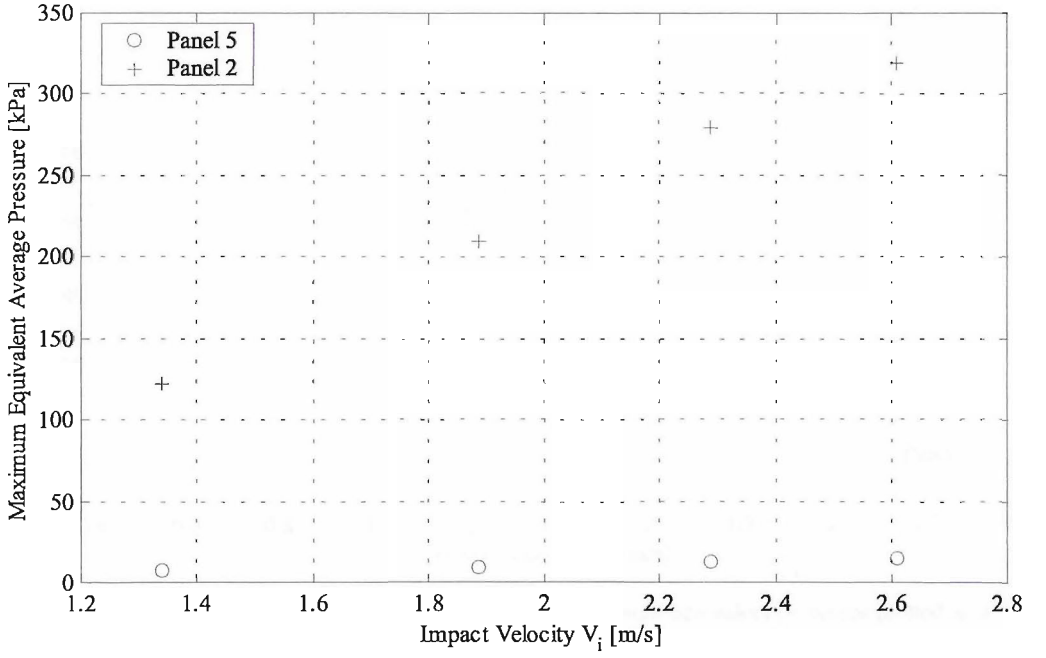

Figure 7 – Variation of the impact pressure along the girth. Equivalent pressure measured for Panel 2 and Panel 5 during same drops. All pressures plotted with respect to Panel 2 impact velocities.

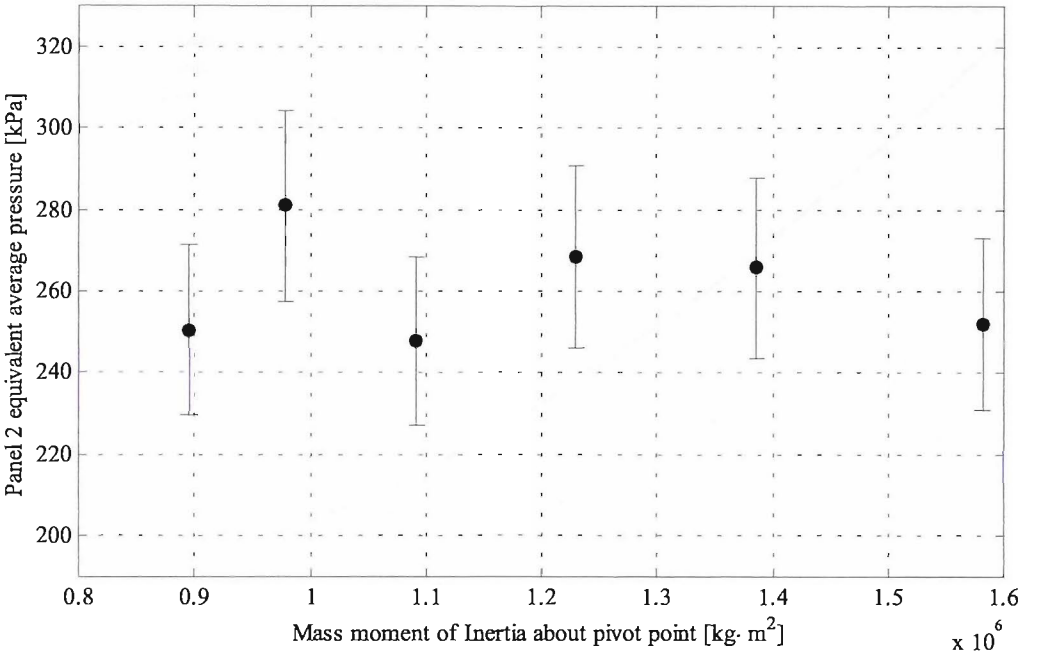

Figure 8 – Effect of the variation of the mass moment of inertia on maximum equivalent average pressures measured at Panel 2.

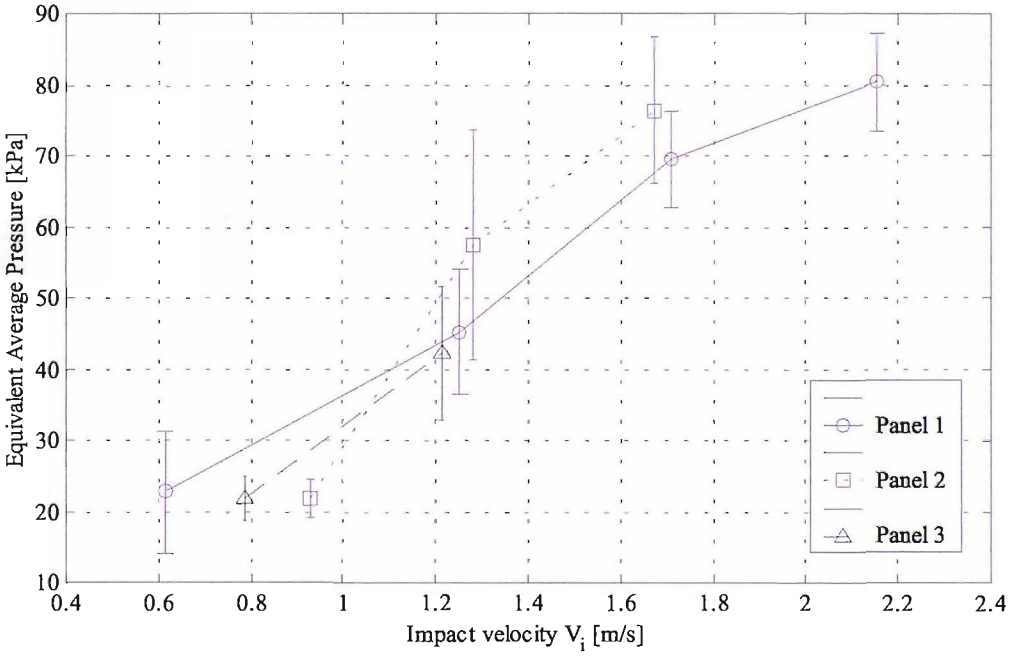

Figure 9 – Regular waves tests with forward speed: mean maximum equivalent pressures plotted as a function of the mean impact velocities. Data points obtained by calculating the average of the impact pressures recorded over each run. Error bars represent the standard deviation of the maximum pressures recorded over each run.

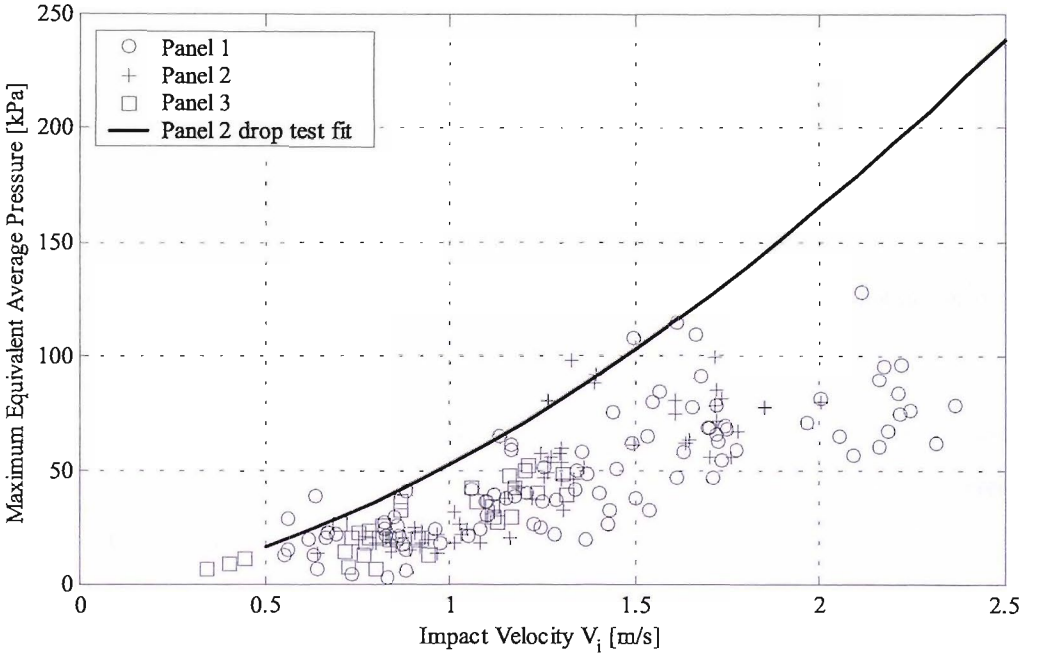

Figure 10 – Comparison of maximum equivalent average pressures obtained from tests in waves and from rotational drop tests (Panel 2 fitting line is reported for reference).

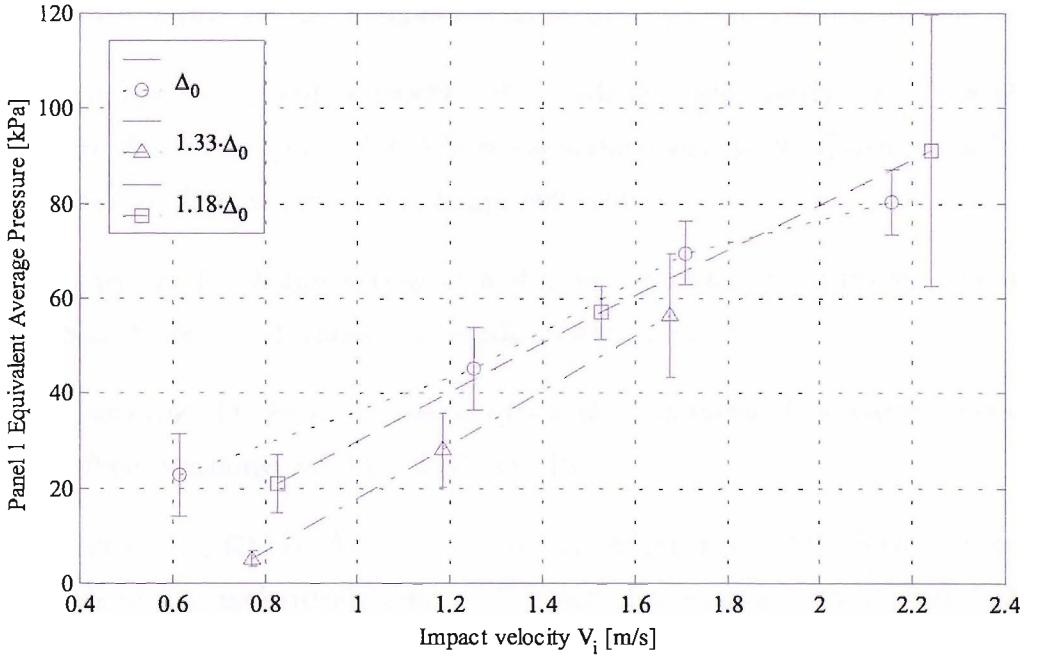

Figure 11 – Regular waves tests: effect of displacement variation on Panel 1 pressures.

References

[1] ABBOTT, I. H., AND VON DOENHOFF, A. E. *Theory of wing sections.* Dover Publications, 1959.

[2] ALLEN, R., AND JONES, R. A Simplified Method for Determining Structural Design-limit Pressures on High Performance Marine Vehicles. In *AIAA/SNAME Advanced Marine Vehicle Conference* (April 1978).

[3] AMERICAN BUREAU OF SHIPPING. Guide for building and classing offshore racing yachts, 1994.

[4] AMERICAN BUREAU OF SHIPPING. Guide for building and classing high-speed craft, 1997.

[5] ANDERSON, JR, J. *Fundamentals of Aerodynamics.* McGraw-Hill, 1991.

[6] ARMAND, J., AND COINTE, R. Hydrodynamic impact analysis of a cylinder. In *Proc. Fifth Intl. Offshore Mechanics and Arctic Engineering Symposium* (Tokyo, Japan, 1987), vol. 1, pp. 609–634.

[7] BAILEY, P. *Manoeuvring of a ship in a seaway.* PhD thesis, Department of Ship Science, University of Southampton, 1999.

[8] BARRICK, D. *Remote sensing of sea state by radar.* U.S. Government Printing Office, Washington D.C., 1972, ch. 12.

[9] BECK, R., REED, A., AND ROOD, E. Application of modern numerical methods in marine hydrodynamics. *SNAME Transactions 104* (1996), 519–537.

[10] BEREZNISTSKI, A. Slamming: the role of hydroelasticity. 333–351.

[11] BERGAN, P., BUENE, L., ECHTERMEYER, T., AND HAYMAN, B. Assessment of FRP Sandwich Structures for Marine Applications. *Marine Structures* (1994), 457–473.

[12] BISHOP, R., AND PRICE, W. *Hydroelasticity of Ships.* Cambridge University Press, 1979.

[13] BISHOP, R., PRINCE, W., AND TAM, P. On the Dynamics of Slamming, 1978. The Royal Institution of Naval Architects.

[14] BISHOP, R., PRINCE, W., AND TEMAREL, P. A Unified Dynamical Analysis of Antisymmetric Ship Response to Waves, 1979. The Royal Institution of Naval Architects.

[15] BISPLINGHOFF, R., ASHLEY, H., AND HALFMAN, R. *Aeroelasticity.* Addison-Wesley, 1955. Library of Congress Catalog Card Number 55-6561.

[16] BOYD, J. Analysis of non-linear vessel motions: Experiments and predictions. In *International Conference on Seakeeping and Weather* (London, UK, February 1995), Royal Institution of Naval Architects.

[17] BRITTING, K. *Inertial Navigation Systems Analysis.* Wiley-Interscience, New York, 1971.

[18] BROWN, K. C., AND JOUBERT, P. N. Pressure Loading of Aluminium Plating. *Marine Technology 27*, 6 (Nov. 1990), 378–386.

[19] BROWN, K. C., JOUBERT, P. N., AND YAN, P. Tests on Yacht Hull Plating. *Marine Technology 33*, 2 (April 1996), 130–140.

[20] BUENE, L., ECHTERMEYER, T., SUND, O., NYGARD, M., AND HAYMAN, B. Assessment of Long Term Effects of Slamming Loads on FRP Sandwich Panels. In *Papers from the FAST'91 Conference* (1991), pp. 365–379.

[21] CAMPBELL, I. The Response of a Tubular Beam to an Inclined Impact. Tech. Rep. 488/1, Wolfson Unit for Marine Technology and Industrial Aerodynamics, November 1983.

[22] CAMPBELL, I. Notes on yacht experimental techniques. Lecture Notes, University of Southampton, Department of Ship Science, 1996.

[23] CAMPBELL, I., WELLICOME, J., AND WEYNBERG, P. An Investigation into Wave Slamming. Loads on Cylinders (OSFLAG 2A) Final Report. Tech. Rep. 317, Wolfson Unit for Marine Technology and Industrial Aerodynamics, March 1977.

[24] CAMPBELL, I., AND WEYNBERG, P. Slam Load Histories on Cylinders. Tech. Rep. 416, Wolfson Unit for Marine Technology and Industrial Aerodynamics, August 1979.

[25] CAMPBELL, I., AND WEYNBERG, P. Measurement of Parameters Affecting Slamming. Tech. Rep. 440, Wolfson Unit for Marine Technology and Industrial Aerodynamics, February 1980.

[26] CARCATERRA, A., CIAPPI, E., IAFRATI, A., AND CAMPANA, E. Shock spectral analysis of elastic systems impacting on the water surface. *Journal of Sound and Vibration 229*, 3 (2000), 579–605.

[27] CARIDIS, P., AND STEFANOU, M. Dynamic Elastic/Viscoplastic Response of Hull Plating Subjected to Hydrodynamic Wave Impact. *Journal of Ship Research 41*, 2 (June 1997), 130–146.

[28] CHUANG, S. Theoretical investigations of slamming of cone shaped bodies. *Journal of Ship Research 13*, 4 (1969), 276–283.

[29] CLAUGHTON, WELLICOME AND SHENOI, Ed. *Sailing Yacht Design - Theory.* Addison Wesley Longman, 1998.

[30] CLOUGH, R., AND PENZIEN, J. *Dynamics of Structures.* McGraw-Hill, 1993.

[31] COTTON, P. D. A feasibility study for a global satellite buoy intercalibration experiment. Research and Consultancy Report 26, Southampton Oceanography Centre, Southampton, UK, 1998.

[32] COTTON, P. D. Analysis of altimeter wave period estimates in the north sea. Technical Report 19, Satellite Observation Systems, Southampton, UK, 1999.

[33] COTTON, P. D. Analysis of co-located jericho coastal in situ and altimeter data. Technical Report 15, Satellite Observation Systems, Southampton, UK, 1999.

[34] CURRY, R. Ocean-Racing Yachts - Structural Criteria. In *Intl. Conference on the Modern Yacht* (March 1998), The Royal Institution of Naval Architects.

[35] CURRY, R. Private written communication, 1999.

[36] DAVIES, C., CHALLENOR, P., COTTON, P., AND CARTER, D. On the measurement of wave period by a radar altimeter. submitted for publication to the Journal of Atmospheric and Oceanic Technology, 2000.

[37] DAVIES, C., COTTON, P., CHALLENOR, P., AND CARTER, D. Validation of wave period measurements from radar altimeter data. In *Proceedings of the CEOS Wind and Wave Validation Workshop* (The Netherlands, 1997), ESA, ESTEC, pp. 75–79.

[38] DET NORSKE VERITAS. Tentative rules for classification of high speed and light craft - Design Principles, Design Loads, 1991.

[39] ELLIOT, J., GRANT, D., HOLMAN, D., WAGEMAKERS, B., AND WOODGER, S. An investigation of the influence of slamming impact on the design of offshore sailing yachts. M.Eng. Group Design Project, School of Engineering Science, Ship Science, University of Southampton, 2002.

[40] ENGLE, A., AND LEWIS, R. A comparison of hydrodynamic impacts prediction methods with two dimensional drop test data. *Marine Structures 16* (2003), 175–182. not very detailed.

[41] FALTINSEN, O. *Sea Loads on Ships and Offshore Structures.* Cambridge University Press, 1990.

[42] FALTINSEN, O. Water Impact and Hydroelasticity, November 1996. Seminar on Hydroelasticity in Marine Technology, Trondheim.

[43] FALTINSEN, O. Water entry of a wedge by hydroelastic orthotropic plate theory. *Journal of Ship Research 43*, 3 (September 1999), 180–193.

[44] FALTINSEN, O. Hydroelastic slamming. *Journal of Marine Science and Technology 5*, 2 (2000), 49–65.

[45] FALTINSEN, O., KVÅLSVOLD, J., AND AARSNES, J. Wave impact on a horizontal elastic plate. *Journal of Marine Science and Technology 5*, 2 (1997), 87–100.

[46] FINOT, J., AND P. CONQ, (GROUPE FINOT, J.-E.-J. F. Private written communication, 1998-2003.

[47] FUNG, Y. *The Theory of Aeroelasticity.* John Wiley & Sons, 1955.

[48] G. VEDIER (BADEN, FRANCE). Private written communication, 2000-2003.

[49] GERRITSMA, J., KEUNING, J., AND VERSLUIS, A. Sailing yacht performance in calm water and in waves. In *The Eleventh Chesapeake Sailing Yacht Symposium* (March 1993), Society of Naval Architects and Marine Engineers.

[50] GILHOUSEN, D. An accuracy statement for meteorological measurements obtained from ndbc moored buoys. In *Proceedigs of the International Symposium on Marine Data Systems* (1986), pp. 198–204.

[51] GRIMSLEY, J. A comparison of prediction methods for impact pressures of high-speed, light craft. BSc Thesis, Webb Institure of Naval Architecture, June 1998.

[52] HAGIWARA, K., AND YUHARA, T. Study of wave impact load on ship bow. *Mitsubishi Juko Giho 11*, 6 (1974), 90–97.

[53] HARRIS, C., Ed. *Shock and vibration handbook*, 4th ed. McGraw-Hill, New York, U.S.A., 1996.

[54] HARTZ, F. The development of scantling requirements in support of the european boat directive, 1998.

[55] HAUGEN, E. *Hydroelastic analysis of slamming on stiffened plates with application to catamaran wetdecks.* Phd, NTNU Trondheim, Norway, 1999.

[56] HAYMAN, B. Recent Research at Det Norske Veritas Concerning Fast Craft. In *Intl. Conference on HIGH SPEED PASSENGER CRAFT* (June 1993).

[57] HAYMAN, B., HAUG, T., AND VALSGÅRD, S. Response of Fast Craft Hull Structures to Slamming Loads. In *First Intl. Conference on Fast Sea Transportation (FAST'91)* (Trondheim, Norway, 1991), pp. 381–398.

[58] HELLBRATT, S., AND VALLBO, S. Practical Aspects on Structural Analysis of a Weight Optimized FRP-Sandwich Stealth Corvette. In *Sandwich Construction 4* (1998), pp. 14–29.

[59] HELLER, S., AND JASPER, N. On the structural design of planing craft. *Transactions of the Royal Institution of Naval Architects 103* (1961), 49–65.

[60] HENRICKSON, W., AND SPENCER, J. A synthesis of aluminum crewboat structural design. *Marine Technology 19*, 1 (January 1982).

[61] HENTINEN, M., AND HOLM, G. Load measurement on the 9.4m sailing yacht "sail lab". In *Thirteenth International Symposium on Yacht Design and Yacht Construction* (Amsterdam, November 1994), HISWA.

[62] HOERNER, S., AND BORST, V. *Fluid-dynamic Lift.* Hoerner Fluid Dynamics, 1975.

[63] HUA, J., AND PQLMQUIST, M. Wave estimation through ship motion measurements - a practical approach. In *International Conference on Seakeeping and Weather* (London, UK, February 1995), RINA.

[64] HUANG, Y., AND SCLAVOUNOS, P. Nonlinear Ship Motions. *Journal of Ship Research 42*, 2 (June 1998), 120–130.

[65] HUTCHINSON, B. Seakeeping studies: A status report. *SNAME Transactions 98* (1990), 263–317.

[66] IACCARINO, R., MONTI, S., AND SEBASTIANI, L. Evaluation of Hull Loads and Motion of a Fast Vessel Based on Computations and Full Scale Experiments. In *NAV2000, Intl. Conference on Ship and Shipping Research* (September 2000).

[67] IAFRATI, A., CARCATERRA, A., CIAPPI, E., AND CAMPANA, E. Hydroelastic analysis of a simple oscillator impacting the free surface. *Journal of Ship Research 44*, 4 (December 2000), 278–289. deals with effect of oscillator stiffness on impact force.

[68] INTERNATIONAL MONOHULL OPEN CLASSES ASSOCIATION (IMOCA). Year book 2002. `http://www.imoca.org`, 2002.

[69] International Sailing Federation Offshore Racing Committee (ISAF ORC). Offshore special regulations v3.19. `http://www.isaf.org`, 2003.

[70] ISO TC188/WG 18. ISO 12215-5 Committee draft. Small craft - Hull construction/scantlings - Part 5: Design pressures, allowable stresses, scantling determination. Published by F. Hartz, ICOMIA, 2000.

[71] Jensen, A., Havsgård, G., Pran, K., Wang, G., Vohra, S., Davis, M., and Dandridge, A. Wet deck slamming experiments with a FRP sandwich panel using a network of 16 fibre optic Bragg grating strain sensors. *Composites Part B:Engineering 31* (2000), 187–198.

[72] J.K.Hammond. Conversion between acceleration, velocity and displacement in the frequency domain. Draft DTA Method Sheet M18.1, 1991.

[73] Jones, N. Slamming Damage. *Journal of Ship Research* (June 1973), 80–86.

[74] Joubert, P. Strength of Bottom Plating of Yachts. *Journal of Ship Research 26*, 1 (1982), 45–49.

[75] Kapsenberg, G., and Brizzolara, S. Hydro-elastic effects of bow flare slamming on a fast monohull. In *Fifth International Conference on Fast Sea Transportation (FAST'99)* (Seattle, August 1999).

[76] Kapsenberg, G., van 't Veer, A., Hackett, J., and Levadou, M. Whipping loads due to aft body slamming. In 24^{th} *Symposium on Naval Hydrodynamics* (Fukuoka, Japan, 2002).

[77] Keuning, P., and van der Werff, T. Rig load measurement and comparison with calculations. In *International HISWA Symposium on Yacht Design and Construction* (Amsterdam, The Netherlands, 1990).

[78] Kim, D., Vorus, W., Troesch, A., and Gollwitzer, R. Coupled hydrodynamic impact and elastic response. In *21st Symposium on Naval Hydrodynamics* (Norway, June 1996), pp. 424–437.

[79] Kincaid, D., and Cheney, W. *Numerical Analysis.* Brooks/Cole, 1996.

[80] KOEHLER, B., AND KETTLEBOROUGH, C. Hydrodynamic impact of a falling body upon a viscous incompressible fluid. *Journal of Ship Research 21*, 3 (1977), 165–181.

[81] KOROBKIN, A. Wave Impact on the Bow End of a Catamaran Wet Deck. *Journal of Ship Research 39*, 4 (Dec. 1995), 321–327.

[82] KREYSZIG, E. *Advanced Engineering Mathematics*, seventh ed. John Wiley & Sons, 1993.

[83] KROGSTAD, H., AND BARSTOW, S. Satellite wave measurements for coastal engineering applications. *Coastal Engineering 37*, 3-4 (1999), 283–307.

[84] KUHN, J., AND SCHLAGETER, E. The effects of flare and overhangs on the motions of a yacht in head seas. In *The Eleventh Chesapeake Sailing Yacht Symposium* (Annapolis, USA, 1993), Society of Naval Architects and Marine Engineers, pp. 261–276.

[85] KVÅLSVOLD, J., AND FALTINSEN, O. Hydroelastic modelling of wetdeck slamming on multihull vessels. *Journal of Ship Research 39*, 3 (September 1995), 225–239.

[86] LAWTHER, A., AND GRIFFIN, M. *Measurement of ship motion.* Academic Press, London (UK), 1980, pp. 131–139.

[87] LEUGEN, J., BABAUD, G., AND THIBERGE, E. High Speed Monohulls - Experimental Determination of Loads on Structure by Models and Full Scale Tests. In *Papers from the FAST'97 Conference* (1997), pp. 719–729.

[88] LLOYD, A. *Seakeeping.* Lloyd, Gosport, United Kingdom, 1998.

[89] LLOYD'S REGISTER OF SHIPPING. Rules and regulations for the classification of special service craft, 1996.

[90] LOADS AND RESPONSES COMMITTEE. Final report and recommendations to the 22nd ittc. In *22nd International Towing Tank Conference* (Seoul and Shanghai, 1999), ITTC.

[91] MANGANELLI, P., WAGEMAKERS, B., AND WILSON, P. A. Investigation of slamming loads using slam patches on a scale model of an open60' class yacht.

In 17^{th} *International Symposium on "Yacht Design and Yacht Construction"* (Amsterdam, The Netherlands, November 2002), HISWA.

[92] MANGANELLI, P., AND WILSON, P. An experimental investigation of slamming on ocean racing yachts. In *Fifteenth Chesapeake Sailing Yacht Symposium* (Annapolis, January 2001), Society of Naval Architects and Marine Engineers.

[93] THE MATHWORKS, INC. *MATLAB Signal Processing Toolbox User's Guide, version 6.1*, December 2002.

[94] MCCROSKEY, W. Unsteady airfoils. *Annual Review of Fluid Mechanics 14* (1982), 285–311.

[95] MCEWEN, L., HOBBS, M.,(SP TECHNOLOGIES LTD., SOUTHAMPTON,UK). Private oral communication, 2002-2003.

[96] MEI, X., LIU, Y., AND YUE, D. K. On the water impact of general two-dimensional sections. *Applied Ocean Research 21*, 1 (February 1999), 1–15.

[97] MEYERHOFF, W. Die berechnung hydroelasticher stösse. *Schiffstechnik 60*, 12 (1965).

[98] MICHEL, W. H. Sea spectra revisited. *MTECH 36*, 4 (1999), 211–227.

[99] MILES, M. Measurement of six degree of freedom model motions using strap-down accelerometers. In 21^{st} *American Towing Tank Conference* (Washington D.C., 1986), ATTC, pp. 369–375.

[100] MIROS A/S. *Wavex System Operating Instructions.* Asker, Norway, 2000.

[101] NAGAI, T., AND CHUANG, S.-L. Review of structural response aspects of slamming. *Journal of Ship Research 21*, 3 (September 1977), 182–190.

[102] NOAA ENVIRONMENTAL MODELING CENTER - MARINE MODELING AND ANALYSIS BRANCH. NCEP MMAB operational wave models, 2001. http://polar.ncep.noaa.gov/waves/.

[103] OAKLEY, O. H. An analytical and experimental study for prediction of ship impact forces in a seaway. Report 69-6, Massachusetts Institute of Technology, Department of Naval Architecture and Marine Engineering, Cambridge, Massachusetts 02139, August 1969.

[104] OCHI, M. Wave statistics for the design of ships and ocean structures. *SNAME Transactions 86* (1978).

[105] OCHI, M., AND BONILLA-NORAT, J. Pressure-velocity relationship in impact of a ship model dropped onto the water surface and in slamming in waves. Tech. Rep. 3153, Naval Ship Research and Development Center, Washington D.C., U.S.A., 1970.

[106] OCHI, M., AND MOTTER, L. Prediction of Slamming Characteristics and Hull Responses for Ship Design. In *SNAME Transactions* (1973).

[107] PAYNE, P. *Planing*, vol. 1 of *Design of high-speed boats*. Fishergate, Annapolis, MD, 1988.

[108] PURCELL, E., ALLEN, S., AND WALKER, R. Structural analysis of the u.s. coastguard island class patrol boat. *SNAME Transactions 96* (1988), 221–246.

[109] RAMOS, J., AND SOARES, C. G. Vibratory Response of Ship Hulls to Wave Impact Loads. 71–87.

[110] REICHARD, R. The Structural Response of Small Craft to Dynamic Loading. In *Fourteenth AIAA Symposium on the Aero-Hydronautics of Sailing* (Nov. 1984), vol. 30, pp. 105–110.

[111] REISSNER, E., AND STEVENS, J. Effect of finite span on the airload distributions for oscillating wings. Tech. Rep. 1195, NACA, 1947.

[112] ROSEN, A. Impact pressure analysis on high-speed craft in waves, through fe-analysis on full-scale and model measurement data. In *Eighth International Symposium on Practical Design of Ships and Other Floating Structures (PRADS)* (Shanghai, China, 2001), Y.-S. Wu, W.-C. Cui, and G.-J. Zhou, Eds., Elsevier Science Ltd., pp. 629–635.

[113] ROSEN, A. Impact pressure distribution reconstruction from discrete point measurements. *International Shipbuilding Progress 52*, 1 (2005), 91–107.

[114] ROSEN, A., AND GARME, K. Slamming studies on high-speed planing craft through full-scale trials and simulations. In *Fifth conference of Fast Sea Transportation (FAST'99)* (Seattle, USA, 1999).

[115] ROSEN, A., AND RUTGERSSON, O. Full-scale trials on a small high speed naval craft with focus on slamming. In *Seventeenth International Conference on Offshore Mechanics and Arctic Engineering* (1998).

[116] SALVENSEN, N., TUCK, E., AND FALTINSEN, O. Ship Motions and Sea Loads. In *SNAME Transactions* (1970).

[117] SAVITSKY, D., AND BROWN, P. Procedures for hydrodynamic evaluation of planing hulls in smooth and rough water. *Marine Technology 13*, 4 (October 1976), 381–400.

[118] SCHNITZER, E., AND HATHAWAY, M. Estimation of hydrodynamic impact loads and pressure distributions on bodies approximating elliptical cylinders with special reference to water landings of helicopters. TN 2889, NACA, 1953.

[119] SELLARS, F. The Influence of Structural Characteristics on Slamming Impact Pressures. *Journal of Ship Research* (March 1971), 49–58.

[120] SELLARS, F. Water impact loads. *Marine Technology 13*, 1 (January 1976), 46–58.

[121] SMITH, S. W. *The Scientist and Engineer's Guide to Digital Signal Processing.* California Technical Publishing, 1997.

[122] SNOWDON, J. *Vibration and Shock in Damped Mechanical Systems.* John Wiley & Sons, 1968.

[123] SPENCER, J. Structural design of aluminum crewboats. *Marine Technology 12*, 3 (July 1975).

[124] STAVOVY, A., AND CHUANG, S. Analytical Determination of Slamming Pressures for High-Speed Vehicles in Waves. *Journal of Ship Research 20*, 4 (Dec. 1976), 190–198.

[125] THEODORSEN, T. General theory of aerodynamic instability and the mechanism of flutter. Tech. Rep. 496, NACA, 1935.

[126] TINCELIN, T. Influence of hull form above the static waterline on seakeeping properties. Tech. rep., TU Delft - Faculteit der Werktuigbouwkunde en Maritieme Techniek, 1999.

[127] TOLMAN, H. Validation of a new global wave forecast system at ncep. In *Ocean Waves Measuremnt and Analysis* (1998), B. Edge and J. Hemsley, Eds., American Society of Civil Engineers.

[128] TOLMAN, H. *User manual and system documentation of WAVEWATCH-III version 2.22.* NOAA / NWS / NCEP / OMB, 2002. technical note 222.

[129] TROESCH, A., AND KANG, C. Hydrodynamic impact loads on three-dimensional bodies. In *16th Symposium of Naval Hydrodynamics* (Berkeley (CA), USA, 1986).

[130] VERHAGEN, J. The impact of a flat plate on a water surface. *Journal of Ship Research 11*, 4 (1967), 211–223.

[131] VON KARMAN, T. The impact of seaplane floats during landing. Technical note 321, NACA, 1929.

[132] VORUS, W. A Flat Cylinder Theory for Vessel Impact and Steady Planing Resistance. *Journal of Ship Research 40*, 2 (June 1996), 89–106.

[133] WAGNER, H. Über stoss und gleitvorgänge an der oberfläche von flüssigkeiten. *Zeitschrift für Angewandte Mathematik und Mechanik 12* (1932), 193–215.

[134] WANG, G., PRAN, K., SAGVOLDEN, G., HAVSGÅRD, G., JENSEN, A., JOHNSON, G., AND VOHRA, S. Ship hull monitoring using fibre optic sensors. *Smart Materials and Structures 10* (2001), 472–478.

[135] WORLD METEOROLOGICAL ORGANISATION. A guide to the code form FM 92-IX Ext. GRIB.

[136] WRAITH, R., BROWN, K., JOUBERT, P., AND YAN, P. The Response of Various Ships Hull Plating Materials to Pressure Loads Caused by Slamming. In *Papers from the FAST'93 Conference* (1993), pp. 461–472.

[137] WRAITH, W. *Pressure Loads on Ship Hull Plating Caused by Slamming.* Ph.D. thesis, University of Melbourne, 1998.

[138] XU, L., TROESCH, A., AND VORUS, W. Asymmetric Vessel Impact and Planing Hydrodynamics. *Journal of Ship Research 42*, 3 (Sept. 1998), 187–198.

[139] YAMAMOTO, Y., LIDA, K., FUKASAWA, T., MURAKAMI, T., ARAI, M., AND ANDY, A. Structural damage analysis of fast ship due to bow flare slamming. 124–136.

[140] ZAHN, P. B., AND GRIM, M. After action determination of encountered seaway. In *Intl. Conf. on Seakeeping and Weather* (London, UK, 1995), RINA, RINA.

[141] ZHAO, R., AND FALTINSEN, O. Water entry of two-dimensional bodies. *Journal of Fluid Mechanics 246* (1993), 593–612.

[142] ZHAO, R., FALTINSEN, O., AND AARSNES, J. Water entry of arbitrary two-dimensional sections with and without flow separation. In *21st Symposium on Naval Hydrodynamics* (Norway, June 1999), National Academy Press, pp. 408–423.

...to Bea and Mathieu